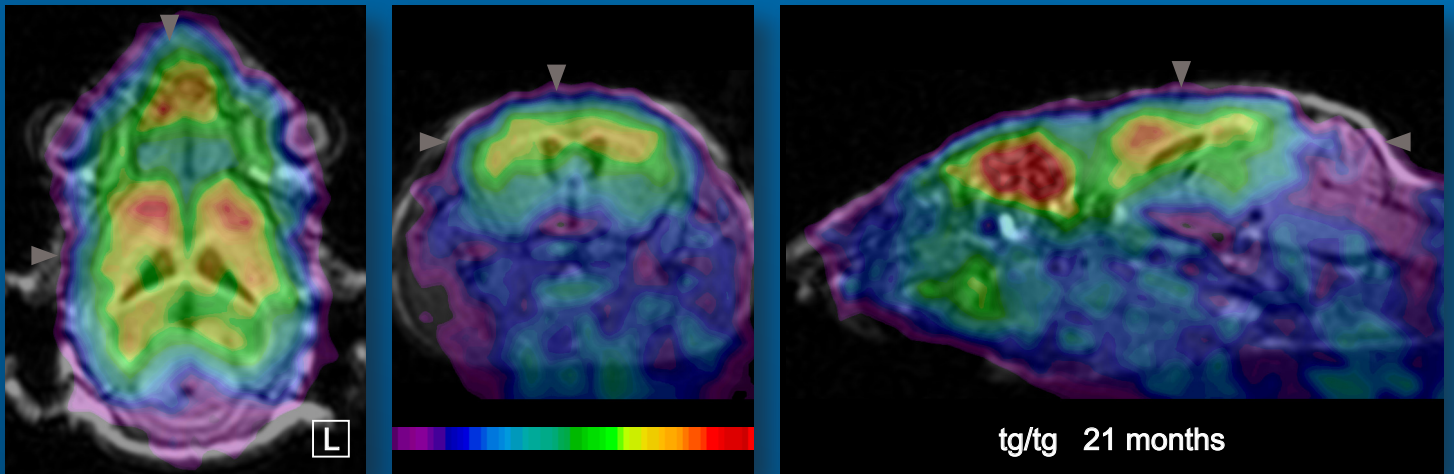
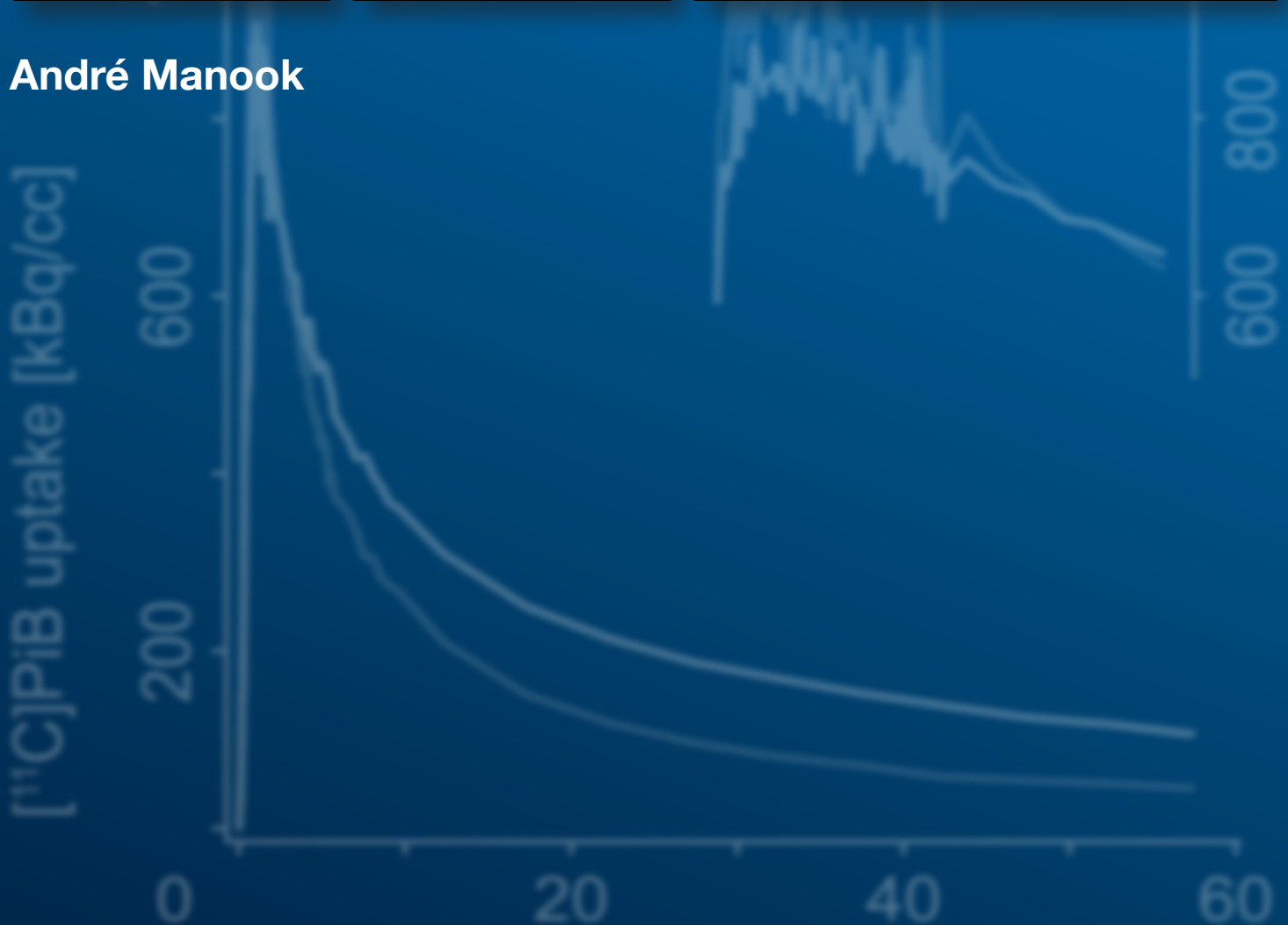


## Dissertation

# Preclinical PET as Translational Tool for Imaging Alzheimer's Disease



André Manook









Fakultät für Medizin  
Nuklearmedizinische Klinik und Poliklinik

## Preclinical PET as Translational Tool for Imaging Alzheimer's Disease

Small-Animal PET Imaging of Beta-Amyloid Plaques with [ $^{11}\text{C}$ ]PiB,  
its Multi-Modal Validation and  
Application to the Evaluation and Ranking of New AD Tracers

**André Manook**

Vollständiger Abdruck der von der Fakultät für Medizin der Technischen Universität München  
zur Erlangung des akademischen Grades eines

**Doctor of Philosophy (Ph.D.)**

genehmigten Dissertation.

**Vorsitzender:** Univ.-Prof. Dr. med. Claus Zimmer

**Prüfer der Dissertation:** 1. Univ.-Prof. Dr. Markus Schwaiger  
2. Univ.-Prof. Dr. Johann Förstl

Die Dissertation wurde am 14. März 2012 bei der Technischen Universität München eingereicht  
und durch die Fakultät für Medizin am 23. März 2012 angenommen.

---

This work has been supported by Deutsche Forschungsgemeinschaft (DFG),  
Karl-Max von Bauernfeind Association and Elite Graduate Network of Bavaria.



For Carolin.

---

## Declaration

I declare on oath that this thesis is my own work. If not mentioned otherwise in the specific section, every imaging procedure, experiment, pre- and post-processing and analysis of data was performed by myself. The majority of results presented here was published in international peer-reviewed journals by myself or in close collaboration with colleagues. Published data has been referenced appropriately.

This work has not been submitted in any form for another degree or diploma at any university or other institution of higher education. Information derived from published or unpublished work of others has been acknowledged in the text and a list of references is given.

Munich, 12 March 2012

André Manook

---

## Abstract

Alzheimer's disease (AD) causes unprecedented ethical, social and economical implications. The disease concept remains unclear and, hence, comprehensible therapeutic targets do not exist. This requires new and reliable approaches to investigate the disease concept further and to create hard evidence on postulated phenomena. Excessive production of amyloid- $\beta$  ( $A\beta$ ) via proteolysis of the amyloid precursor protein (APP) and the subsequent oligomerization and aggregation to  $A\beta$  plaques in the brain are considered to be initial pathological events and a major early and causal hallmark of AD. Therefore, non-invasive and quantitative  $A\beta$  imaging with positron emission tomography (PET) in humans is by now considered a helpful technique in this quest. Preclinical  $A\beta$  imaging in rodent disease models has been limited to very few studies and is still challenging. Recent improvements of small-animal PET ( $\mu$ PET) performance have facilitated in vivo imaging of rats and mice and there is an abundance of available transgenic (Tg) mouse models of AD. Together, they should provide for a valuable method in translational research such as developing specific imaging markers and monitoring new therapeutic approaches. However, intrinsic methodological constraints such as image resolution of PET and applicability of available research models have so far limited the feasibility of PET imaging in transgenic mouse models of AD.

The development and evaluation of a feasible protocol for small-animal PET imaging of  $A\beta$  plaques in mouse brain is presented as a first major contribution of this thesis. For this, the established "gold standard" radiotracer [ $^{11}\text{C}$ ]PiB was used with specific activities commonly used in human studies. In vivo mouse brain magnetic resonance (MR) images for anatomical reference were acquired with a clinical 1.5 Tesla (T) system. An initially unpublished, homozygous APP/PS1 transgenic mouse line (ARTE10) with low inter-animal variability was characterized for its potential applicability to in vivo imaging and employed to measure  $A\beta$  burden at different disease stages in homozygous and hemizygous animals. Extensive multi-modal cross-validations for the PET results in this mouse model with ex vivo and in vitro methodologies, including regional brain biodistribution, dual-label digital autoradiography, protein quantification with ELISA, fluorescence microscopy and semi-automated histological quantification are described as a second major contribution. This includes an additional all-in-one experimental design as a toolbox for translational applications. Employment of the established combined methodology for the evaluation and ranking of two novel lead compounds for AD imaging, as examples, 2-(*p*-[ $^{11}\text{C}$ ]Methylaminophenyl)-7-methoxy-

imidazo[2,1-*b*]benzothiazole ( $[^{11}\text{C}]\text{IBT}$ ) and 2-(4'-bromophenyl)-6-iodoimidazo[1,2-*a*]pyridine ( $[^{124}\text{I}]\text{BrIMPY}$ ), is shown as a third major contribution.

Specific in vivo  $[^{11}\text{C}]\text{PiB}$  uptake in individual brain regions with A $\beta$  plaque deposition was demonstrated and validated in all animals of a large study cohort including homozygous AD animals as young as nine months. Corresponding to the extent of A $\beta$  plaque pathology, old homozygous AD animals (21 months) showed the highest uptake followed by old hemizygous (23 months) and young homozygous mice (9 months). In all AD age groups the cerebellum was shown to be suitable as an intracerebral reference region. PET results were cross-validated and consistent with all applied ex vivo and in vitro methodologies. This also verified the validity and applicability of the animal model for PET imaging. The reliability and validity of the all-in-one design was verified. Specific in vivo uptake of  $[^{11}\text{C}]\text{IBT}$  and  $[^{124}\text{I}]\text{BrIMPY}$  in A $\beta$ -containing telencephalic brain regions with comparable ex vivo binding patterns to PiB and excellent correlation with A $\beta$  plaque pathology was shown by applying the combined experimental concept.

The results confirm that the experimental setup for non-invasive  $[^{11}\text{C}]\text{PiB}$  imaging of A $\beta$  plaques in a novel APP/PS1 mouse model of AD provides a feasible, reproducible and robust protocol for small-animal A $\beta$  plaque imaging. The experimental framework with this model allows for longitudinal imaging studies with follow-up periods of approximately one and a half years. The representative and successful evaluation of new PET and SPECT imaging agents with high sensitivities for in vivo A $\beta$  detection confirm that the developed experimental design provides a toolbox for AD research in transgenic mice and, hence, the foundation for translational Alzheimer neuroimaging.

**Keywords:**

Alzheimer's disease, neurodegeneration, amyloid-beta plaque, small-animal PET, tracer, PiB, BTA, IBT, IMPY, transgenic mouse, homozygous, APP/PS1, autoradiography, biodistribution, ELISA, histological plaque quantification

---

## Zusammenfassung

Die Alzheimer'sche Krankheit (Alzheimer's disease, AD) bringt beispiellose ethische, gesellschaftliche und wirtschaftliche Auswirkungen mit sich. Das Verständnis der Erkrankung ist weiterhin im Unklaren, weshalb nachvollziehbare therapeutische Angriffspunkte weitgehend fehlen. Dies erfordert neue und verlässliche Ansätze zur weiteren Untersuchung verschiedener Hypothesen und zur Untermauerung von bestehenden Postulaten der Krankheit. Die überschüssige Produktion von Amyloid- $\beta$  (A $\beta$ ) durch Abspaltung aus dem Amyloid Precursor Protein (APP) sowie die nachfolgende Oligomerisierung und Aggregation hin zu A $\beta$  Plaques im Gehirn werden als anfängliche pathologische Ereignisse und als eine der frühen und ursächlichen Kennzeichen der AD angesehen. Aus diesem Grund betrachtet man mittlerweile die nicht-invasive und quantitative A $\beta$  Bildgebung im Menschen, unter Verwendung der Positronen-Emissions-Tomografie (PET), als hilfreiche Technik auf der Suche nach den Ursachen. Allerdings ist die präklinische A $\beta$  Bildgebung in Nagetiermodellen bisher auf sehr wenige Studien beschränkt und weiterhin mit großen Herausforderungen verbunden. Jüngste Verbesserungen in der Leistungsfähigkeit von Kleintier-PET Geräten ( $\mu$ PET) ermöglichen die in vivo Bildgebung in Ratten und Mäusen. Im Zusammenspiel mit der Fülle verfügbarer transgener (Tg) Mausmodelle für die AD sollte  $\mu$ PET eine wertvolle Methode für translatorische Forschung sein, zum Beispiel zur Entwicklung spezifischer bildgebender Substanzen oder der Verfolgung neuer Therapieansätze. Intrinsic methodische Beschränkungen, wie zum Beispiel die Bildauflösung der PET und die Anwendbarkeit vorhandener Tiermodelle, haben bisher jedoch die Brauchbarkeit der PET Bildgebung in transgenen Mausmodellen der AD begrenzt.

Die Etablierung und Evaluation eines praktikablen Protokolls zur Kleintier-PET Bildgebung von A $\beta$  Plaques im Maushirn wird als der erste große Beitrag dieser Dissertation dargestellt. Hierfür wurde der etablierte "Goldstandard" Tracer [ $^{11}\text{C}$ ]PiB mit spezifischen Aktivitäten, wie sie in menschlichen Studien üblich sind, angewendet. Zur anatomischen Orientierung wurden in vivo Magnetresonanz (MR) Bilder des Maushirns mit einem klinischen 1.5 Tesla (T) Kernspintomographen aufgenommen. Eine zunächst unveröffentlichte, homozygote transgene APP/PS1 Mauslinie (ARTE10), deren Phänotyp geringe Schwankungen zwischen den einzelnen Tieren aufweist, wurde für ihre mögliche Anwendbarkeit in der in vivo Bildgebung charakterisiert. Daraufhin wurden die Tiere verwendet, um den A $\beta$  Gehalt in unterschiedlichen Erkrankungsstadien in homozygoten und hemizygoten Tieren zu messen. Die umfangreiche

multi-modale Kreuzvalidierung der PET-Ergebnisse in diesem Mausmodell, unter Verwendung von ex vivo und in vitro Methoden, wird als zweiter großer Beitrag dieser Arbeit beschrieben. Zu den angewendeten Validierungsmethoden zählen regionale Hirnbiodistribution des Tracers, digitale Autoradiographie mit zwei Isotopen, Bestimmung des A $\beta$ -Gehalts mittels ELISA, Fluoreszenzmikroskopie und eine semi-automatisierte histologische Quantifizierung. Diese Validierungsexperimente schließen einen zusätzlichen, kombinierten Experimentaufbau als eine Art „Werkzeugkasten“ für translatorische Anwendungen ein. Die Anwendung dieser kombinierten Methodik auf die Evaluation und Einordnung neuer Ausgangsverbindungen zur Bildgebung der AD wird als dritter großer Beitrag dieser Arbeit präsentiert. Als Beispiele zur Anwendung des „Werkzeugkastens“ werden 2-(*p*-[<sup>11</sup>C]Methylaminophenyl)-7-methoxyimidazo[2,1-*b*]benzothiazol ([<sup>11</sup>C]IBT) und 2-(4'-bromophenyl)-6-iodoimidazo[1,2-*a*]pyridin ([<sup>124</sup>I]BrIMPY) verwendet.

Als Ergebnis der Arbeit konnten die spezifische in vivo Aufnahme von [<sup>11</sup>C]PiB in verschiedenen Hirnregionen mit A $\beta$  Pathologie gezeigt werden. Dies wurde in allen Tieren einer großen Studienkohorte validiert, welche homozygote AD-Modelltiere mit einem Alter von neun Monaten, einschloss. Entsprechend dem Ausmaß ihrer A $\beta$  Plaque Pathologie, zeigten alte homozygote Tiere (21 Monate alt) die höchste Traceraufnahme, gefolgt von hemizygoten (23 Monate alt) und jungen homozygoten Mäusen (9 Monate alt). In allen Altersgruppen der AD-Modelle konnte gezeigt werden, dass das Kleinhirn als intrazerebrale Referenzregion sehr gut geeignet ist. Die PET-Ergebnisse wurden kreuzvalidiert und stimmten mit allen angewendeten ex vivo und in vitro Methoden überein. Zusätzlich wurde damit auch die Validität und Anwendbarkeit des Tiermodells für die PET-Bildgebung nachgewiesen sowie die Verlässlichkeit und Gültigkeit des kombinierten Experimentkonzepts bestätigt. Schließlich konnte mithilfe dieser kombinierten Experimente die spezifische in vivo Aufnahme der neuen Tracer [<sup>11</sup>C]IBT und [<sup>124</sup>I]BrIMPY in telenzephalen Hirnregionen mit hohem A $\beta$ -Gehalt gezeigt und die mit PiB vergleichbaren ex vivo Bindungsmuster und exzellenten Übereinstimmungen mit der A $\beta$  Plaque Pathologie demonstriert werden.

Die Ergebnisse bestätigen, dass der experimentelle Aufbau für die nicht-invasive [<sup>11</sup>C]PiB Bildgebung von A $\beta$  Plaques in einem neuen APP/PS1 Mausmodell der AD ein praktikables, reproduzierbares und stabiles Protokoll zur A $\beta$  Plaque Bildgebung im Kleintier erbringt. Aufgrund des geringen Alters der verwendeten homozygoten Tiere erlaubt das Versuchssystem unter Verwendung dieses Modells longitudinale Bildgebungsstudien über einen Zeitraum von ungefähr eineinhalb Jahren. Die repräsentative und erfolgreiche Evaluation

neuer PET und SPECT Verbindungen, die eine hohe Empfindlichkeit für den in vivo Nachweis von A $\beta$  hatten, bestätigte, dass das entwickelte Experimentdesign eine Art „Werkzeugkasten“ zur Erforschung der AD in transgenen Mäusen liefert und so eine Grundlage für die translatorische Bildgebung der Alzheimer'schen Krankheit schafft.

**Stichworte:**

Alzheimer'sche Krankheit, Neurodegeneration, Amyloid-beta Plaque, Kleintier-PET, Tracer, PiB, BTA, IBT, IMPY, transgene Maus, homozygot, APP/PS1, Autoradiographie, Biodistribution, ELISA, Histologische Plaque Quantifizierung



---

## Acknowledgements

Every effort in research is related to people working together, sharing their expertise or providing necessary facilities. This thesis is a marked expression of this culture, in particular for two reasons: first, the majority of the methodology applied for this thesis needed to be established in our lab and, second, there is a high level of interdisciplinarity in this project with strong interfaces to various disciplines in medicine, neuroscience, biology, chemistry, physics and mathematics.

First of all, I would like to thank my supervisor *Markus Schwaiger* for taking me into his team and for supporting my entrance to the TUM PhD program, for his professional support and his caring about the perspectives of my research. His professionalism and strategical thinking will remain an example on my future paths. *Alex Drzezga's* supervision was a good and strengthening experience. His deep insights from amyloid imaging in humans were an inspiration for possible applications at the bench. His strong scientific criticism from the clinical perspective was further improving the quality of my results. My mentor, *Hans Förstl*, made time for every request from my side. His relaxed, friendly and interested attitude always provided motivation and left me with a smile. *Alfred Buck's* personal research experience with molecular imaging in small animals made him a mentor who understood the challenges that I was facing. His words were balancing and soothing when work sometimes appeared slower and the outcomes fewer than colleagues were used to from clinical imaging. It is much appreciated that he took his mentorship seriously and travelled from Zurich to Munich when required. *Hans-Jürgen Wester* was one of four acting supervisors next to Markus Schwaiger. With my own background located in medicine, the scientific discussions with this excelling radiochemist were enlightening and inspiring. Also, he granted me unrestricted and long-lasting access to his facilities whenever I asked for it. *Gjermund Henriksen* was my close colleague on the radiochemistry side from the beginning. His trust in my research work and his supervising support was substantial and he made radiosyntheses possible beyond the usual. *Behrooz H. Yousefi* not only is the brilliant mind that moulds new compounds for an added repertoire of nature. He also has been a genuine and supportive supervisor to me and I am deeply grateful for his friendship.

The funding by organizations is only possible because of the people who see a value in supporting you. *Marlene Schneider* at TUM Scholarship Counselling was giving her best to provide me with contacts to potential funding in a situation where most resources were no

longer accessible. She truly cares about the students who approach her. *Olivia Schmid* at TUM Talent Factory took the baton from Marlene Schneider and channeled me towards the president of my university, Wolfgang A. Herrmann. Her caring and support gave an extra flavor to my application and was surely promoting. I am very grateful to *Wolfgang A. Herrmann*, for supporting my long endeavor by granting me financial and moral support with the TUM Presidential Science and Engineering Fellowship and the admission into the Elite Graduate Network of Bavaria. The thesis could not have been finished without his strong support. *Manfred Gratzl* together with *Karen Schmidt-Bäse* and *Karin Metzrath* were the first to help me enter a graduate research training group by Deutsche Forschungsgemeinschaft. *Helmut Adelsberger* made my acceptance to the very young TUM PhD program possible. Together with *Katrin Offe*, later, he did a great job in coordinating our academic activities and helped with short-term funding at a time when other resources were not available.

There could be no thesis like this without the good collaboration with our industry partners. *Michael Schoor* at TaconicArtemis, Cologne, was very informal about providing an unpublished transgenic mouse model at a time when my quest for a suitable research model was close to loosing perspective. It was a lucky coincidence that hopefully helped both sides. *Heinz von der Kammer* at Evotec, Hamburg, readily granted access to their research facilities and an abundance of required materials. His hospitality and good cooperation in an industry environment felt unusual and was a great experience. *Andreas Bolzer* at Carl Zeiss Microimaging, Munich, helped to solve the problems related to very large file sizes of highly resolved tiled microscopy images by granting temporary access to latest imaging software.

The people from whom I learned in workaday life, discussed, improved and performed experimental workflows are the colleagues who I will always link with precious work experiences. *Antje Willuweit* was originally a collaborator at Evotec and came to be a good friend for spurring on the publication of the valuable data that we had gathered at our sites. Her keen sense for precision and pragmatic solutions has frequently kept me in awe. *Stephan Platzer* introduced me to all necessary basics of rodent neurohistology with an ardent tinge for perfection. I have never met a medical doctor after him who had such sophisticated skills in staining chemistry combined with vast knowledge and intuition that would come in handy at the right point in time. *Kaspar Matiasek* took me to the advanced stages of rodent head and brain dissection and also helped me to maximize speed. Without his counsel, many important experimental components could not have been implemented in the way they are presented, here. *Thomas Brill* and *Julia Henke* never hesitated to help me when I came up with new experimental issues in animals. They provided every means possible to teach me the correct

experimenting procedures with small animals and were themselves willing to learn new ones for this sake. *Andreas Voss* has shown an ambition to help me in an unprecedented way. He could have simply introduced me to the basic applications of advanced microscopy but he stayed with me for several all-nighters and weekends to guarantee for good images under time pressure. *Sybille Reder* has not only been the good soul of our preclinical PET lab but also did everything possible to help me succeed with more or less complicated experimental workflows. She termed the combined multi-modal design the "champagne experiment" and we still need to open that bottle, Sybille. Equally, *Sabine Pirsig*, *Annette Frank* and *Galina Bursova* have given helpful hands and teachings. Clock watching was not their thing but persistently staying with the task at hand until we succeeded.

*Indy* and *Richard* not only supported me in ways that close friends may support a friend who is looking for a light at the end of the PhD tunnel. With their professional expertise they also were the documenting photographers of my experiments and both of them frequently provided me with private funding whenever grants or scholarships had run out. *Jenny* gave great help in formatting this text when time pressure was peaking. *Dörte*, *Christa-Marianne*, *Andrea* and *Benjamin* provided guidance and healing along edgy paths. Their helping activity gave strength, shape and clarity at special times. My parents, *Bärbel* and *Samuel*, led me into life in ways beyond common education. The lively and subtle expressions of their love and caring will always be with me.

In appreciation of the animals whose bodies and tissues were taken to yield the results presented in this study. May the sacrifice be of value and hint a way towards better experimental designs.



---

## Brief contents

Declaration .....	iv
Abstract .....	v
Zusammenfassung .....	vii
Acknowledgements .....	xi
Brief contents .....	xv
Contents .....	xvii
Thesis outline.....	1
<b>Part I. Introduction .....</b>	<b>3</b>
1. Introduction .....	5
2. Alzheimer's disease .....	7
3. Amyloid-beta .....	13
4. Brain PET imaging of A $\beta$ in small animals .....	21
<b>Part II. Results.....</b>	<b>33</b>
5. Introduction .....	35
6. PET imaging of A $\beta$ with [ $^{11}$ C]PiB in mouse brain .....	39
7. Quantitative multi-modal validation of PiB PET imaging in AD mice .....	61
8. Evaluation and ranking of new AD tracers .....	79
<b>Part III. Discussion .....</b>	<b>85</b>
9. Introduction .....	87
10. Small-animal PET .....	89
11. Research model.....	97
12. Validation experiments .....	99
13. Novel imaging markers .....	105
14. Conclusion.....	107
<b>Part IV. Material and methods.....</b>	<b>115</b>
15. Introduction .....	117
16. Animals .....	119
17. Radiosynthesis .....	121
18. Anesthesia .....	125

19. Substance administration .....	127
20. Small-animal PET .....	129
21. Mouse brain MRI .....	133
22. PET data analysis .....	135
23. Biodistribution .....	139
24. Tissue processing .....	141
25. Autoradiography .....	145
26. Neurohistological staining .....	147
27. Microscopy .....	149
28. Histological quantification of relative A $\beta$ plaque burden and plaque size distribution .....	151
29. A $\beta$ protein quantification with ELISA .....	153
30. Combined multi-modal experiment .....	155
31. Statistical analysis .....	157
<b>Appendix .....</b>	<b>159</b>
32. List of figures .....	161
33. List of tables .....	163
34. List of abbreviations .....	165
35. Links and URLs .....	169
36. List of publications within scope of thesis .....	171
37. Bibliography .....	175

---

## Contents

Declaration .....	iv
Abstract .....	v
Zusammenfassung .....	vii
Acknowledgements .....	xi
Brief contents .....	xv
Contents .....	xvii
Thesis outline.....	1
<b>Part I. Introduction .....</b>	<b>3</b>
1. Introduction .....	5
2. Alzheimer's disease .....	7
2.1 Definition.....	7
2.2 Epidemiology and economic burden.....	7
2.3 Diagnosis .....	8
2.4 Biomarkers.....	9
2.5 Therapeutic options .....	10
2.6 Disease concepts .....	11
3. Amyloid-beta .....	13
3.1 A $\beta$ protein – discovery, origin and structure.....	13
3.2 Amyloid hypothesis .....	15
3.3 Imaging target for PET.....	17
4. Brain PET imaging of A $\beta$ in small animals .....	21
4.1 Transgenic research models of amyloidosis .....	21
4.2 Small-animal PET scanners.....	23
4.3 A $\beta$ tracers in the preclinic .....	24
4.4 PET studies in mouse models of AD .....	27
4.5 Tracer development program at TUM .....	30
4.5.1 [ $^{11}\text{C}$ ]imidazo[2,1- <i>b</i> ]benzothiazole (IBT) - a novel amyloid tracer .....	30
4.5.2 [ $^{124}\text{I}$ ]BrIMPY - a novel 6-iodo-2-phenyl-imidazo[1,2- <i>a</i> ]pyridine (IMPY) .....	31
<b>Part II. Results.....</b>	<b>33</b>
5. Introduction .....	35
5.1 Scope and objectives .....	35
5.2 Description of projects .....	36
6. PET imaging of A $\beta$ with [ $^{11}\text{C}$ ]PiB in mouse brain .....	39
6.1 Prerequisites and foundations.....	39

6.1.1	PET and MRI scanning .....	39
6.1.2	Image co-registration of PET to MRI .....	40
6.1.2.1	Semi-automated manual overlay of early PET .....	40
6.1.2.2	Sequential dual-tracer PET with [ <sup>18</sup> F]FDG .....	41
6.2	Measuring small-animal [ <sup>11</sup> C]PiB PET images.....	43
6.2.1	Definition of regions.....	43
6.2.2	PET with MRI in study groups .....	45
6.2.3	Characterization of ARTE10 cerebellum as reference region.....	48
6.2.4	Calculating binding potentials and parametric images of mouse brain .....	49
6.2.5	PET test-retest scans .....	52
6.3	Specificity and locality of [ <sup>11</sup> C]PiB binding .....	53
6.3.1	Specific PiB binding in the mouse CNS .....	53
6.3.2	Extracerebral tracer retention in frontal proximity to brain.....	56
7.	Quantitative multi-modal validation of PiB PET imaging in AD mice .....	61
7.1	Study design .....	61
7.2	Cross-validation of PET in study groups.....	62
7.2.1	Quantification of [ <sup>11</sup> C]PiB binding in PET.....	63
7.2.1.1	Group behaviour of time-activity curves .....	64
7.2.1.2	Analyzing PET with different methods.....	64
7.2.2	Regional brain biodistribution of [ <sup>11</sup> C]PiB ex vivo .....	65
7.2.3	Autoradiography with [ <sup>3</sup> H]PiB ex vivo .....	67
7.2.4	Histological plaque quantification in neocortex of transgenic mice.....	68
7.2.4.1	Thioflavin S and Aβ40/42 antibodies for plaque quantification.....	68
7.2.4.2	Relative Aβ plaque area and plaque size distribution .....	70
7.2.5	Aβ40 and Aβ42 protein levels (ELISA) .....	72
7.2.6	Overview of cross-validation results .....	73
7.3	Combined multi-modal dual-label experiment.....	75
8.	Evaluation and ranking of new AD tracers .....	79
8.1	Combined multi-modal experiment with [ <sup>11</sup> C]IBT and [ <sup>3</sup> H]PiB .....	79
8.2	Multi-modal ex vivo experiment with [ <sup>124</sup> I]BrIMPY.....	82
	<b>Part III. Discussion .....</b>	<b>85</b>
9.	Introduction .....	87
10.	Small-animal PET .....	89
10.1	Overview of PET results .....	89
10.2	Co-registration and unspecific binding .....	90
10.3	Previous PET studies .....	91
10.4	Quantification of tracer binding.....	93
10.4.1	Standardized uptake values and similar measures .....	93
10.4.2	Reference tissue approaches.....	93
11.	Research model .....	97

---

12. Validation experiments .....	99
12.1 Histological quantification .....	99
12.2 ELISA .....	101
12.3 Dual-label digital autoradiography.....	102
12.4 Specificity of PET tracer binding .....	103
13. Novel imaging markers .....	105
13.1 [ <sup>11</sup> C]IBT.....	105
13.2 BrIMPY.....	106
14. Conclusion.....	107
14.1 Summary .....	107
14.2 Contribution.....	107
14.3 Translational value .....	109
<b>Part IV. Material and methods.....</b>	<b>115</b>
15. Introduction .....	117
16. Animals .....	119
17. Radiosynthesis .....	121
17.1 General procedures for radiosynthesis.....	121
17.2 General procedure for <i>N</i> - <sup>11</sup> C-methylation of primary and secondary amines.....	121
17.3 Adaptations for substance administration in mice .....	122
17.3.1 Alcohol content.....	122
17.3.2 Specific activity of the applied tracer .....	122
17.4 Radioligands .....	122
17.4.1 <i>N</i> -[ <sup>11</sup> C-methyl]-6-OH-benzothiazole ([ <sup>11</sup> C]PiB) .....	122
17.4.2 2-( <i>p</i> -[ <sup>11</sup> C]Methylaminophenyl)-7-methoxyimidazo[2,1- <i>b</i> ]benzothiazole ([ <sup>11</sup> C]IBT).....	122
17.4.3 2-(4'-bromophenyl)-6-iodoimidazo[1,2- <i>a</i> ]pyridine ([ <sup>124</sup> I]BrIMPY) .....	123
18. Anesthesia .....	125
19. Substance administration.....	127
20. Small-animal PET .....	129
20.1 General PET scanning procedure.....	129
20.2 Sequential dual-tracer PET scans with [ <sup>11</sup> C]PiB and [ <sup>18</sup> F]FDG.....	131
20.3 CNS removal during PET.....	131
21. Mouse brain MRI .....	133
22. PET data analysis .....	135
22.1 General image data preprocessing .....	135
22.2 Image co-registration and quality control.....	135
22.3 Volume-of-interest (VOI) definition.....	136
22.4 Quantification of dynamic [ <sup>11</sup> C]PiB PET data.....	137
23. Biodistribution .....	139

23.1 Regional brain biodistribution .....	139
23.2 Cranial biodistribution of [ <sup>11</sup> C]PiB.....	139
24. Tissue processing .....	141
24.1 Gene expression analysis (quantitative RT-PCR).....	141
24.2 Mouse brain for histology and autoradiography .....	142
24.3 Mouse brain tissue for quantitation of Aβ protein levels .....	142
24.4 Mouse cranium for [ <sup>3</sup> H]PiB ex vivo autoradiography.....	142
25. Autoradiography.....	145
25.1 Digital autoradiography .....	145
25.2 Tritium plate autoradiography .....	146
25.3 Quantification of tracer retention on autoradiographs .....	146
26. Neurohistological staining .....	147
26.1 Thionin fast nuclear stain (Nissl).....	147
26.2 Thioflavin S staining .....	147
26.3 Aβ40 and Aβ42 immunohistochemistry .....	147
27. Microscopy.....	149
28. Histological quantification of relative Aβ plaque burden and plaque size distribution .....	151
29. Aβ protein quantification with ELISA.....	153
30. Combined multi-modal experiment.....	155
31. Statistical analysis .....	157
<b>Appendix .....</b>	<b>159</b>
32. List of figures.....	161
33. List of tables.....	163
34. List of abbreviations .....	165
35. Links and URLs .....	169
36. List of publications within scope of thesis .....	171
36.1 International peer-reviewed journals .....	171
36.2 International conferences .....	172
36.3 National conferences.....	173
36.4 Other publications .....	173
37. Bibliography .....	175

---

## Thesis outline

The thesis is subdivided into four major parts:

PART ONE gives a general introduction towards the basic themes of the thesis and outlines the motivating aspects for this kind of work. It presents amyloid-beta imaging with PET in the context of Alzheimer's disease and necessary considerations when bringing it to a preclinical level. This includes short reviews on research models, PET technology and available radioligands focused towards the core of the thesis.

PART TWO describes the outcomes of the thesis in three major chapters beginning with the basic steps of small-animal PET imaging of amyloid-beta plaques, culminating in an extensive quantitative cross-validation battery and ending with two exemplary applications of the final experimental setup.

PART THREE discusses challenges of the small-animal PET approach as well as the value of the applied research model in this context. It goes on by looking at sensitive aspects of the validation methodologies and the qualities of two novel imaging markers for preclinical in vivo imaging. The discussion ends with a conclusion of the presented work. It includes a summary of the claimed contributions of this thesis along with some thoughts on its translational value.

PART FOUR contains all methods that were applied to yield the results presented in this thesis. The majority of methods were established from scratch. Contributions of colleagues are properly mentioned in the relevant section. The sequence in which methods are described is chosen to reflect the real workflow of experiments and analyses.

The APPENDIX comprises parts for more detailed reference within the thesis like lists of figures and tables and abbreviations. It also provides a list of conference abstracts and publications that were published within the scope of this thesis.



---

# **Part I.**

## **Introduction**



---

## 1. Introduction

The introduction begins with a note on Alzheimer's disease (chapter 2). It mentions the definition (chapter 2.1) and the reasons for the worries about its social impact (chapter 2.2). An outline on the development of the diagnostic criteria for AD is given (chapter 2.3) followed by biomarkers (chapter 2.4). A few therapeutic options are indicated (chapter 2.5). The Alzheimer's chapter closes with disease concepts (chapter 2.6) besides amyloid-beta showing how little the disease can be grasped even today. Amyloid-beta is the imaging target in this thesis and is therefore presented in a chapter on its own (chapter 3). It provides some impressions on the protein itself (chapter 3.1), the hypotheses on its role in AD (chapter 3.2) and a few reasons for choosing it as an imaging target (chapter 3.3).

By the end of chapter 3, the interest in small-animal PET imaging for the amyloid-beta protein may be more obvious. As it requires a suitable research model first, chapter 4 begins with a short outline on prominent rodent models (chapter 4.1) that could be considered for the task. It then provides a concise perspective on small-animal PET scanners (chapter 4.2) followed by a mini-overview on preclinically evaluated A $\beta$  ligands (chapter 4.3). Of these, only very few have been used in small-animal PET imaging studies (chapter 4.4). Chapter 4 ends with a description of our AD tracer development program as the bridge towards results (chapter 4.5).



## 2. Alzheimer's disease

### 2.1 Definition

Alzheimer's disease (AD) is the well-known term for the most common form of dementia which the 10<sup>th</sup> Revision of International Statistical Classification of Diseases and Related Health Problems (ICD-10) [271] defines as a primarily neurodegenerative disease of unknown etiology but distinguishing neuropathological and neurochemical characteristics. This definition is surprisingly close to what Alois Alzheimer presented orally on 3 Nov 1906 [4] and published one year later [5]. Since then, the two core pathological hallmarks of AD still are amyloid- $\beta$  (A $\beta$ ) plaques and neurofibrillary tangles [25,176,11]. This definition relies on a histopathological post-mortem diagnosis while the clinical (ante-mortem) definition of the disease is not as straightforward and needs, yet, to be clearly established [107].

### 2.2 Epidemiology and economic burden

Worldwide, more than 35 million people have Alzheimer's disease. The prevalences in North America and Western Europe are comparable with around six million affected patients [58,11,160]. In Germany, it is at about 1.3 million [20,160]. Projection analyses by Brookmeyer et al. towards the year 2050 [26] predict an increase of AD prevalence by a factor of about 2.5 (Figure 1).

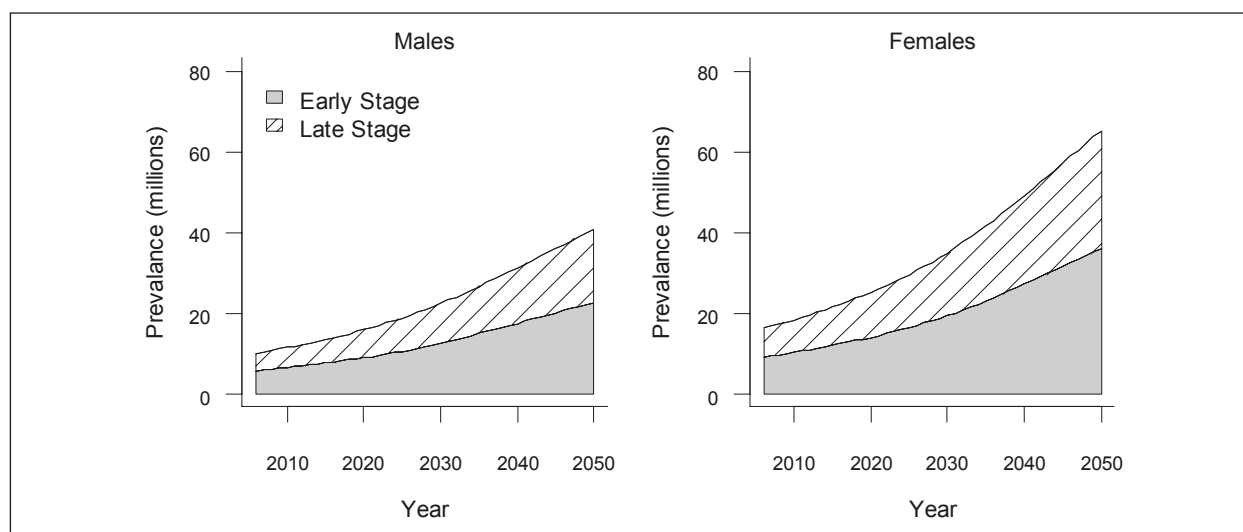


**Figure 1: Prediction of global Alzheimer's disease prevalence development.**

Worldwide projections of Alzheimer's prevalence (in millions) for the years 2006–2050, by stage of disease: males (*left panel*) and females (*right panel*). Reprinted with permission from [26]. Copyright (2007) Elsevier.

Brookmeyer et al. also estimated the effects of different intervention scenarios regarding the delay of disease onset and disease progression. They postulated that a therapeutic intervention that delays disease progression by an average of 2 years would decrease nearly 7 million late-stage cases by 2050 [26].

In Germany, total costs of care for AD patients in 2007 were about € 40 billion [160] of which about 60 % are usually accounted for by informal care as provided by family members [268].

These few numbers may explain why funding efforts and research initiatives to prevent, diagnose and treat AD have increased substantially. For example, the Obama Administration just announced a \$ 156 million investment in the framework of their National Alzheimer's Project Act over the next two years [248] and the European Union has just called out an initiative on the optimization of neurodegeneration biomarkers [57].

### 2.3 Diagnosis

In July 1984, criteria for the clinical diagnosis of Alzheimer's disease were established and published by the National Institute of Neurological and Communicative Disorders and Stroke (NINCDS) and the Alzheimer's Disease and Related Disorders Association (ADRDA) workgroup. At that time, there was a clear notion that AD was a clinical-pathological entity [173,107]. It took a few decades to realize that the correspondence between clinical symptoms and the underlying pathology is not necessarily consistent [107]. In April 2011, the revised criteria were published under the auspices of the National Institute on Aging (NIA) and Alzheimer's Association and clearly indicated the reconceptualization of the former notion on unity [107,123,174,229].

Diagnosis of AD begins with verifying general dementia symptoms, first. Briefly, there should be a notable decline relative to previous levels of activity and an interference with daily routines together with cognitive and behavioral impairments that are detected by history-taking and cognitive assessment (e.g. mini-mental status examination (MMSE) or clinical dementia rating (CDR)) [174]. In this process, treatable causes for dementia (e.g. metabolic, toxic, infectious) need to be considered and excluded [162]. The next step is the diagnosis of either *probable* or *possible* AD dementia. In short, insidious onset, worsening of cognition and memory impairment (amnestic presentation) are the clinical hallmarks of *probable* AD while atypical courses or etiologically mixed presentations of the disease are classified as *possible* [174].

## 2.4 Biomarkers

Implementation of biomarkers for the diagnosis of AD was strongly propagated long before the NINCDS-ADRDA criteria were revised [55]. Their inclusion is considered to be one of two major novelties in the revised criteria [107]. However, McKhann and colleagues remain conservative and state that they *do not advocate the use of AD biomarker tests for routine diagnostic purposes at the present time* [174]. Hence, biomarkers were not mentioned in chapter 2.3 on AD diagnosis but are outlined separately, here.

First, it should be noted that "biomarker" in the context of Alzheimer's disease is defined to comprise fluid analytes and imaging measures alike. Even though an extensive battery of such biomarkers has been analyzed [49,22], the revised criteria constrain themselves to the five most widely studied markers that can be classified into two categories [107]: First, markers of A $\beta$  accumulation (Positron emission tomography (PET) for amyloid, A $\beta$ 42 in cerebrospinal fluid (CSF)) and, second, markers of neuronal degeneration (PET with [ $^{18}$ F]-fluoro-deoxy-D-glucose (FDG), structural magnetic resonance imaging (MRI), tau in CSF). These two categories reflect the current and predominant notion on the pathophysiology of AD which regards the accumulation of A $\beta$  in plaques and tau protein deposition in neurofibrillary tangles in correlation to neuronal injury.

Current developments in biomarker studies open up new perspectives on the combination of biomarkers. For one, a distinct temporal behavior of different markers was realized (Figure 2), for example, that biomarkers for A $\beta$  grow to be abnormal first and neuronal injury biomarkers become abnormal later [49,107]. Further, and at least as interesting, researchers begin to combine biomarkers for multifactorial approaches [231] and more differentiated understanding of pathophysiology.

In the context of this thesis, a statement by Jack and colleagues to the future of biomarkers is of relevance: *obtaining standardized, reliable, and reproducible diagnostic caliber readouts of biomarker tests must be possible in any setting in which biomarkers are applied – research, clinical trials, or clinical care* [107].

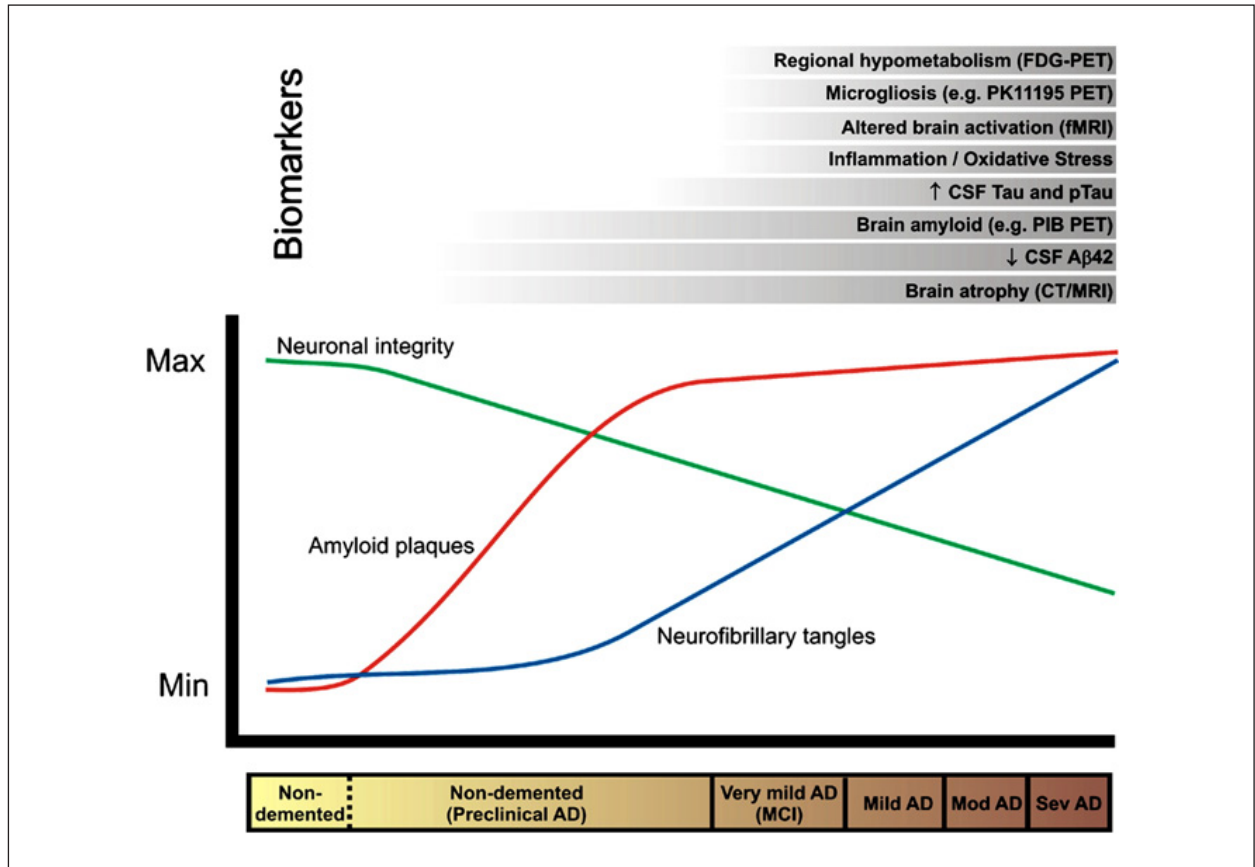


**Figure 2: Temporal hierarchy of biomarkers in the progression of Alzheimer's disease.**

Hypothesized relationship between the time-course of changes in various biomarkers in relation to the neuropathology and clinical changes of Alzheimer's disease. Reprinted with permission from [49]. Copyright (2009) Elsevier.

## 2.5 Therapeutic options

At the moment, there are only two classes of pharmaceuticals that have been shown to provide some symptomatic relief in randomized controlled trials: Cholinesterase inhibitors (donepezil, rivastigmine, galantamine) and an NMDA receptor antagonist (memantine) [11].

Besides these two, there basically are as many experimental disease-modifying drugs available as there are devised concepts on the disease [43,44,196], but only some of them have been brought to clinical trials [11]. In essence, many of these experimental drugs aim at preventing A $\beta$  deposition (e.g. secretase inhibition [163]) or at reducing A $\beta$  plaque load (e.g.  $\beta$ -sheet breaking [270] and vaccination [210,183]). Enormous industrial efforts, large screening campaigns and medicinal chemistry programs have led to several drugs for both approaches that are currently in clinical phase 3 trials [44], for example, the gamma-secretase inhibitor semagacestat [61] and the monoclonal antibody bapineuzumab [205,122].

Apart from that, two recent studies received public attention and may be worth mentioning: Clarc et al. addressed the hypometabolic states in AD by administering intranasal insulin in a randomized, double-blind, placebo-controlled pilot study that also used FDG PET as an outcome measure [48]. Cramer et al. medicated APP/PS1 mice [50] with the apolipoprotein E (ApoE) targeted retinoid X receptor (RXR) agonist, bexarotene, and observed a phenomenal clearance of soluble A $\beta$  (> 50 % within just 72 hours).

Addressing similar pathophysiological mechanisms, surgical approaches have been tried as well. For example, Goldsmith targeted cerebral blood flow (CBF) by omental transposition [72] and Suthana et al. observed memory enhancement after deep-brain stimulation in the entorhinal area [235].

Elmar Graessel and colleagues very recently reported that a more encompassing non-pharmacological treatment approach to Alzheimer's disease [75] may compare well to the common antidementia drugs. They termed their intervention MAKs: 'M' for motor stimulation, 'A' for activities of daily living, 'K' for cognitive stimulation (it is a German research group), and 'S' for a spiritual element (for example, discussing topics such as happiness or singing a song).

The spectrum of experimental therapeutic approaches and the insufficiency of approved pharmacological treatment options for AD [230] reflect how little the disease is still understood.

## 2.6 Disease concepts

The quest for slowing down disease progression or at best reversal of symptoms is intrinsically linked to the understanding of Alzheimer's disease. Thinking about risk factors can be a helpful first step. Risk factors can be classified into modifiable and non-modifiable. Modifiable ones are of interest for aspects of disease prevention. The well-known factors that influence many other diseases also have an impact on AD: obesity, alcohol and smoking combined with lacking physical activity [19,6,83,152]. Socially important, modifiable risks are lower education and lacking mental activity that hint towards the concept of cognitive reserve [249] as well as social inactivity [63]. Does this imply that AD is a disease related to a certain kind of laziness?

The strongest non-modifiable risk factors for acquiring AD are age [58] and (female) gender [255]. Beyond that, Ballard et al. state that *the amount of risk of Alzheimer's disease that is attributable to genetics is estimated to be around 70%* [67,17,11] in the sporadic form of AD (see also chapter 3.1). Homozygosity for the epsilon-4 allele at the ApoE locus on

chromosome 19 is the biggest and one of the best-examined genetic risk factors [47]. However, it still remains the only definite locus [85].

Beyond the risk factors is the labyrinth of molecular paradigms. They have evolved and accumulated over decades and each time it was believed that a significant solution towards cure was found. Alois Alzheimer described plaques and tangles [5] and both are in the realm of protein abnormalities. Amyloid-beta is the major constituent of plaques and is given its own chapter in this thesis (chapter 3). The defining component of neurofibrillary tangles is an abnormally hyperphosphorylated and aggregated form of tau [125] which like A $\beta$  is hypothesized to be cytotoxic [124]. Synaptic failure may be caused by these abnormal proteins [218] or even be a normal age-related process [166]. Failure of the cholinergic system was a relatively early finding [51] and spurred the development of acetylcholine esterase inhibitors (chapter 2.5). Damaged mitochondria [207,93,255] and oxidative stress via released oxidizing free radicals may lead to impaired glucose transport [165] and, hence, hypometabolism. Inflammation as demonstrated by activated microglia and reactive astrocytes is another important phenomenon of which it is not clear whether the abnormal proteins or the neurons themselves are causing it [46,272]. Interestingly, about three decades ago, Stanley Prusiner hypothesized that Alzheimer's disease may be a prion-like infectious disease [195] and this concept appears to be in quite some revival [227,117]. In a way, this notion would reduce vaccination attempts against A $\beta$  to absurdity.

What is Alzheimer's disease? How many diseases is Alzheimer's disease or is it a normal process of aging? Is the kaleidoscope of genetic, biochemical and histological phenomena we observe in AD patients guiding us towards helpful solutions or would it be necessary to take a completely different perspective? The answer seems to be, we do not know, even more than 100 years after it was described academically for the first time. The research community is torn apart and controversies on seemingly established findings appear frequently [178,254]. This may be a saddening perspective in regard to projected epidemiologic developments in this field (chapter 2.2, Figure 1). Peter Whitehouse and colleagues are clear about this [265]: *We must look beyond the molecular paradigm and understand AD as a multifaceted condition intimately related to aging.* This is one way to go. The other is to also bring the molecular paradigm onto a more stable foundation by developing reliable tools for the verification of postulated concepts.

---

## 3. Amyloid-beta

### 3.1 A $\beta$ protein – discovery, origin and structure

Alois Alzheimer described his histopathological findings as: *In the center of an otherwise almost normal cell there stands out one or several fibrils due to their characteristic thickness and peculiar impregnability. Numerous small miliary foci are found in the superior layers* [171]. The *small miliary foci*, still are one of the two pathognomonic features of AD and are widely called "amyloid- $\beta$  plaques", today, after Glenner and Wong extracted and sequenced *beta-protein* ( $\beta$ -pleated sheet structure) from meningeal cerebrovascular amyloid in 1984 [69].

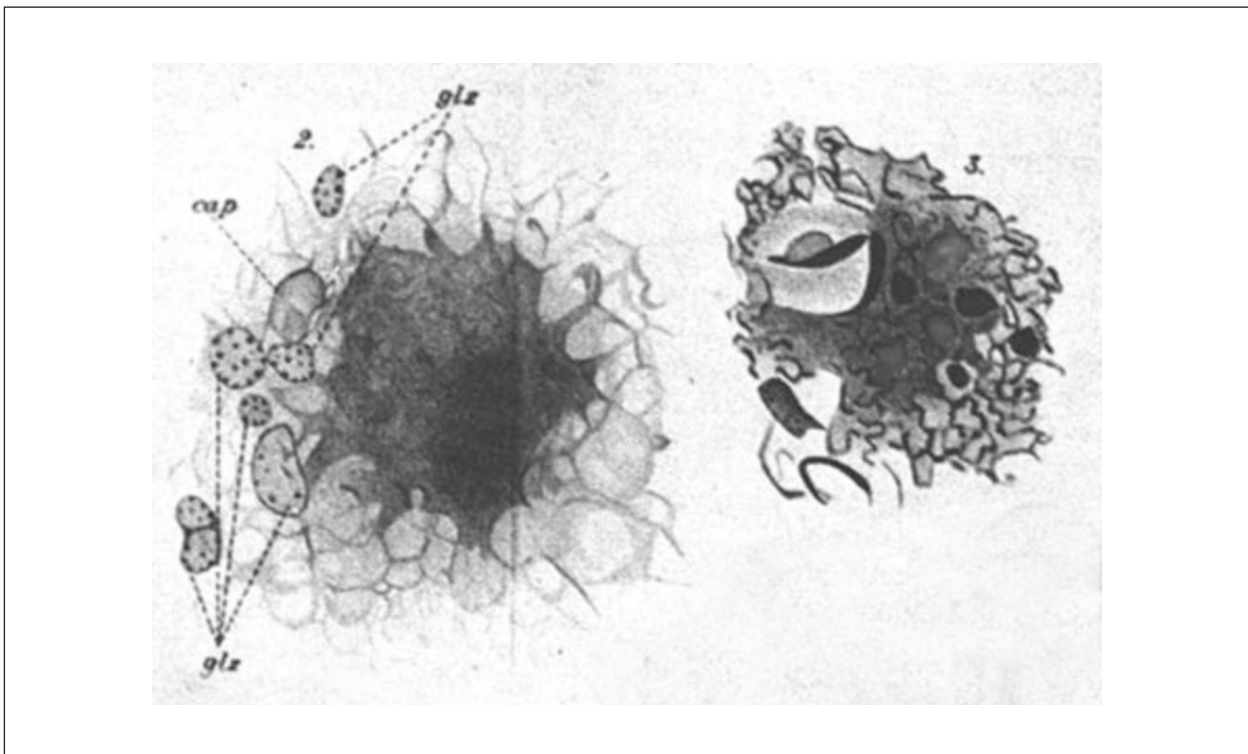


**Figure 3: Plaques of Auguste D.**

Pictures drawn with Abbe's camera lucida. Shown are just items 2 and 3 taken from "Tafel XX". Reprinted with permission from [170]. Copyright (2006) Springer.

Knowing that all patients affected by Down's syndrome (trisomy 21) develop AD-like neuropathology from around 40 years of age, Glenner and Wong also performed their protein extraction on post-mortem Down Syndrome brains and found homology between both protein species [68]. Hence, they closed their paper with the hypothesis that the *beta-protein* in AD patients should be linked to a genetic defect on chromosome 21. The discovery of the protein

lead to the cloning of the amyloid precursor protein (APP) gene and its mapping to chromosome 21 close to the duplicated parts in trisomy 21 in 1987 [120,240]. Then, Haass et al. were among the first to generate A $\beta$  in vitro (transfected human cells) [81].

A key feature of A $\beta$  protein is its propensity for fibrillogenesis [127]. In 1996, Lomakin et al. suggested a simple mechanistic model for nucleation-dependent polymerization (NDP) of A $\beta$  [157]. In this model, a critical protein concentration determines whether polymerization can happen or not. If it is exceeded there is a lag time before polymerization occurs. This simple model uses two stable states of A $\beta$ , only: A $\beta$  monomers in aqueous solution and A $\beta$  fibrils, a process reminiscent of a typical phase transition [7]. Evolving imaging technology like atomic force microscopy brought to light that this model is overly simplistic and that there are transient intermediate A $\beta$  species involved [138]. For A $\beta_{1-42}$ , Arimon et al. suggested a possible sequence from A $\beta$  monomers to protofibrils, protofibril bundles, bundle sacking, nodular fibrils, to finally reach smooth fibrils [8]. Figure 4A provides an electron microscopic impression of these protofilaments for A $\beta_{1-40}$  and A $\beta_{1-42}$ . The efforts to understand the structure of A $\beta$  better [247] have good reason. In case, A $\beta$  would be a true cause for AD, the development of formation inhibitors [71] would require better knowledge about possible target sites. Furthermore, the identification of possible binding sites for A $\beta$  radioligands (Figure 4B) would help the development of further imaging markers for A $\beta$ .

Binding sites for A $\beta$  ligands are not yet established but merely hypothesized. Cai et al. classify possible binding sites according to three broad categories of typical PET ligands, based on the A $\beta$  staining dyes Congo Red and Thioflavin T, as well as FDDNP (an aminonaphthalene) [30]. Lockhart et al. suggest three high-affinity binding sites for Thioflavin T derivatives (like Pittsburgh compound-B (PiB)) and claim that two additional binding sites have higher capacity than the one usually identified in previous binding studies [155]. Hypothesized locations of these binding sites are indicated in Figure 4B. Returning to Alzheimer's *miliary foci*, it needs to be kept in mind that A $\beta$  plaques are complicated multi-component structures that largely contain A $\beta$  fibrils but not only these.

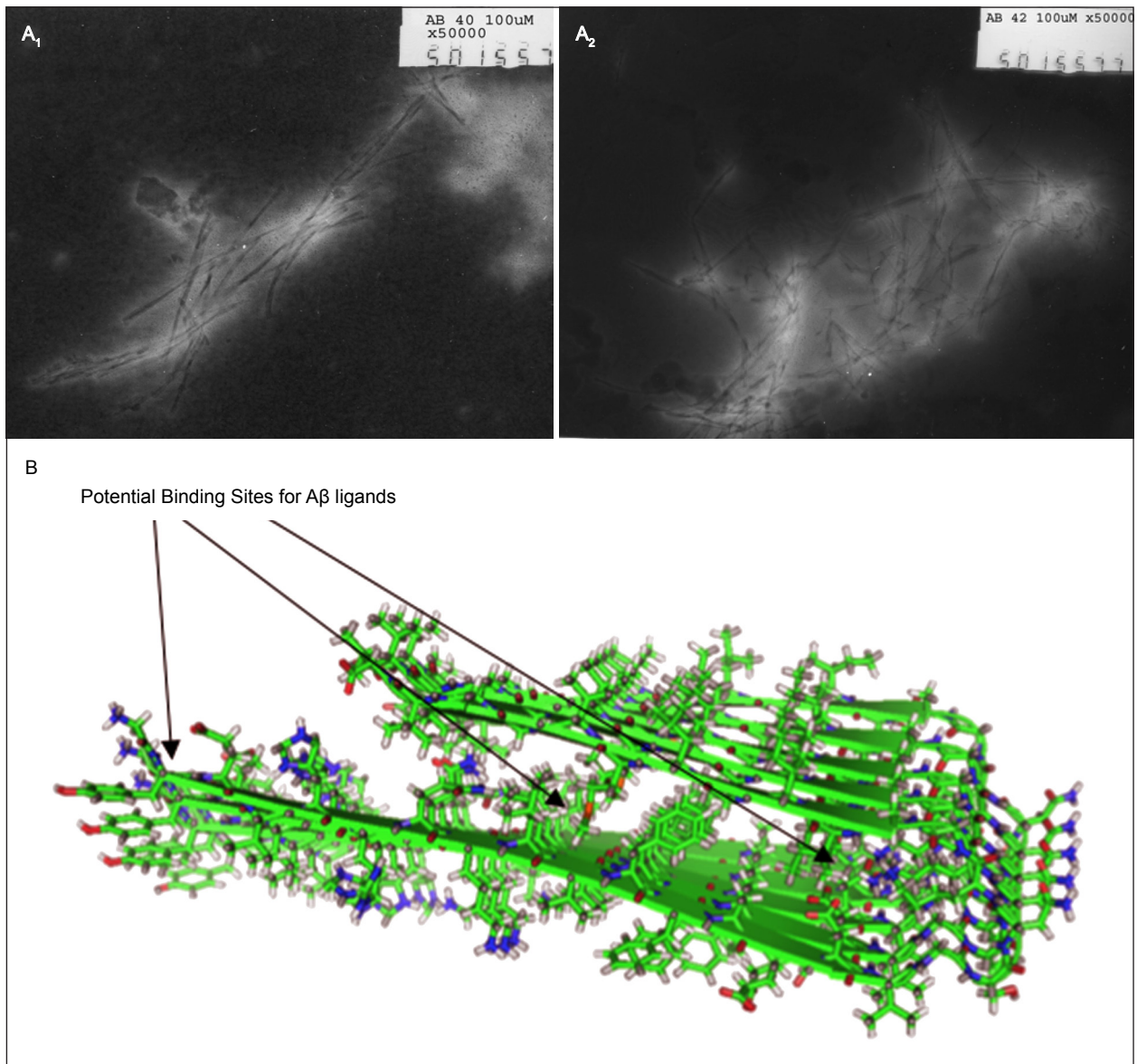


**Figure 4: In vitro  $A\beta$  fibrils and underlying protofilament model.**

(A) Transmission electron microscopy (TEM) images of in vitro  $A\beta_{1-40}$  (A<sub>1</sub>) and  $A\beta_{1-42}$  aggregates (A<sub>2</sub>) fixed using a negative staining material (uranyl acetate). Magnification: 50000. (B) Structural model for protofilament in  $A\beta_{1-40}$  fibrils. Potential binding sites for  $A\beta$  radioligands are marked with arrows. Quarternary fibril structure closely follows structural models provided by Tycko et al. [246]. Potential binding sites for AD radioligands are indicated with arrows. Panels (A) reprinted with permission from [278]. Copyright (2011) American Chemical Society.

### 3.2 Amyloid hypothesis

On the quest for the causes of neurodegeneration in Alzheimer's disease, the amyloid hypothesis remains the major concept for possible explanations [80]. The amyloid hypothesis is intrinsically linked to the genetics of Alzheimer's disease [86] most of which was learned by studying familial forms of AD (FAD). Half a century before  $A\beta$  was identified, this early-onset variant of the disease (in patients < 60 years) with autosomal-dominant inheritance had been

observed [159]. In 1991, Goate et al. reported the first mutation in APP related to FAD [70]. Two further genes, PSEN1 and PSEN2, were also linked to FAD [209,153,202,224]. They encode the presenilins which form the catalytic center of  $\gamma$ -secretase, one of three secretases responsible for the proteolysis of APP to A $\beta$ . Even though the mutations in APP, PSEN1 and PSEN2 are responsible for less than 5 % of all AD cases (FAD), they are fully penetrant and, hence, always cause onset of the disease [239].

The important aspect of these autosomal-dominant mutations for the amyloid hypothesis is that all of them change APP processing to produce more A $\beta$ 42 [211,275]. The amyloid hypothesis [86] outlines a cascade in which this increased A $\beta$ 42 production and accumulation is the starting point for A $\beta$ 42 oligomerization and diffuse A $\beta$  deposits. The A $\beta$  oligomers lead to inflammatory responses (microglial and astrocytic activation), A $\beta$  plaque formation and cause synaptic and neuritic injury. As a consequence, neuronal ionic homeostasis is changed, oxidative stress occurs and kinase/phosphatase activities are possibly modulated towards increase of tau tangle formation. The cascade ends in neuronal dysfunction and cell death as the cellular substrate for Alzheimer's dementia [82].

The weaknesses of the amyloid hypothesis are expressed in several ways. For example, the cascade links A $\beta$  to tau pathology only insufficiently [84]. Transgenic mouse models with APP and PSEN mutations show modest or no neuronal loss [104,105,116,192] or tau pathology. Furthermore, the Nun Study showed A $\beta$  plaques in cognitively normal individuals [101] and A $\beta$ 42-immunization cleared A $\beta$  plaques in AD patients but did not prevent progression of their neuronal loss [97].

Therefore, John Hardy who besides Dennis Selkoe originated the amyloid hypothesis in 1991 [86] brings into play two alternative hypotheses [84]. One, he called *presenilin inhibition hypothesis* and the other *physiological A $\beta$  hypothesis*. The latter is interesting as it fosters an opposite role for A $\beta$ 42 as a rapid protectant from cerebral hemorrhages.

Christian Haass summarizes his attitude to the amyloid hypothesis in a way that currently seems common in the field: *As an Alzheimer's researcher, I strongly support the amyloid cascade hypothesis but feel we have not obtained definitive proof that A $\beta$  is the causative agent of neurodegeneration, nor have we conclusively identified what forms of A $\beta$  initiate neurodegeneration* [80].

### 3.3 Imaging target for PET

The considerable role of A $\beta$  in the pathogenesis of Alzheimer's disease has been shortly outlined above (chapter 3.2). It explains the strong motivation and large efforts of the last two decades to develop PET ligands that would "stain" A $\beta$  plaques, or even better A $\beta$  oligomers, in vivo.

Regarding available in vitro stains for A $\beta$ , one of the standard textbooks for histological techniques describes: *Since its introduction by Bennhold in 1922 [16], the highly selective affinity of the dye Congo red for amyloid, and the subsequent green birefringence when viewed with polarizing microscopy, has been a sine qua non for amyloid demonstration [259].* Further stains are crystal violet, Thioflavin T [252] and Thioflavin S besides the silver and immune stains [56,259].

This may explain why Congo red was used as a starting point for analyzing in vitro binding behavior of A $\beta$  ligands by Klunk et al. in 1989 [135] and for developing derivatives like Chrysamine G by the same group [130]. The poor brain entry of these agents [134] caused the developments to more focus on Thioflavin T as a chemical precursor for A $\beta$  ligands [136] which finally lead to synthesis of [ $^{11}\text{C}$ ]PiB [169]. In parallel, Barrio et al. developed [ $^{18}\text{F}$ ]FDDNP [13] based on the aminonaphtalene DDNP [108]. Even though this class of compound was not known for histological amyloid stains, before, [ $^{18}\text{F}$ ]FDDNP was providing for the first in vivo PET images for A $\beta$  in humans [226]. Shortly after, the first clinical in vivo PET imaging study with [ $^{11}\text{C}$ ]PiB was reported [131]. These first PiB PET images in comparison to FDG PET have been reprinted often and are also shown, here (Figure 5).

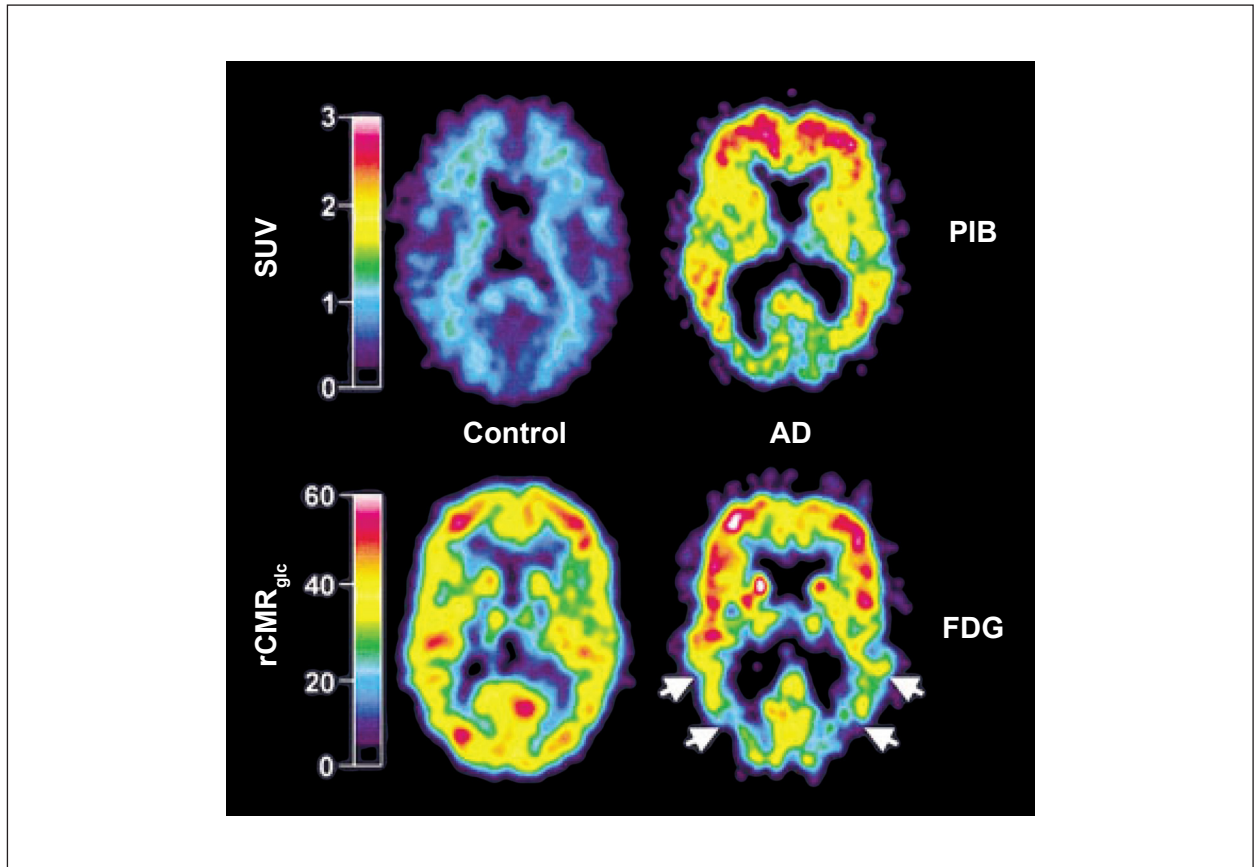


**Figure 5: First published [ $^{11}\text{C}$ ]PiB PET images in humans.**

PIB standardized uptake value (SUV) images demonstrate a marked difference between PIB retention in Alzheimer's disease (AD) patients and healthy control (HC) subjects. PET images of a 67-year-old HC subject (*left*) and a 79-year-old AD patient (MMSE = 21; *right*). (**top**) SUV PIB images summed over 40 to 60 minutes; (**bottom**) [ $^{18}\text{F}$ ]FDG  $r\text{CMR}_{\text{glc}}$  images ( $\mu\text{mol}/\text{min}/100\text{ml}$ ). The left column shows lack of PIB retention in the entire gray matter of the HC subject (*top left*) and normal [ $^{18}\text{F}$ ]FDG uptake (*bottom left*). Nonspecific PIB retention is seen in the white matter (*top left*). The right column shows high PIB retention in the frontal and temporoparietal cortices of the AD patient (*top right*) and a typical pattern of [ $^{18}\text{F}$ ]FDG hypometabolism present in the temporoparietal cortex (*arrows*; *bottom right*) along with preserved metabolic rate in the frontal cortex. PIB and [ $^{18}\text{F}$ ]FDG scans were obtained within 3 days of each other. Reprinted with permission from [131]. Copyright (2004) John Wiley and Sons.

Before  $\text{A}\beta$  imaging probes were available or used in PET, in 1994, Klunk et al. described the potential advantages of small molecule probes for  $\text{A}\beta$  and the motivation for non-invasive imaging of  $\text{A}\beta$  [129]:

- quantify  $\text{A}\beta$  deposition in vivo (quantitation)
- study pattern of  $\text{A}\beta$  deposition in different brain regions (locality, regional density)
- follow temporal sequence of  $\text{A}\beta$  deposition in longitudinal studies (temporality)
- correlate  $\text{A}\beta$  temporality to clinical disease stages (causality)

- help diagnosis of AD
  - aid early diagnosis at presymptomatic stages of AD (early detection)
  - identify clinically atypical AD (increase clinical sensitivity)
  - separate AD from other dementias (differential diagnosis)
- monitor effectiveness of therapies (monitoring)
- research
  - understand AD pathophysiology
  - verify amyloid hypothesis

A decade of research in PET imaging of AD has confirmed and enhanced these motivations and provided substantial evidence for the liability of this approach [254] such that A $\beta$  PET has become an accredited biomarker for the diagnosis of AD (chapter 2.4).



---

## 4. Brain PET imaging of A $\beta$ in small animals

### 4.1 Transgenic research models of amyloidosis

Mutations in APP, PSEN1 and PSEN2 are related to autosomal-dominant FAD (chapter 3.2). As they guarantee onset of the disease [239] mutated APP, PSEN1 or PSEN2 are good candidate genes for the generation of transgenic animal models. Hence, most transgenic mouse models of amyloidosis overexpress one or several of these mutant human genes [116]. Bertram and Tanzi note 29 mutations for APP, 166 for PSEN1 and 10 for PSEN2 [18]. The most common APP mutation used for transgenic mice is the Swedish APP mutation (APP<sub>swe</sub>, K670N/M671L) [45]. The Indiana mutation (APP<sub>ind</sub>, V717F) [179] is also used and present in two of the models presented in Table 1. The Research Model database of the Alzheimer Research Forum [1] harbors more than 100 mouse models of amyloidosis, namely 59 models with APP mutations, 17 with PSEN1, 6 with PSEN2 and 27 with double-cross variants (APP and PSEN1/2).

The prerequisite for preclinical PET imaging of A $\beta$  is the identification of a suitable animal research model. In the context of PET, some aspects of the model are of particular importance. Non-invasiveness is one of the special features of PET imaging which predisposes it for longitudinal studies. These can only be performed if animal loss rates are within reasonable limits. Hence, low mortality of the model towards old age would be of advantage. Onset of A $\beta$  plaque deposition is relevant in the same context as the emergence of a first specific PET signal towards old ages would also hamper longitudinal approaches. Further, one of the key prerequisites for a good model are A $\beta$  plaque morphology and composition that mimic human AD as closely as possible such that PET results can provide translational value. Moreover, the presence of an intracerebral reference region with no or low target (like the cerebellum) is a very practical need for quantifying mouse PET data. Alternative quantification methods that require real-time blood information on tracer activity and metabolites during PET scans are far from being feasible in mice.

Beyond these feasibility aspects for the design of a reasonable small-animal PET study, neuropathophysiological conditions and limitations of the model need to be considered depending on the motivations of the study. For example, there are different degrees of aggressiveness in the amyloid pathology. In Table 1, the TgCRND8 mouse line is among the models with most aggressive amyloidosis. However, it also suffers from high mortality rates and substantial A $\beta$  deposition in the cerebellum. APP/PS1-21 mice show early onset of A $\beta$

plaque deposition but also seem to reach A $\beta$  plaque saturation levels quickly [193] and display a plaque morphology that appears rather uncommon in comparison to human patients. Whatever the considerations for the individual study design may be, all of these models are incomplete [198]. They are not models for Alzheimer's disease even though they are usually called 'AD models' or 'AD mice' but merely models of different kinds of amyloidosis. Two important neuropathological phenomena reflect this model dilemma: first, despite heavy A $\beta$  plaque burden most amyloidosis models do not show neuronal loss [104,105,116,192] which is the final and sad key feature of AD. Second, models that carry APP and PSEN mutants do not develop tangle pathology which is one of the two pathological hallmarks of AD. Knowledge and consideration of these limitations are key conditions to devise a reasonable study design. Table 1 presents an overview of common transgenic mouse lines that were considered for use in this thesis. Previously published A $\beta$  PET imaging studies in transgenic mice are noted in the table and reflect that there may be similar reasoning for the choice of model within the research community.

model	publi- cation year	reference	transgenes	allele	plaque onset (cortex)	mortality	pathology in cerebellum	PET imaging
PDAPP (line 109)	1995	[65]	PDGFB- APPV717F	tg, tgtg	5 - 6 m (tgtg) 8 - 9 m (tg)		- (**) [113]	
Tg2576	1996	[98]	PrP-APPswe	tg	6 - 11 m	20% (p.c.), 40 - 50 % [64]	+ (*) [98]	[245,146]
APP23	1997	[232]	thy1-APPswe	tg	6 - 9 m	survival [15]: 70% (15 m), 40% (18 m), 30% (21 m)	-- (*) [233]	[161]
PS1 x Tg2576	1998	[96]	PrP-APPswe x PDGF- PS1M146L	tg	3 m		+ (*) [172,74]	[132]
TgCRND8	2001	[38]	PrP-APPswe,ind	tg	2 - 3 m	50% (8 m ) [38]	++ [38]	
PS2APP	2003	[200]	thy1-APPswe x PrP-PS2N141I	tg	5 m	25% (24 m) (15% in wt) [258]	- (*) [200]	
APP/PSdE9	2004	[109]	PrP-APPswe + PrP-PS1dE9	tg	4 - 5 m	40% (12 m) (p.c.)	+ (*) [250]	
APP/PS1- 21	2006	[197]	thy1-APPswe + thy1-PS1L166P	tg	1.5 m		+ (*) [197]	[193]
APP/PS1 (ARTE10)	2009	[267]	thy1-APPswe +thy1- PS1M146V	tgtg	3 m (tgtg)	15% (12 m) tgtg	-- (*) [267] and -- (**) [164], this thesis	[277,278, 164]

**Table 1: Common transgenic mouse models for amyloidosis.**

Models are ordered according to year of first publication. A $\beta$  pathology in cerebellum is classified with (--) very low, (-) low, (+) present and (++) strong and (\*) qualitative observation, (\*\*) quantitative observation. tg: hemizygous, tgtg: homozygous. (p.c.): Willuweit et al. personal communication. Table includes information from [267].

## 4.2 Small-animal PET scanners

In 1995, Bloomfield et al. reported the first dedicated small-animal PET scanner [21], two decades after the first human brain PET scans had been performed [243,260]. However, the first small-animal PET images of rat brain with a benzodiazepine receptor tracer were taken with a clinical PET scanner in 1991 [103]. This chapter is to provide for a few practical considerations on the use of a small-animal PET scanner. Similar to the challenging choice of a potentially applicable rodent model, a small-animal PET scanner needs to be appropriate for the size of rodents to be scanned. Table 2 provides an overview of scanners the majority of which are commercially available. Reports on A $\beta$  PET imaging in rodents that used the corresponding scanner are included in the table.

A decade ago, Arion Chatziioannou has given good reviews on the challenges related to small-animal PET [37,36] and the according requirements for a scanner of this kind: *to obtain as many counts as possible and to localize these counts as accurately as possible in the smallest amount of time and with the minimum amount of available probe* [37]. His descriptions are as valid, today as then and, hence, Table 2 contains two key specifications: spatial resolution and sensitivity. It is notable that these specifications are valid for the center field-of-view (CFOV), only, and that sensitivities and resolutions drop quickly when moving out of CFOV. This needs to be considered for the study design (e.g. dual-animal scans) and precise placement of animal organs (e.g. brain) in the CFOV. In addition, the overall FOV size is of importance as it enables or limits the measurement of whole body tracer distributions or image-derived input functions.

In our lab, profound experience was gathered with three PET cameras (MOSAIC, Focus 120 and Inveon) scanning mice and rats. With regard to the specifications, it needs to be considered that mouse neocortex is of about 1 to 1.5 mm thickness and mouse cerebellum about 2.5 mm [62]. This illustrates the thin line between scanner performance data and neuroanatomical structures in mice to be resolved and measured when the radiotracer floods in, washes out and binds to target. It also explains the need for strong validation of mouse brain PET [59,60].

model	manufacturer	performance evaluation	sensitivity [%]	spatial resolution [mm]	FOV axial [cm]	FOV transaxial [cm]	A $\beta$ imaging in rodents
microPET P4	Concorde	[237]	1.4	1.8	7.8	19	[132]
microPET R4	Concorde	[137]	0.9	1.8	7.8	10	[280]
MOSAIC	Philips	[99]	0.7	2.7	12	12.8	
ATLAS	National Institutes of Health (NIH)	[217]	2.0	1.9	2.0	6.0	[245]
Focus 120	Concorde / Siemens	[126]	7	1.4	7.6	10	[164], this thesis
Focus 220	Concorde / Siemens	[238]	4	1.3	7.6	19	[161,146,223,242]
Inveon	Siemens	[12,121,257]	11	1.4	12.7	10	[277,278,164,193], this thesis
eXploreVISTA	GE Healthcare	[262]	4	1.7	4.8	6.7	
ClairvivoPET	Shimadzu	[177]	8.2	1.5	15.1	10.2	
quadHIDAC	Oxford Positron Systems	[208]	0.9	1.1	28	16	
LabPET Solo	Gamma Medica	manufacturer	4	1.3	3.7	10	
Nano PET/CT	Bioscan	manufacturer	8.3	1.2	10	9.4	

**Table 2: Small-animal PET scanners and some performance specifications.**

System sensitivity, spatial resolution and dimensions of field-of-view (FOV) are the three PET scanner parameters that are included in the table for their practical relevance to A $\beta$  PET imaging in rodents. PET imaging reports in rodent models of amyloidosis are noted for the scanner that was used by this study. Spatial resolution and sensitivity data for center field-of-view (CFOV), spatial resolution as full width at half maximum (FWHM).

### 4.3 A $\beta$ tracers in the preclinic

Chapter 3.3 introduced A $\beta$  as an imaging target and the potential value related to labeling the protein in vivo. This chapter attempts to provide an overview of the radioligands for A $\beta$  that have been evaluated in small-animals beyond the conventional tracer characterization paradigm (Table 3) which first needs to verify the principally good characteristics of the radiotracer. The criteria for a "good" radiotracer could be summarized as [88,140,30]:

- moderate polarity / neutrality to pass the blood-brain barrier (BBB)
- small size to pass BBB
- high affinity for binding sites
- high selectivity for the target (i.e. low non-specific binding)
- moderate lipophilicity for brain entry but low plasma protein binding
- specificity to certain protein subspecies (e.g. A $\beta$ 42 > A $\beta$ 40)

- correlation to pathology
- fast pharmacokinetics
  - high initial uptake
  - fast washout
  - clearance of free and non-specifically bound tracer
- in-vivo stability (circulation and brain)
- easy radiolabeling
- high radiochemical yield
- radiochemical purity

These criteria are at first tested with in vitro binding assays using synthetic protein aggregates (A $\beta$  fibrils) or brain tissue homogenates, general ex vivo biodistribution studies in wild-type animals to assess whole body tracer distribution and pharmacokinetics, metabolite analyses for blood and brain and partition coefficients in octanol-phosphate buffered saline solutions ( $\log P_{\text{oct/PBS}}$ ) (see chapter 4.5 for exemplary results of this kind). These classes of experiments are common and standardized procedure in the fields of radiochemistry and nuclear medicine which explains that they are not mentioned in Table 3.

Then, further specific methods for the ex vivo and in vivo evaluation of the tracer can be applied. For example, in vitro autoradiography is a simple application in which the tracer is incubated to brain sections similar to histological stains. This can be enhanced to ex vivo autoradiography for which the tracer is administered to the living animal to verify its in vivo labeling qualities.

Every research group has developed its own evaluation regimens without standardized processes. This experimental individuality may be indicated by Table 3. The murine research models of amyloidosis that were applied for these studies are presented in chapter 4.1.

PIB is the most widely used tracer in the field. This explains the relatively high number of preclinical evaluation studies for its assessment, as well.

A few aspects can be noted from Table 3. First, different models are used for preclinical evaluation, which may hamper comparability of data between similarly performed studies. Second, only single or few experimental modalities are used in addition to common testing. Third, only few studies attempt to combine several modalities to strengthen the validity of their outcomes.

label	tracer	backbone	first reference	year	model	method	reference
$^{18}\text{F}$	FDDNP	amino-naphthalene	[13]	1999	triple transgenic rat	PET, inAR	[242]
					macaque	PET	[185]
					Tg2576	PET	[146]
$^{11}\text{C} / ^3\text{H} /$ fluorescent	PiB	BTA	[168]	2002	PS1/APP	in vivo multiphoton microscopy	[168]
					baboon	PET	[169]
					Tg2576, PDAPP, APP-PS1	multiphoton microscopy	[10]
					PS1/APP	PET, bdCNS, BindAssay	[132]
					Tg2576	PET	[245]
					APP23	PET, exAR, inAR	[161]
					APP/PS1 (ARTE10)	PET, exAR, dlexAR, bdCNS, bdCranium	[164], this thesis
APP (n.f.s.)	PET	[223]					
fluorescent	methoxy-X04	BTA	[128]	2002	PS1/APP	multiphoton microscopy	[128]
$^{123}\text{I} / ^{125}\text{I}$	IMPY	phenyl-imidazole	[143]	2002	Tg2576	exAR	[143]
					PSAPP	inAR, exAR	[141]
$^{11}\text{C}$	SB-13	stilbene	[190]	2003	TgCRND8	inAR	[190]
$^{18}\text{F}$	FEM-IMPY FPM-IMPY	phenyl-imidazole	[28]	2004	rhesus monkey, normal mice	PET	[28]
fluorescent	BF-108	benzoxazole	[234]	2004	rat ( $\text{A}\beta$ -micro-infused) APP23	ex vivo fluorescence	[234]
	BF-145	benzoxazole	[187]	2004	APP23	ex vivo fluorescence	[187]
$^{18}\text{F} /$ fluorescent	BF-168	benzoxazole	[186]	2004	PS1/APP, APP23	ex vivo fluorescence, exAR	[186]
NIRF	AOI987	oxazine	[92]	2005	APP23	in vitro fluorescence, in vivo NIRF	[92]
	NIAD-4	BTA	[181]	2005	APP (n.f.s.)	multiphoton microscopy	[181]
$^{11}\text{C} /$ fluorescent	BF-227	benzoxazole	[139]	2007	PS1/APP	exAR	[139]
$^{11}\text{C}$	MeS-IMPY	phenyl-imidazole	[221]	2007	rhesus monkey	PET	[221]
$^{18}\text{F}$	O-Fet-PiB	BTA	[280]	2008	rat ( $\text{A}\beta$ -micro-infused)	PET	[280]
NIRF	NIAD-16	BTA	[199]	2008	APP (n.f.s.)	in vitro stain	[199]
$^{18}\text{F}$	Florbetapir	stilbene	[203]	2008	rhesus monkey, APP/PS1	PET (monkey), exAR (mouse)	[39]
					APP/PS1-21	PET, exAR	[193]

<sup>18</sup> F	Phe-BTAs	BTA	[223]	2009	APP (not further specified)	PET	[223]
<sup>18</sup> F	AminoPhe-BTAs	BTA	[222]	2009	normal rat, rhesus monkey	PET	[222]
<sup>11</sup> C	FPEG chalcone	chalcone	[188]	2009	Tg2576	exAR	[188]
<sup>18</sup> F	FPEG flavone	flavone	[189]	2009	Tg2576	exAR	[189]
<sup>3</sup> H	AZD2184	BTA	[112]	2009	APP/PS1	inAR, exAR	[112]
<sup>11</sup> C / <sup>3</sup> H	AZD4694	BTA	[118]	2010	Tg2576	exAR	[118]
<sup>11</sup> C	IBT	IBT	[278]	2011	APP/PS1 (ARTE10)	PET, dlexAR, bdCNS	[278]
<sup>18</sup> F	IBT	IBT	[277]	2011	APP/PS1 (ARTE10)	PET, dlexAR, bdCNS	[277]

**Table 3: A $\beta$  radioligands applied in vivo or ex vivo in animal models of amyloidosis and non-human primates.**

Overview of experimental modalities used for the preclinical evaluation of novel radioligands and research models applied for these tasks. List is in chronological order in respect to first publication of the ligand. General biodistribution studies for brain uptake analysis were not considered for this table. NIRF: near-infrared fluorescent, n.f.s.: not further specified, inAR: in vitro autoradiography, exAR: ex vivo autoradiography, dlexAR: dual-label ex vivo autoradiography, bdCNS: regional brain biodistribution, bdCranium: biodistribution of (extracerebral) cranial organs, BindAssay: Radioligand Binding Assay, PET: in vivo PET (see also Table 1 and Table 2)

#### 4.4 PET studies in mouse models of AD

In perspective to the wealth of new A $\beta$  radioligand developments, it is notable that only few studies reported the use of in vivo PET imaging for A $\beta$  in transgenic mouse models of AD as already indicated in the tables of chapters 4.1 and 4.2 [132,245,161,146,223,277,278,164,193]. Of these studies, Toyama et al. [245] (Figure 6A), Klunk et al. [132] (Figure 6B) and Maeda et al. [161] (Figure 6C) are currently the ones that are well-known in the field. All three of them used [<sup>11</sup>C]PiB for their attempts to visualize A $\beta$  in very old hemizygous mice. Among all murine A $\beta$  PET imaging studies with [<sup>11</sup>C]PiB besides the reports from our group, only Maeda et al. reported positive outcomes with the claim that very high specific activities of the tracer were the prerequisite for that.

Both, Klunk and Toyama et al. concluded that PET imaging using PiB is not possible in transgenic mouse models. Speculations on the reasons for the rather unexpected negative results of [<sup>11</sup>C]PiB binding in transgenic mice currently focus on two phenomena. Firstly, Klunk et al. claimed that there are only a very low number of high-affinity binding sites for [<sup>11</sup>C]PiB in plaques of PS1/APP mice as compared to severely affected human AD tissue, a notion that was further supported by the work of Ye et al. [274]. In addition, they hypothesized that the presence of specific human tissue components in plaques besides A $\beta$  may help PiB

binding in humans compared to mice and, further, that the long time frame of A $\beta$  deposition in human brain allows for many post-translational and post-deposition modifications [132]. The latter appears as the second major argument for differences between mice and men and it was further supported by Maeda et al. who demonstrated co-localization of [ $^{11}\text{C}$ ]PiB binding to N-terminally truncated and pyroglutamylated immunoreactive plaques in their APP23 model [161].

The reporting of negative PET imaging outcomes in transgenic mouse models of AD continued also with other tracers like [ $^{18}\text{F}$ ]FDDNP [146] or [ $^{18}\text{F}$ ]fluorophenyl-BTAs [223]. This may reflect the validity of the arguments mentioned above or it may be an expression of joint methodological challenges related to this kind of imaging work. Whatever the reasons may be, it has been holding off many valuable research projects related to imaging marker and therapy developments.

To illustrate the challenges in more detail, PET images from the three [ $^{11}\text{C}$ ]PiB studies mentioned above are shown in Figure 6. Panel A (Toyama et al. [245]) contains two coronal views onto the same PET study (30 - 40 min frame) in a frontal and posterior position to delineate [ $^{11}\text{C}$ ]PiB uptake in frontal cortex and cerebellum of a 22 month old Tg2576 mouse. The regions were identified in summed images of the whole PET study (not shown here). Visually, a difference between the target (cortex) and the reference region (cerebellum) cannot be seen. This was confirmed analytically by retrieving time-activity curves for these regions. Panel B in Figure 6 shows a similar outcome in a 12 month old PS1APP mouse described by Klunk et al. [132]. The presented field of view is larger and contains the top third of the animal. Yellow crosshairs are centered to the brain. The time frame is not further specified. The full delineation of the brain suggests that early frames were included. A visual distinction of tracer uptake between different brain regions cannot be seen. The imaging results by Toyama and Klunk et al. may be related to their choice of model. More likely, they may be attributable to their imaging technology (NIH ATLAS and microPET P4, see Table 2 in chapter 4.2) which only offers to resolve structures within about 2 mm. Two years after Toyama and Klunk et al., Maeda et al. presented the first successful imaging study [161] applying a more advanced PET camera (microPET Focus 220) and the APP23 mouse line. The major argument of Maeda et al. for their success is described by the PET image (30 - 60 min frame) shown here (Figure 6C). Three arrows point to structures in corresponding coronal views of the brain that likely are the CA1 (top) and the amygdala (bottom right) of hippocampus [62]. Fluorescence staining showed clusters of plaques in these regions. According to Maeda et al., the two smaller clusters (right

side of image) could not be identified in PET with conventional specific activities of the tracer. In this context, it may be noteworthy that the size of these two clusters was in a millimeter to submillimeter range [62].

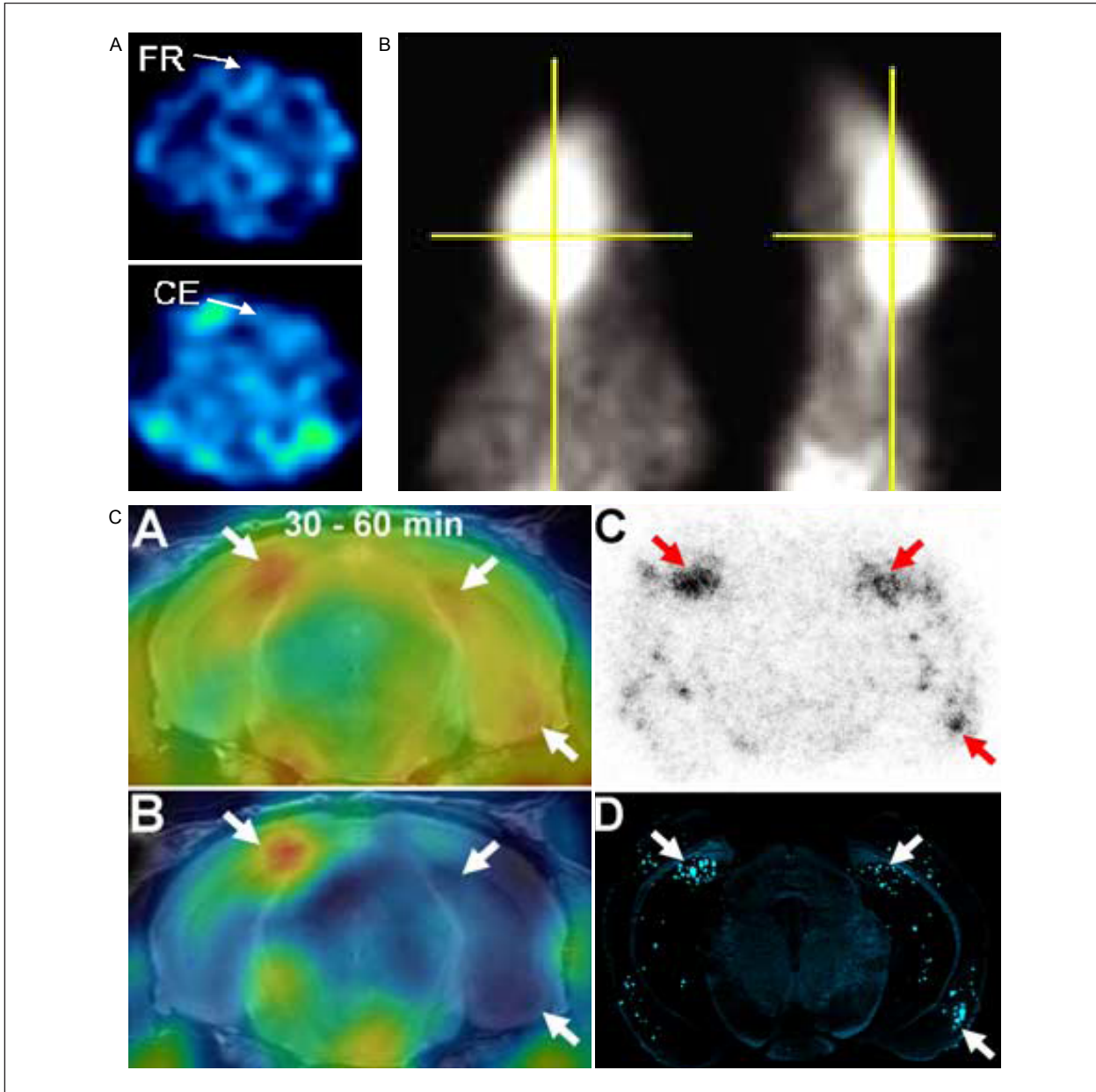


**Figure 6: Previous PET imaging studies with [ $^{11}\text{C}$ ]PiB in transgenic mice.**

(A) [ $^{11}\text{C}$ ]PiB in Tg2576. Age: 22 months (female). Frame: 30 - 40 min. PET scanner: NIH ATLAS. View: coronal. Top: frontal cortex (FR), bottom: cerebellum (CE). (B) [ $^{11}\text{C}$ ]PiB in PS1/APP. Age: 12 months. Frame: not specified. PET scanner: microPET P4. View left: axial, right: sagittal. (C) [ $^{11}\text{C}$ ]PiB in APP23. Age: 20 months. Frame: 30 - 60 min. PET scanner: microPET Focus 220. View: coronal. Subpanels (A) and (B) show the same mouse and are shown to indicate the contribution of specific radioactivity of the radioligand to sensitive in vivo detection of A $\beta$  plaques. Specific activity in (A): 200 GBq/ $\mu\text{mol}$  with high dose 37 MBq injection, in (B): 20 GBq/ $\mu\text{mol}$  with low dose 3.7 MBq injection. Subpanel (C): Ex vivo [ $^{11}\text{C}$ ]PiB autoradiography at 30 min p.i. of the same mouse and subsequent fluorescence staining with non-radioactive BTA-1 (subpanel (D)). Arrows indicate clusters of amyloid lesions corresponding to intense spots in subpanel (A). Panel (A) reprinted with permission from [245]. Copyright (2005) Springer. Panel (B) reprinted with permission from [132]. Copyright (2005) Society for Neuroscience. Panel (C) reprinted with permission from [161]. Copyright (2007) Society for Neuroscience.

## 4.5 Tracer development program at TUM

### 4.5.1 [<sup>11</sup>C]imidazo[2,1-*b*]benzothiazole (IBT) - a novel amyloid tracer

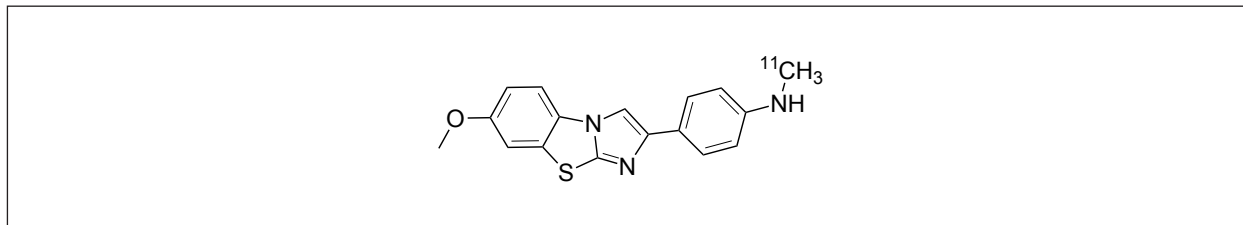


**Figure 7: Chemical structure of [<sup>11</sup>C]IBT.**

2-(*p*-[<sup>11</sup>C]Methylaminophenyl)-7-methoxyimidazo[2,1-*b*]benzothiazole [278].

The development of improved tracers for imaging of A $\beta$  plaques in our group led to the expansion of possible 2-phenylbenzo-*[d]*thiazole (BTA) and 2-phenylimidazo[1,2-*a*]pyridine (IMPY) pharmacophores towards 2-phenylimidazo[2,1-*b*]benzothiazoles (IBTs) which are hybrids of BTA and IMPY backbones. They have two nitrogens and a sulfur in the core heteroaromatic system. Thus, the structural motif is electron-rich and planar with lipophilic properties similar to that of BTA and IMPY series [278].

The predicted lipophilicity properties (LogP, CLogP) and polar surface area (tPSA) of IBT, IMPY and BTA backbones (Figure 8) show that the IBT core possesses comparable lipophilicity and polar surface area to BTA and IMPY, respectively. This supports the hypothesis that IBTs, when fitted with appropriate substituents, may represent suitable A $\beta$  imaging agents.

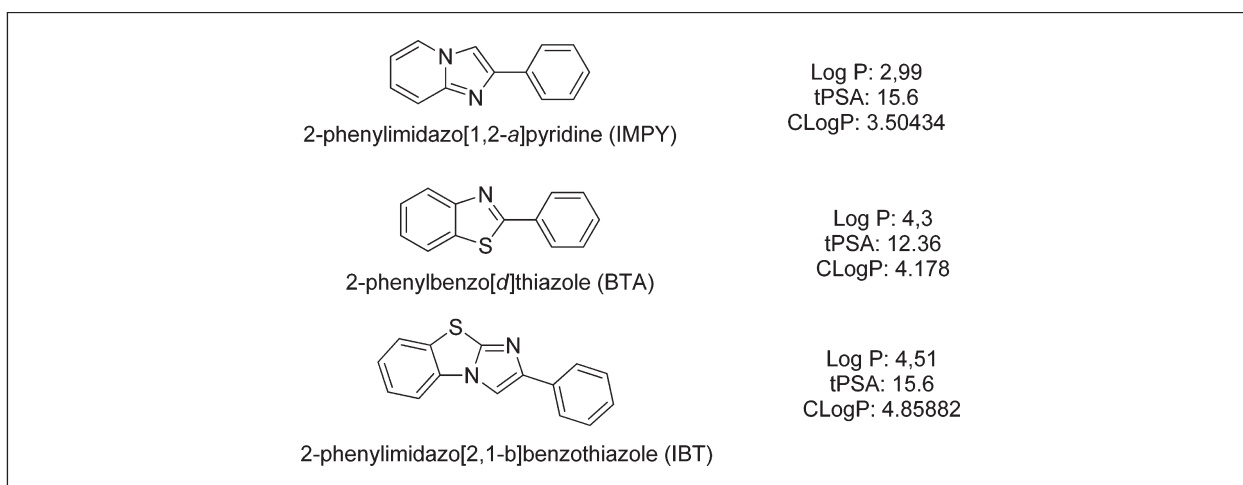


**Figure 8: IBT - a hybrid of BTA and IMPY backbones.**

Anticipated lipophilicity and total polar surface area of IMPY, BTA, and IBT scaffolds. Reprinted with permission from [278]. Copyright (2011) American Chemical Society.

A series of IBTs with variations to their hydrogen bond donating and accepting substituents and their lipophilicity was synthesized. The compounds were tested for their binding affinities to A $\beta$  fibrils in vitro, and selected compounds were obtained as  $^{11}\text{C}$ -labeled versions for evaluation of their brain uptake kinetics in Balb-C mice [278]. The lead compound (Figure 7) in terms of brain uptake kinetics (high initial uptake and fast clearance), in vivo stability and in vitro binding affinities (Table 4) was selected for further biological evaluation as presented in the results (chapter 8.1).

			$[^{11}\text{C}]\text{IBT}$	$[^{11}\text{C}]\text{PiB}$
<b>Binding Assay</b>	<b>inhibition [%]</b>	<b>A<math>\beta</math><sub>1-40</sub></b>	95	88
		<b>A<math>\beta</math><sub>1-42</sub></b>	97	83
	<b>K<sub>i</sub> [nM]</b>	<b>A<math>\beta</math><sub>1-40</sub></b>	3.5	6
		<b>A<math>\beta</math><sub>1-42</sub></b>	5.8	13
<b>Brain uptake [%ID/g]</b>	<b>5 min</b>		9.12 $\pm$ 0.89	7.20 $\pm$ 0.78
	<b>30 min</b>		1.27 $\pm$ 0.16	0.80 $\pm$ 0.09
	<b>5 / 30 min ratio</b>		7.18 $\pm$ 2.31	9.00 $\pm$ 2.74
<b>Lipophilicity</b>	<b>logP<sub>oct/PBS</sub></b>		1.7 $\pm$ 0.05	1.5 $\pm$ 0.11
<b>Fate of label [% intact tracer]</b>	<b>blood</b>	<b>10 min</b>	15 $\pm$ 5	20 $\pm$ 5
		<b>30 min</b>	7 $\pm$ 2	11 $\pm$ 2
	<b>brain</b>	<b>10 min</b>	95 $\pm$ 2	96 $\pm$ 1
		<b>30 min</b>	91 $\pm$ 3	92 $\pm$ 3

**Table 4: Properties of  $[^{11}\text{C}]\text{IBT}$**

In vitro and ex vivo characteristics of the IBT lead compound in comparison to  $[^{11}\text{C}]\text{PiB}$  [169]. Data derived from [278].

#### 4.5.2 $[^{124}\text{I}]\text{BrIMPY}$ - a novel 6-iodo-2-phenyl-imidazo[1,2-a]pyridine (IMPY)

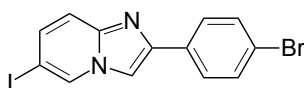


**Figure 9: Chemical structure of BrIMPY**

2-(4'-bromophenyl)-6-iodoimidazo[1,2-a]pyridine [276].

Ten years ago, 2-(4'-dimethylaminophenyl)-6-iodoimidazo[1,2-a]pyridine (IMPY) was reported for the first time [143]. Since then, its derivatives were presented as potential A $\beta$  tracers [140,144,281,142] and several structure-activity relationship and in vivo biodistribution studies were published [145,182,29].

Previous compounds in the IMPY-series were rapidly metabolized, with only 30 - 40 % total radioactivity in mouse and rat brain at 2 - 3 min corresponding to the intact tracer. The proposed mechanism is mainly *N*-demethylation [141,220] to yield radiolabeled monomethyl derivatives of IMPYs. Thus, despite the use of [<sup>123</sup>I]IMPY for imaging  $\beta$ -amyloid in brains of patients with AD [182] there is a rationale for the development of IMPY derivatives with improved stability against metabolism as was done in our group.

A series of IMPYs was synthesized and evaluated with the goal to develop IMPY derivatives that combine high binding affinity for A $\beta$  and high metabolic stability in vivo. The compounds were tested for their binding affinities to A $\beta$  fibrils in vitro, and selected compounds were obtained as <sup>125</sup>I- and <sup>124</sup>I-labeled versions for evaluation of their brain uptake kinetics in normal Balb-C mice.

The properties of the identified lead compound BrIMPY with a bromo-group instead of a *N,N*-dimethylamino substitution at 4'-position are summarized in Table 5 in comparison to the classic IMPY [276]. In vivo stability analyses showed the half-life of BrIMPY in blood and brain to be longer than 60 min [276] compared to about 8 min for IMPY analogues [220]. Hence, this BrIMPY was selected to enter a three-modal biological evaluation in the ARTE10 line in our lab (chapter 8.2).

			BrIMPY	IMPY
Binding Assay	inhibition [%]	A $\beta$ <sub>1-40</sub>	40	75
		A $\beta$ <sub>1-42</sub>	82	94
	K <sub>i</sub> [nM]	A $\beta$ <sub>1-40</sub>	104	–
		A $\beta$ <sub>1-42</sub>	7.48	8.95 ± 0.72 (*)
Brain uptake [%ID/g]	5 min		5.44 ± 0.88	2.12 ± 0.05
	30 min		1.00 ± 0.18	1.26 ± 0.46
	5 / 30 min ratio		5.79 ± 2.72	1.96 ± 1.07
Lipophilicity	logP <sub>oct/PBS</sub>		1.89 ± 0.16	1.65 ± 0.15

**Table 5: Properties of novel [<sup>124</sup>I] / [<sup>125</sup>I]BrIMPY compared to IMPY.**

In vitro and ex vivo characteristics of the BrIMPY lead compound in comparison to IMPY [143]. (\*) binding to human A $\beta$  plaques as measured by Cai et al. [31]. Data derived from [276].

---

**Part II.**

**Results**



---

## 5. Introduction

### 5.1 Scope and objectives

The work for this thesis began one year after the first publication of clinical images with [<sup>11</sup>C]PiB in human AD patients [131]. Preclinical data for this promising new AD radioligand was scarce but motivating. The principle in vivo uptake of PiB had been analyzed in six healthy middle-aged baboons using a clinical PET scanner [169]. Shortly after, the good in vivo binding behavior of PiB had directly been observed with multiphoton microscopy in three transgenic AD mouse models using the fluorescent properties of the unlabeled ligand [10]. Data on PET studies with animal models of AD were not available.

Establishing PET imaging in small-animals for AD ligands had obvious motivations, like directly correlating underlying neuropathology to imaging findings, evaluating newly developed ligands and monitoring therapeutic agents in preclinical studies. PiB was a promising tracer that had already been introduced and used in the clinic and, therefore, was nearby for first use in small animals, also. Transgenic animal models for AD had been in development for a decade and the multiphoton microscopy study mentioned above had proven in vivo binding of PiB to A $\beta$  plaques in more than one AD model line.

A small-animal PET scanner had just been installed at our site and, hence, the next step towards small-animal PET imaging of A $\beta$  plaques was to find a way for demonstrating specific in vivo binding of [<sup>11</sup>C]PiB in a suitable animal model of AD.

Among the many questions that required answering in the initial approach to the project were:

- What research model to choose and how to access it at very old ages?
- How to handle (fragile) animals for proper acquisition of dynamic PET data?
- How to identify animal neuroanatomy in PET images?
- How to retrieve quantitative information on tracer binding from PET?
- Which experimental modalities to choose for correlations to PET?

Three major objectives were defined for the project:

1. Establish a robust experimental design to demonstrate the association between a pseudo-color coded pixel of an in vivo PET image on the computer screen and its underlying neuropathology in a suitable amyloid-beta rodent model of AD.
2. Apply the developed setup and create standardized reference data with the common AD tracer PiB to yield specific and quantifiable PET data.
3. Apply the experimental toolbox to new good candidate AD tracers developed by our research group for their evaluation and ranking.

## 5.2 Description of projects

All objectives were fully addressed. Care has been taken to maintain their tripartite character in the three major subdivisions of results. To better tell the story and to more clearly link the necessary experimental stages, some aspects of the second part needed to be foreclosed at the end of the first.

Chapter 6 focuses on *qualitative* results and begins with the contribution to the basic characterization of the ARTE10 mouse model in regard to possible imaging purposes. It then describes the creation of the PiB PET images and the steps that were required to achieve reliable time-activity data for quantification of the tracer. Furthermore, the hypothesis that the cerebellum may be a valid intracerebral reference region is proven. This repertoire is the foundation for introducing the calculation of binding potentials. The first part ends with an analysis of specificity and locality of [<sup>11</sup>C]PiB binding in the mouse cranium and demonstrates specific intracerebral PiB binding.

Chapter 7 uses the skills and knowledge that were developed before to focus on the *quantitation* of independent experimental results from a large mouse study collective in relation to PET. It describes a battery of experiments for the specific characterization of the ARTE10 mouse model for PET imaging and the multi-modal *cross-validation* of the imaging method. It ends with the presentation of a combined multi-modal experiment as a robust and validated "toolbox" to retrieve maximal validation information to the binding properties of a PET radiotracer.

Chapter 8 presents the *application* of the standardized experimental "toolboxes" that were validated in chapter 7. Exemplary datasets for two of the many new PET tracers for AD that were developed by our group are presented. It is shown how the combined multi-modal dual-

label experiment described at the end of part II can be used completely or in parts to gain reliable information for the evaluation and ranking of new good-candidate AD radiotracers.



---

## 6. PET imaging of A $\beta$ with [ $^{11}\text{C}$ ]PiB in mouse brain

### 6.1 Prerequisites and foundations

#### 6.1.1 PET and MRI scanning

The first promising PET images with [ $^{11}\text{C}$ ]PiB were yielded in our lab by scanning a 23 month old hemizygous ARTE10 mouse. In Figure 10, image modalities are already co-registered but shown separately, for better illustration of the challenges involved with reading a cranial mouse PET image without additional anatomical information. Figure 10A shows tracer uptake in a time frame between 20 and 30 min. The outlines of the animal are roughly delineated in magenta color and provide some basic anatomical orientation. Panel A<sub>1</sub> corresponds to an axial view in humans and shows two symmetric semilunar tracer uptake zones and a frontal centered hotspot. Similarly, panel A<sub>3</sub> depicts the hotspot on a sagittal plane. Posterior of this high uptake a shape is demarcated that has similarities with sagittal mouse brain anatomy.

Locatability of tracer uptake prompted the addition of in vivo MRI scanning for better neuroanatomical orientation. MR images were taken the same day as PET about 10 hours apart and [ $^3\text{H}$ ]PiB was administered during the MR acquisition for later correlation purposes. Figure 10B presents MR images of the mouse head in radiological orthogonal perspective. Panel B<sub>2</sub> shows major parts of mouse brain anatomy in a 5 mm grid. Thicker grid lines provide reference relative to Bregma. On the horizontal section, they intersect on the median line between frontal ventricular parts. From top to bottom of the panel, the following anatomical regions could be well identified: olfactory bulb, frontal neocortex, striatum, ventricles, hippocampus with indications of thalamus, colliculus and cerebellum. Panel B<sub>3</sub> shows how the MR signal with the coil was strongest about 5 mm behind Bregma and getting weaker frontal of the olfactory bulb.

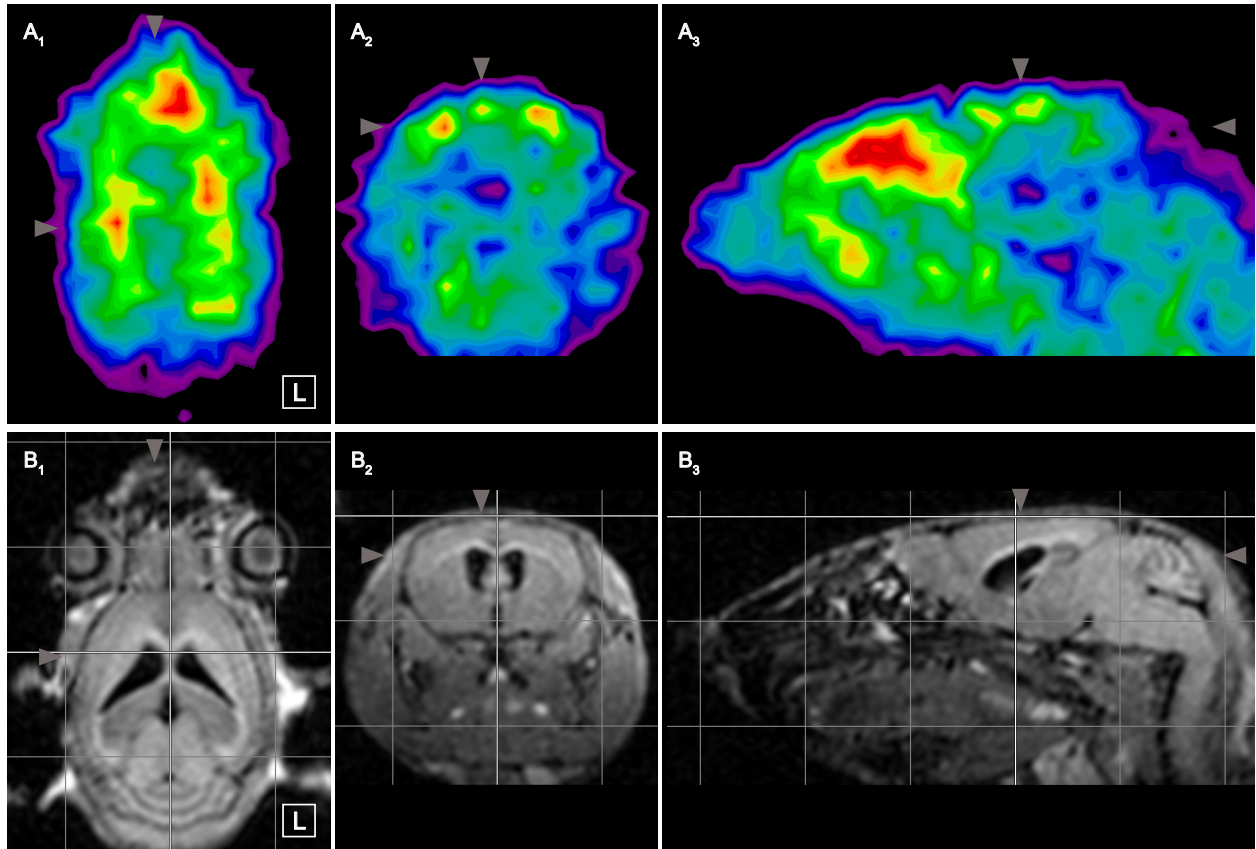


**Figure 10: Exemplary [ $^{11}\text{C}$ ]PiB PET and MRI of a transgenic mouse before image fusion.**

[ $^{11}\text{C}$ ]PiB PET and *in vivo* 1.5 T cranial MR images of the same mouse taken the same day in sequential imaging sessions. **(A)** Cranial [ $^{11}\text{C}$ ]PiB uptake in a 60 min PET acquisition (shown here: 20 - 30 min frame). **(B)** Cranial 1.5 T MR taken with a 23 mm microscopy coil over 46 min after [ $^3\text{H}$ ]PiB administration. Images are presented in radiological orthogonal perspective. MRI is shown with 5 mm grid and image origins (thicker grid lines) at Bregma to denote orthogonal MRI space according to Paxinos atlas [62] coordinates. *Columns* from left to right show horizontal (1), coronal (2) and sagittal (3) views. PET color look-up-table is *UCLA* (Pmod) with lower thresholds set to still visualize the cerebellum. MRI color look-up-table is *Gray* (Pmod). *Arrowheads* indicate slice positions. Slice coordinates (corresponding to Paxinos atlas) are: horizontal Bregma -1.90 mm, coronal Bregma -0.10 mm and sagittal 0.65 mm lateral. Images from the same animal are shown in panels (A) in Figure 15, Figure 17 and Figure 19 (23 month old female hemizygous APP/PS1 mouse).

## 6.1.2 Image co-registration of PET to MRI

### 6.1.2.1 Semi-automated manual overlay of early PET

The image co-registration of PET to MRI was performed in several stages. First, MR images were aligned to Paxinos mouse brain atlas space [62] for good correspondence of *in vivo* and *in vitro* topology. The resulting *in vivo* MR atlas space is indicated by the coordinate grid in Figure 10B with origins at Bregma. Then, PET data from the first minutes of the scan was co-registered to the MRI with several quality control steps including motion correction. An overview of the co-registration process is given in Figure 11.

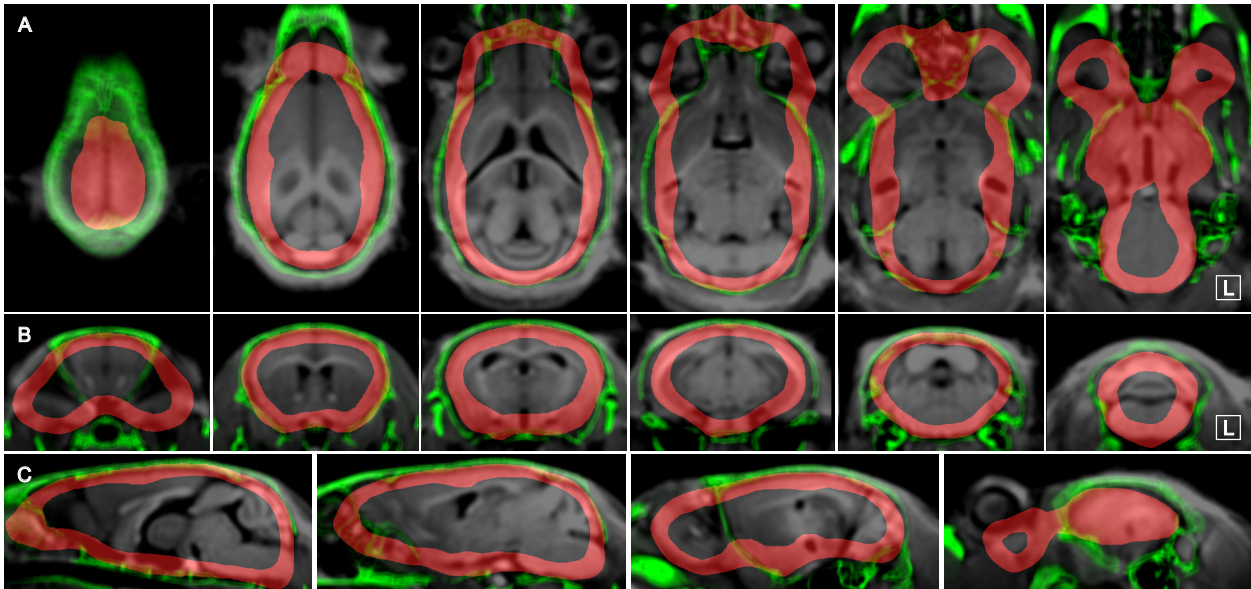


**Figure 11: Mouse brain PET/MRI image co-registration.**

Principle of manual co-registration process as applied for all PET data of this study. Proximity of frontal cortex to extracerebral regions with high unspecific [ $^{11}\text{C}$ ]PiB retention as shown in Figure 3 requires precise co-registration for reliable PET analyses. Three co-registered image modalities are shown in each panel: PET template of early (1-4 min) radiotracer entrance (*red*), MRI template (*gray*) and cranial CT (*green*). CTs and MRIs are co-registered to Paxinos space along all axes. *Top row (A)*: horizontal views from top to bottom (1.0 mm apart). *Middle row (B)*: coronal views from nose to back of head (2.1 mm apart). *Bottom row (C)*: sagittal views from median to left (1.4 mm apart). Figure published in [164].

#### 6.1.2.2 Sequential dual-tracer PET with [ $^{18}\text{F}$ ]FDG

[ $^{18}\text{F}$ ]FDG nicely delineates the mouse brain. Hence, it was implemented as an intermediate step for better image co-registration in a sequential dual-tracer PET paradigm together with [ $^{11}\text{C}$ ]PiB. Animals did neither move during nor in between both PET acquisitions. The relatively even [ $^{18}\text{F}$ ]FDG distribution in the mouse brain as shown in green color in Figure 12 facilitated the co-registration of FDG PET to the prepared MR space (Figure 10B) and the same transformation was applied to the PiB PET image. Figure 12 shows an orthogonal (panel A) and axial overview (panel B) of a representative sequential dual-tracer study co-registered to the corresponding MR image in a 23 month old control mouse. After the automated PiB PET transformation, the results of the manual co-registration procedure (chapter 6.1.2.1) were verified.

The PiB PET is color-coded in red. It indicates that the tracer was primarily taken up in tissues outside of the brain in this animal. The hotspot that was mentioned before (chapter 6.1.1) was located here, to be frontal and around the olfactory bulb. Strongest co-localization information (*yellow*) of both tracers was seen in the eye cavities and along the central nasal cavities. These observations were helpful in the context of unspecific [ $^{11}\text{C}$ ]PiB uptake (chapter 6.3.2.).

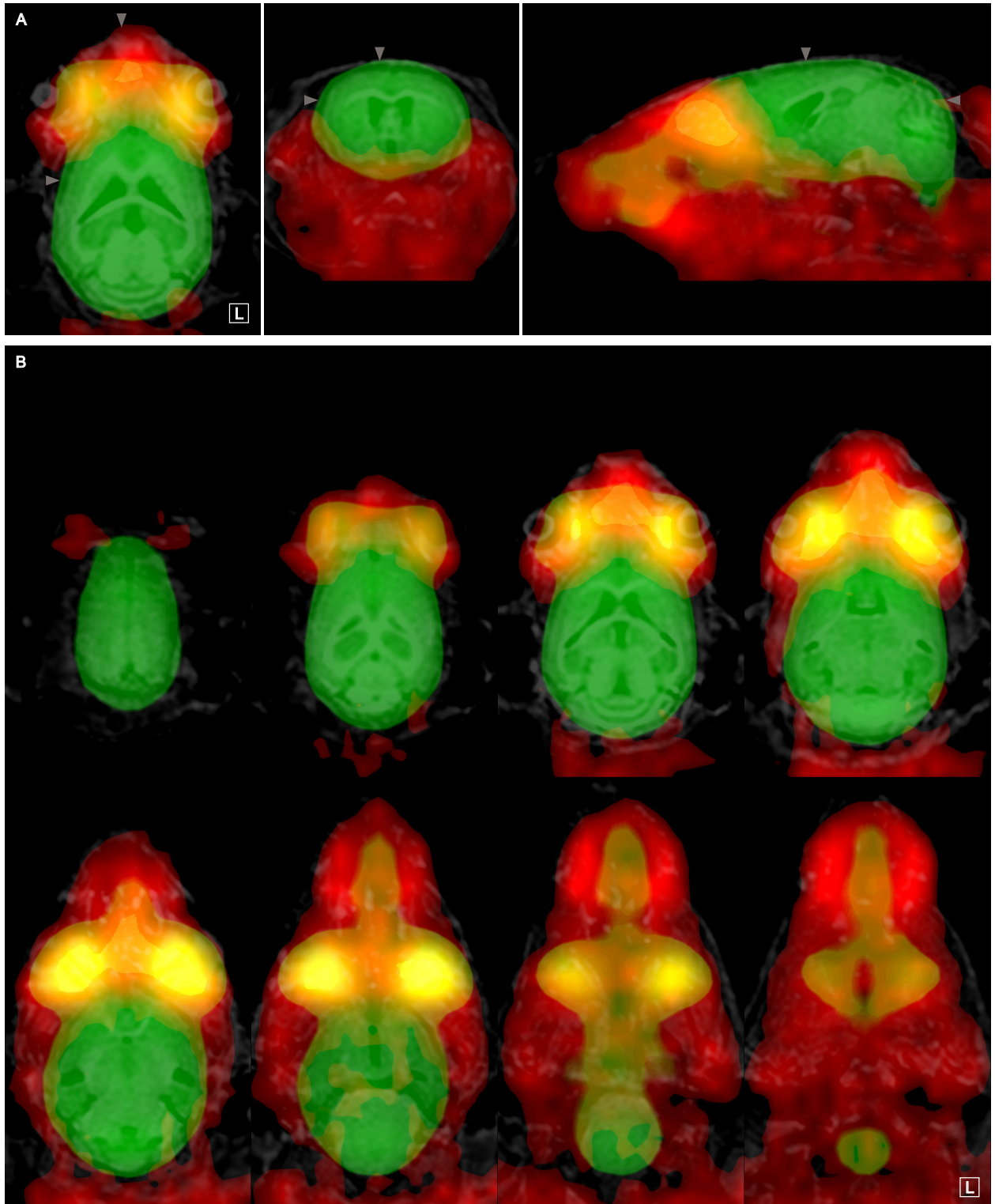


**Figure 12:  $[^{11}\text{C}]\text{PiB}$  /  $[^{18}\text{F}]\text{FDG}$  sequential PET in healthy control.**

For reliable image co-registration (see also Figure 11) and evaluation of extracerebral tracer uptake, several transgenic and control animals were additionally injected with  $[^{18}\text{F}]\text{FDG}$  immediately after their  $[^{11}\text{C}]\text{PiB}$  scan via the other lateral tail vein and without moving the animals. Shown, here, are the orthogonal views (A) at the same locations as in the other figures and the horizontal views (B) from top to bottom (1 mm apart) of a 23 month old control animal which was scanned for 120 min with  $[^{11}\text{C}]\text{PiB}$  (60 min) (red) and  $[^{18}\text{F}]\text{FDG}$  (60 min) (green) without being moved in the scanner and which received an MR scan, the same day. The  $[^{18}\text{F}]\text{FDG}$  image was co-registered to the MR scan and the resulting transformation matrix applied to the  $[^{11}\text{C}]\text{PiB}$  image. The static 30 min frames of the last halves of each scan are shown in combination without any manual co-registration among these datasets. Co-localization (yellow) shows that, in this animal, the hardieran glands have the largest contribution to unspecific  $[^{11}\text{C}]\text{PiB}$  uptake in the eye cavities. Arrowheads (gray) in (A) indicate slice positions. The coordinates for horizontal slices (corresponding to Paxinos

mouse brain atlas) are Bregma -1.90 mm, for coronal Bregma -0.10 mm and for sagittal 0.65 mm lateral (right side). Figure published in [164]

## 6.2 Measuring small-animal [ $^{11}\text{C}$ ]PiB PET images

### 6.2.1 Definition of regions

A template atlas of volumes-of-interest (VOIs) was created on an MR template space yielded as an average from all co-registered MR images that were acquired from ARTE10 animals (Figure 13). Creating VOIs in this standardized way was possible because all animals (control and transgenic) were bred on the same genetic background. This provided for very low variability of brain and skull volumes and shapes. The major target regions were defined as volumes of 101 mm<sup>3</sup> (right and left neocortex) and 49 mm<sup>3</sup> (cerebellum). Figure 14 provides a 3D view onto these target regions with a skull CT as anatomical orientation in the image.

It shall be noted that the regional definition for neocortex was kept consistent wherever possible, i.e. the regional definition was identical for in vivo PET, ex vivo autoradiography and histological quantification of A $\beta$  plaques. Slight deviations from this region definition were sometimes unavoidable and are indicated in the relevant sections.

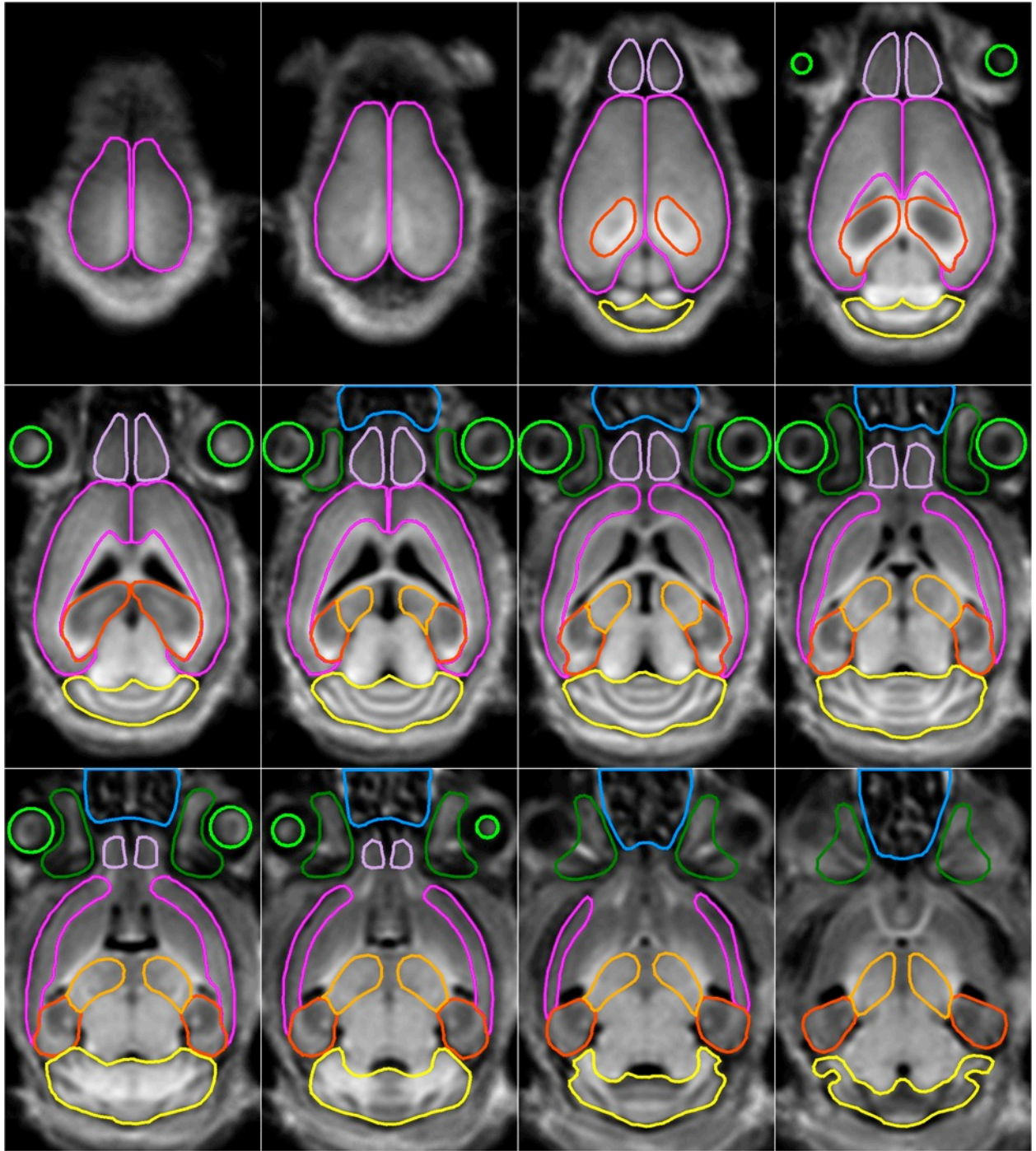


**Figure 13: Volume-of-interest definition.**

Volumes-of-interest (VOI) were defined on horizontal sections of mouse brain MRI template in Paxinos atlas space [62]. Defined paired and non-paired neuroanatomical and cranial structures are cortex (neocortex (*magenta*) and hippocampus (*red*)), thalamus (*orange*), olfactory bulb (*lavender*), cerebellum (*yellow*), eyebulbs (*bright green*), harderian glands (*dark green*), nasal sinuses (*light blue*). The same region definition was used for autoradiographs and microscopic sections. Figure published in [164].

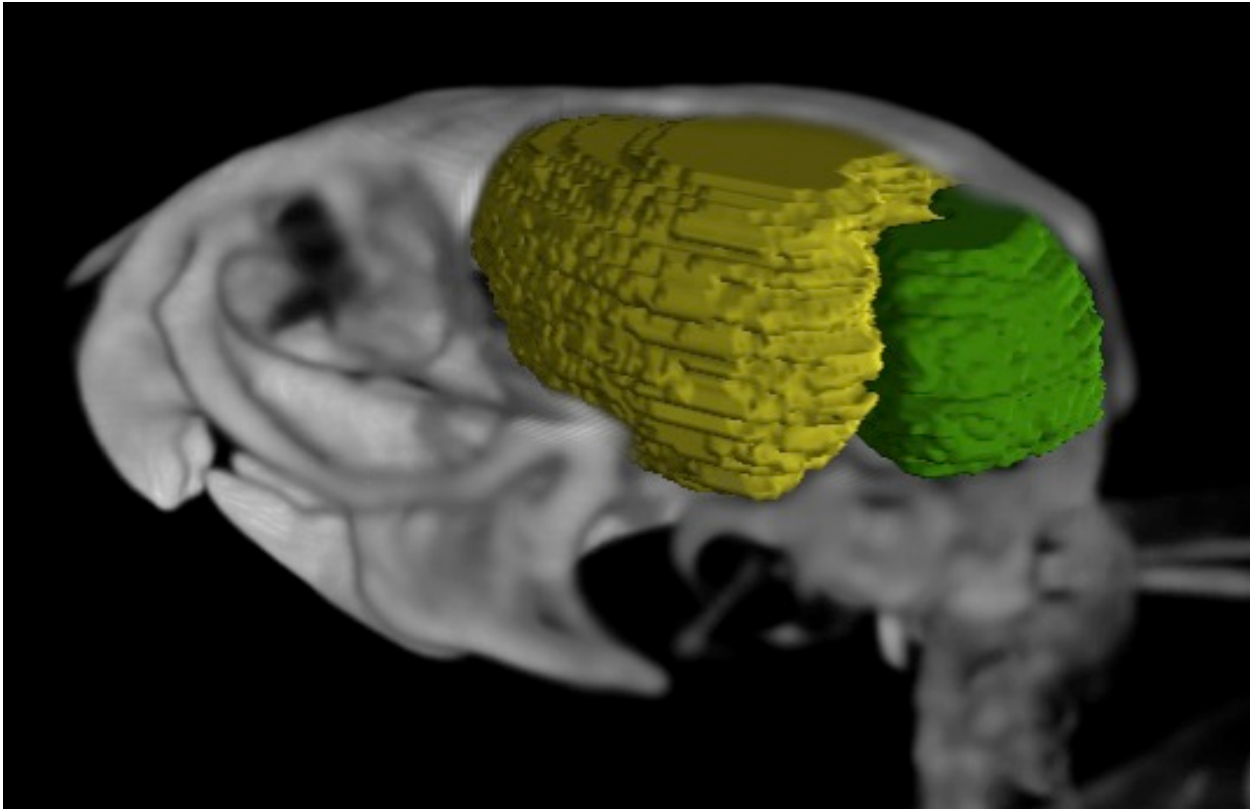


**Figure 14: 3D view of VOI definition.**

3D perspective of neocortical (*yellow*) and cerebellar (*green*) VOI definition in an Inveon-CT image of an APP/PS1 mouse (the left lateral posterior skull octant was cut out to show VOI definition). Reprinted with permission from [278]. Copyright (2011) American Chemical Society.

### 6.2.2 PET with MRI in study groups

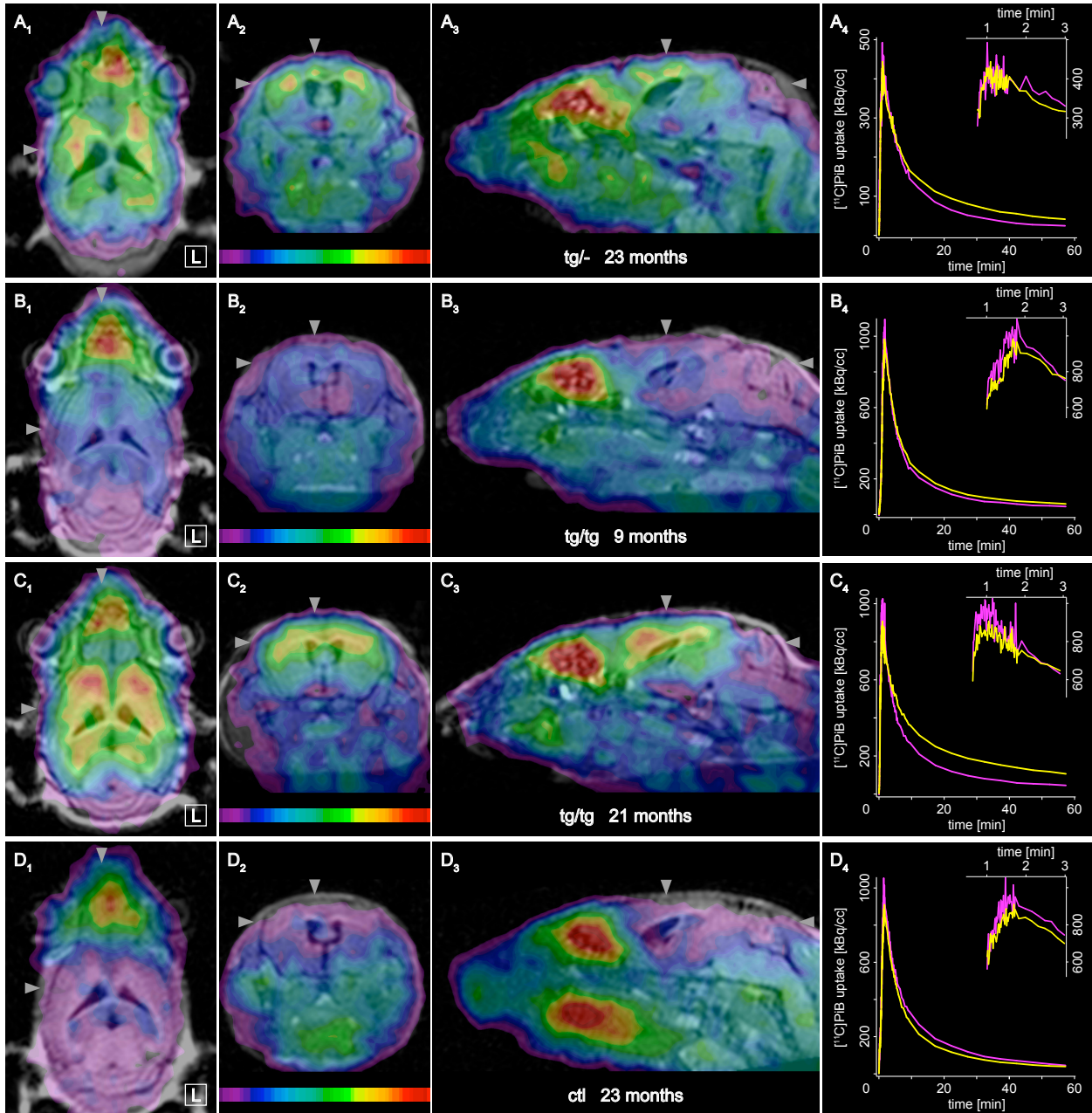
At this point, it was possible to reliably create co-registered mouse brain PET-MR images and to retrieve dynamic tracer uptake information from pre-defined anatomical regions. To gain cross-sectional imaging information from the ARTE10 model at different stages of amyloid-beta deposition a large study cohort was designed (chapter 7.1) according to expected extent of A $\beta$  plaque pathology and to provide consistency with previously published PET imaging studies in mice. It included three transgenic study groups, namely "old" homozygous ARTE10 animals (21 months) where tracer uptake was expected to be highest, "old" hemizygous animals (23 months) with expected intermediate uptake and "young" homozygous mice (9 months) with expected lowest uptake that could reasonably be detected in PET, as well as corresponding control groups (non-transgenic animals of the same inbred strain).

Figure 15 presents a first summary of the single steps presented above. It shows PET-MR images from four animals representative of the four major study groups.

The observations on tracer uptake as described in chapter 6.1.1 could now be rendered more precisely. The semilunar uptake zones (Figure 15, first column) were congruent with the brain hemispheres and the tracer hotspot was located towards the frontal tips of the olfactory bulbs. The crescent-shaped uptake posterior to the hotspot on sagittal sections (Figure 15, third column) was corresponding to neocortex.

Time-activity curves (TACs) of neocortex and cerebellum are shown for each animal. The cerebellum was included as a, yet, hypothetical reference region based on qualitative evidence from our colleagues (histology). The measured cerebellar TACs, themselves, provided further evidence for the cerebellum as a feasible reference region. Initial cerebellar uptake was always higher than initial cortical uptake and cortical TACs of control animals fell below cerebellar TACs early. In contrast, for each transgenic animal the cortical TAC showed higher values than the cerebellar TAC from around 3 min p.i. and remained distinctly separable. From about 10 min p.i., each transgenic animal could be assigned to its study group by its neocortex-cerebellum TACs. The characteristics of the individual TACs were indeed common to their study group as shown in a later figure on averaged group behavior of TACs (Figure 21).

At this point, PET images were calibrated with an external standard, only. The possible quantification discrepancies with this external calibration were noticeable from the data presented in panel A<sub>4</sub> of Figure 15 compared to the other panels in the right column of the same figure. Even though the amount of injected tracer as measured by the difference between full and empty syringe before and after injection is comparable between the animals in panels A and B, the initial peak of brain uptake in panel A is only about half of that in panel B.



**Figure 15: Small-animal [ $^{11}\text{C}$ ]PiB PET/MRI overview for different stages of A $\beta$  burden.**

[ $^{11}\text{C}$ ]PiB PET co-registered to in vivo 1.5 T cranial MRI of the same mouse. Overview of cranial tracer uptake shows images of four representative animals from the major study groups in radiological orthogonal perspective (20 - 30 min frame). (A) 23 month old female hemizygous APP/PS1 mouse (weight: 20.8 g, injected dose: 14.7 MBq, color scale 37 - 144 kBq/cc), (B) 9 month old female homozygous APP/PS1 mouse (weight: 22.2 g, injected dose: 15.2 MBq, color scale 60 - 350 kBq/cc) (C) 21 month old female homozygous APP/PS1 mouse (weight: 24.5 g, injected dose: 24.2 MBq, color scale 73 - 280 kBq/cc), (D) 23 month old female C57BL/6J control mouse (weight: 29.9 g, injected dose: 15.1 MBq, color scale: 66 - 300 kBq/cc). Columns from left to right show horizontal (1), coronal (2) and sagittal (3) views. The right column (4) shows corresponding neocortical (yellow) and cerebellar (magenta) time-activity curves (TACs). Inset (5) shows initial tracer dynamics on a smaller time scale (1 to 3 min) to delineate the peak of uptake required for quantification of PET data. Difference between transgenic and control animals is significant for each study group visibly and analytically. For the young homozygous animal, it is seen in the lower color scale range. Cortex in B<sub>2</sub> shows uptake towards blue and cyan. Same structures show lowest uptake in D<sub>2</sub> (magenta, corresponding to cerebellum). TACs confirm visual perception: neocortex TAC in B<sub>4</sub> intersects cerebellum TAC and stays above it (neocortex-to-cerebellum ratio > 1) while neocortex TAC in D<sub>4</sub> remains below the cerebellum TAC (ratio < 1). PET color look-up-table is UCLA (Pmod) with lower thresholds set to still visualize the cerebellum. Arrowheads indicate slice positions. Slice coordinates (corresponding to Paxinos atlas) are: horizontal Bregma -1.90 mm, coronal Bregma -0.10 mm and sagittal 0.65 mm lateral. Image scale is double size of reality. Further results for these animals are shown in Figure 17 and Figure 19. Figure published in [164].

### 6.2.3 Characterization of ARTE10 cerebellum as reference region

Available standardized time-activity curve data for different regions of the mouse brain triggered the next analytical steps towards measuring tracer binding. This issue was not only related to the calibration of tracer binding in PET but also to other experimental modalities like autoradiography and biodistribution in which tracer binding needed to be quantified and where the development and application of external standards would have provided for a myriad of new challenges. A reliable intracerebral reference region that qualified for analytical reference tissue approaches could have solved this question for all concerned experimental modalities.

Up to this point, good evidence was accumulated about the very low or non-existent A $\beta$  load in the cerebellum and, hence, there was a strong anticipation that the cerebellum may be used as such a reference region. To prove this hypothesis and to potentially validate the cerebellum as a reference region, a histological quantification method for A $\beta$  plaques (plaque load analysis) was applied to the cerebellum with three different staining modalities (antibodies against A $\beta$ 40 and A $\beta$ 42 and Thioflavin S fluorescence). The method was used in a modified variant for the characterization of the ARTE10 model, before.

The A $\beta$ 42 antibody was providing for the fluorescent channel with the highest signal-to-noise ratio and was therefore the most reliable signal for the analysis of a potentially target-free region. The quantification results with the A $\beta$ 42 antibody (Figure 16) were always lower than 0.09 % compared to neocortex of tg-tg-young animals which was larger than 3.09 %. The average cerebellar binding of the A $\beta$ 42 antibody per group was  $0.02 \pm 0.01$  % (range: 0.01 - 0.03) for tg-old,  $0.01 \pm 0.00$  % (range: 0.01 - 0.02) for tg-tg-young,  $0.04 \pm 0.03$  % (range: 0.01 - 0.09) for tg-tg-old and  $0.02 \pm 0.01$  % (range: 0.01 - 0.02) for ctl-old. No significant differences could be seen between the groups: ctl-old to tg-tg-young ( $p = 0.59$ ), tg-tg-young to tg-old ( $p = 0.25$ ) and tg-tg-young to tg-tg-old ( $p = 0.17$ ).

Thioflavin S showed unspecific binding behavior in tissues without A $\beta$  deposits (Figure 19D). Nevertheless, the highest unspecific results in cerebellum were far below the lowest specific results in neocortex (0.82 vs 3.53 %). The average cerebellar binding of Thioflavin S per group was  $0.36 \pm 0.05$  % (range: 0.32 - 0.44) for tg-old,  $0.25 \pm 0.06$  % (range: 0.16 - 0.33) for tg-tg-young,  $0.30 \pm 0.04$  % (range: 0.25 - 0.36) for tg-tg-old and  $0.66 \pm 0.13$  % (range: 0.45 - 0.82) for ctl-old. Although differences between groups were significant, here, it was the control groups that showed slightly higher binding than the transgenic animals, which suggested unspecific binding.

It was notable that even old homozygous animals with very high A $\beta$  plaque burden in neocortex showed an anti-A $\beta$ 42 signal in the cerebellum comparable to the cerebellum of young and healthy control animals and to the neocortex of old control animals (Figure 16). These results for the cerebellum quantitatively confirmed that this region could be used as a reference region.

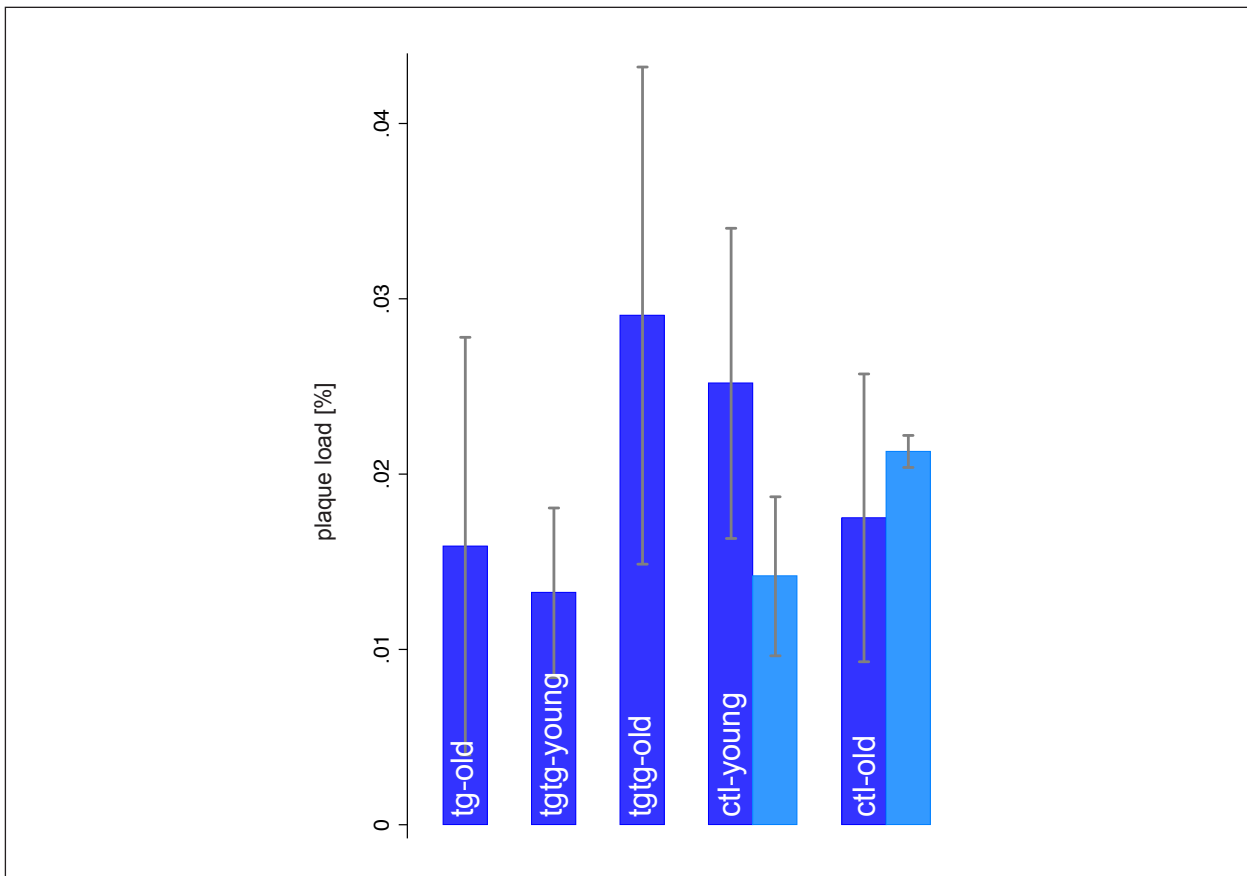


**Figure 16: Cerebellum with very low A $\beta$  plaque load over all ages.**

A $\beta$  plaque burden in cerebellum as measured by applying a computerized image analysis and object recognition algorithm (Acapella™) using the A $\beta_{x-42}$  antibody signal. All study groups presented in this work are shown. Additionally, neocortical results from control groups (*light blue*) are included as further reference for A $\beta$ -free tissue.

#### 6.2.4 Calculating binding potentials and parametric images of mouse brain

Figure 17 shows a first insight into the potential of using the cerebellum as a reference region. The individual in vivo radioligand binding was examined by calculating the binding potential with a reference tissue approach using the cerebellum. Parametric images of regional A $\beta$  plaque burden for representative animals were created with the 2-step multilinear reference tissue model 2 (MRTM2).

The PET data in Figure 17 is the same as in Figure 15. Here, the fields of view are restricted to the brain as kinetic modeling of the tracer outside the BBB with an intracerebral reference region would not provide for physiologically reasonable results. The common calibration scale shows that tracer kinetic modeling provided for comparability of data. It also shows that the quantification discrepancies with external calibration mentioned above (Figure 15A<sub>4</sub> and B<sub>4</sub>) were resolved and that differences in absolute tracer uptake did not necessarily reflect the binding behavior of the tracer. The voxel-wise calculated uptake pattern (Figure 17) presented itself familiar to the "raw" PET data (Figure 15) with a few exceptions. As the cerebellum was defined to be the reference region, it no longer showed tracer uptake. Furthermore, the distribution of the tracer in the control animal seen best in the horizontal view of Figure 17D slightly changed. Binding was restricted to inferior colliculus and lower structures. Chapter 7.2.2 will present results that were consistent with this observation.

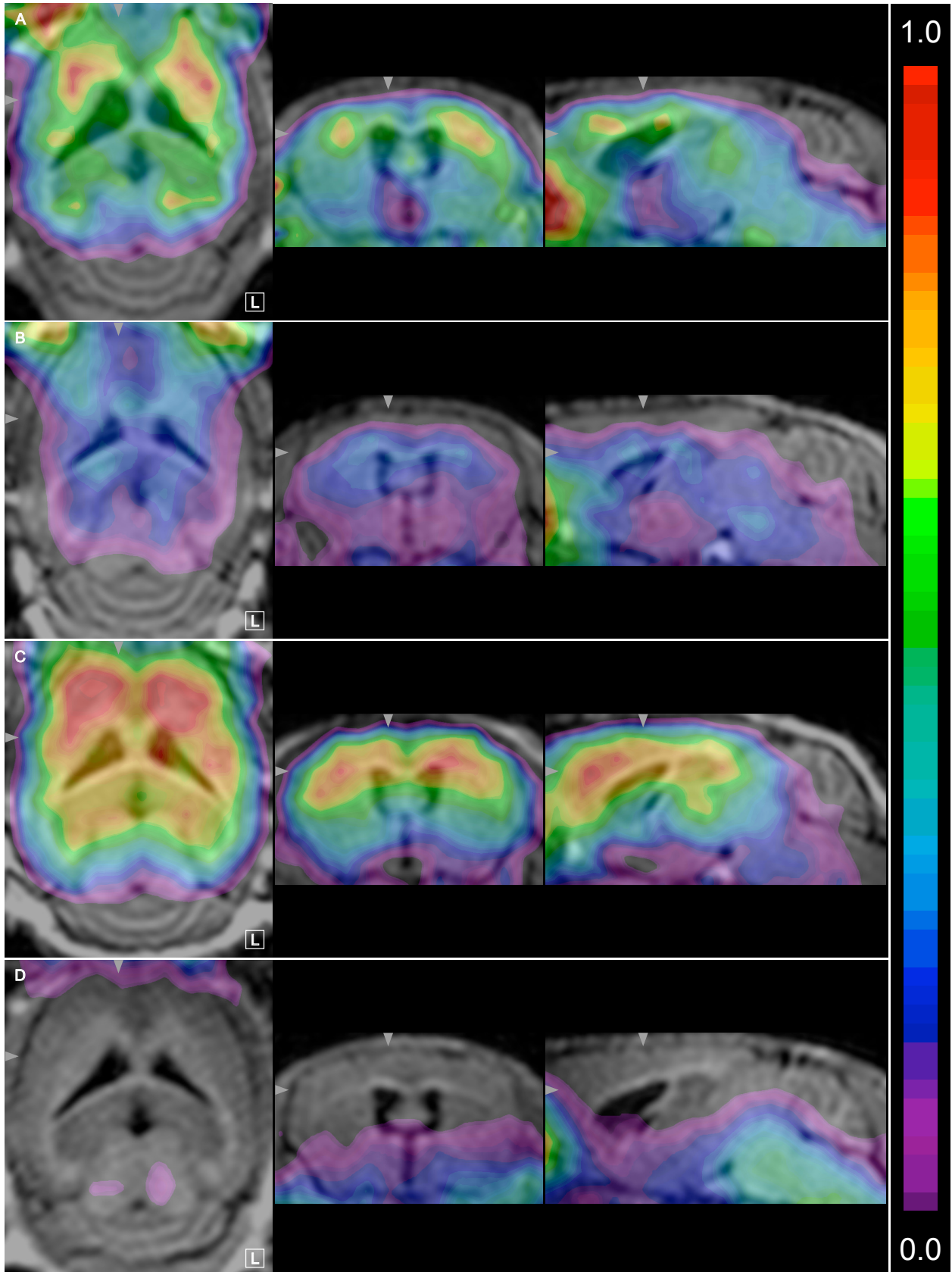


**Figure 17: [ $^{11}\text{C}$ ]PiB PET binding potential maps for mouse brain.**

PET binding potential maps for [ $^{11}\text{C}$ ]PiB in ARTE10 and control mouse brain. (A) 23 month old female hemizygous APP/PS1 mouse, (B) 9 month old female homozygous APP/PS1 mouse, (C) 21 month old female homozygous APP/PS1 mouse, (D) 23 month old female C57BL/6J control mouse. PET color look-up-table is UCLA (Pmod). Arrowheads (gray) indicate slice

positions. The shown coordinates are identical to those shown in Figure 15. For horizontal slices (corresponding to Paxinos mouse brain atlas [62]) they are Bregma -1.90 mm, for coronal Bregma -0.10 mm and for sagittal 0.65 mm lateral (right side). Figure published in [164].

### 6.2.5 PET test-retest scans

A concluding aspect of the proof-of-principle PET measurements was the repetitive imaging of the same animals within a time period in which relevant neuropathological changes would not be expected. This was necessary to verify that the developed PET measurement methodology would provide for reproducible and, hence, reliable binding results of the tracer.

Therefore, several animals were scanned at least twice with identical PET scan protocols one week apart. The stability of the time-activity curve (TAC) retrieval process can be seen from the data presented in Figure 18. As the cerebellum was validated as a reference region, TACs could now be made comparable by normalizing all TACs of each PET scan to 100 % cerebellum. Figure 18 expresses the stability of PET data in two ways: visually by near-congruence of target and reference TACs as well as analytically by similar binding potentials. The test-retest results of PET experiments also reflected the robustness of the image co-registration and VOI definition process mentioned above.

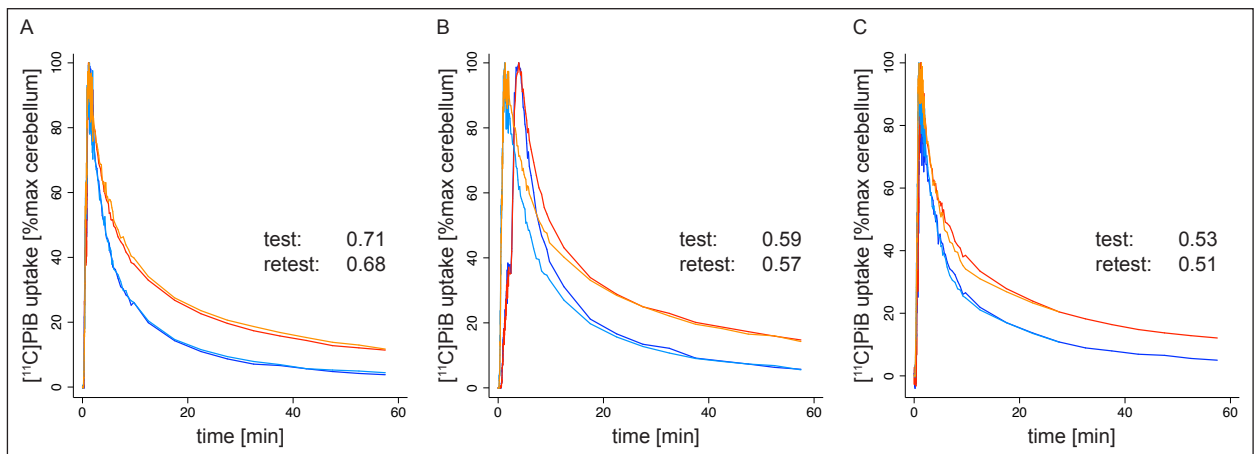


**Figure 18: PET test-retest results.**

Three mice from the tg<sup>tg</sup>-old study group were scanned twice with the same PET imaging protocol. Scans were about one week apart. Time activity curves show dynamic neocortical (red and orange) and cerebellar (dark blue and light blue) uptake during first (darker colors) and second (lighter colors) scan. Peak of cerebellar  $[^{11}\text{C}]\text{PiB}$  uptake was taken as maximum for each scan. Middle panel shows how the injection during the retest scan was slower than during the test scan while the specific uptake tail of the curves approach each other. One retest scan (C) was for 30 min while all other scans were of 60 min duration. Binding potential values ( $\text{BP}_{\text{ND}}$ ) as estimated with MRTM2 are noted in each panel for test/retest scans. Figure published in [164].

### 6.3 Specificity and locality of [ $^{11}\text{C}$ ]PiB binding

After the examination of in vivo imaging protocols for robustness and reliability, it was necessary to return to two essential questions that had already arisen with the very first PET images with [ $^{11}\text{C}$ ]PiB in transgenic mice (Figure 10A): is the intracerebral uptake of the radiotracer an expression of specific binding and is the high uptake of the tracer around frontal parts of the brain related to specific or extracerebral binding?

#### 6.3.1 Specific PiB binding in the mouse CNS

The results mentioned until this point indicated that there was tracer uptake in neuroanatomical regions like the neocortex where specific binding would be expected in transgenic animals. To show that this uptake was truly representing specific binding, [ $^3\text{H}$ ]PiB was included in the routine PET and MRI paradigm as shortly mentioned in chapter 6.1.1. It was administered during the MR scan about 10 hours after [ $^{11}\text{C}$ ]PiB injection to use it as correlating ex vivo information to in vivo PiB binding. Methods were put together to yield correlating experimental information from within the same animals. In this way, digital [ $^3\text{H}$ ]PiB ex vivo autoradiography, Thioflavin S fluorescence and immunofluorescence staining against A $\beta$ 40 and A $\beta$ 42 were used to examine the specificity of [ $^{11}\text{C}$ ]PiB binding in PET. The left column in Figure 17 shows the horizontal (modeled) PET data as presented in the left column of Figure 19.

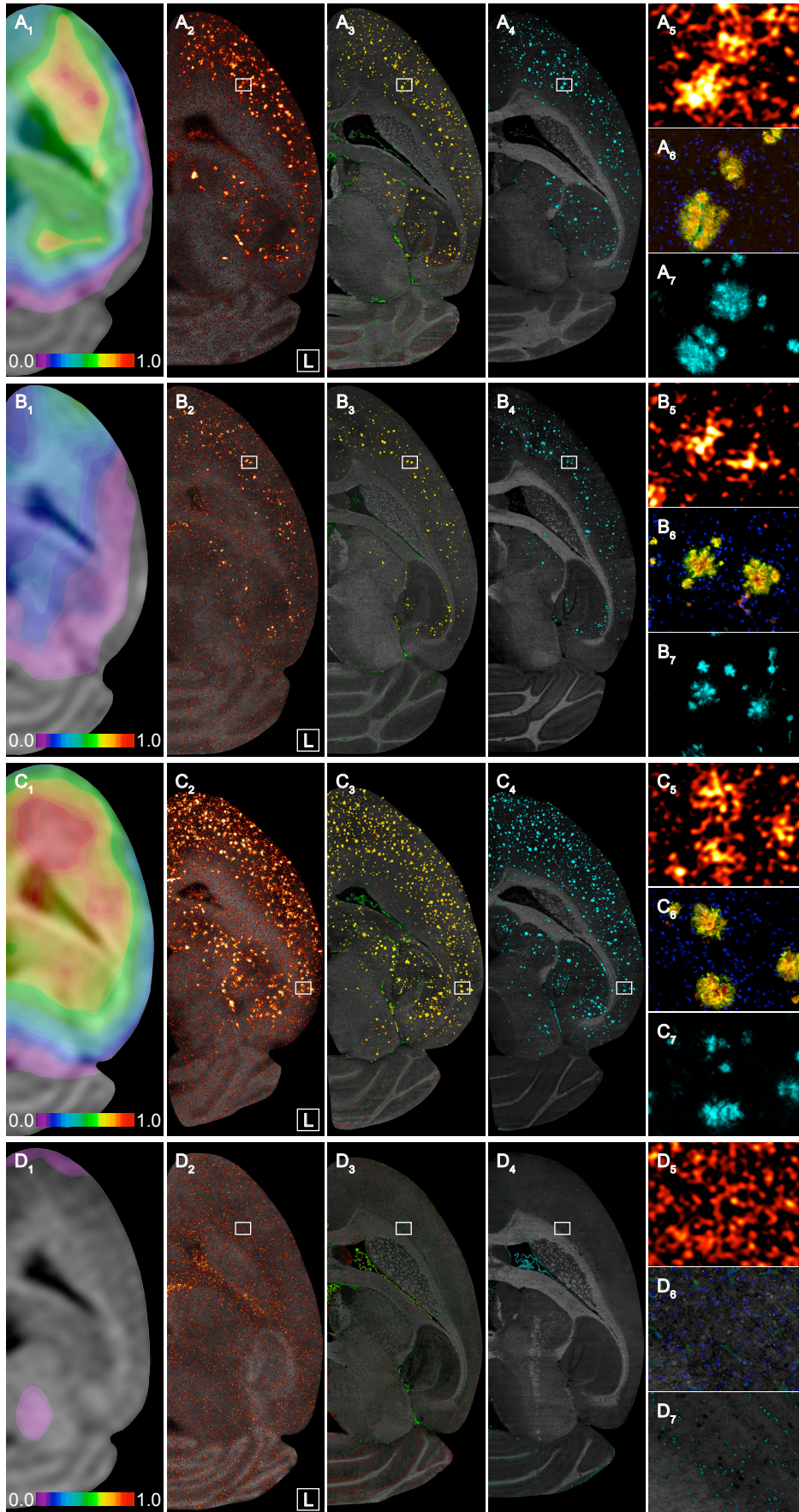


**Figure 19: Mouse A $\beta$  plaque pathology in vivo and ex vivo.**

PET binding potential maps for [ $^{11}\text{C}$ ]PiB and corresponding autoradiography and fluorescence microscopy images of neighboring horizontal brain sections showing data from the same animals presented in Figure 15. Left brain halves are shown. Frontal cortex is at top and cerebellum at bottom of each panel. (A) 23 month old female hemizygous APP/PS1 mouse, (B) 9 month old female homozygous APP/PS1 mouse, (C) 21 month old female homozygous APP/PS1 mouse, (D) 23 month old female C57BL/6J control mouse. *Column (1)*: Binding potential maps for [ $^{11}\text{C}$ ]PiB (BP<sub>ND</sub>, MRTM2) matched to MRI. Shown is the same horizontal level as in Figure 15 and Figure 17. Color table is UCLA (Pmod). Width of color scale represents 3 mm in reality. *Column (2)*: Digital [ $^3\text{H}$ ]PiB ex vivo autoradiograph with optical image (*gray*) of a brain section of the same animal, killed 1 hour p.i.. Color table is Red Hot (ImageJ). *Column (3)*: Double immunofluorescence microscopy for A $\beta$ 40 (*green*) and A $\beta$ 42 (*red*). Anatomical reference (*gray*) is provided by control channel (Cy3). *Column (4)*: Thioflavin S fluorescence (FITC excitation, *cyan*). Anatomical reference (*gray*) is provided by DAPI fluorescence. *Right column*: Identical A $\beta$  plaque constellations of adjacent sections (as marked by white rectangle in columns (1) to (3)). *Top panel (5)*: magnification of digital autoradiograph as seen in *column (2)*. *Middle panel (6)*: corresponding magnified view of A $\beta$ 40/A $\beta$ 42 stain as seen in *column (3)*. *Bottom panel (7)*: corresponding magnified view of Thioflavin S stain as seen in *column (4)*. Columns (2) to (4) show directly neighboring 10  $\mu\text{m}$  thick sections of the left brain half from bottom to top of skull at about 1.9 mm below Bregma. Width of zoom panels in rightmost column represents 350  $\mu\text{m}$  in reality. Complete orthogonal views for binding potential maps are shown in Figure 17. Figure published in [164].

Visual inspection of co-registered PET binding potential maps to MR images (Figure 19, column 1) revealed distinct activity retention in the cortex of all transgenic mice corresponding to their stage of amyloidosis, whereas for all control animals the cortex appeared to be free of specific activity uptake. In transgenic mouse brain the activity uptake expanded throughout the entire cortex, with slightly stronger signal in frontal neocortical compared to hippocampal regions and a stronger signal in the thalamus. Analogously, corresponding autoradiography slices (Figure 19, column 2) showed a homogeneously dotted pattern of intensive multi-focal tracer retention throughout the cortex of transgenic mice with a fully symmetric right-left appearance. Particularly high uptake was detected in the neocortex, hippocampus and thalamus. The strong uptake in the thalamus was notable due to very high tracer retention in fewer but much larger plaques. Plaques were also present in the olfactory bulb although smaller in size (data not shown). Without exception, the cerebellum was free of specific [ $^3\text{H}$ ]PiB uptake in autoradiography. The entire brain of control animals did neither show focal nor diffusely increased neocortical tracer uptake. A clear difference in the amount of [ $^3\text{H}$ ]PiB uptake, corresponding to different stages of A $\beta$  plaque burden, was noted even visually. Hence, the representative samples of the four major study groups showed corresponding results of ex vivo [ $^3\text{H}$ ]PiB uptake in autoradiography to [ $^{11}\text{C}$ ]PiB uptake as measured in PET. In addition, individual uptake patterns were in full correspondence to the patterns of anti-A $\beta$ 40/42 (Figure 19, column 3) and Thioflavin S stains (Figure 19, column 4) done on neighboring sections.

The qualitative observations alone clarified that [ $^{11}\text{C}$ ]PiB binding in the brain of ARTE10 mice was specific. These observations were supplemented by detailed quantitative analyses of all these experimental modalities (chapter 7).

### 6.3.2 Extracerebral tracer retention in frontal proximity to brain

PET images from all animals were showing considerable [ $^{11}\text{C}$ ]PiB retention in regions of the mouse head that appeared to be extracerebral, possibly around nasal and eye cavities, but very close to the brain (Figure 10A). To distinguish specific PiB uptake in brain from probably unspecific extracerebral uptake and for further validation of the PET imaging and co-registration protocol, variants of the general in vivo and ex vivo experiments were performed.

The sequential [ $^{11}\text{C}$ ]PiB / [ $^{18}\text{F}$ ]FDG PET study (chapter 6.1.2.2) included five old homozygous and five control animals. In addition to the helpful information for image co-registration, the automatic overlay of both PET images provided clear spatial localization of the brain and made possible to confirm that the high frontal [ $^{11}\text{C}$ ]PiB retention was indeed located outside the brain (Figure 12).

Additionally, the in vivo PET protocol was modified to a two-step in vivo / ex vivo PET protocol, in which complete heads without brains of four young male homozygous and four young male control animals were scanned from about 35 min to 65 min p.i. (Figure 20B). The remaining [ $^{11}\text{C}$ ]PiB retention in exclusively extracerebral anatomical structures clearly showed the same uptake pattern as seen in PET in vivo.

To confirm the findings from in vivo and ex vivo PET, 20 animals (from a regional brain biodistribution study, chapter 7.2.2) were also used to measure [ $^{11}\text{C}$ ]PiB uptake in various cranial organs (Figure 20C). The organs with the most prominent [ $^{11}\text{C}$ ]PiB uptake were the harderian and parotid gland and the eyebulbs. In general, tracer retention varied unsystematically between animals of the same groups and no differences could be detected between transgenic and control animals.

To further validate unspecific extracerebral tracer retention, ex vivo [ $^3\text{H}$ ]PiB autoradiographs of a complete transgenic homozygous mouse head showed the exact locations of unspecific tracer retention in various anatomical structures very accurately (Figure 20A). Exposition time needed to be shortened to achieve good resolution of extracerebral tissues. For this reason, only few plaques can be seen. The analogy of the unspecific extracerebral uptake pattern in ex vivo [ $^3\text{H}$ ]PiB autoradiography and ex vivo [ $^{11}\text{C}$ ]PiB PET of the head can be seen well.

As the olfactory bulb reaches in between the anatomical structures that have been characterized with high unspecific tracer uptake, it was included in [ $^{11}\text{C}$ ]PiB regional brain biodistribution, [ $^3\text{H}$ ]PiB autoradiography, Thioflavin S and A $\beta$ 40/42 histological analyses

whenever possible. In general, it showed smaller and fewer plaques and lower uptake values, confirming that it was not involved in the higher tracer retention regions around it.

The spectrum of results, above, validated the high unspecific tracer uptake to be extracerebral and model-independent. The proximity of frontal brain parts to extracerebral anatomical structures, in particular present within the eye cavities, confirmed the importance of very accurate image co-registration for reliable PET analyses (chapter 6.1.2).

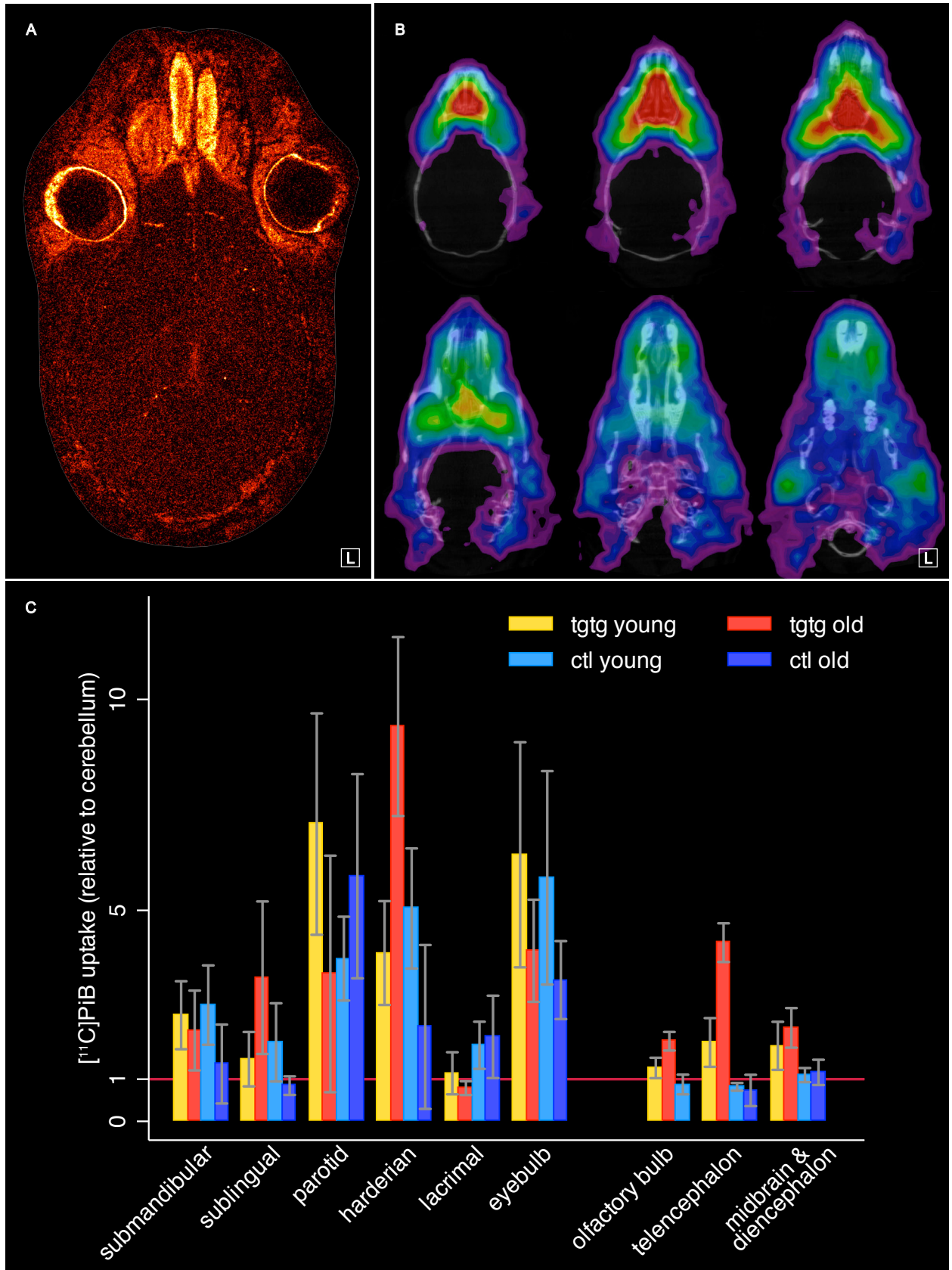


**Figure 20: Extracerebral tracer retention.**

High  $[^{11}\text{C}]\text{PiB}$  uptake in regions frontal to the brain were accurately validated to be extracerebral. (A) Cranial  $[^3\text{H}]\text{PiB}$  ex vivo autoradiography. 15  $\mu\text{m}$  thick section of a complete mouse head showing exact anatomical locations of unspecific tracer retention (male tg tg, 16 months old). Exposition time needed to be shortened to achieve good resolution of extracerebral tissues. For this

reason, only few plaques can be seen in the brain. Color table: *Red Hot* (ImageJ) **(B)** CNS removal during [ $^{11}\text{C}$ ]PiB PET. 9 month old male homozygous APP/PS1 mouse was scanned in vivo for 30 min before the complete brain was extracted and scanned for further 30 min together with the skull. The skull of the ex vivo [ $^{11}\text{C}$ ]PiB PET scan is co-registered to a cranial CT for better orientation and shown on six horizontal slices which are 1 mm apart (top left horizontal level at about -1.9 mm Bregma in correspondence to all other figures). Both parotid glands can be seen on bottom section. Color table is *UCLA* (Pmod) **(C)** Ex vivo biodistribution of [ $^{11}\text{C}$ ]PiB relative to cerebellar uptake in (extracerebral) glandular tissues and eyebulbs in both homozygous and both control study groups. Cerebral biodistribution data from the same animals as presented in Table 8 is included graphically as reference. Data show that olfactory bulb does not contribute to high surrounding uptake in harderian glands and eyebulbs. Column heights represent means, error bars represent standard deviation. Figure published in [164].



---

## 7. Quantitative multi-modal validation of PiB PET imaging in AD mice

The first part of results described the necessary experimental steps towards successful PET imaging with [<sup>11</sup>C]PiB in mouse brains. It provided the prospect that these small-animal PET data should be quantifiable such that the severity of amyloid-beta plaque load could be distinguished between different animals. To more rigorously characterize the nature of PiB binding in the ARTE10 mouse model and to validate its applicability to quantifiable amyloid-beta PET imaging, several *ex vivo* measures needed to be analyzed on a large scale basis for a direct correlation to *in vivo* PiB binding results. This approach required a clear study design with study groups representative of distinct amyloid-beta disease stages and corresponding control groups. In general, the design needed to provide for as many validating experiments to cross-sectional PET imaging per animal as possible.

### 7.1 Study design

Altogether 61 animals in five study groups entered the study program for [<sup>11</sup>C]PiB imaging such that groupwise and pairwise comparisons were possible. Group age definition of animals was chosen to be “young” (9 months) and “old” (21 and 23 months). Three transgenic study groups comprising hemizygous (tg-old) and young and old homozygous (tgtg-young, tgtg-old) animals were included to provide comparability with previous reports (tg-old) and also to show how the imaging outcome can be improved by using homozygous animals. The two control study groups (ctl-young and ctl-old) were designed to match gender and age and to additionally control for any differences among the controls regarding gender (female and male subgroups). Regarding body weight, female transgenic animals tended to weigh less than female controls and female controls weighed less than male controls. The unavoidable differences in weight had no detectable influence on the results presented, here. Table 6 shows a detailed description of the study collective and the combination of experiments performed for each subgroup.

study group	sub-group	age [months]	weight [g]	PET	injected dose [MBq]	MRI	CT	auto radio	histological quantification		ELISA	biodistribution	
									Thio-flavin S	A $\beta$ 40/A $\beta$ 42		brain	cranium
tg-old	5 ♀	23.2 ± 0.1	24.5 ± 1.2	5	13.9 ± 3.1	5		5	5	5	2		
tgtg-young	5 ♀	9.2 ± 0.0	22.4 ± 0.5	5	28.9 ± 7.9	5		5	5	5	2		
	4 ♂	9.4 ± 0.1	27.1 ± 0.5	4	32.3 ± 4.6	1							
	5 ♂	9.0 ± 0.0										5	5
	2 ♀	9.1 ± 0.1	25.3 ± 2.1	2	63.4 ± 3.7		2	2	2	2	2	2	
tgtg-old	4 ♀	21.1 ± 0.1	23.3 ± 0.6	5	22.4 ± 2.6	4		4	5	5	4	1	1
	4 ♀	21.6 ± 0.0	21.9 ± 0.9	4	32.0 ± 2.7						4	4	4
ctl-young	5 ♀	9.4 ± 0.1	25.6 ± 0.8	5	15.8 ± 1.9	5		2	5	1			
	5 ♂	9.0 ± 0.0	31.0 ± 0.3	5	25.5 ± 3.3	5							
	5 ♀	9.3 ± 0.0										5	5
	2 ♀	9.0 ± 0.6	32.7 ± 1.0	2	51.2 ± 1.4		2	2	2	2		2	
ctl-old	5 ♀	23.6 ± 0.1	29.8 ± 1.9	5	20.7 ± 3.3	5		4	5	2			
	5 ♂	23.0 ± 0.0	33.3 ± 1.5	5	11.9 ± 3.1	5							
	5 ♂	23.2 ± 0.0										5	5
SUM				47		35	4	24	29	22	22	24	20

**Table 6: Mouse study collective and numbers of mice per experiment**

Five study groups were defined, three of them with transgenic APP/PS1 mice, the others with age- and gender-matched controls. Major subgroups were female. *Old* refers to an age of about 23 (hemizygous (*tg*)) and 21 months (homozygous (*tg*)). *Young* is defined as an age of 9 months. Young homozygous study group (*tg*-*young*) and both control groups (*ctl*) were designed to reveal possible gender effects. As an overview and orientation, numbers in each cell state how many animals per subgroup were analyzed in the corresponding experiment. Mean ages, weights and injected doses are shown for each subgroup including standard deviation. *tg*: hemizygous APP/PS1, *tg*: homozygous APP/PS1, *ctl*: C57BL6/J control animals. Table published in [164].

## 7.2 Cross-validation of PET in study groups

Many methodological challenges are related to mouse brain PET with [ $^{11}\text{C}$ ]PiB. Therefore, after having shown qualitatively that PiB was bound specifically in ARTE10 mouse brain, the second step was to strengthen the initial principle findings by showing how quantitation of PiB binding in PET directly relates to alternative independent experimental measures in the same animals. This approach required the killing of animals after PET and therefore caused a cross-sectional study design (Table 6). The cross-validations were performed in two flavors. First, to provide for statistical power of results, a minimum group size of five was chosen. Hence, the overall number of animals to be scanned and analyzed from all study groups required streamlining of the experimental workflow, for example, in the context of efficient use of the synthesized

radiotracer. Hence, not every available experimental modality could be included, here, for example, regional brain biodistribution or dual-tracer analysis. Therefore, a second experimental design was devised to include every available experimental method. The results of this combined multi-modal dual-label experiment including four young animals are described in chapter 8.1.

The following sections describe the experimental modalities for cross-validation and will be closed with a summarizing scatterplot matrix containing all individual results. All modalities except biodistribution were performed in the same animals that were scanned with PET. The design of study groups for regional brain biodistribution was kept the same to guarantee for representative group results.

### **7.2.1 Quantification of [<sup>11</sup>C]PiB binding in PET**

For a large-scale and groupwise in vivo assessment of cerebral A $\beta$  plaque deposition, 47 animals in five study groups were scanned at least once with [<sup>11</sup>C]PiB. 35 of these animals also received an in vivo MR brain scan on a human clinical (Table 6). The individual in vivo radioligand binding was examined with decay-corrected time-activity curves by calculating the binding potential with a reference tissue approach using the cerebellum. The binding potential values for neocortex estimated by the 2-step multilinear reference tissue model 2 (MRTM2) for the whole study collective showed highly significant separation of all transgenic animals from controls and a clear distinction of AD animals belonging to different study groups.

It was now possible to describe the binding behavior that was shown for representative animals, before (Figure 17), more generalized for each study group. Old homozygous ARTE10 animals (tgtg-old) exhibited highest activity retention, followed by old hemizygous (tg-old) and young homozygous mice (tgtg-young). The tg-old animals were at all scans in between the homozygous groups while their results were generally closer to those of the tgtg-young group. In control animals no kind of specific tracer uptake within the entire brain was ever observed (Figure 17, Figure 24 and Table 8).

In general, no significant differences in activity uptake were found between old and young or female and male control animals. Further, no significant difference was found between male and female young homozygous animals. Also, there were no differences between right and left hemispheric tracer uptake observed in all animals.

The stability of PET measurements themselves was already shown in the first part of results (chapter 6.2.5), i.e. whether PET provided for similar results when the experimental conditions remained unchanged. Another important question was regarding the consistency of these analytical results, i.e. was the separability of results caused by the applied method or was it a true reflection of reality as shown by independent alternative analyses. Answering this second question required multiple calculations on the whole study collective as presented in this section.

### 7.2.1.1 Group behaviour of time-activity curves

A visibly perceptive measure of consistency was created by group-wise averaging of time-activity curves normalized to 100 % cerebellum per study group (Figure 21). Each group comprises animals of equal age and transgene status and, hence, comparable amyloid-beta neuropathology would be expected. The general behavior of individual TACs as shown representatively in Figure 15 remained the same after averaging of TACs from five animals per group. It is notable that the averaged TACs also show how neocortical averages stay above cerebellar averages. This provided first and visible evidence that the differences measured in PET may be consistent between groups.

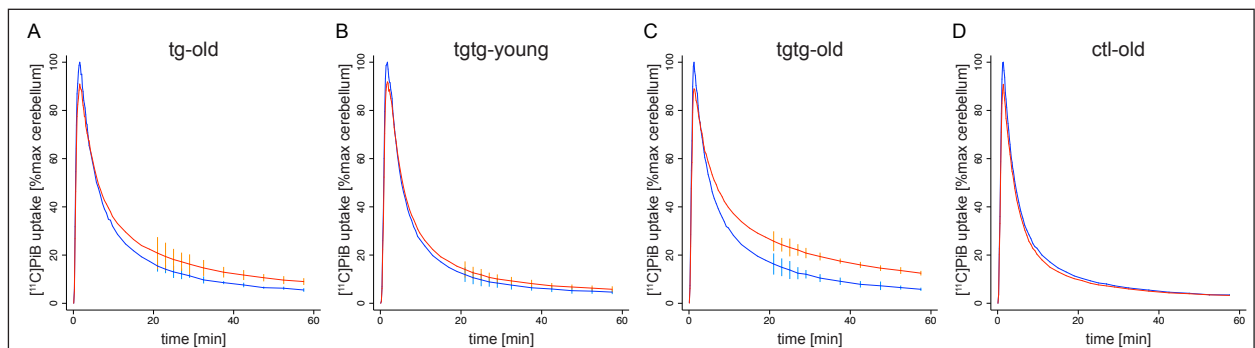


**Figure 21: Time-activity curve averages per group.**

Averaged neocortical (*red*) and cerebellar (*blue*) time-activity curves (TACs) for the major study groups. The behavior of individual TACs as shown in Figure 15 is also reflected in the groupwise behavior. Peak of cerebellar [<sup>11</sup>C]PiB uptake was taken as maximum for each animal. Vertical bars depict one standard deviation from group average. (A) tg-old, (B) tggg-young, (C) tggg-old and (D) ctl-old. Figure published in [164].

### 7.2.1.2 Analyzing PET with different methods

Quantification of PET data in small animals is not yet standardized such that calculating alternative measures for radioligand binding was an additional validating step to further prove the robustness and consistency of specific [<sup>11</sup>C]PiB uptake besides what was already mentioned above (Figure 21). Table 7 shows the averages of in vivo PiB binding results for

each of the major study groups as measured with three different methods. All study groups could be clearly distinguished from each other.

The first method applied was the major method being used for [ $^{11}\text{C}$ ]PiB in the thesis (MRTM2) and was already described in chapter 6.2.4. The third, static ratios, was the simplest way to quantify PET data by dividing the tracer uptake values taken from a volume-of-interest from a specified time period. The second method was a more elaborated ratio approach by using TAC integrals (Table 7).

study group	BP <sub>ND</sub> (MRTM2 [102])		tissue integral ratio [106]		target-to-reference ratio (20-30 min static)	
	mean $\pm$ SD	p-value	mean $\pm$ SD	p-value	mean $\pm$ SD	p-value
ctl-old (N = 5)	-0.08 $\pm$ 0.01	< 0.001	0.0007 $\pm$ 0.0005	< 0.001	0.90 $\pm$ 0.02	< 0.001
tg <sub>tg</sub> -young (N = 5)	0.12 $\pm$ 0.04	0.001	0.0614 $\pm$ 0.0034	0.074	1.20 $\pm$ 0.06	0.002
tg-old (N = 5)	0.28 $\pm$ 0.06	< 0.001	0.0948 $\pm$ 0.0310	< 0.001	1.38 $\pm$ 0.06	< 0.001
tg <sub>tg</sub> -old (N = 7)	0.51 $\pm$ 0.13		0.1747 $\pm$ 0.0240		1.68 $\pm$ 0.12	

**Table 7: Robustness of PET results.**

PET results shown as averages for the major study groups with neocortex as target region and cerebellum as reference region. Results were tested for differences between groups corresponding to the staging of A $\beta$  load in these groups (i.e. p-value for difference to group below). Names of study groups correspond to Table 6. Table published in [164].

These quantitative group results showed consistency between three independent analysis methods and a close association with the visible behavior of averaged TACs (Figure 21). In addition, they confirmed the visual perception of the representative animal PET data shown in Figure 17. The detailed [ $^{11}\text{C}$ ]PiB binding results of all animals individually will be presented at the end of this results section in association with the other experimental modalities.

### 7.2.2 Regional brain biodistribution of [ $^{11}\text{C}$ ]PiB *ex vivo*

This biodistribution study was developed to gain differential tracer uptake information from different parts of the mouse brain. It needed to be performed independently of PET measurements as described in the beginning of chapter 7.2. A combination with PET will be presented in chapter 7.3.

Twenty animals from the homozygous transgenic study groups and matched controls were used for *ex vivo* regional brain biodistribution of [ $^{11}\text{C}$ ]PiB at 30 min p.i.. Mouse brains were dissected into four regions: 1. telencephalon as the major target region, 2. olfactory system for

its proximity to high extracerebral uptake regions, 3. cerebellum as the reference region and 4. diencephalon and midbrain as the remaining brain structures. The cerebellum was used as the reference region for ratio calculations of individual %ID/g values. Here, telencephalon was chosen as the primary target region for reasons of efficacy and speed during dissection with a short-living isotope like  $^{11}\text{C}$ . It comprised the mouse cortex, i.e. neocortex and hippocampus, and the striatum.

The target-to-reference ratios for telencephalon confirmed the *in vivo* PET measurements for neocortex in these study groups. The results for the old homozygous animals showed a large difference to the young homozygous mice ( $p < 0.001$ ). This corresponded to the large differences between these two groups as seen in all the other experimental modalities (Table 8).

The young transgenic animals could easily be separated from the controls ( $p = 0.012$ ). Differences between the young and old control groups were not significant ( $p = 0.090$ ). In the control groups, it is notable that the tracer uptake for the telencephalic region relative to cerebellum was reversed ( $< 1$ ).

A similar behavior of relative uptake of [ $^{11}\text{C}$ ]PiB was found in the other two target regions. The PiB uptake in the olfactory system in transgenic mice is specific, but considerably lower than in cortical regions. Young transgenic animals even had no significantly higher uptake than young controls ( $p = 0.491$ ) corresponding to a low A $\beta$  plaque load in the olfactory bulb at younger ages. The relative tracer uptake in old homozygous animals was slightly higher than in young ones ( $p = 0.027$ ) but by far not as distinct as for the telencephalon. This confirmed the findings by our colleagues who characterized the ARTE10 model and was consistent with our observations of smaller and fewer plaques in the olfactory bulb. This result was also notable in the context of unspecific tracer binding. The olfactory bulb reaches in between extracerebral structures with high unspecific tracer uptake but was not a contributing region for these high uptakes.

Relative [ $^{11}\text{C}$ ]PiB uptake of the remaining basal brain structures (diencephalon and midbrain) was already significantly higher in young transgenic animals than in controls ( $p = 0.031$ ) (Table 8). However, in old homozygous animals it was not significantly higher to the young ones ( $p = 0.318$ ). The difference between young and old control groups was not significant ( $p = 0.114$ ). For this region, it is notable that the relative tracer uptake was not reversed in the control groups ( $> 1$ ). The relative [ $^{11}\text{C}$ ]PiB uptake behavior presented in Table 8 is also shown graphically in Figure 20C as reference to [ $^{11}\text{C}$ ]PiB uptake in extracerebral structures.

study group	olfactory system	telencephalon	diencephalon and midbrain
tgtyg-young	1.27 ± 0.24	1.87 ± 0.58	1.79 ± 0.57
tgtyg-old	1.90 ± 0.22	4.23 ± 0.46	2.22 ± 0.47
ctl-young	0.87 ± 0.23	0.82 ± 0.09	1.10 ± 0.17
ctl-old		0.67 ± 0.12	1.11 ± 0.13

**Table 8: Regional brain biodistribution of [<sup>11</sup>C]PiB.**

Mouse brain was dissected into four regions (olfactory system, telencephalon, cerebellum and remaining brain structures) 30 min p.i.. Results show mean [<sup>11</sup>C]PiB uptake ratios (± SD) of the three target regions relative to cerebellum (initially measured as %ID/g) for the homozygous study groups and both control groups. Data are reported graphically in Figure 20C as reference to extracerebral [<sup>11</sup>C]PiB distribution. Table published in [164].

### 7.2.3 Autoradiography with [<sup>3</sup>H]PiB ex vivo

Ex vivo autoradiography with [<sup>3</sup>H]PiB was one of the prime correlating methods to [<sup>11</sup>C]PiB PET. The same tracer (PiB) with a long-lasting and high-resolution label (tritium) could be measured directly on a large number of brain sections. Required exposure times and the maximum number of samples that can be measured in a single imaging session asked for a compromise between imaging techniques. Conventional plate autoradiography offers higher throughput at lower sensitivities while digital autoradiography is limited to few samples at higher sensitivities. Both modalities were used to supplement and validate each other and to achieve sufficiently large sample sizes. Extensive ex vivo autoradiography of brain slices was performed to verify that the cortical tracer uptake values as measured by PET represent true binding of [<sup>11</sup>C]PiB to cortical A $\beta$  plaques. All animals in this analysis had a PET scan with [<sup>11</sup>C]PiB, before.

Visual perception of differences in ex vivo tracer uptake between the study groups (Figure 19) could be confirmed quantitatively by measuring a total of 64 slides from 24 animals of the study collective yielding 248 observations for the cortical region (Table 6). Target region definition was identical to region definition used for PET (chapter 6.2.1, Figure 13).

The neocortex-to-cerebellum ratios of [<sup>3</sup>H]PiB uptake fully reflected the in vivo PET findings for the same target region. The average ratios for tg-old were 1.90 ± 0.26 (range: 1.46 - 2.11), for tgtyg-young 1.25 ± 0.07 (range: 1.19 - 1.33), for tgtyg-old 2.54 ± 0.27 (range: 2.13 - 2.71) and for ctl-old 0.93 ± 0.02 (range: 0.90 - 0.95). Statistical significance of differences between groups was tested for ctl-old against tgtyg-young ( $p < 0.001$ ), tgtyg-young against tg-old ( $p = 0.004$ ) and tg-old against tgtyg-old ( $p = 0.002$ ) corresponding to the staging of A $\beta$  load in these groups.

No significant differences in tracer uptake were found between right and left neocortical regions in all animals and between old and young control animals.

### **7.2.4 Histological plaque quantification in neocortex of transgenic mice**

Quantification of A $\beta$  plaque burden on histological sections of mouse brain with a single antibody for the detection of all A $\beta$  was already performed for the characterization of the ARTE10 model.

To validate PET measurements, the method was repeated for the animals that were scanned in PET. For this, the method was adapted to frozen brain sections and enhanced towards the differentiated detection of A $\beta_{x-40}$  and A $\beta_{x-42}$  components with immunofluorescence. In addition, Thioflavin S staining was included for the quantification of A $\beta$  plaques.

Brain sections were stained with Thioflavin S (29 animals) and with double immunofluorescence against A $\beta_{x-40}$  (anti-A $\beta$ 40) and A $\beta_{x-42}$  (anti-A $\beta$ 42) (22 animals) for the histological quantification of A $\beta$  plaque load and plaque size distribution (Table 1) by applying a computerized image analysis and object recognition algorithm similar to the one that was used for the characterization of the ARTE10 model. All animals in this analysis had a PET scan with [ $^{11}\text{C}$ ]PiB, before.

#### **7.2.4.1 Thioflavin S and A $\beta$ 40/42 antibodies for plaque quantification**

The correlations between Thioflavin S quantification with each of the antibodies and with their compound signal are presented in Figure 22. Furthermore, Thioflavin S recognized a similar amount of relative A $\beta$  plaque load as the anti-A $\beta$ 40/42 compound signal (Figure 23A). Also, the anti-A $\beta$ 40/42 compound result (Figure 23A) reflects that the anti-A $\beta$ 40 and anti-A $\beta$ 42 measurements are mostly co-localized.

Thioflavin S staining was excellent for analyzing tissues with A $\beta$  deposits. However, it showed some unspecific binding in A $\beta$ -free regions depending on the neuroanatomical location, in contrast to the specific A $\beta$  antibodies. Among the regions we have measured, the highest unspecific values were found in thalamus of control animals. We expect this to be mostly related to the texture of the regional brain tissue. It may also be method-related as exposition and measurement parameters were kept identical for each stain and were adjusted to measurements in the neocortex.

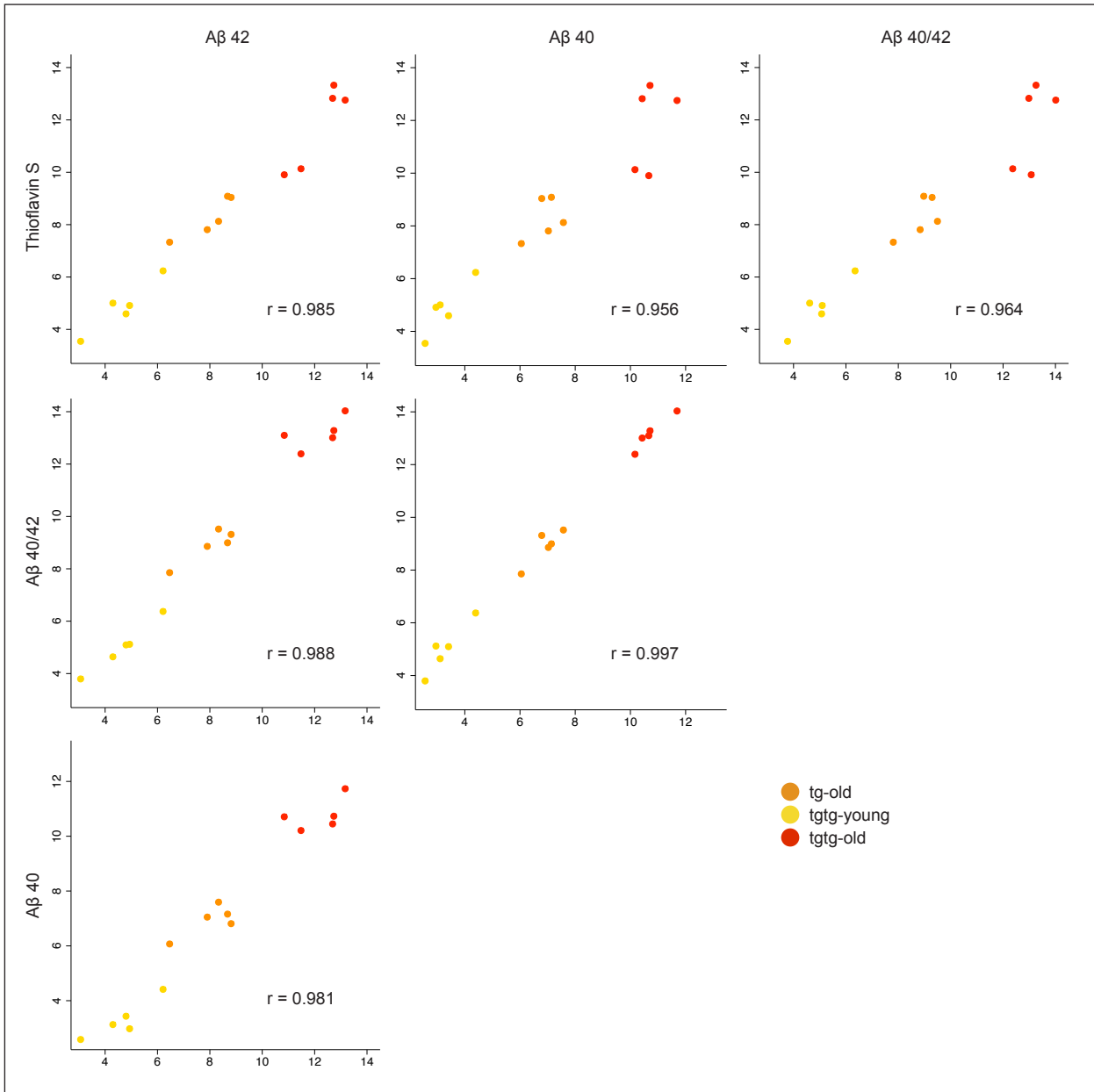


**Figure 22: Thioflavin S and Aβ40/42 antibodies for histological quantification of Aβ plaques.**

Aβ plaque burden was analyzed on histological sections stained with Thioflavin S and double immunofluorescence against Aβ40 and Aβ42 by applying a semi-automatic imaging algorithm. All animals were analyzed in PET, before. Scatter plot matrix showing individual relative plaque areas (%) for neocortex of the transgenic study groups in all three staining modalities including the compound signal of the Aβ40/42 antibodies. The results show how plaque area quantification with Thioflavin S tightly correlates to the specific antibodies. Hence, it was used representatively in Figure 24. Pairwise correlation coefficients ( $r$ ) for each pair of modalities are noted in each panel. The study groups in the scatter matrix are identified by color: tg-old (*orange*), tgtg-young (*yellow*) and tgtg-old (*red*). Figure published in [164].

### *7.2.4.2 Relative A $\beta$ plaque area and plaque size distribution*

Relative plaque areas and plaque size distributions were measured using a very large dataset for robust analysis of neocortex with Thioflavin S (643 observations) and A $\beta$ 40/42 antibodies (158 observations) (Figure 23).

The results from histological A $\beta$  plaque quantification in neocortex also were consistent with in vivo PET results for the same region. Highest values were observed for the tgtk-old group, followed by tg-old and tgtk-young.

The results of plaque load as measured by Thioflavin S are reported in text, here. Their values in target regions with A $\beta$  deposits were representative for the analysis with A $\beta$ 40/42 antibodies as shown above (Figure 22). Plaque load based on Thioflavin S binding in neocortex was measured for tg-old as  $7.72 \pm 1.03$  % (range: 6.27 - 9.07 %), for tgtk-young as  $4.68 \pm 0.70$  % (range: 3.53 - 5.37 %), for tgtk-old as  $11.78 \pm 1.63$  % (range: 9.88 - 13.31 %) and for ctl-old as  $0.61 \pm 0.17$  % (range: 0.34 - 0.79 %). Differences between groups were tested corresponding to the staging of A $\beta$  load in these groups (ctl-old against tgtk-young, tgtk-young against tg-old and tg-old against tgtk-old). The difference between all groups was highly significant ( $p < 0.001$ ). For all relative plaque load observations, no differences were found between right and left brain sides in all animals and between old and young control animals.

Plaque sizes considerably increased with age in hemizygous and homozygous animals (Figure 23B). After histogramming the individual plaque sizes for each transgenic group, and estimating kernel density functions, we could calculate that the differences between plaque size distributions of all transgenic study groups were highly significant ( $p < 0.001$ ). While relative plaque areas and size compositions were significantly different between the old study groups, the size composition of plaques in neocortex at old ages appeared to have a similarity independent of genotype.

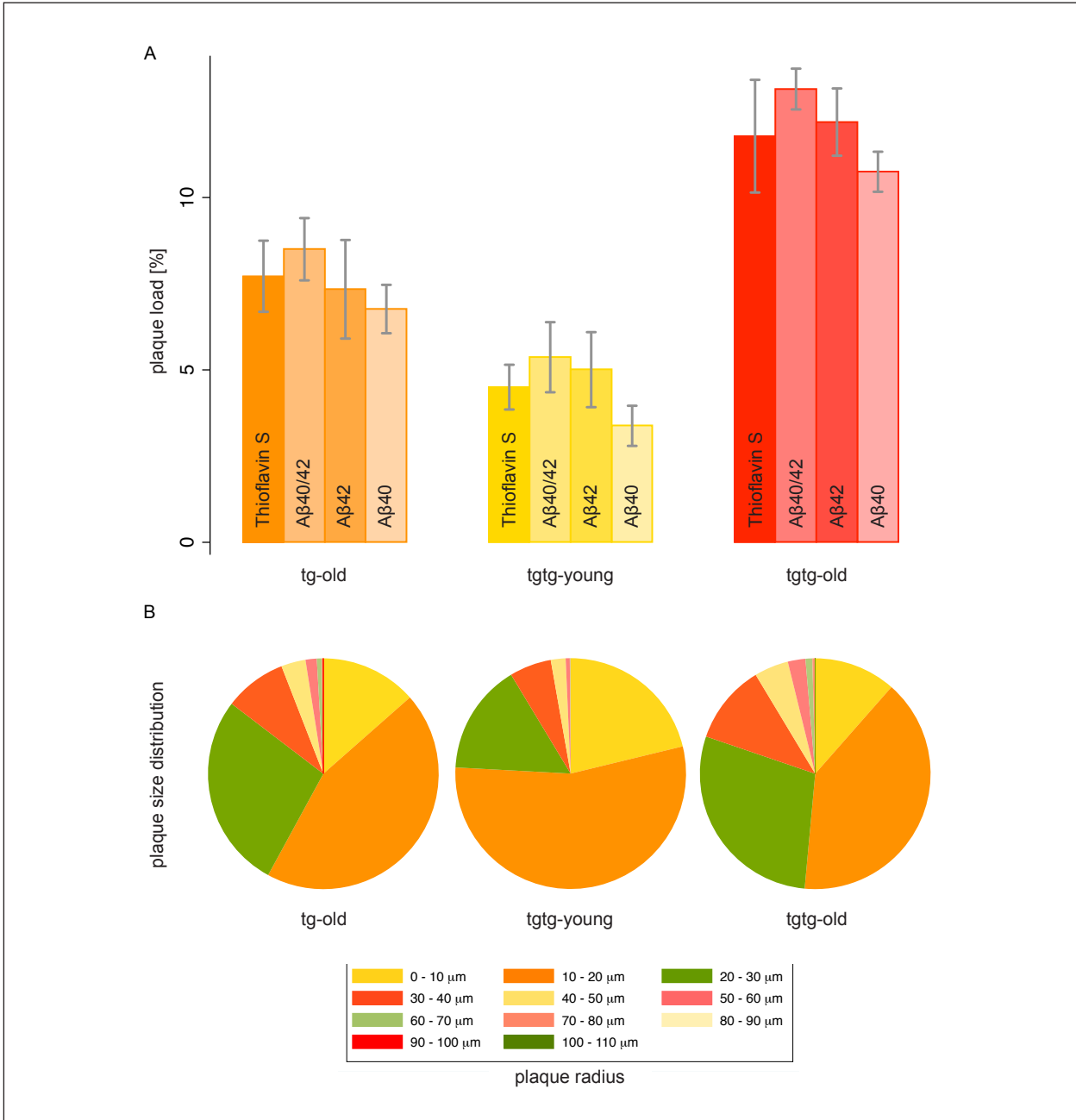


**Figure 23: Histological Aβ plaque burden and plaque size distribution in neocortex.**

Aβ plaque burden and size of individual plaques were analyzed on histological sections stained with Thioflavin S and double immunofluorescence against Aβ40 and Aβ42 by applying a semi-automatic imaging algorithm. All animals were analyzed in PET, before. Shown here, are the results for neocortex of the transgenic study groups: tg-old (*orange*), tggg-young (*yellow*) and tggg-old (*red*). **(A)** Aβ plaque burden of each transgenic group as measured by Thioflavin S, compound anti-Aβ40/42, anti-Aβ42 and anti-Aβ40. Compound anti- Aβ40/42 result shows co-localization of both Aβ species. **(B)** Plaque size distribution in each transgenic study group. Here, the anti-Aβ42 signal was used for its highest signal-to-noise. Its strong association with the Thioflavin S signal is shown in Figure 22. Color-coding for pie-charts was chosen for best comparability between charts and for sufficient contrast of components. Figure published in [164].

### 7.2.5 A $\beta$ 40 and A $\beta$ 42 protein levels (ELISA)

For the basic characterization of the ARTE10 model, detailed differential A $\beta$  protein analyses were performed in combination with the quantification of A $\beta$  plaque burden and very tight correlations between these two were already shown. To further validate our PET imaging results brain tissue of 14 animals that received a PET scan was biochemically quantified for human A $\beta_{x-40}$  and A $\beta_{x-42}$  protein (Table 6). Differential extraction procedures were applied in order to determine the levels of either soluble or insoluble forms of A $\beta$  species for all samples.

For reasons of consistency and to benefit from the abundance of already available ELISA data that was yielded for the characterization of the ARTE10 model, the brain part that was chosen for this ELISA analysis was a brain hemisphere without cerebellum and, hence, contained telencephalon and the largest part of diencephalon and midbrain without the olfactory system.

In general, our results confirmed the analyses performed for the characterization of the model with one notable deviation. Group-wise averaged results for all measured A $\beta$  protein species are presented in Table 9. Individual results and correlation of insoluble A $\beta$  protein levels to results from PET imaging are shown in chapter 7.2.6. Detailed individual results of ELISA analyses are also shown in (Table 10) for the corresponding experiments and are described there.

The results presented in Table 9 reflect the amyloidosis levels in the study groups and correspond to PET measurements and the other modalities. It is notable that the observed A $\beta$ 42/A $\beta$ 40 ratio of insoluble protein in old homozygous animals was inverted relative to the model characterization data.

study group	soluble protein				insoluble protein			
	A $\beta_{x-40}$		A $\beta_{x-42}$		A $\beta_{x-40}$		A $\beta_{x-42}$	
	mean ± SD	p-value	mean ± SD	p-value	mean ± SD	p-value	mean ± SD	p-value
tg-old	325.8 ± 14.8	0.801	350.5 ± 20.6	0.444	437147.6 ± 67719.6	0.085	349995.4 ± 60339.2	0.121
tgtg-young	248.4 ± 163.3	0.005	298.4 ± 116.7	0.011	114642.5 ± 17499.7	0.002	143578.0 ± 14739.4	0.002
tgtg-old	790.2 ± 144.2		574.5 ± 63.2		912837.3 ± 325172.7		585911.4 ± 177963.1	

**Table 9: A $\beta$ 40 and A $\beta$ 42 protein levels (ELISA) for transgenic study groups.**

Soluble and insoluble A $\beta_{x-40}$  and A $\beta_{x-42}$  protein fractions (picogram protein per milligram wet tissue) for mouse brain tissue of animals that had a PET scan. Results were tested for differences between groups corresponding to the staging of A $\beta$  load in these groups (i.e. p-value for difference to group below). Names of study groups correspond to Table 6. Individual results are shown in Figure 24.

### 7.2.6 Overview of cross-validation results

The [<sup>11</sup>C]PiB imaging study was designed to provide as many validation experiments to PET imaging in every animal as possible, in order to analyze the relationship of in vivo radioligand binding in PET to relative ex vivo tracer uptake in brain biodistribution and autoradiography, to histological A $\beta$  plaque burden and to A $\beta$  protein levels (Table 6).

Neocortex, i.e. complete cortex without hippocampus, was used as the primary target region. It was defined in the same way on horizontal PET slices (Figure 13) and horizontal autoradiographical and histological sections. As described above (chapter 7.2.5), region definition for ELISA analysis was a bit different and provided for slightly weaker correlations of A $\beta$  protein levels with the other methods.

Figure 24 provides a complete overview of these relationships for the animals of the three transgenic study groups and the old control group. In general, [<sup>11</sup>C]PiB binding in PET was correlating strongly with ex vivo tracer uptake and in vitro A $\beta$  load. In addition, each study group was clearly separate from each other in all experimental modalities (shown by different color for each study group). The summary of data not only demonstrates the robustness of small-animal PET results and their consistency with the validation experiments but also provides further evidence that small-animal PET truly measure specific binding of the radiotracer.

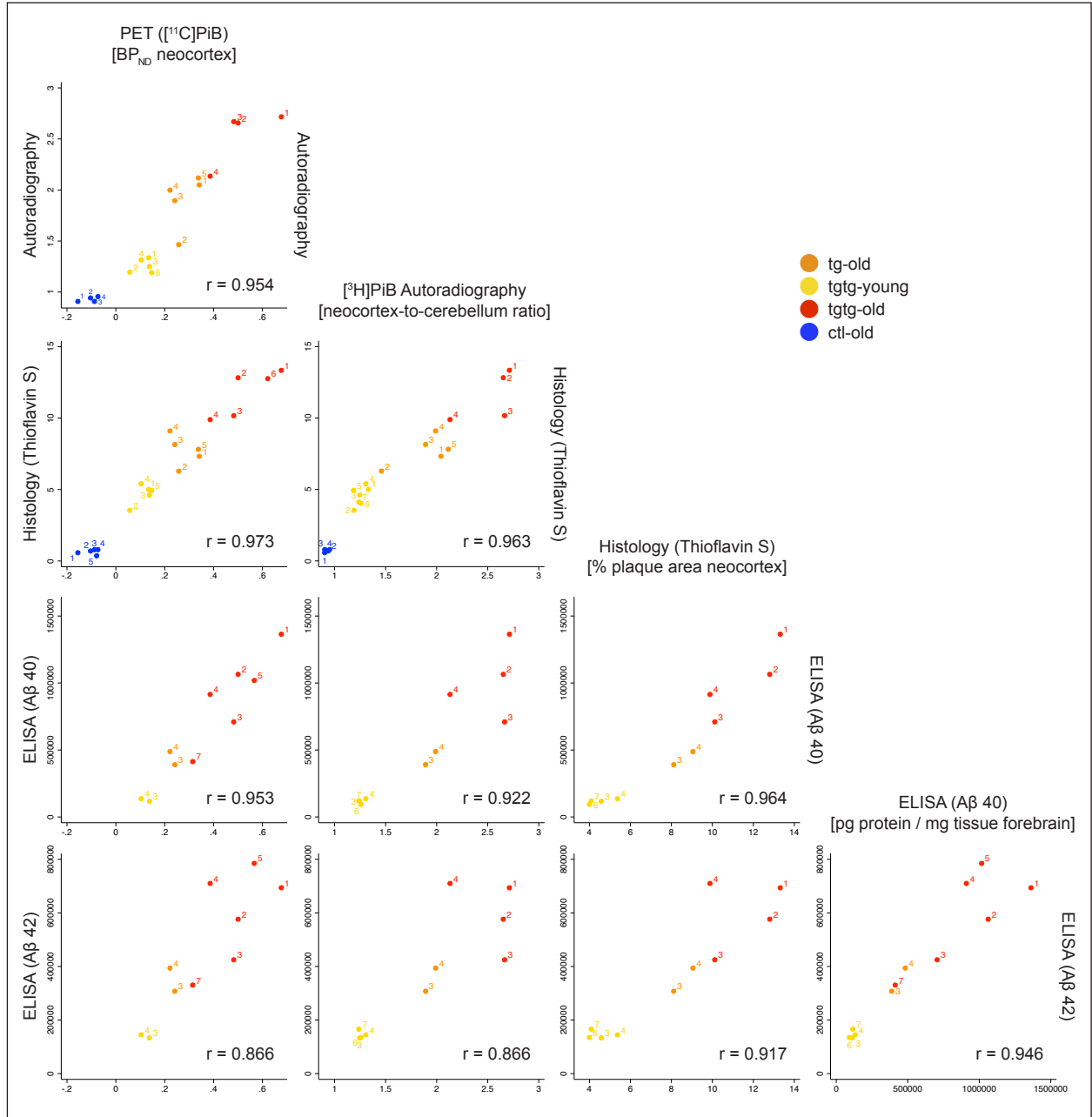


**Figure 24: Cross-validation of PET with other modalities.**

The experimental modalities that were individually described in the chapters above and that were performed in the same animals scanned with PET were combined in a scatterplot matrix for best possible overview of the experimental results and their relationships (see Table 6 for reference). The four major study groups of the study collective are included. The primary column is the left one: it presents the correlation of in vivo  $[^{11}\text{C}]\text{PiB}$  PET binding potential in mouse neocortex with relative neocortical  $[^3\text{H}]\text{PiB}$  uptake in autoradiography, with relative neocortical A $\beta$  plaque burden as stained by Thioflavin S and with insoluble A $\beta$ 40 and A $\beta$ 42 protein levels in forebrain. Remaining scatter plots show robustness, consistency and validity of the cross-validation. Neocortex was used as the primary target region except for ELISA (A $\beta_{x-40}$  and A $\beta_{x-42}$  protein levels) where the whole forebrain was used according to previous protocols. Data across the modalities was acquired from tissue of the same animals (Table 6). Individual animals are identified by their unique number code within their study group. The coloring of study groups in the scatter plots shows how each group is fully separated from each other. Color code: tg-old (orange), tgtg-young (yellow), tgtg-old (red) and ctl-old (blue). Pairwise correlation coefficients ( $r$ ) for each pair of modalities are noted in each scatterplot. Histological quantification with Thioflavin S was used representatively for all histological quantification results because of its tight correlation with anti-A $\beta$ 40/42 as described in Figure 22. Here, the animals presented in Figure 15, Figure 17 and Figure 19 are coded with #5 (tg-old), #5 (tgtg-young), #1 (tg-old) and #1 (ctl-old). Figure published in [164].

### 7.3 Combined multi-modal dual-label experiment

The experience gathered with many experimental modalities up to this point led to the development of an experimental design as "crème de la crème" including every analysis that was potentially available. The idea behind such compact design was to not only provide maximum possible cross-validation information but also to potentially save animal lives by getting the most out of one.

Two major features were added to this multi-modal approach compared to what had already been performed, before. First, regional brain biodistribution with [ $^{11}\text{C}$ ]PiB. Regions that were analyzed with different VOIs in the in vivo PET image of the whole brain could physically be separated and tracer uptake in these regions measured independently. Second, the simultaneous administration of [ $^3\text{H}$ ]PiB and [ $^{11}\text{C}$ ]PiB at the beginning of the experiment enabled the direct correlation of two different labels. This was implemented for two major reasons: first, the animal needed to be killed after PET for biodistribution but ex vivo autoradiography with [ $^3\text{H}$ ]PiB should still be possible and, second, different labelings of the same compound could be compared in digital dual-label autoradiography. This required the workflow to be fast enough for retrieving a signal with [ $^{11}\text{C}$ ]PiB at a half-life of about 20 min. Furthermore, a working dual-label design like this could potentially provide for later comparisons of different ligands to PiB. It is notable that this co-injection approach guaranteed for identical specific activity of both labels.

The new design required tuning towards efficiency and speed in the workflow and adaptations in the biodistribution dissection process for later conformance to ELISA protocols. At the same time, the efficient use of a single radiosynthesis of [ $^{11}\text{C}$ ]PiB for scanning two animals sequentially in PET had to be given up in favor of the complex experimental approach. It may be noted, here, that the complete experimental concept was first realized in late winter 2008. At that time, we already had the third-generation small-animal PET system, Siemens Inveon with docked CT, installed in our lab. From that time on, PET scans were always performed in docked CT mode providing for constant transformation matrices between PET and CT and, hence, a slightly easier image co-registration process.

Four animals from the young study groups (2 tg<sub>tg</sub>-young, 2 ctl<sub>-young</sub>) were given a bolus cocktail of [ $^{11}\text{C}$ ]PiB/[ $^3\text{H}$ ]PiB in the PET scanner and their brain tissue processed immediately after 30 min of PET/CT imaging for regional brain biodistribution, dual-label digital autoradiography, histological A $\beta$  plaque quantification with Thioflavin S and anti-A $\beta$ 40/42 and

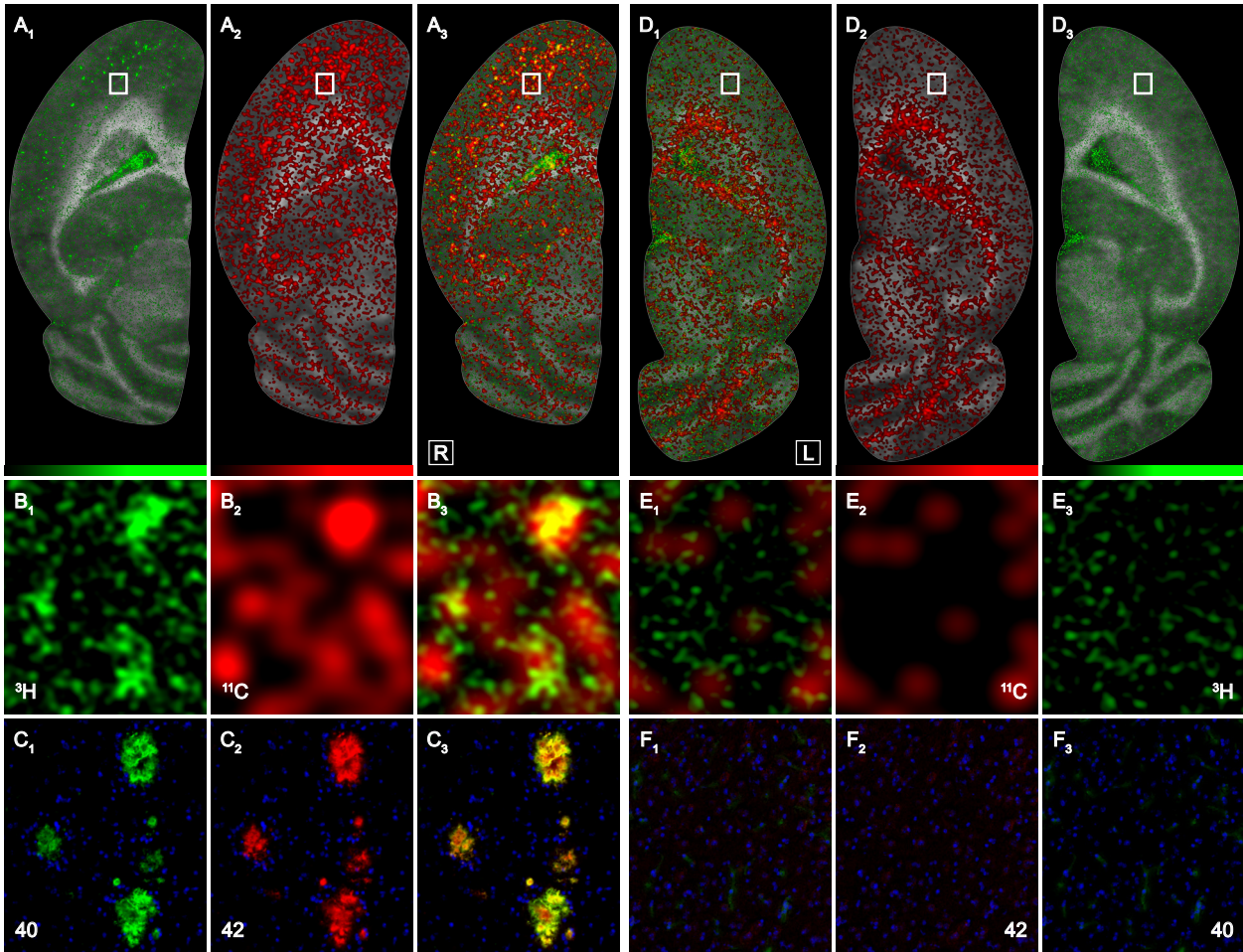
A $\beta$ 40/42 ELISA. The injected activities and weights of the animals are noted in Table 6. Injected doses of [ $^{11}\text{C}$ ]PiB in these two subgroups was higher than in the rest of the study collective to retain a sufficient signal for [ $^{11}\text{C}$ ]PiB autoradiography while specific activities were remaining on the common clinical routine level.

PET images of mice from the tg $\beta$ g-young group have already been shown in Figure 15, Figure 17 and Figure 19. To reduce redundancy and to focus on the novelty of this experimental design, Figure 25 shows the good correspondence of ex vivo [ $^{11}\text{C}$ ]PiB and ex vivo [ $^3\text{H}$ ]PiB autoradiography together with double anti-A $\beta$ 40/42 fluorescent stains of a neighboring section. The individual analytical results for all four animals are shown in Table 10. All results are consistent and in the range of the results reported for the whole tg $\beta$ g-young study group, above (chapter 7.2).

This combination experiment showed how well the results from different experimental modalities correlate on the level of individual animals and how activity uptake in PET is real tracer uptake. Also, these individual results confirmed that young homozygous animals could clearly be distinguished from control animals in all modalities. Furthermore, it showed the consistency and robustness of the groupwise results described above on an individual analysis level.

**Figure 25: Multi-modal combined experiment with [ $^3\text{H}$ ]PiB / [ $^{11}\text{C}$ ]PiB cocktail.**

Single multi-modal in vivo / ex vivo combination experiment with 4 animals from the young study groups (2 tg $\beta$ g-young and 2 ctl-young) showing the whole spectrum of results on an individual level. After a bolus injection of a [ $^{11}\text{C}$ ]PiB/[ $^3\text{H}$ ]PiB cocktail, the animals passed a 30 min CT/PET scan, were then killed for immediate [ $^{11}\text{C}$ ]PiB regional brain biodistribution and dual-label digital autoradiography. Brain halves used for biodistribution were analyzed for A $\beta$  protein levels. The other brain halves were stained with Thioflavin S and anti-A $\beta$ 40/42 and used for histological plaque quantification. *Columns (1) to (3)*: 9 month old female homozygous APP/PS1 mouse ("AD1") and *Columns (4) to (6)*: 9 month old female C57BL/6J control mouse ("CTL1"), presented in a mirror fashion. Ex vivo [ $^{11}\text{C}$ ]PiB (*red*) / [ $^3\text{H}$ ]PiB (*green*) dual-label digital autoradiographs with underlying optical scans of horizontal 12  $\mu\text{m}$  half brain sections of AD1 (right brain) (**A** and **B**) and CTL1 (left brain) (**D** and **E**) (marked with asterisk (\*) in Table 10 and corresponding magnified views of double immunofluorescence stains for A $\beta$ 40 (*green*) and A $\beta$ 42 (*red*) of neighboring sections for the same region (**C** and **F**). All four modalities are shown individually (*outer two columns*) and co-localized (*central columns*). Limits of green and red color look-up-tables represent minimum and maximum of measured signal. The analytical results of all experiments are shown in Table 10 below this figure. Figure published in [164].



modality			AD1*	AD2	CTL1*	CTL2
PET [BP <sub>ND</sub> neocortex]			0.06	0.06	-0.06	-0.07
Biodistribution [ <sup>11</sup> C]PiB [region-to-cerebellum ratio]		olfactory system	1.00	1.07	1.05	0.98
		telencephalon	1.24	1.24	0.92	0.92
		diencephalon and midbrain	1.26	1.47	1.22	1.10
Autoradiography [neocortex-to-cerebellum ratio]		[ <sup>11</sup> C]PiB	1.88	2.10	0.72	0.95
		[ <sup>3</sup> H]PiB	1.26	1.24	0.90	0.97
Histology [% plaque area neocortex]		Thioflavin S	4.00	4.10	0.54	0.41
		Aβ <sub>x-40</sub>	3.63	3.57		
		Aβ <sub>x-42</sub>	5.88	6.14	0.02	0.01
Aβ protein levels (forebrain) [pg protein / mg tissue wet weight]	soluble	Aβ <sub>x-40</sub>	272.0	212.1		
		Aβ <sub>x-42</sub>	267.3	191.3		
	insoluble	Aβ <sub>x-40</sub>	91522.8	117849.6		
		Aβ <sub>x-42</sub>	134335.4	164156.0		

**Table 10: Multi-modal combined experiment with [<sup>3</sup>H]PiB / [<sup>11</sup>C]PiB cocktail.**

See legend to Figure 25. Table published in [164].



---

## 8. Evaluation and ranking of new AD tracers

The combined multi-modal dual-label experimental design (chapter 7.3) was providing an experimental template for the evaluation and ranking of new PET tracers. For example, another (novel) PET tracer than could be implemented in the protocol and directly compared to [<sup>3</sup>H]PiB binding. The results yielded for PiB in the ARTE10 line presented in chapter 7 would then provide reference data for better understanding of the new tracer and its multi-modal correlates. The experimental setup has been applied in our lab for these kind of comparisons and evaluations of lead compounds and alternative research models. Two exemplary project descriptions shall concisely illustrate how every single experimental step described in the chapter, before, and the strong cross-validation of these methodologies led towards an ability for translational work in this field.

### 8.1 Combined multi-modal experiment with [<sup>11</sup>C]IBT and [<sup>3</sup>H]PiB

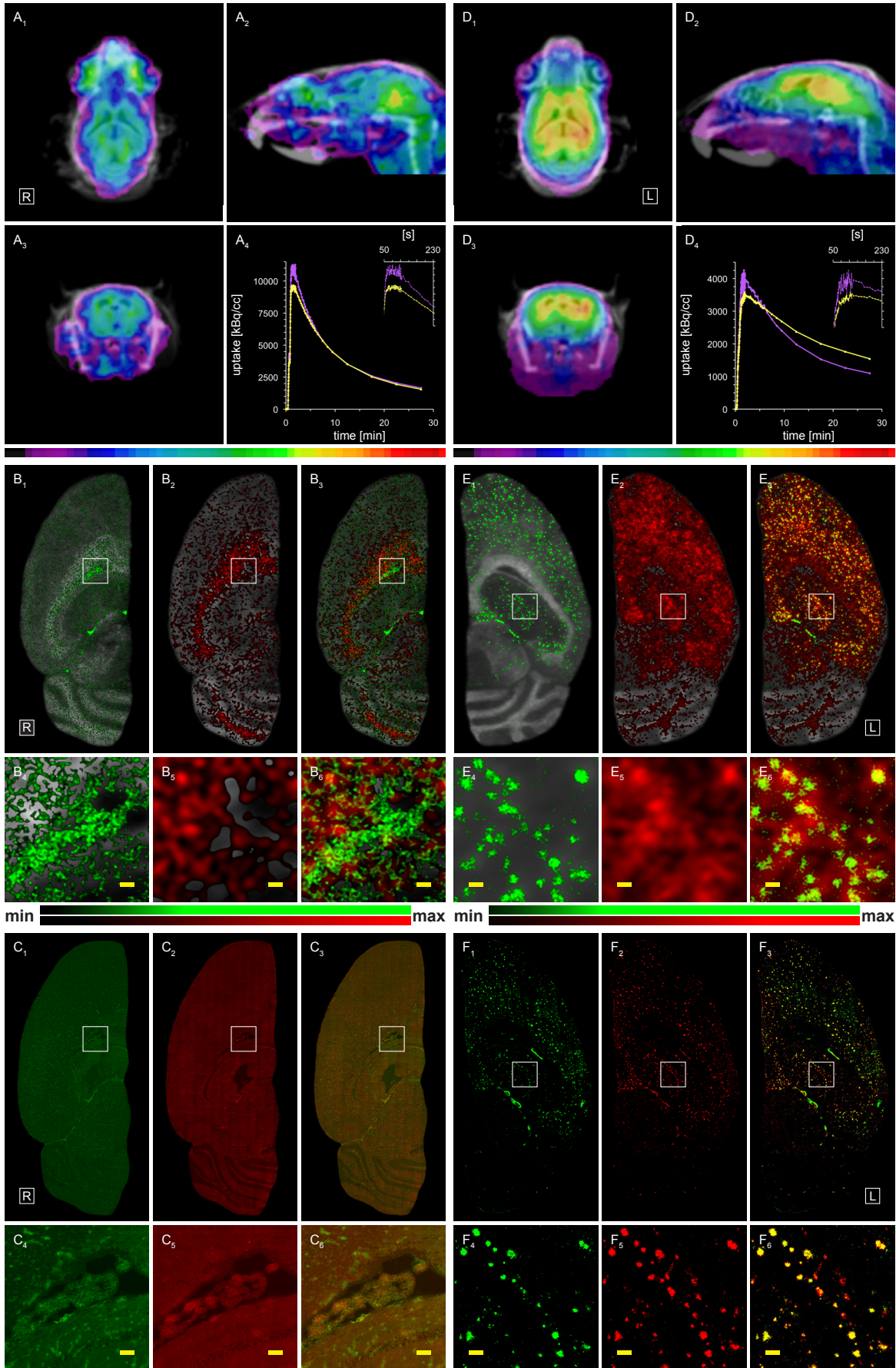
The IBT lead compound that was introduced in chapter 4.5.1 was chosen for further biological evaluation *in vivo* with the combined experimental concept. These experiments were performed in two 22 month old homozygous APP/PS1 mice (corresponding to tgtg-old study group, chapter 7.1) and two age- and gender-matched control mice (slightly younger but comparable to ctl-old study group). The animals were injected with a single bolus of a mixture consisting of [<sup>11</sup>C]IBT (transgenic:  $46.8 \pm 4.8$  MBq; controls:  $73.8 \pm 18.3$  MBq) and [<sup>3</sup>H]PiB ( $7.2 \pm 0.5$  MBq) into the tail vein and scanned in the docked PET/CT system for 30 min. As in the combined PiB study (chapter 7.3) control animals were injected with higher doses of [<sup>11</sup>C]IBT. Each PET/CT data set was co-registered to an average template of five age-, gender- and model-matched MRI data sets (Figure 26, panels A<sub>1-3</sub>, C<sub>1-3</sub>) for regional anatomical allocation of tracer uptake and also for defining volumes-of-interest similar as described in chapter 6.2.1. The telencephalon was defined as the common target region for PET and autoradiography to guarantee for maximum possible consistency of these modalities with the dissection method in biodistribution. Visually, the distribution of [<sup>11</sup>C]IBT uptake in the same time frame (20 - 30 min) as used for [<sup>11</sup>C]PiB (chapter 6.2.2) showed a very similar pattern: panels D in Figure 26 compare well to panels C in Figure 15 (old homozygous animals). Equally, the IBT distribution in the control brain (Figure 26, panels A) was similar to PiB (Figure 15, panels D) including the higher uptake in midbrain regions. Notably, the nasal hotspot phenomenon that was observed with PiB (e.g. Figure 10) was less distinct with IBT.

The time-activity curves (TACs) from telencephalon and cerebellum were measured with an equally high temporal resolution during the first three minutes as described before in all animals (Figure 26, A<sub>4</sub> and C<sub>4</sub>). The general kinetics were similar to the results with PiB. Initial cerebellar uptake was always higher than initial cortical uptake and cortical TACs of control animals fell below cerebellar TACs early. In contrast, for each transgenic animal the cortical TAC had a flatter slope from the peak of uptake and displayed higher values than the cerebellar TAC from around 8 min p.i. and remained distinctly separable. The shapes of TACs were clearly different from PiB TACs. They showed slower washout and seemingly higher tracer retention indicated by much flatter tracer kinetics compared to PiB.

Thirty minutes after the injection of the [<sup>11</sup>C]IBT/[<sup>3</sup>H]PiB cocktail, the animals were decapitated, the brain was immediately removed, and the hemispheres were separated. One hemisphere was taken for dual-label digital autoradiography; the other was dissected for regional brain biodistribution. Ratio analyses of dual-label autoradiography (tritium and carbon-11) and brain biodistribution verified the cortical [<sup>11</sup>C]IBT tracer uptake values as measured by PET and also that the [<sup>11</sup>C]IBT uptake represents true binding of [<sup>11</sup>C]IBT to cortical A $\beta$  plaques (Figure 26B and E and Table 11). The tritium and carbon-11 autoradiography channels and immunohistochemistry stains (Figure 26, C, F) showed good agreement with the binding patterns of [<sup>3</sup>H]PiB.

**Figure 26: Multi-modal combined experiment with [<sup>11</sup>C]IBT / [<sup>3</sup>H]PiB cocktail.**

Single multi-modal *in vivo* / *ex vivo* combination experiment with 4 animals from the old study groups (2 tg<sup>tg</sup>-old and 2 c<sup>tl</sup>-young) showing a large spectrum of results on an individual level. After bolus injection of a [<sup>11</sup>C]IBT/[<sup>3</sup>H]PiB cocktail, the animals passed a 30 min CT/PET scan, were then killed for immediate [<sup>11</sup>C]IBT regional brain biodistribution (one brain half) and dual-label digital autoradiography (other brain half). The same sections used for autoradiography were later stained with anti-A $\beta$ <sub>40/42</sub>. Telencephalon was chosen as the common target region for all measurements. Cerebellum was used as the reference region for ratio analyses. *Left image half (A) to (C)*: 22 month old female C57BL/6J control mouse ("CTL1", weight = 28.9 g; injected dose of [<sup>11</sup>C]IBT = 86.8 MBq) and *right image half (D) to (F)*: 22 month old female homozygous APP/PS1 (ARTE10) mouse ("AD1", weight = 25.2 g; injected dose [<sup>11</sup>C]IBT = 50.2 MBq). Autoradiography and histology is presented in a mirror fashion. *Top panels (A) and (D)*: [<sup>11</sup>C]IBT PET/CT co-registered to matched cranial *in vivo* 1.5 T MRI template. Overview of cranial tracer uptake in radiological orthogonal perspective (20 - 30 min frame) showing horizontal (A<sub>1</sub>, D<sub>1</sub>), sagittal (A<sub>2</sub>, D<sub>2</sub>), and coronal (A<sub>3</sub>, D<sub>3</sub>) views and corresponding cortical (*yellow*) and cerebellar (*magenta*) time-activity curves (A<sub>4</sub>, D<sub>4</sub>) with an *inset* showing initial tracer dynamics on a smaller time scale (over 3 min) depicting the peak of uptake. PET color look-up-table is UCLA (Pmod) with lower thresholds set to still visualize the cerebellum. *Middle panels (B) and (E)*: *ex vivo* [<sup>11</sup>C]IBT (*red*) / [<sup>3</sup>H]PiB (*green*) dual-label digital autoradiographs with underlying optical scans of horizontal 12  $\mu$ m half brain sections of CTL1 (right brain) (B) and of AD1 (left brain) (E) killed immediately after PET (30 min p.i.). Automated separation of isotope signals shows [<sup>3</sup>H]PiB (B<sub>1</sub>, E<sub>1</sub>) and [<sup>11</sup>C]IBT (B<sub>2</sub>, E<sub>2</sub>) individually and co-localized (B<sub>3</sub>, E<sub>3</sub>). White outlined squares in B<sub>1-3</sub> and E<sub>1-3</sub> are of 1 mm size and magnified in B<sub>4-6</sub> and D<sub>4-6</sub>. Locations have been chosen to show differences in nonspecific binding (B<sub>4-6</sub>) and identical plaque constellations (E<sub>4-6</sub>). Additional scale bars (*yellow*) are 100  $\mu$ m. Color lookup-tables: *green*, [<sup>3</sup>H]PiB; *red*, [<sup>11</sup>C]IBT, ranges of minimum to maximum of each acquisition. Cerebral *ex vivo* biodistribution values from the same experiment (other half of brain) are shown in Table 11 (animals shown in figure are marked with asterisk (\*) in table). *Bottom panels (C) and (F)*: *ex vivo* immunohistochemistry images with the same sections as in autoradiography. Anti-A $\beta$ <sub>x-40</sub> (*green*, C<sub>1</sub>, F<sub>1</sub>) and anti-A $\beta$ <sub>x-42</sub> (*red*, C<sub>2</sub>, F<sub>2</sub>) antibodies stain individually and colocalized (C<sub>3</sub>, F<sub>3</sub>). White outlined squares in C<sub>1-3</sub> and F<sub>1-3</sub> are of 1 mm size and magnified in C<sub>4-6</sub> and F<sub>4-6</sub>. Locations have been chosen to verify autoradiography results (C<sub>4-6</sub>) and (F<sub>4-6</sub>). Additional scale bars (*yellow*) are 100  $\mu$ m. The analytical results of all experiments are shown in Table 11 below this figure. Figure reprinted with permission from [278]. Copyright (2011) American Chemical Society.



modality (for [ <sup>11</sup> C]IBT)	CTL1*	CTL2	AD1*	AD2
PET [static ratio, 20 - 30 min]	0.94	0.98	1.42	1.28
biodistribution	0.87	0.88	2.34	1.93
autoradiography	1.06 ± 0.16	0.84 ± 0.08	2.45 ± 0.72	2.5 ± 0.23

**Table 11: Multi-modal combined experiment with [<sup>11</sup>C]IBT / [<sup>3</sup>H]PiB cocktail.**

See legend to Figure 26. Table reprinted with permission from [278]. Copyright (2011) American Chemical Society.

## 8.2 Multi-modal ex vivo experiment with [<sup>124</sup>I]BrIMPY

BrIMPY is a very recent lead compound from our group. Its good in vitro properties and general brain uptake behavior relative to common IMPY were shown in chapter 4.5.2. Hence, it was chosen for further biological evaluation in a first proof-of-principle ex vivo study with three combined modalities in two animals (transgenic and control). In this case, the protocol abstained from dual-label mode as sufficient correlation information between Thioflavin S fluorescence and ex vivo [<sup>3</sup>H]PiB binding had already been gathered in the previous studies.

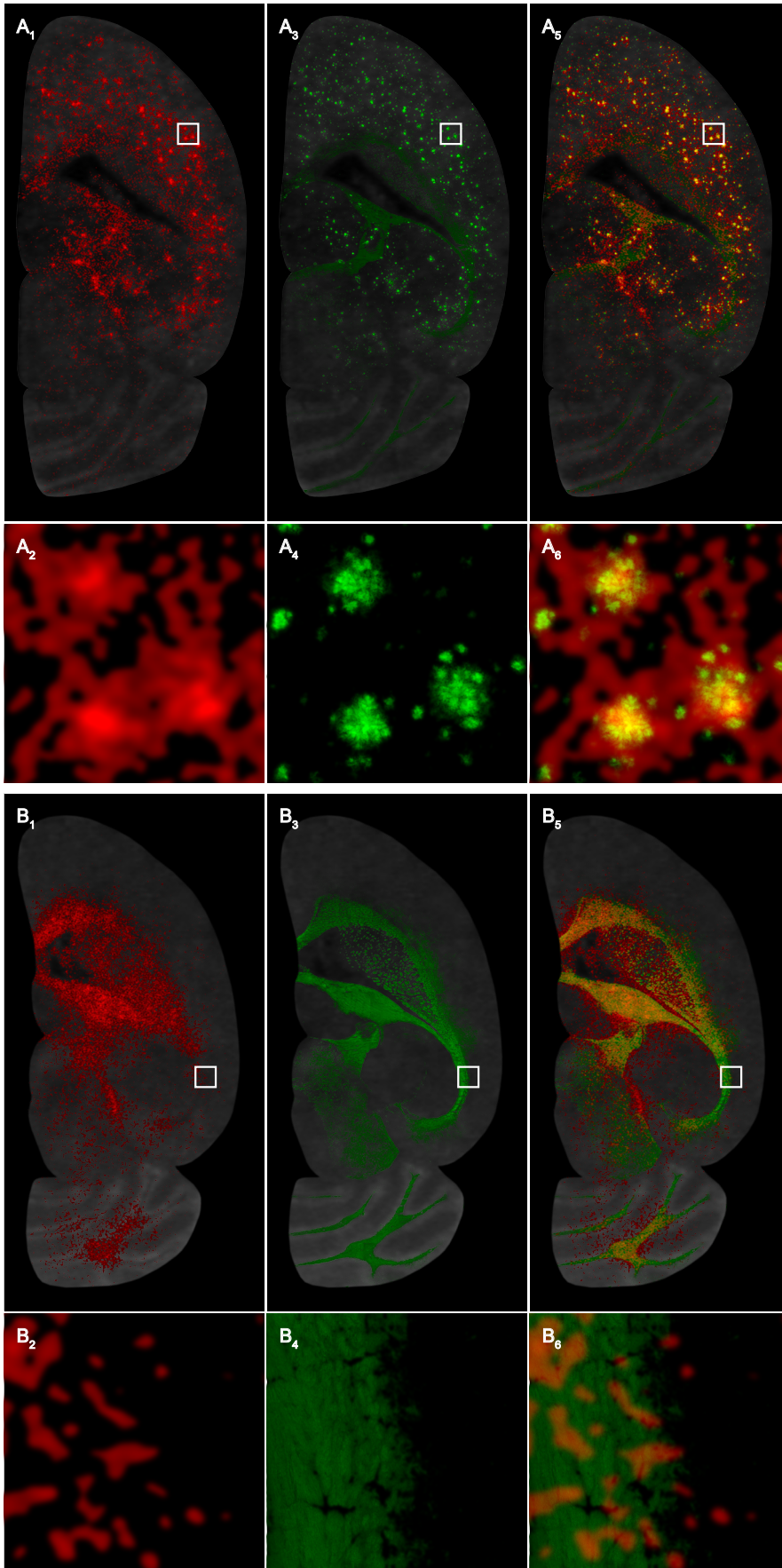
modality (for [ <sup>124</sup> I]BrIMPY)	AD	CTL
biodistribution	1.21	0.94
autoradiography	1.57	0.81

**Table 12: Combined ex vivo [<sup>124</sup>I]BrIMPY experiment.**

See legend to Figure 27. Reprinted from [276].

**Figure 27: Combined ex vivo [<sup>124</sup>I]BrIMPY experiment.**

After a bolus injection of [<sup>124</sup>I]BrIMPY, one transgenic (A) and one control animal (B) were killed 60 min p.i. for ex vivo regional brain biodistribution (right brain half) and digital autoradiography (left brain half). The same brain sections used for autoradiography were stained with Thioflavin S. (A): 18 month old male homozygous APP/PS1 mouse ("AD") (weight: 43.1 g, injected dose: 3.4 MBq) and (B) 18 month old male C57BL/6J control mouse ("CTL") (weight: 31.1 g, injected dose: 8 MBq). *Top rows of each panel (1, 3 and 5):* overviews of left 12 μm thick half brain sections superimposed on optical image (gray). *Bottom rows of each panel (2, 4 and 6):* magnified views from region identified by white squares in row above (neocortex of AD and hippocampal white matter of CTL). *Left column:* Ex vivo [<sup>124</sup>I]BrIMPY autoradiography (red), *Middle column:* Thioflavin S fluorescence of identical section used for autoradiography (green), *Right column:* Co-localization of [<sup>124</sup>I]BrIMPY and Thioflavin S staining as fusion image of autoradiography and Thioflavin S fluorescence (co-registered by rigid transformations). Table 12 shows analytical results of the experiment as telencephalon-to-cerebellum ratios for regional brain biodistribution and digital autoradiography. Reprinted from [276].



[<sup>124</sup>I]BrIMPY administration was followed by ex vivo regional brain biodistribution and (single-label) digital autoradiography 1 hour p.i.. The brain section that was acquired in autoradiography was then stained with Thioflavin S for validation of A $\beta$  binding. [<sup>124</sup>I]BrIMPY was given to an 18 months old male homozygous APP/PS1 mouse (3.4 MBq) and an age- and gender-matched control (8 MBq). Again, the control animal received a higher dose of tracer because of expected faster washout kinetics in animals without target. Quantitative results of ex vivo autoradiography and regional brain biodistribution of [<sup>124</sup>I]BrIMPY are shown in Table 12. Telencephalon was defined as the common target region for all modalities used in this experiment to yield best possible consistency.

Ex vivo [<sup>124</sup>I]BrIMPY autoradiography and Thioflavin S fluorescence stains indicate an excellent correlation of [<sup>124</sup>I]BrIMPY binding and A $\beta$  plaque pathology. Enlarged areas were chosen to show correlation of [<sup>124</sup>I]BrIMPY uptake and neocortical A $\beta$  plaques in transgenic animal (Figure 27A<sub>2, 4, and 6</sub>) and only tiny uptake to corpus callosum lateral to CA1 of the hippocampus in control animal (Figure 27B<sub>2, 4 and 6</sub>). [<sup>124</sup>I]BrIMPY uptake in control is tuned slightly higher to visualize nonspecific tracer distribution better without binding to neocortical regions. This shows that binding of [<sup>124</sup>I]BrIMPY in mouse brain is A $\beta$ -selective. Ratio analyses of autoradiography and brain biodistribution (Table 12) verified that the visual perception that [<sup>124</sup>I]BrIMPY tracer uptake represents true binding of [<sup>124</sup>I]BrIMPY to cortical A $\beta$  plaques.

---

## **Part III.**

### **Discussion**



---

## 9. Introduction

Nearly three decades had to pass until the first diagnostic criteria for Alzheimer's disease [173] were revised and published in *ALZHEIMER'S & DEMENTIA* about one year ago [174]. The reason for their long survival may be their success and reliability for the diagnosis of probable AD [174] or it may be the confusing complexity and incoherence of massively collected new evidence on the disease [123]. Whatever the reasons may be, a new component of the revised criteria is of indirect relevance for the contributions of this thesis: clinical PET imaging is now included as a potential biomarker for A $\beta$  and synaptic dysfunction in AD [174]. Reisa Sperling and colleagues provided the recommendations from the National Institute on Aging (NIA) towards defining preclinical stages of AD and state: *Although recent advances in biomarkers have revolutionized our ability to detect evidence of early AD pathophysiological processes there is still a need for novel biomarker development. In particular, although the current biomarkers provide evidence of A $\beta$  deposition, an in vivo marker of oligomeric forms of A $\beta$  would be of great value. Imaging markers of intraneuronal pathology, including specific markers of specific forms of tau/tangles and alpha-synuclein, are also needed* [229].

The need for these more specific imaging markers of A $\beta$ , tau and alpha-synuclein [229] also requires a preclinical framework with robust and feasible translational imaging tools to enable the evaluation and ranking of new tracers. Previous PET imaging studies with [<sup>11</sup>C]PiB in different AD mouse models were not successful, despite high A $\beta$  plaque loads [132,245,147] and the only successful study with this reference tracer for AD relied on very high specific activities of the tracer [161]. Therefore, researchers were led to principally question the feasibility and potential of the imaging method for translational AD research [132,274,33,241].

This supports the potential value of this thesis which presents a cross-validated feasibility study for [<sup>11</sup>C]PiB imaging in transgenic AD mice with methods, protocols and imaging technology that are usually available for and accessible to standard PET centers around the world. Also, the setup has already shown to be helpful for the evaluation of new in vivo markers of A $\beta$  and could easily be adapted to the investigation of other types of imaging markers.



---

## 10. Small-animal PET

The recent controversy on the principle value of amyloid PET imaging in humans [178,254] could be transferred to the preclinical level and amyloid PET imaging in mice and might thus be even aggravated. In particular so, because only one research group besides ours managed to report positive results with [<sup>11</sup>C]PiB in a single publication [161]. Hence, there is good reason for questioning the value of small-animal PET in this field and as Fischer et al. said *the ability to study genetically modified mice in neuroscience using PET depends on the careful evaluation of the PET methodology and its in vivo quantification accuracy* [59]. It is a claim of this thesis that this evaluation was performed properly.

### 10.1 Overview of PET results

A feasible, reproducible and robust preclinical A $\beta$  plaque PET imaging setup was developed to reliably detect a specific signal in transgenic AD mice that are even young enough to allow for longitudinal follow-up studies. It could be shown that the measured uptake of [<sup>11</sup>C]PiB with PET in individual transgenic animals at different disease stages was robust and strongly correlated with several independent experimental methods in the same animals.

The old hemizygous AD group was selected to correspond to animal ages used in previous imaging studies [132,245,161]. In general, the results of this group tended to be relatively close to the young homozygous animals. These results show the value of the homozygous animals of this APP/PS1 mouse model for imaging: the reliable specific PET signal in young animals in combination with a virtually normal life span and low premature death rate of homozygous mice allows for sufficiently long follow-up studies.

The PET results in control animals are notable as they indicate a volume of distribution ratio < 1 (cerebellum as reference) and hence a larger volume of distribution for the cerebellum than for neocortex. This finding is consistent with Maeda et al. [161] and is probably related to white matter binding of the tracer in the cerebellum in contrast to the target region which does not contain white matter. This is further supported by the regional brain biodistribution results which also yielded ratios < 1 for telencephalon-to-cerebellum ratios of injected tracer doses normalized to tissue weight.

## 10.2 Co-registration and unspecific binding

The considerable amount of unspecific PiB retention in tissues outside of the brain (like the salivary and harderian glands and nasal epithelium) is likely to be model- and even tracer-independent as the phenomenon appeared unsystematically in all transgenic as well as control animals with comparable uptakes (Figure 20C). This hypothesis is supported by a number of observations. A recent report describes A $\beta$  deposition in nasal epithelia of Tg2576 mice [119] but at concentrations that were lower than in the brain of the same mice by a factor of about 1000. Also, the A $\beta$  deposits appeared rather diffuse. As it was not possible to show specific in vivo [ $^{11}\text{C}$ ]PiB binding even in old brains of these mice [245], nasal epithelium is an unlikely contributor for measurable specific tracer uptake. Even more important, pathways for cerebrospinal fluid (CSF) to nasal lymphatics have been well documented in several species including rodents [110,114,53]. Johnston and colleagues infused a CSF tracer (Microfil) into the cranial subarachnoid space post-mortem to outline the pathways of CSF outflow [114]. Their results in rodents show nice correspondence to what was observed in the whole head [ $^3\text{H}$ ]PiB autoradiography, here (Figure 20A).

Previous A $\beta$  PET imaging studies in mice [132,245,161,146,193] do not provide information on whether the applied PET technologies have been able to resolve the uptake in extracerebral regions neighboring the olfactory bulb and the frontal cortex (chapter 4.4, e.g. Figure 6B). In this thesis, these tissues were identified as potential and strong error sources for which spill-over effects may need to be accounted for. The horizontal views in the B and D panels of Figure 15 (chapter 6.2.2) and Figure 17 (chapter 6.2.4) very slightly show this effect in the animals that have no or low amount of target. Slightest deviations in co-registration could therefore cause frontal neocortical tracer uptake to be considerably overestimated.

This highlights the importance of precise PET image co-registration to MRI such that volumes-of-interest can be defined reliably. It may appear counterintuitive at first but fully automated co-registration procedures via docked PET-CT systems, stereotactic frames with fiducial markers or software co-registration algorithms may not provide the co-registration precision on a near voxel-level as required for this type of work. Just to elaborate frames with markers as one example, Chow et al. [40] and Guo et al. [79] have shown good registration accuracies in the range of around one voxel (in small-animal PET). However, these studies primarily describe how well fiducial markers may be aligned among different modalities. They do not take into account animal motion during transport of the frame between scanners or repeated animal motion during intravenous injection. Also, to keep protocols with stereotactic frames reliable

animals need to remain fixed in these frames while all image modalities are performed. This is not always feasible as shown in this thesis.

A good manual method has been reported by Pfluger et al. for human MRI-SPECT data [191]. It inspired a comparable approach to the mouse PET data used, here. When trained well, manual image co-registration of well pre-processed small-animal data yields excellent and very reliable results. This is partly confirmed by the study of Chow et al., mentioned above, in which mean manual co-registration accuracy was reported to be 0.507 mm relative to the automated method at 0.335 mm [40].

### 10.3 Previous PET studies

Currently, there are few published studies that report the *in vivo* use of A $\beta$  radioligands with small-animal PET. In an APP/PS1 model different to ARTE10, Klunk et al. detected an uptake of [ $^{11}\text{C}$ ]PiB of 100 - 120% in the entire cerebrum relative to PS1 mice [132]. Their results were not statistically significant, which may have been due to the small sample size (1 transgenic versus 1 control animal per age group) and the global VOI-based approach employed (large VOI encompassing the entire brain, no reference region). In another study, Toyama et al. included a reference tissue-based analysis in their study with six Tg2576 mice at a mean age of 22 months, using the cerebellum as a reference region [245]. Although they calculated significantly higher binding ratios in the transgenic mice, Toyama et al. concluded that their study could not prove specific binding of [ $^{11}\text{C}$ ]PiB to A $\beta$  plaques due to the overall small difference in absolute tracer uptake between transgenic and control animals. This may have been due to the presence of A $\beta$  plaques in the cerebellum of this animal model [98]. It is notable that Toyama et al. found the peak uptake of [ $^{11}\text{C}$ ]PiB to be significantly lower in all brain regions in transgenic than in wild-type mice. They hypothesize this to be an expression of decreased cerebral blood flow (CBF) [184]. It should be kept in mind that their comparisons rely on %ID/ml calibrations, as discussed below. Kuntner et al. [146] scanned nine animals of the same model (Tg2576) at an age of 13 to 15 months with [ $^{18}\text{F}$ ]FDDNP and also applied a reference tissue approach to yield distribution volume ratios (DVRs). They report DVRs close to unity for all brain target regions (including neocortex), i.e. no measurable specific binding, and no difference to control animals.

A recent study by Poisnel et al. [193] reported the first positive results with [ $^{18}\text{F}$ ]Florbetapir in five hemizygous transgenic animals of an APP/PS1-21 mouse model [197]. Cortex-to-cerebellum ratios were reported longitudinally from an age of 3 (ratio ~1.3) to 12 months

(ratio ~1.6). Some aspects of this study appear to be different to previous imaging studies in murine AD models [132,245,161,146] and to the results reported in this thesis. Positive imaging results were yielded with very young hemizygous animals. Cortex-to-cerebellum ratios in 3 month old hemizygous animals correspond to the results reported here in 9 month old homozygous animals (chapter 7.2.1.2). Combining the fact that high nonspecific white matter uptake (e.g. in the cerebellum) has been reported for [<sup>18</sup>F]Florbetapir [204] and that the applied APP/PS1-21 model contains plaques in the cerebellum [197], these results should further decrease measured static ratios. On the other hand, if nonspecific binding to cortical white matter was stronger than in cerebellum, spill-over to the thin cortical grey matter (1 - 2 mm) would provide for high ratios not related to target binding. Hence, PET imaging with [<sup>18</sup>F]Florbetapir in transgenic mice may require further investigations in other mouse models of AD like ARTE10 and direct ex vivo imaging correlates.

The sole report on successful in vivo [<sup>11</sup>C]PiB imaging with PET in a single transgenic mouse model (APP23) claimed extraordinarily high specific activities of their PiB preparation (max. 291 GBq/μmol) to be required for imaging of Aβ plaques in their animals [161]. The very high specific activities that are claimed to be the major reason for successful PET imaging in mice by Maeda et al. are not obtainable at many PET centers which may explain why these results have not been reproduced by others. Furthermore, the proportionality between tracer uptake and Aβ plaque load as derived from a small-animal PET study may not be transferable to humans, if 10 to 20-fold higher specific activities are applied in the animal model.

Another relevant aspect of the study of Maeda et al. is that reasonable tracer uptake has been found only in animals > 21 months of age, despite the high specific activity preparations. This further limits the applicability of this imaging protocol for follow-up studies as the average life span of APP23 mice is around two years [232,148].

For this thesis, a range of specific activities from low (7 GBq/μmol) to high (80 GBq/μmol) was used without noticeable differences in imaging outcomes. Significant tracer uptake in regions with Aβ plaques was demonstrated in transgenic mice as young as 9 months injected with  $28.9 \pm 7.93$  MBq of [<sup>11</sup>C]PiB in an average specific activity of 11 GBq/μmol. Hence, these specific activities were considerably lower and better comparable to that routinely applied in studies of AD patients (range: 11.1 - 14.8 GBq/μmol). An even higher molar amount of [<sup>3</sup>H]PiB (2.5 nmol) was used for the ex vivo autoradiography studies compared to our in vivo PET studies (1.6 nmol of PiB) which both demonstrated specific binding of the tracer to Aβ plaques.

## 10.4 Quantification of tracer binding

Calibration of small-animal PET data to gain comparability between independent imaging sessions is a considerable challenge. Depending on the intricacy of the experiment, weekly or even daily quality control checks of the PET scanner and standardized calibration measurements in cylindrical phantoms with suitable or, even better, identical radioactive labels are initial basics.

### 10.4.1 Standardized uptake values and similar measures

Standardized uptake values (SUVs), %ID·kg/g or %ID/ml are measures that relate activity concentration in a defined VOI of a PET image to injected dose and body weight of the scanned subject [244,23]. Under certain conditions, they work well with [<sup>18</sup>F]FDG in humans. In small animals like a mouse the anatomical and physiological circumstances are different and SUVs become unreliable without precautionary measures. In a non-invasive imaging setting, the tracer is administered via the lateral tail veins. The injected dose of the tracer measured as the difference between full and empty syringes is quite robust for humans. Intravenous access to tail veins of small rodents is not as stable even in very trained hands. Measurements of dissected tails after PET scans tend to reveal substantial amounts of tracer despite excellent intravenous access at the time of injection. An example was already described in chapter 6.2.2 (Figure 11): injected doses and weights were comparable between two animals but peaks of uptake varied by a factor of about two. For imaging work with [<sup>18</sup>F]FDG in mice, Wynne Schiffer and colleagues [213] proposed a well working method by drawing a blood sample 45 min after intravenous injection to normalize the SUVs. It is notable that all of the above mentioned previous amyloid imaging studies in mice (chapter 4.4) use %ID·kg/g [132,245,146], %ID/ml [161] or SUVs [193] for presentation of TACs and to make their presented PET images comparable. However, they are using tracers that are very different to [<sup>18</sup>F]FDG and omit drawing blood samples for adjustments of injected doses.

### 10.4.2 Reference tissue approaches

A valid reference region located within the boundaries of the blood-brain barrier (BBB) is an essential prerequisite for using *relative* quantification approaches for tracer binding in the brain [76]. Its attraction lies in the ease-of-use compared to *absolute* methods. This fact explains why it is common to use the cerebellum as an intracerebral reference region in preclinical amyloid imaging studies [245,161,146,242,193]. The validity of this approach is usually not proven but postulated based on available characterization information for the

applied models. The cerebellum is not of the same relevance for those who generate amyloid models than for the ones who use them for imaging. Therefore, characterization studies tend to provide only *qualitative* observations on the A $\beta$  plaque load in the cerebellum if they mention it at all.

One may go further and wonder why the cerebellum of models like Tg2576, Tg2576 x PS1 and APP/PS1-21 is used as a reference region for imaging [132,245,146] without detailed investigations even though the original characterization studies [98,172,74,197] reported A $\beta$  plaques in this region. It is one of the claims of this thesis that, for the first time, the cerebellum of an A $\beta$  mouse model was validated as a feasible intracerebral reference region for imaging with very low A $\beta$  burden.

Once a reference region is established, its implementation is possible in static and dynamic analysis methods. Ex vivo modalities like autoradiography and biodistribution force static measurements at a defined post-injection time-point as they require the killing of the animal. These (static) time-points can be artificially chosen in dynamic in vivo PET data as well. Toyama et al. measured static PET ratios in a 12 - 30 min time frame [245] and Poisnel et al. exclusively report in vivo ratios based on 30 - 60 min frames [193]. In this thesis, the focus was not on a static ratio analysis. However, the method was additionally used to principally prove consistency and stability of data analysis in 20 - 30 min frames (chapter 7.2.1.2, Table 7). Also, it is important to note that all these ratios were measured in a bolus injection paradigm at seemingly arbitrary time-points of the PET scan instead of a steady-state design [228,151,35,34]. Hence, dynamic flow changes may be a measured component [34]. Toyama et al. and Kuntner et al. noticed substantially lower maximum brain uptake of radioactivity in transgenic mice compared to controls and ascribed this to decreased cerebral perfusion [245,146]. These observations on significantly different blood flow between transgenic and control animals should advise caution in the use of static ratios without previous steady-state examinations or verification with other analysis methods. Additionally, specific time frames for static ratio measurements need to be chosen well and verified depending on the experimental conditions, the applied tracer and the used model. Static ratio measurements may provide for some reliability if comparisons are between animals of the same strain and same tracer with comparable bolus injection kinetics for each scan. The rather low sensitivity and binary behavior of static ratios analyses was indirectly described by Maeda et al. [161] who presented dynamic ratio curves only to show a principle difference

between transgenic and control animals. This confirms the potential value of and need for more sophisticated quantification strategies in this field.

A well-known advantage of PET is its potential to quantify underlying biology by acquiring tracer uptake in dynamic acquisition mode [228]. Four major challenges for the retrieval of reliable dynamic data in small animals are, first, stable intravenous access for injections during the scan, second, standardized kinetics of the bolus injection paradigm, third, control of animal motion and, fourth, high time resolution of image reconstructions for the initial flooding of the tracer to properly retrieve the peak of uptake. Then, the availability of dynamic data grants the opportunity for modeling the kinetics of the imaging agents in tissue [225].

There was promising evidence from analyzing human PET data that reference tissue models may be well working models for estimation of [ $^{11}\text{C}$ ]PiB binding [158,175]. Only two of the few published amyloid PET imaging studies in mice used tracer kinetic modeling for the quantification of potentially specific tracer binding in transgenic mouse brains [161,146]. Kuntner et al. used Logan's graphical analysis [156] to retrieve DVRs [146] without further validation of the applied method. The primary in vivo PET binding measure of Maeda et al. [161] was binding potential ( $\text{BP}_{\text{ND}}$ ) estimated with the simplified reference tissue model (SRTM) [150]. They validated their model estimations with a commonly expected approach [194] by estimating binding measures with alternative independent methods, in their case with the multilinear reference tissue model (MRTM) [102] and Logan's graphical analysis (with  $\text{BP}_{\text{ND}} = \text{DVR} - 1$ ). Even though Maeda et al. performed ex vivo experiments, they did not quantitatively correlate them to in vivo binding results. They only speculated that *radiotracer binding in the hippocampus and neocortex was significantly correlated with age, in line with the progression of amyloidogenesis in these areas* [161] based on a hypothesis of linear progression whilst saturation effects in  $\text{A}\beta$  plaque load development were known [113,172,41,73,200,66].

The primary model that was chosen for estimation of specific [ $^{11}\text{C}$ ]PiB binding in this thesis was the 2-step multilinear reference tissue model (MRTM2) [102] similar to the MRTM which was also applied by Maeda et al. There were several reasons for the choice of model: first, the plan was to create parametric maps and, second, the estimation method should be consistent with the one used for VOI-wise calculations of binding potential. Third, MRTM is slightly less prone to noise [102] and, hence, parametric maps calculated with MRTM2 showed considerably fewer artefacts. Fourth, the 2-step approach allowed for reducing the degree of freedom by one in the final estimations via parameter pre-estimations. Finally and probably most

important, the abundance of available ex vivo data for the mice studied in PET for cross-validations provided "wet" evidence for the best choice of reference tissue model. Still, the choice of model was also validated by calculating two alternative in vivo measures: first, the *interval method* of two dynamic tissue ratio methods suggested by Ito et al. [106] and, second, static ratios for the time frame of 20 to 30 min (Table 7) and showed very consistent group-wise behavior. The static ratio calculations indirectly confirmed that 20 - 30 min is a reasonable time frame for ratio analyses with [ $^{11}\text{C}$ ]PiB in the ARTE10 model. Strictly, this still does not prove that MRTM2 is a generally valid model for estimation of [ $^{11}\text{C}$ ]PiB retention in transgenic mice. However, the tight associations with the large spectrum of ex vivo data across study groups and ages make it a well-working model for [ $^{11}\text{C}$ ]PiB binding in ARTE10.

Hence, this thesis claims to have contributed two significant international novelties to this field by, first, calculating parametric binding maps for [ $^{11}\text{C}$ ]PiB in transgenic mice and showing their good correspondence with underlying neuropathology and, second, the broad and strong cross-validation of analyzed in vivo PET data with several ex vivo modalities from the same animals. This kind of experimental ex vivo validation potential is what clearly distinguishes preclinical from clinical imaging.

---

## 11. Research model

In contrast to the abundance of available transgenic AD models with high content of cortical A $\beta$  plaques [9], good preclinical models for imaging A $\beta$  deposits have still been lacking [33,241,236,256]. Even two years after the report by Maeda et al. [161], Carpenter and colleagues stated that *the use of preclinical models for the identification and optimization of amyloid-targeted molecular imaging agents is not possible due to the lack of good preclinical models of amyloid deposits in the human brain* [33] and very recently, Svedberg and colleagues confirmed that *the absence of good animal models for AD has also hampered the possibility to demonstrate this [in vivo blocking studies] in animals* [236]. As described in the introduction (chapter 4.1), the quest for and the choice of an appropriate animal model for specific in vivo imaging of certain neurodegeneration phenomena is challenging and probably one of the key factors to success or failure of a well designed study. Several factors may be responsible for the discrepancy of the positive findings in this thesis compared to previous work - the animal model is likely to be one of them.

Various ex vivo analyses with A $\beta$  ligands in AD mice [141,132,279,267] and in vivo fluorescent labeling [10,87] would suggest that the in vivo measurement of A $\beta$  plaque load in mice with PET should be possible. In humans, negative PiB imaging in severely amyloid-positive patients with the arctic APP mutation has been observed [214] and may indicate a parallel phenomenon to negative PiB-PET results in animal models. In which way different A $\beta$  isoform patterns [180] and their degree of fibrillarity [14] or translational modifications of A $\beta$  peptides (e.g. N-terminal truncations and pyroglutamylations) [161,91,77,111] contribute to PET imaging results remains to be examined further.

The potential value of the double-transgenic APP/PS1 mouse line ARTE10 for in vivo A $\beta$  plaque imaging was recently noticed by Svedberg and colleagues: *Using a new transgenic animal model, ARTE10, ex vivo studies using [3H]PiB clearly showed intense labeling of amyloid plaques, indicating that the type of transgenic animal is influencing the possibilities for preclinical animal PET imaging* [236].

A number of characteristics of this model [267] are potentially favorable for amyloid PET imaging in mice and probably contribute to the observed positive findings:

1. A $\beta$  plaques showing similar tripartite morphology (dense A $\beta$  core, corona of dystrophic neurites and glial inflammation) and composition (e.g. insoluble A $\beta$ 42 > A $\beta$ 40) to those in human AD (in contrast to models like APP23 and Tg2576 with A $\beta$ 42 << A $\beta$ 40 [161]),
2. early-onset of plaque load at ages of 3 months (homozygous) and 5 months (hemizygous) with rapid progression of plaque load,
3. low inter-animal variability (in contrast to models like APP23 [232] with high variability of A $\beta$  plaque expression),
4. low premature mortality (15 % in homozygous mice at an age of 12 months, in contrast to other commonly used models with up to 50 % mortality [38,64]) and viability up to normal old age,
5. no gender effects in hemi- as well as homozygous animals (in contrast to other APP/PS1 models [261] and Tg2576 [32]),
6. co-inherited transgenes and a C57BL/6 background leading to good breeding capabilities of a double homozygous line for both APP and PS1.

Furthermore, while some other models develop A $\beta$  deposits in the cerebellum over time [98,197], it was shown, here, that the cerebellum of this model stays free until old age and can therefore be used for reference tissue approaches. This is an important feasibility advantage as alternative methods for analysis require arterial input information and calibration to injected dose both of which remain methodological challenges as mentioned above.

The homozygous animals live to normal old age with low mortality and show earlier onset and more rapid progression of A $\beta$  plaque deposition compared to hemizygous animals. They are therefore good candidates for at least one and a half years of longitudinal imaging as could be shown in the PET findings of this thesis. In the context of longitudinal studies, it needs to be noted that while plaque burden is steadily progressive in ARTE10 it also follows a saturation curve [267]. This seems to be a common phenomenon in models of amyloidosis like Tg2576 [41], APP/PS1 [172,73,66,273], PDAPP [113] and PS2APP [200] mice after they reached ages of 12 to 15 months. Hefendehl et al. postulate that the amount of soluble A $\beta$  is the primary and limiting factor in plaque growth and further state that towards older ages of animals the exponential demand for soluble A $\beta$  to incorporate into plaques might exceed the production [87]. It is notable that saturation contradicts the hypothesis of linear A $\beta$  increase in previous A $\beta$  PET imaging studies with very old mice [161] and asks for caution in longitudinal designs.

---

## 12. Validation experiments

The experimental methods applied for the validation of PET measurements, here, are commonly used to verify individual aspects of tracer binding. For this thesis these methodologies were adapted, enhanced and combined in new ways to retrieve maximum possible correlating information to PET from within the same animals. Hence, it may be worth to discuss some results and methodological aspects, here, beyond the fact that full consistency could be shown across all modalities.

### 12.1 Histological quantification

The image analysis algorithm applied for the characterization of the ARTE10 model as described in [267] was adapted and enhanced for the use with fresh frozen brain material, different staining agents and combined fluorescence channel measurements. The algorithm provides for quantitative assessment of plaque load, number per area and size distribution of amyloid plaques in defined regions of the mouse brain. It is based on Acapella™ image analysis software and implements multi-channel segmentation and dynamic thresholding for elimination of tissue background and artefacts thus outperforming the common global threshold based methods [264,41,73]. Different attempts have been made to implement computer-assisted analysis for quantification of amyloid plaques on human and mouse brain sections [264,41,27,73,42,267,273,87,206].

A frequent difficulty of image analysis is identification of false positive structures arising from background staining and tissue artefacts, thereby lowering the specificity and reliability of object recognition. Background staining due to the use of primary monoclonal mouse antibodies on fresh frozen mouse brain tissue ("mouse-on-mouse") can be a particular challenge. The established staining protocol with the primary monoclonal mouse A $\beta$ 40-antibody was well suppressing this phenomenon from a qualitative perspective (Figure 19 and Figure 26). However, the very sensitive detection algorithm picked up the tiny nonspecific background signals in the A $\beta$ 40 channel. This false positivity was well confined by minimally increasing the cut-off for minimum plaque size detection. It caused a slight loss of specific signal that is reflected in the overall slightly lower results for A $\beta$ 40 quantification compared to the other channels (Figure 23A). The validity and reliability of this approach was successfully tested against the fluorescence channels for anti-A $\beta$ 42 or Thioflavin S.

The plaque quantification results, here, differ somewhat from the results for the characterization of the ARTE10 model [267]. Our colleagues measured relative plaque burden in 19 to 20 months old transgenic mice of 10.5 % (hemizygous) and 35.2 % (homozygous). In this thesis, the measured relative plaque burden in even older animals was lower and the results lay closer together (around 5 % and 12 %, respectively). There may be several methodological reasons for this. Firstly, frozen brain material was the underlying tissue instead of paraffin sections. Secondly, primary antibodies with selectivity for A $\beta$ 40 and A $\beta$ 42 were used instead of an all-encompassing A $\beta$  antibody as used by Willuweit et al. [267]. Thirdly, staining protocols were different and adapted to simultaneous antibody staining on frozen tissue. Fourth, the parameters for the automated plaque detection algorithm needed to be adjusted to histological material, stain and microscopy exposure times.

Thioflavin S is an easy to use fluorescent staining agent that was used for A $\beta$  plaque quantification by others, before [264,73]. As it is the parent substance for PiB there was a strong anticipation that the quantification of in vitro Thioflavin S binding to A $\beta$  plaques on fresh-frozen sections of mouse brain reflects in vivo [ $^{11}\text{C}$ ]PiB and ex vivo [ $^3\text{H}$ ]PiB binding well. Thioflavin S was not used with this analysis method of A $\beta$  plaque quantification in this mouse model, before, and it is a claim of this thesis that this stain was validated as a robust and comparably easy method for A $\beta$  plaque quantifications by analyzing the relation of Thioflavin S sensitivity to anti-A $\beta$ 40/42 sensitivities for A $\beta$  plaque detection in a pairwise manner (Figure 22).

The anticipation regarding the familiarity of Thioflavin S and PiB was confirmed in two ways: first, Thioflavin S recognized a similar amount of relative A $\beta$  plaque load as the anti-A $\beta$ 40/42 compound signal (Figure 23A). This seems to parallel the comparable affinities of PiB for both A $\beta$  species [278]. Second, the highest correlations in the cross-validation approach were found for histological Thioflavin S quantification relative to in vivo [ $^{11}\text{C}$ ]PiB and ex vivo [ $^3\text{H}$ ]PiB binding (Figure 24) and therefore confirmed the original expectations.

Another claim of this thesis is that this plaque detection algorithm was used for the analysis of group-wise plaque size distributions for the first time. The reason to do so was the assumption that binding of [ $^{11}\text{C}$ ]PiB to A $\beta$  loaded brain regions is probably influenced not only by total plaque volume (measured indirectly by plaque load) but also by individual plaque size and type [154,263]. Far more than one million plaques were histogrammed and an important phenomenon could be shown: while the differences between distributions were highly

significant among all transgenic study groups, the distributions were significantly shifted towards larger plaques in older animals independent of zygosity. This is in accordance with Hefendehl et al. who found that older mice with a higher plaque load form fewer new plaques [87]. These observations further support the saturation kinetics theory on A $\beta$  plaque development over age in mice and may also be an explanation for the old ages of mice that were required to show successful PET imaging at all [161].

## 12.2 ELISA

A $\beta$ 42/40-ratios towards 1.5 as measured by protein analyses in brain homogenates distinguish animal models of amyloidosis [109,100] including the ARTE10 line [267] from others [98,232]. They provide for a higher translational value of these models for at least two major reasons: first, in humans, the increase in the A $\beta$ 42/40-ratio is seen as a key event in A $\beta$  metabolism [82] and, hence, these models are regarded to be closer to human pathophysiology. Second, as A $\beta$ 42 is regarded as the more pathological A $\beta$  species compared to A $\beta$ 40, one goal in the development of new imaging markers is to increase specificity towards A $\beta$ 42.

Given the importance of insoluble A $\beta$ 42/40-ratios, a discrepancy of results obtained in this thesis (chapter 7.2.5, Table 9) to the data published on this model [267] needs to be elaborated in more detail. The ratio of insoluble A $\beta$ 42/40 in hemi- and homozygous ARTE10 was published to be around 1.5. In contrast, in this thesis in 21 month old homozygous animals a A $\beta$ 42/40-ratio of 0.64 was measured.

A method aspect may be a sufficient explanation: a single step in the experimental workflow was different to what our colleagues did before homogenized brain tissue samples were frozen before first centrifuging. The effect of freeze-thaw cycles on protein measurements is well known which explains the frequent need for validation of these measurements depending on storage temperatures and number of freeze-thaw cycles of samples [251,215,149]. Another explanation would be closely linked to the pathophysiology in very old homozygous animals. Most mouse models of AD develop substantial cerebral amyloid angiopathy (CAA) in late life [89,266]. A $\beta$ 40 is less fibrillogenic but essential for the development of vascular amyloid while A $\beta$ 42 is regarded to be key in parenchymal amyloid seeding [90,89]. Hence, with heavily increasing CAA in old age, the total A $\beta$  composition may indeed change. The ELISA, here, did not distinguish between vascular and parenchymal brain compartments. Furthermore, the old homozygous mice analyzed, here, were 10 months older than the animals from the previous

measurements [267]. Therefore, it may be possible that in addition to a methodological deviation a new pathophysiological characteristic of this mouse model incidentally came to light because of the very old age of the animals.

Beyond these considerations on A $\beta$  composition, it needs to be clarified that the primary goal of these ELISA measurements was the correlation of A $\beta$  protein content to in vivo tracer binding and not the analysis of A $\beta$  ratios. The correlation of protein content to PET measures was shown and stabilized by cross-validations (Figure 24).

Returning to the freeze-thaw cycle, it may also contribute to slightly lower correlation coefficients for ELISA measurements relative to PET and the other experimental modalities (Figure 24). This adds to the fact that the target region definition for this analysis was different. To achieve consistency of these ELISA measurements with the already available characterization data [267] and published radioligand binding data [132], brain hemispheres without cerebellum were taken. This had two effects that may provide for higher variability of data: first, relatively more brain tissue without target (A $\beta$ ) was measured and, second, the thalamus (as part of the diencephalon) was included. The thalamus was the only brain structure in this animal model with giant and sometimes microcalcified plaque cores [267]. This has been observed in other APP/PS1 mouse models as well [269,263] which explains why the thalamus was a target region in these mice in recent in vivo MRI imaging studies [52,263]. As the thalamus was usually not a component in the major target region definition and as it contains plaques of a significantly different composition, the slightly weaker correlations with ELISA may be explained by this fact.

### 12.3 Dual-label digital autoradiography

Ex vivo dual-label autoradiography after injection of a cocktail with two different labels offers the opportunity to compare two tracers with different physical half-life without influence of their specific activity and show fine differences on binding of [ $^{11}\text{C}$ ]PiB (Figure 25) and [ $^{11}\text{C}$ ]IBT (Figure 26) relative to [ $^3\text{H}$ ]PiB in mouse brain tissue. While [ $^{11}\text{C}$ ]PiB and [ $^{11}\text{C}$ ]IBT were also taken up slightly by white matter (Figure 25D<sub>2</sub>, Figure 26B<sub>2</sub>) including cerebellar white matter, [ $^3\text{H}$ ]PiB binding appeared inverted in the cerebellum (less to white than grey matter). It may be that the very low energy of tritium caused the low unspecific [ $^3\text{H}$ ]PiB uptake to remain below the limit of detection. Another, yet vague hypothesis is that isotope effects appear with the unspecific tracer binding that is different between white and gray matter. The phenomenon, however, stays unclear and requires further investigation.

Nonspecific [ $^3\text{H}$ ]PiB binding was mostly observed in vessels (seen best in the choroid plexus). Both versions of PiB (i.e. labeled with either  $^3\text{H}$  or  $^{11}\text{C}$ ) had a similar specificity to A $\beta$  plaques. The specific activities of the combined tracers were the same as they were applied in a cocktail bolus.

The measurement of uptake ratios relative to cerebellum in autoradiography is less reliable with [ $^{11}\text{C}$ ]PiB, as slight deviations in thickness within a section has direct influence on the ratios. This effect is negligible when using [ $^3\text{H}$ ]PiB ratios due to less energy of tritium.

## 12.4 Specificity of PET tracer binding

In a very recent debate [24], the party that opposed the value of A $\beta$  PET imaging in humans [178], principally questioned whether current AD PET ligands do bind to A $\beta$  at all. In return, the supporters of A $\beta$  PET imaging listed good counter-evidence [254]. Achieving good specificity of a PET tracer is the bread-and-butter job of many radiochemists around the world. Preclinical A $\beta$  PET imaging in mice can play a pivotal role as claimed in this thesis: while specific binding in clinical data can only be proven implicitly and with indirect or post-mortem methods, the verification potential in the work with small animals is explicit. A large number of animals categorized in homogenous study groups and well-matched controls were scanned with PET for this thesis. The brains of these animals were usually retrieved the same day as PET and immediately analyzed with a spectrum of independent methods. The correlation results are summarized in Figure 24 and this thesis claims that the challenge by Moghbel et al. regarding the specificity of the predominant A $\beta$  PET tracer ([ $^{11}\text{C}$ ]PiB) is met, here, by presenting explicit and highly correlating "wet" evidence for specific binding from the bench.



---

## 13. Novel imaging markers

### 13.1 [<sup>11</sup>C]IBT

The results of the multi-modal combined experiment with [<sup>11</sup>C]IBT as a novel lead compound to be evaluated and ranked showed specific binding to A $\beta$  plaques in telencephalic regions of ARTE10 mice (chapter 8.1). The regional distribution of the tracer in PET with good differentiation between cortex and cerebellum as well as its kinetics expressed by TACs was comparable to [<sup>11</sup>C]PiB. For PET measurements, the telencephalic VOI definition as shown in Figure 14 (chapter 6.2.1) was used to remain full consistency across the applied methods. Binding of the tracer in PET was expressed with static ratios for the same time frame (20 - 30 min) that was used for PiB (chapter 7.2.1.2). The static ratio approach was acceptable for this experiment as the primary objective here was not the fine distinction of amyloid burden among different animals. Furthermore, more sophisticated tracer quantification in small-animal PET with a novel ligand would have required repeating major parts of the test battery that was run for PiB (chapter 7)

Three details for IBT different to PiB were noted. First, the strong tracer uptake around nasal cavities could not be observed in this magnitude for IBT. An explanation for this could be found in the second detail regarding tracer kinetics. TACs were indicating a slightly slower washout phase which was more obvious in the transgenic than in the control animal (Figure 26, panels A<sub>4</sub> and D<sub>4</sub>). Metabolism could be a reason. As mentioned in chapter 4.5.1, IBT is a hybrid of BTA and IMPY. The latter have been shown to suffer from a fast N-demethylation in vivo [220]. Although it cannot be excluded that N-demethylation may also be relevant for IBTs, the results from the speciation of radioactivity in brain and blood after intravenous injection of [<sup>11</sup>C]IBT in mice (chapter 4.5.1, Table 4) indicate a high stability of the compound in mice. Furthermore, the binding behavior in in vivo and ex vivo experiments with [<sup>11</sup>C]IBT also contradict metabolism as they have shown full comparability to [<sup>11</sup>C]PiB. Therefore, the slower washout could rather be related to strong binding of IBT to A $\beta$  plaques or a small trapping effect which would keep the tracer from escaping CSF to nasal lymphatics. The third detail is related to the ratios that were measured in the ex vivo modalities. They are slightly lower than what would be expected for PiB in the tg<sub>tg</sub>-old group (age of 21 - 21 months). Kung et al. described high nonspecific white matter binding of TZDM and IMPY on Tg2576 mouse brain

sections [144]. Therefore, IBT, because of its hybrid nature, may also bind to white matter binding a little bit more.

The observations described above implicitly state the value of the developed combined multi-modal experimental concept. The functionality and stability of the "toolbox" enables standardized and reliable comparisons and judgements on the value of new ligands.

## 13.2 BrIMPY

Data presented on [<sup>124</sup>I]BrIMPY in this thesis is showing very recent work from our group. Hence, the shown dataset is limited to an ex vivo paradigm on a proof-of-principle basis (two animals). The major objective of the ex vivo paradigm performed for the evaluation of BrIMPY was to show its metabolic stability (besides its specificity for A $\beta$  plaques, for sure). The overall uptake of BrIMPY in blood and brain of Balb-C mice at 5 min, 30 min, 120 min and 24 hours was very promising compared to classic IMPYs [220].

The data was collected at 60 min p.i., i.e. at a time-point when more than 50 % of still intact tracer was in blood and brain of the animals. BrIMPY was specifically binding to A $\beta$  plaques ex vivo at 60 min p.i. as shown by Thioflavin S fluorescence on the same section. The ex vivo imaging behavior and uptake patterns of BrIMPY compare well to the binding behavior of tracers like PiB and IBT presented before. Besides the good specificity, the results of ratio analyses in an old homozygous animal (age 18 months), in particular for biodistribution, revealed slightly lower ratios compared to IBT and PiB as would be expected for an IMPY-like compound that binds to white matter more as described above (chapter 13.1).

The ratio value compares to PiB in young animals (tg<sup>tg</sup>-young group). What kind of signal BrIMPY will reveal in PET or SPECT remains to be seen but certainly the ratios are in favor of a successful in vivo imaging study. To conclude, [<sup>124</sup>I]BrIMPY is ready for the next stage of in vivo evaluation.

---

## 14. Conclusion

### 14.1 Summary

In summary, feasible and robust small-animal PET imaging of A $\beta$  plaque deposition with [ $^{11}\text{C}$ ]PiB in an APP/PS1 mouse model of Alzheimer's disease was established. The cerebellum of the model was verified to be a valid intracerebral reference region for in vivo and ex vivo tracer quantification purposes. The imaging setup was applied to a study collective including three different transgenic mouse study groups and matched control groups. Specific and quantitative tracer binding in PET was cross-validated with ex vivo and in vitro methods. The transgenic study groups represented different disease stages according to their A $\beta$  pathology and could well be distinguished with PET. Group results were consistent in all experimental modalities and individual results correlated tightly. This also clarified the value and validity of this APP/PS1 mouse model for PET imaging of A $\beta$ . The reported PET imaging protocol includes clinical MRI for good mouse neuroanatomy reference and uses readily achievable levels of specific activity of the tracer. It grants successful high-contrast imaging down to ages of at least nine months and, thus, provides the opportunity for at least one and a half years of longitudinal studies. The established imaging setup and its multi-modal cross-validation protocol were successfully applied to the ranking and evaluation of two novel imaging markers for A $\beta$  as examples for truly translational A $\beta$  plaque imaging of Alzheimer's disease in a preclinical model.

### 14.2 Contribution

The contributions of this work can be looked upon from at least two different angles: their value for the preclinical PET research community and their impact towards clinical applications. In general, the development of the experimental setup was always oriented towards feasibility, reproducibility and robustness and guided by clinical quality standards. This section summarizes the claims on contribution and novelty made in the various parts of the thesis. The aspects that are, to the best of our knowledge, believed to be true novelties within the international research community at the time of submitting the thesis are marked with an asterisk (\*).

### **In vivo imaging**

- PET imaging of A $\beta$  plaques with [ $^{11}\text{C}$ ]PiB in mice under common conditions (\*)
- clinical MRI (1.5 T) for mouse brain anatomy
- specific activities of the radiotracer as in clinical routine (\*)
- successful imaging in relatively young animals
- sequential dual-tracer scans in a mouse model of amyloidosis
- in vivo / ex vivo mouse skull and brain PET (\*)

### **Animal model of amyloidosis (ARTE10 line)**

- deployment and characterization for in vivo imaging (\*)
- cerebellum validated as reference region (\*)
- homozygous mice for imaging (\*)
- comprehensive cross-sectional study design

### **PET quantification**

- binding potential maps for [ $^{11}\text{C}$ ]PiB in a rodent model corresponding to underlying neuropathology (\*)
- tracer-kinetic modeling of mouse brain PET data
- robustness of PET analysis verified
- "wet" validation of [ $^{11}\text{C}$ ]PiB quantification in PET (\*)

### **Validation experiments**

- cross-sectional study design with three study groups representative of different A $\beta$  burden
- combination of several ex vivo and in vitro methods in direct relation to PET within the same animals
- Biodistribution:
  - [ $^{11}\text{C}$ ]PiB distribution in cranial organs (\*)
  - [ $^{11}\text{C}$ ]PiB distribution in distinct brain regions (\*)
- Autoradiography:
  - whole head ex vivo [ $^3\text{H}$ ]PiB autoradiography (\*)
  - high-throughput [ $^3\text{H}$ ]PiB autoradiography
  - dual-label [ $^{11}\text{C}$ ]/[ $^3\text{H}$ ]PiB autoradiography (\*)

- Histological quantification of A $\beta$  plaques:
  - individual and colocalized signals for A $\beta$ 40 and A $\beta$ 42 (\*)
  - validation of Thioflavin S for A $\beta$  analysis with Acapella™ (\*)
  - plaque size distribution analysis with Acapella™ (\*)

### Combined multi-modal approach

- composite of 5 independent experimental modalities (12 when including submodalities) within the same animal and experimental session for maximal correlation to PET (\*)

### Novel imaging markers

- in vivo and ex vivo evaluation and ranking of [ $^{11}\text{C}$ ]IBT (\*)
- ex vivo evaluation of [ $^{124}\text{I}$ ]BrIMPY (\*)

## 14.3 Translational value

Which are the limitations and opportunities of the work presented in this thesis in the context of translational imaging of neurodegeneration?

We "humanize" mice [167] and rats via genetics, surgery and nutrition by applying different degrees of brutality. When the "model" is ready, we begin to wonder about "its" transferability to humans. On the quest to solve the riddle, we employ miniaturized technology that is working at its very limits. The limitations of models and methods provide for challenges beyond the original objectives. Care needs to be taken that their validations do not become ends in themselves.

The work presented in this thesis may evoke fundamental questions. Are transgenic models of amyloidosis artificial? The answer is: Absolutely, yes. Can they still provide insights with translational value? Definitely. Is it possible to misuse small-animal PET and to present great looking images and data without any underlying substance? Principally, yes [94]. Could it also be used to gain valuable knowledge that ultimately helps the diagnosis of human patients? Definitely. Let there be a few considerations on pros and cons.

The artificiality of (transgenic) mouse models is obvious. Their blood volume is two to three thousand times smaller than ours which, for example, has immediate impact on tracer formulations. Mice are killed by alcohol intoxication when clinical tracer formulations are applied without adaptations. Even though 99 % of the mouse genome has direct counterparts

in humans [78] their physiology (e.g. life span, behavior and brain complexity) cannot be compared. For example, despite heavy A $\beta$  loads in their brains mouse models of AD (including the ARTE10 line) do not show severe behavioral disturbances quite in contrast to humans. In general, the classic human behavioral phenotype of severe AD can simply not be observed in rodent models, be it because it isn't there or because we are not able to detect it.

Mice belong to the few mammals that do not develop amyloid deposits naturally towards older ages [192] in contrast to, for example, humans, dogs, monkeys and polar bears [219]. It appears somewhat bizarre that we force them to do so, artificially, and our lack of understanding the disease also causes the models to become insufficient. APP/PS1 mouse models, for example, do not develop neurofibrillary tangles - a hallmark of AD.

Integrating pathological human genotypes into mice is furthermore not necessarily causing familiar disease phenotypes. For example, thalamus is involved in human A $\beta$  pathology only towards late stages of the disease [25]. In mice, it is involved early on and unusually large plaques can be observed beginning at ages around 9 months [52,263]. Furthermore, plaques develop over decades in human patients and within weeks in mice. It may be expected that biochemical and neuropathological modifications around and within plaques should be different depending on their exposition to time. More importantly, Alzheimer's dementia is a disease characterized by neurodegeneration, but neuronal loss cannot be observed in the commonly used transgenic models of amyloidosis. These are a just a few aspects on the limitations of the animal models that are often referred to as 'AD mice', a term that easily deludes when these rodents are not an integral part of your workaday life.

On the other hand, mouse models of AD do indeed reflect aspects of the disease well. To some extent, it is intriguing how similar the pathological architecture of A $\beta$  plaques can be mimicked in mouse brain. Beyond what was mentioned in chapter 11 for the ARTE10 line, the development of CAA and related changing A $\beta$  compositions [89] as well as phenomena like nasal A $\beta$  plaque deposition [119] are examples that show interesting parallels to humans.

Artificiality of the model may not be bad, overall, as it is part of our scientific culture to isolate traits and look at them individually first, and then putting them back together, again. All it takes is a strong model characterization for the task at hand (chapter 7) as a steppingstone for more applied work (chapter 8).

PET physics on the size level of mice also asks for caution [95]. Partial volume and recovery [3] need to be considered continuously. Distinguishing grey and white matter uptake in mouse brain with PET may rather be wishful thinking than a real possibility with this imaging method.

Still, the work for this thesis has shown that when small-animal PET is applied conscientiously and prudently global cortical amyloid burden in mice can be measured well. Applying reference tissue approaches for tracer quantification keeps the method non-invasive and provides strong potential for longitudinal studies. Longitudinal designs would not only be a prerequisite for therapy monitoring purposes but would also save animal lives.

Concerning the radiotracers used in PET for this thesis, [<sup>11</sup>C]PiB and [<sup>11</sup>C]IBT, it is of note that <sup>11</sup>C-labelling is limited to certain PET centers with a cyclotron close-by and an experienced radiochemistry department. The short half-life of the isotope (20 min) does not allow long transportation and forces to care about every passing minute in experimental designs. The recently emerging alternatives are <sup>18</sup>F-labeled A $\beta$  ligands with a convenient half-life of 110 min that considerably eases this situation. However, clinical data from all available <sup>18</sup>F-labeled AD tracers show that these compounds are nonspecifically taken up by white matter in substantial amounts [204]. Distinctly having to consider grey and white matter uptake in human PET studies may be disagreeable but possible. However, this distinction is unlikely in mouse PET. What are the consequences? Seemingly specific uptake of the tracer in mouse cortex may mostly be spill-over from neighboring brain regions without target but considerable amount of white matter. From this perspective, tracers like [<sup>11</sup>C]PiB and [<sup>11</sup>C]IBT may currently be the best alternatives for preclinical imaging in small animals. Certainly, these claims require further investigation and it is likely that new tracer developments will resolve these issues.

*Of course, the sine qua non for the validation of an in-vivo A $\beta$  tracer is the in-vivo–postmortem correlation study in humans*, said Klunk et al. [133]. This sounds reasonable but what are the ethical implications? Shall we browse nursing homes and hospices for demented residents who are "willing" to have their brains scanned with PET shortly before they die? Within all the existing limitations on the preclinical level, this is an aspect that is seen as its major value – animals are allowed to be killed and, thus, explicit "wet" evidence from the bench for imaging behavior in PET can be collected immediately. Hence, the *sine qua non* can be fulfilled in the pre-clinic even more precisely, at the time point of imaging. Broad and strong cross-validation of analyzed in vivo PET data with several ex vivo modalities from the same animals was possible. This approach is what clearly distinguishes preclinical from clinical imaging [253].

Keeping the perspective towards clinical applications while doing the preclinical work is an important mindset in order not to get trapped in a "virtual" and decoupled world of diagnosis and therapy of mouse models of AD. It may be intellectually spurring to create a model, to devise an experimental therapy and, then, to cure the model [50] but what good does it do for your next-door neighbor who is affected by Alzheimer's? Until today, it seems, not much.

In all likelihood, the best outcomes may be achieved when there is mutual understanding between the preclinical and clinical levels of work. Hence, Mathias Jucker inspires to lift the quality of preclinical experimental designs: *A promising avenue to improve the predictive value of mouse models for clinical studies would be to adapt aspects of the design, quality control and transparency of clinical studies in humans* [116]. The work for this thesis was intuitively guided by these principles. Therefore, a broad and stable preclinical dataset for PiB PET in three distinct study groups of the ARTE10 line with helpful age-definitions is now available as reference for further work. Its translational value seems promising (Figure 28).

The protocols that were devised, established and validated for this thesis offer a kind of "toolbox" which is neither limited to a model nor a tracer nor even a target. Two examples for the interchangeability of these aspects have been provided and the results may lead to the application of new AD tracers in human patients. On the other hand, difficulties in clinical imaging like, for example, nonspecific tracer uptake could be addressed preclinically. At the moment, one of the highest expectations towards the translational value of this work probably is the prospect of longitudinal studies with therapy monitoring in analogue of a recent clinical PiB PET study that followed a clinical phase 2 trial with bapineuzumab [201]. Applying the established setup from our lab, it should easily be possible to monitor novel therapy approaches like the very recent bexarotene study [50]. Imaging the therapeutic process may only be a minor component in the whole research endeavor but it could be a valuable contribution on the path to solidly evaluate new drugs and to further improve the understanding of AD pathophysiology.

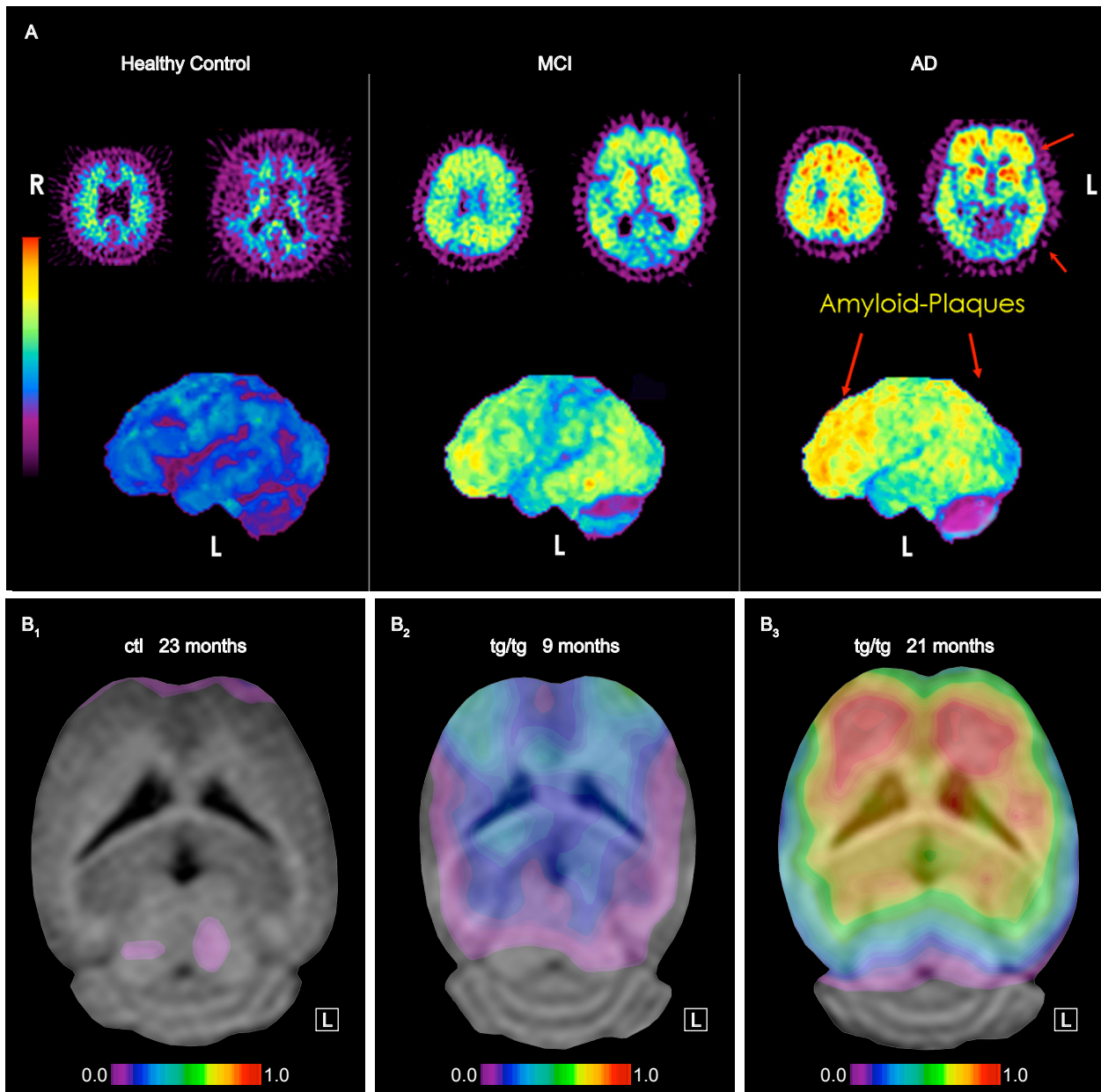


**Figure 28: Translational potential of A $\beta$  PET imaging in transgenic mice.**

(A) Human [11C]PiB PET (40 - 70 min p.i.): Surface projections (3DSSP) of typical [11C]PiB PET findings displayed on the left hemisphere of a healthy control person (*first column*), a MCI patient (*second column*) and a patient with dementia of the Alzheimer's type (*third column*). Color coding: yellow/red high tracer uptake indicating amyloid-plaque deposition, blue/black low/no tracer uptake, indicating no amyloid-plaque deposition. (B) Mouse [11C]PiB PET: horizontal PET binding potential maps for [11C]PiB in homozygous ARTE10 and control mouse brain about 2 mm below Bregma estimated with MRTM2 (see also Figure 17). (B<sub>1</sub>) 23 month old female C57BL/6J control mouse, (B<sub>2</sub>) 9 month old female homozygous APP/PS1 mouse and (B<sub>3</sub>) 21 month old female homozygous APP/PS1 mouse. PET color look-up-table for panels (B) is UCLA (Pmod). Panel (A) reprinted with permission from [54]. Copyright (2010) Springer.



---

## **Part IV.**

### **Material and methods**



---

## 15. Introduction

This final part describes all methods that were needed to yield the results presented in chapters 6, 7 and 8. The majority of methods listed needed to be established or at least adapted. The sequence of listings is chosen to correspond to the logic of the experimental workflow and also reflects the basic flow of the results part. For example: after radiosynthesis (chapter 17), the animal is anesthetized (chapter 18) and the radiotracer injected (chapter 19) for the PET scanning (chapter 20). This logic is as consistently followed as possible until this part comes to its end and the multi-modal "toolbox" (chapter 30) is described.

All method protocols are written as detailed and concise recipes that can be immediately followed without further reference. When experimental protocols by others were providing inspiration or when they were implemented they are properly referenced in the corresponding section.



---

## 16. Animals

Experiments were carried out with the approval of the institutional animal care committee (Regierung von Oberbayern, Munich, Germany) and in accordance with the German Animal Welfare Act (Deutsches Tierschutzgesetz). Animal husbandry followed the regulations of European Union (EU) guideline No. 86/609.

All experiments were performed in hemizygous (tg) and homozygous (tgg) APP/PS1 mice (B6;CB-Tg(Thy1-PSEN1\*M146V/Thy1-APP\*swe)-10Arte) (TaconicArtemis GmbH, Cologne, Germany) on a congenic C57BL/6J genetic background and commercially available age- and gender-matched controls (Harlan-Winkelmann, Borcheln, Germany and Janvier, Le Genest-St-Isle, France).

Animals were kept under temperature-controlled environmental conditions (18 - 20 °C, 50 - 60 % relative humidity) on a 12:12 light-dark cycle (light from 6 am to 6 pm) and fed a standard diet (Altromin 1326 mouse pellets, Altromin, Lage, Germany) with free access to food and potable water until the start of the experiments and after (no fasting). They were group-housed (maximum of 5 individuals per group) in individually ventilated type III cages (Ehret, Emmendingen, Germany) with dust-reduced wood shavings as bedding. All animals underwent a minimum of 10 days acclimatization period.



---

## 17. Radiosynthesis

### 17.1 General procedures for radiosynthesis

All radiotracer preparations and formulations were performed by Behrooz H. Yousefi (PiB (chapter 17.4.1), IBT (chapter (17.4.2), BrIMPY (chapter 17.4.3)) and Gjermund Henriksen (PiB). Formulations of used tracers were optimized and adapted to physiology of mice (e.g. alcohol content in relation to blood volume (chapter 17.3.1)) and experimental workflows (e.g. adaptation of specific activity for sequential PET scans with single radiosynthesis (chapter 17.3.2)).

All commercial reagents and solvents were used without further purification unless otherwise specified. Cyclotron-produced [ $^{11}\text{C}$ ]CO<sub>2</sub> was converted to [ $^{11}\text{C}$ ]CH<sub>3</sub>I by the catalytic gas-phase iodination reaction via [ $^{11}\text{C}$ ]CH<sub>4</sub> (GE MeI MicroLab) and converted [ $^{11}\text{C}$ ]CH<sub>3</sub>OTf by distillation through a column of AgOTf impregnated on  $\alpha$ -alumina. Subsequent radiolabeling and purification was carried out in a fully automated synthesizer from Scintomics (Fuerstenfeldbruck, Germany).

### 17.2 General procedure for N- $^{11}\text{C}$ -methylation of primary and secondary amines

10  $\mu\text{mol}$  of the amine compound was dissolved in anhydrous acetone (250  $\mu\text{l}$ ). The vial was sealed and flushed with and maintained under argon. The [ $^{11}\text{C}$ ]CH<sub>3</sub>OTf produced, swept with a He-flow at 50 ml/min, was trapped in the reaction vial at room temperature. The reaction vial was heated to 65 °C over 30 s and kept at this temperature for 3 min. Thereafter the reaction mixture was diluted with 1 ml of a mixture of MeCN:0.1 M ammonium formate (ratio in the range of 27.5:72.5 to 40:60, V/V), loaded into a 2 ml injection loop and transferred onto a Chromolith C18 (ID: 10 mm; length: 100 mm; Merck). The column was eluted with a mobile phase consisting of MeCN:0.1 M ammonium formate (ratio in the range of 27.5:72.5 to 40:60, V/V) at a flow rate of 10 ml/min. In-line HPLC detectors included a UV detector (Sykam) set at 254 nm and a radioactivity detector (Bioscan Flow-Count fitted with a PIN detector). The fraction containing the product was collected and diluted 1:1 with water. The mixture was applied to a Sep-Pak C18 and the cartridge subsequently washed with 10 ml water. The product was eluted with ethanol and diluted to the desired concentration with phosphate

buffered saline. The pH of the final solution was between 7 and 8. Radiochemical purities were > 98 % as determined by analytical HPLC with specific activity in a range: 7.4 - 76.7 GBq/ $\mu$ mol.

## 17.3 Adaptations for substance administration in mice

### 17.3.1 Alcohol content

The fraction containing the product was collected in a rotary evaporation flask containing 1 ml of 1 % HCl in EtOH and evaporated to dryness under reduced pressure. The product was dissolved in 1 to 2 ml of phosphate buffered saline (PBS). The pH of the final solution was between 7 and 8.

### 17.3.2 Specific activity of the applied tracer

For [ $^{11}\text{C}$ ]PiB scans, usually two animals sequentially underwent PET scans with the tracer as prepared from a single synthesis. In order to inject an identical chemical amount of substance for the two scans, an amount of authentic standard *N*-methyl-6-OH-BTA-1 was added to the first injectate. This resulted in a specific activity of the preparations in the range 300 - 400 mCi/ $\mu$ mol (11.1 - 14.8 GBq/ $\mu$ mol).

## 17.4 Radioligands

### 17.4.1 *N*-[ $^{11}\text{C}$ -methyl]-6-OH-benzothiazole ([ $^{11}\text{C}$ ]PiB)

2-(4'-amino-phenyl)-6-OH-benzothiazole (6-OH-BTA-0) and 2-(4'-*N*-methylamino-phenyl)-6-OH-benzothiazole (6-OH-BTA-1) were purchased from ABX Biochemicals, Radeberg, Germany, and used as precursor for [ $^{11}\text{C}$ ]PiB synthesis.

Please, see chapter 17.2 (General procedure for  $\text{N-}^{11}\text{C}$ -methylation of primary and secondary amines).

### 17.4.2 2-(*p*-[ $^{11}\text{C}$ ]Methylaminophenyl)-7-methoxyimidazo[2,1-*b*]benzothiazole ([ $^{11}\text{C}$ ]IBT)

2-(*p*-aminophenyl)-7-methoxyimidazo[2,1-*b*]benzothiazole was prepared from substituted 2-aminobenzothiazoles and appropriately substituted phenacylhalides after deacetylation [278] and used as precursor for [ $^{11}\text{C}$ ]IBT synthesis.

Please, see chapter 17.2 (General procedure for N-<sup>11</sup>C-methylation of primary and secondary amines).

#### **17.4.3 2-(4'-bromophenyl)-6-iodoimidazo[1,2-a]pyridine (<sup>124</sup>I]BrIMPY)**

Hydrogen peroxide (50 µl, 3 % w/v) was added to a mixture of 50 µl of the corresponding trimethyltin precursor, 2-(4'-bromophenyl)-6-(trimethyltin)imidazo[1,2-a]pyridine, (1 µg/µl EtOH), 50 µl of 1 M HCl, and [<sup>124</sup>I]NaI in a sealed vial. The reaction was allowed to proceed for 30 min at room temperature and terminated by addition of 100 µl of saturated NaHSO<sub>3</sub>. To reaction mixture was added ethanol (100 µl) after neutralization with saturated sodium bicarbonate solution. The combined mixture was purified by HPLC using a reversed-phase, Chromolith C18 (ID: 10 mm; length: 100 mm; Merck), with an isocratic solvent consisting of 70 % acetonitrile: 30 % ammonium formate (0.1 %) at a flow rate of 3.0 ml/min. The fraction containing the product was collected and diluted 1:1 with water. The mixture was applied to a Sep-Pak C18 classic and the cartridge subsequently washed with 10 ml water. The product was eluted with ethanol and diluted to the desired concentration with phosphate buffered saline. The pH of the final solution was between 7 and 8. The purity of the final product was checked by HPLC (> 95 %).



---

## 18. Anesthesia

Inhalation anesthesia was used for PET scans, metabolites and biodistribution experiments. Anesthesia was begun 15 min ahead of experimental procedures by placing the animal in a cage ventilated with isoflurane (3 %) and oxygen (3.5 l/min) with a pre-calibrated vaporizer. During the experiments, anesthesia was maintained by 0.6 % to 2 % isoflurane and 3.5 l/min oxygen via a nose cone, depending on length of scan such that the respiratory rate stayed at 80-100/min. Body temperature was held at 37 °C with a temperature-controlled heating pad.

Peritoneal antagonisable triple anesthesia with medetomidine, midazolam and fentanyl (MMF) was used for all animals during the MR scan.

Whenever anesthetized the eyes of each animal were protected with dexpanthenol eye ointment.



---

## 19. Substance administration

All injections were performed under isoflurane inhalation anesthesia. An application catheter system for reliable intravenous access to the lateral tail veins was prepared using 30 gauge needles, polyethylene tubing (0.28 mm inner diameter), superglue and 1 ml syringes (Figure 29). To achieve reliable and long-term access, an elastic hollow vessel-loop was used as a tourniquet for catheter placement. The catheter and syringe were initially filled with isotonic sodium chloride solution. The functional catheter was stabilized at the injection site with superglue.

For dual-tracer PET scans, a catheter system was placed in each of the two tail veins for independent application of the radiotracers.

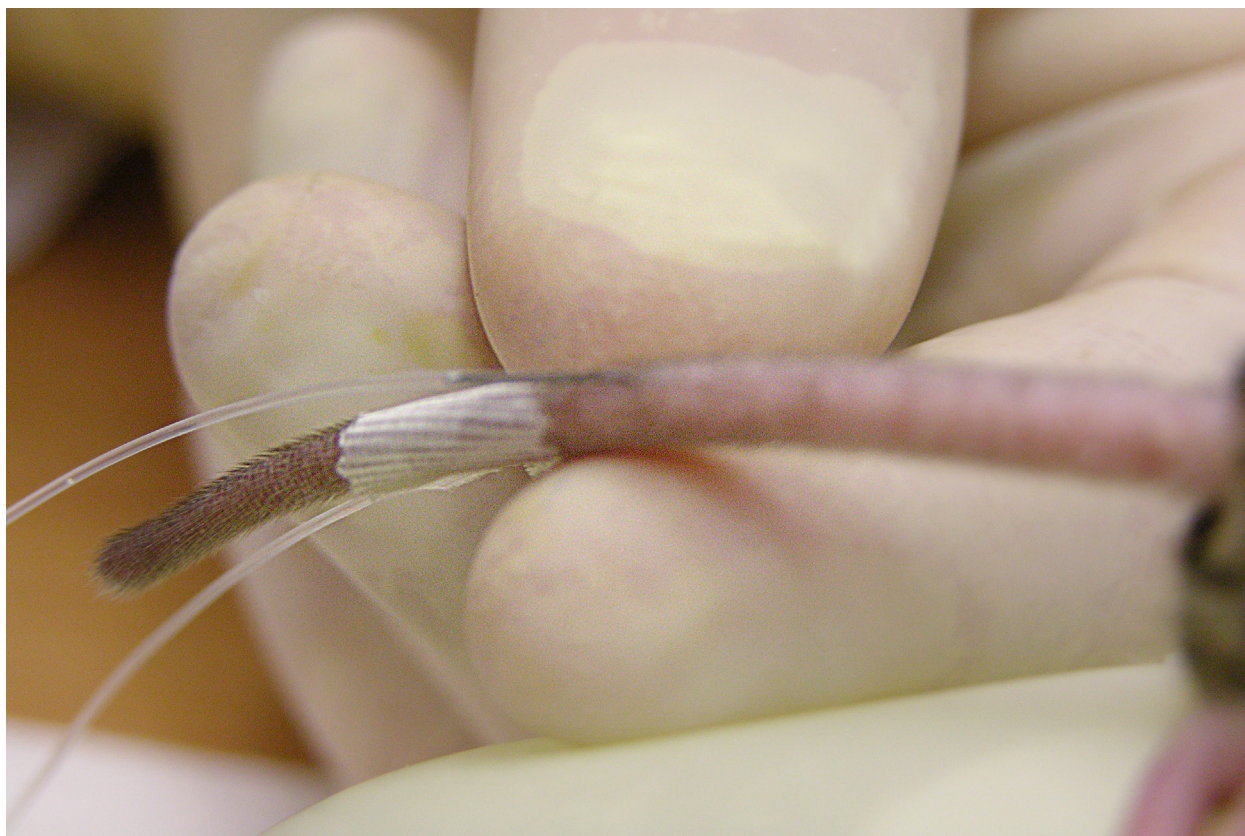


**Figure 29: Simultaneous access to lateral tail veins with self-built catheters.**

30 gauge needles were manually taken apart to obtain the steel needle, only. Needle base was inserted to a 10 cm long polyethylene tubing and fixed with superglue. A second needle was kept intact, its tip inserted to the other side of the tubing and also fixed with superglue. Photography: Richard Stry.



---

## 20. Small-animal PET

### 20.1 General PET scanning procedure

The majority of small-animal PET data was acquired with a microPET Focus F120 scanner (Siemens Medical Solutions, Malvern, USA) [238]. In the combined multi-modal experiments including the evaluation of novel imaging markers, PET data was acquired with a docked Siemens Inveon PET/CT system (Siemens Medical Solutions, Knoxville, USA) [12,121,257].

After induction of anesthesia and placement of the catheter systems, the animals were placed with their heads in the center of the field of view (Figure 30) and were fixed in the scanner in prone head-first position (HFP). At the beginning of the PET scanning procedure, a 9 min transmission scan ( $^{68}\text{Ge}$  rod source, Focus F120) or CT scan (Inveon) was performed in all animals.

The tracer was given via the catheter system intravenously in a slow bolus, followed by flushing with isotonic saline solution such that the total applied volume was  $0.22 \pm 0.06$  ml. The amount of injected activity was controlled real-time with registered prompts such that they ranged between 150000 to 200000 at the end of tracer application, ensuring a dead time  $< 5\%$  at 30 min p.i.. The radioactivity in the syringe was measured immediately before and after injection with a Capintec CRC 15R (Capintec Inc, NJ, USA) dose calibrator. The time between measurements was 2 to 3 min.

Dynamic data acquisition was performed in 3D listmode for 30 or 60 min starting immediately with injection of the tracer. The emission data were normalized and corrected for decay and dead time. The resulting sinograms were reconstructed with FBP (filtered back-projection using a ramp filter with a cut-off at the Nyquist frequency) into 2, 3, 6, 12, 60 and 120 frames of equal length used for motion correction, ratio measurements and image production and 52 frames (24 x 10 s, 12 x 30 s, 10 x 120 s, 6 x 300 s) and 162 frames (120 x 1 s, 24 x 10 s, 8 x 30 s, 10 x 300 s) for time-activity-curve (TAC) generation. The image volume consisted of  $128 \times 128 \times 95$  voxels, with a size of  $0.866 \times 0.866 \times 0.796$  mm<sup>3</sup> per voxel for the Focus F120 scanner and  $128 \times 128 \times 159$  voxels, with a size of  $0.776 \times 0.776 \times 0.796$  mm<sup>3</sup> per voxel for the Inveon scanner. Test-retest studies (1 week apart) with five transgenic animals showed robustness of PET results for these measurements in mouse brain.

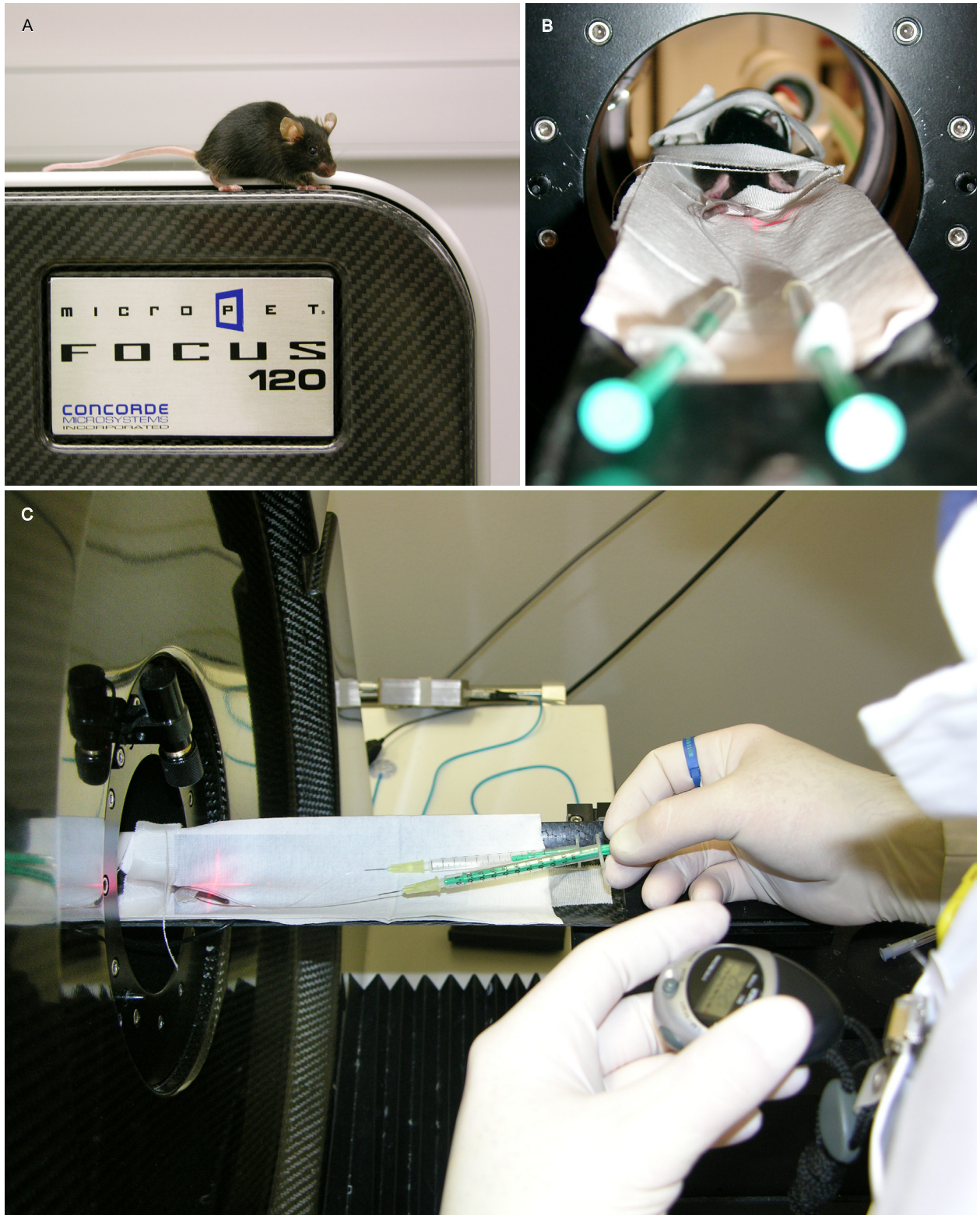


**Figure 30: Mouse PET imaging with Focus 120.**

(A) Old hemizygous ARTE10 mouse discovering top of the PET scanner, (B) View into PET bore: animal placed in central field-of-view with two independent patent tail vein catheters in place shortly before tracer administration, (C) Live intravenous injection with second-wise documentation of time for tracer administration and flushing. Photography: Richard Stry.

## 20.2 Sequential dual-tracer PET scans with [<sup>11</sup>C]PiB and [<sup>18</sup>F]FDG

To gain additional information for manual PET and MRI co-registration and to verify that the anatomical localization of unspecific [<sup>11</sup>C]PiB uptake in vivo is extracerebral, about one fifth of the animals in our PET imaging protocol were scanned sequentially with [<sup>11</sup>C]PiB and [<sup>18</sup>F]FDG (30 or 60 min) without being moved in the PET scanner (Figure 12).

## 20.3 CNS removal during PET

The preparation of animals and scanning setup were identical to the general PET protocol described above. At 30 min p.i., the scan was interrupted and the animal was guillotined. The complete brain (including the olfactory bulb) was taken out of the skull such that cerebral and cranial anatomical structures remained intact. The remaining head and the isolated brain were placed separately in the field-of-view of the scanner for another 30 min (ex vivo [<sup>11</sup>C]PiB PET, Figure 20).



## 21. Mouse brain MRI

MR scans were performed the same day as PET, immediately following the application of [ $^3\text{H}$ ]PiB for later autoradiographic analyses. Anesthesia was switched to peritoneal MMF and the animal was transferred to the MR scanner (Figure 31). Animals were placed prone head-first (HFP) in the MRI scanner (Philips Achieva 1.5 T clinical MRI system).



**Figure 31: Mouse brain MR imaging with Philips Achieva 1.5 T.**

(A) Clinical MRI system (Philips Achieva 1.5 T) and (B) 23 mm microscopy coil set. (C) Mouse placed in the central field-of-view and (D) larger view onto mouse with 23 mm microscopy coil placed over head. Photography: Richard Stry.

Mouse CNS MRI was performed using a 23 mm microscopy coil fixed horizontally over the head of the animal. A Philips T1-weighted 3D turbo gradient echo sequence with an inversion

pre-pulse was used: flip angle 8°, TR 13 ms (shortest), TE 4.3 ms (shortest), TI 860 msec, FOV 64 mm, pixel matrix 256<sup>2</sup> reconstructed to 512<sup>2</sup>, section thickness 0.25 mm, interpolated to 0.125 mm. The scan time of the sequence is 46 min 11 sec.

Details of the MRI sequence for mouse brain were devised by Markus Settles.

---

## 22. PET data analysis

### 22.1 General image data preprocessing

All in vivo image data was processed and analyzed with PMOD 3.2 software package (Pmod Technologies, Zürich, Switzerland). All PET, MRI and CT image datasets were scaled to calibrated kBq/cc and saved in float format. Orientation of planes was conform to radiological human brain standard such that the Z-axis was perpendicular to horizontal sections. The median sagittal plane was co-registered to the median sagittal plate (no. 101) of Paxinos atlas [62]. Image origins were set to Bregma (0,0). All datasets were controlled for motion of the animal during the PET scan in image reconstructions with 60 and 120 frames of equal length, i.e. 60 s and 30 s per frame.

### 22.2 Image co-registration and quality control

To create an in vivo correspondence to the Paxinos atlas space [62], sagittal atlas plate no. 101 was loaded into Pmod. The anterior-posterior and left-right axis of a high-resolution mouse head CT was aligned, the sagittal plane co-registered to the Paxinos plate and origins set to Bregma (0,0) (Figure 32). The co-registered CT was cropped to a bounding box of 12 x 18 x 8 mm (x, y, z). Spatial correspondence to brain structures was verified with co-registered MRI datasets.

All MRI datasets were co-registered to the Paxinos atlas space provided by the aligned CT (Figure 10B). An MRI template was created using the automatic rigid matching functionality of Pmod with the normalized mutual information dissimilarity function for all individual MRI datasets.

To improve the manual co-registration of [<sup>11</sup>C]PiB scans, about one fifth of the animals also received [<sup>18</sup>F]FDG for 30 to 60 min immediately after the [<sup>11</sup>C]PiB scan without being moved to provide for identical transformation matrices of both scans. The advantage of [<sup>18</sup>F]FDG to delineate brain morphology was used for a more reliable co-registration of PiB scans (Figure 12).

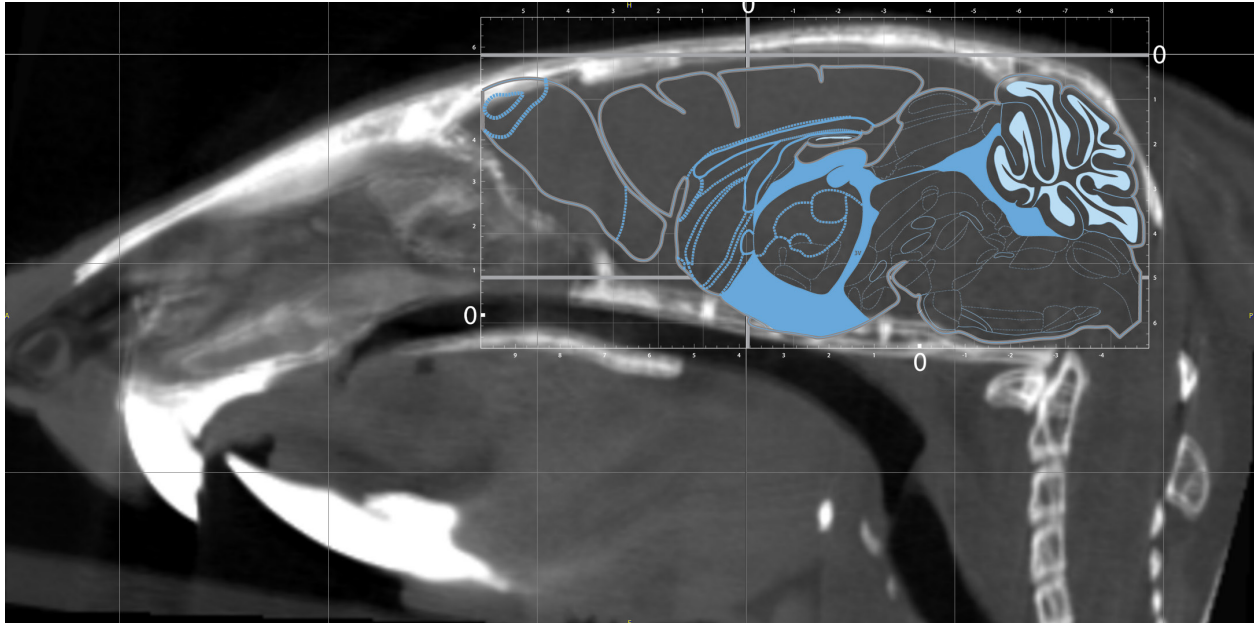


**Figure 32: Co-registration of sagittal ex vivo brain plate to in vivo CT.**

CT was chosen as initial co-registration modality for the sagittal Paxinos illustration (0.04 mm lateral) [62] because Bregma can be identified better in CT than in MR images. A compromise had to be found between the neurocranial shape in CT and the sagittal illustration created from in vivo stereotactic and ex vivo histological data. The genetic background as well as the weight range is comparable between the animals used, here, and Franklin and Paxinos who used 26 adult C57BL/J6 mice at an age of 3 months and a weight range of 26 - 30 g. Sagittal illustration is reprinted with permission from [62]. Copyright (2007) Elsevier.

A two-step matching process of PET data was used. A PET template of early tracer entrance (first 4min) (Figure 11) was created for initial automatic rigid matching with the normalized mutual information dissimilarity function [212]. Automatic matching results were verified and corrected if necessary by applying the following quality control procedure: the PET template was color-coded with a red binary look-up-table (LUT) and the energy window set for the contour to delineate the brain. The PET study was color-coded with a green binary LUT and the energy window set accordingly. This quality control step was performed at various energy contour levels in all three planes of view and the co-registration corrected manually if necessary. This procedure was repeated with the co-registered MRI datasets as individual references. The pre-matched PET study was colored with a binary LUT and evaluated on all orthogonal slices using at least three different energy windows for the LUT contour.

### 22.3 Volume-of-interest (VOI) definition

An MRI template in Paxinos atlas space was created from the individual co-registered MRI datasets of all transgenic animals of this study and, together with a high-resolution CT scan, used as the basis for VOI definition (Figure 13) according to Paxinos atlas [62] and the mouse brain atlas provided by the Allen Institute for Brain Science [115]. Paired brain structures were

defined individually for right and left side and were also merged. The mouse brain cortex was defined in two subvolumes (neocortex and hippocampus). The following cerebral VOIs were defined (right and left sides of paired structures summed, volumes reported in brackets as mm<sup>3</sup>): whole brain (504.8), cerebellum (48.7), neocortex (101.3), hippocampus (39.4), thalamus (15.0) and olfactory bulb (14.6). Additionally, three extracerebral VOIs were defined for the evaluation of unspecific tracer retention: nasal sinus (39.9), harderian glands (32.3) and eyebulbs (14.4).

## 22.4 Quantification of dynamic [<sup>11</sup>C]PiB PET data

To assess varying PiB retention of individual animals within the study collective and to verify the consistency of results, three quantification methods were used similar to Maeada et al. [161]. First, [<sup>11</sup>C]PiB uptake in the target region was divided by [<sup>11</sup>C]PiB uptake in the cerebellum as measured in a static 10 min-frame (20 - 30 min). Second, the tissue ratio methods as proposed by Ito et al. [106] were calculated. Third, the multilinear reference tissue model 2 (MRTM2, [102]) was fitted to cortex time-activity curves (TACs) (merged neocortex) after reduction of parameters by estimating individual efflux rate constants for [<sup>11</sup>C]PiB from the reference region ( $k_2'$ ) with the MRTM [102] and four regional cortical time-activity curves (Table 7).

Parametric images of [<sup>11</sup>C]PiB retention ( $BP_{ND}$  maps (MRTM2)) were generated for four representative mice (Figure 17 and Figure 19). For all analyses, the cerebellum was used as the reference region (Figure 16). To quantify the dynamic data, TACs with high initial time resolution (162 frames: 120 x 1 s, 24 x 10 s, 8 x 30 s, 10 x 300 s) were used (Figure 15, Figure 18, Figure 21).



---

## 23. Biodistribution

### 23.1 Regional brain biodistribution

Identical conditions as used for in vivo PET imaging were implemented: Animals were kept under inhalation anesthesia (isoflurane) on a temperature-controlled heating pad (36 °C) until death (Figure 33). All animals were killed by decapitation at 30 min p.i. The entire brain was taken out and cut along the median sagittal line. One half was dissected into: 1.) olfactory bulb including ventral olfactory regions towards the olfactory tubercle, 2.) cerebellum, 3.) cortex and 4.) the remaining brain structures (diencephalon and midbrain) (Table 8). The other half of the brain was rapidly frozen for histology. Radioactivity in weighed tissues was determined using an automatic NaI(Tl) well-type  $\gamma$ -detector (Wallac 1480-011 Automatic Gamma Counter, PerkinElmer, Waltham, MA, USA), related to a standard and used for calculation of the injected dose per gram tissue (%ID/g).

A 30 min PET scan was acquired for all animals from the tg<sup>tg</sup>-old group immediately before biodistribution and ELISA assays of their brain tissues.

### 23.2 Cranial biodistribution of [<sup>11</sup>C]PiB

Additional to regional brain biodistribution, cranial organs were dissected as some of them are positioned very closely to frontal regions of the brain. Individual uptake behavior of the submandibular gland, sublingual gland, parotid gland, eyeballs (without muscles and optic nerve), internal lacrimal gland and harderian gland were assessed (Figure 20C).



**Figure 33: Ex vivo biodistribution with [ $^{11}\text{C}$ ]PiB.**

Old transgenic mice awaiting biodistribution. 9 mice in simultaneous isoflurane anesthesia awaiting sequential intravenous [ $^{11}\text{C}$ ]PiB administration via lateral tail vein catheter for cranial biodistribution and metabolite analyses. Conditions were kept identical to conditions during PET scanning. Photography: Indranath Neogy.

---

## 24. Tissue processing

### 24.1 Gene expression analysis (quantitative RT-PCR)

Tails of mice were preserved and deep-frozen at -75 °C until processing. Genotype of all mice was re-evaluated and confirmed with quantitative RT-PCR (qRT-PCR) after experiments in our lab to control for correct gene status identification.

The relative quantity of the human APP<sup>swe</sup> and the human PS1M146V transgenes was determined using the LightCycler technology (Roche Applied Science). First, standard curves were generated to determine the efficiency of PCRs with specific primers for APP: 5'-AAGATGCAGCAGAACGGCT-3' and, 3'-CAGATCTAGCTCCAGGAAGGAGA-5', and for PS1: 5'-GAGCCCTCGAAATTCGTTGA-3' and 3'-TATCTCTTGCCGTCCTCGTGT-5'. PCR amplification (95 °C and 1 s, 56 °C and 5 s, and 72 °C and 5 s) was performed in a volume of 20 µl containing LightCycler-FastStart DNA Master SYBR Green I mix (Roche Applied Science), 0.5 µM primers, 2 µl of a genomic DNA (gDNA) dilution series of a hemizygous ARTE10 mouse and additional 3 mM MgCl<sub>2</sub>. Melting curve analyses of the PCR products revealed single peaks at 82 °C for APP, and 86 °C for PS1 respectively, with no visible primer dimers. Quality and size of the qPCR product were determined applying the DNA 500 LabChip system using the 2100 Bioanalyzer (Agilent Technologies). Single peaks at the expected size of 85 bp for APP, and 146 bp for PS1 were observed in the electropherograms of the samples respectively. In an analogous manner, the qPCR protocol was applied to determine the PCR efficiency of murine APP gene intron, using the specific primers 5'-CCACAGGAGTTGCGGGAAT-3' and 5'-AGTGTCTATCTACGGACCGAGT-3'. Melting curve analysis revealed a single peak at approximately 85 °C with no visible primer dimers. Bioanalyzer analysis of the PCR product showed one single peak of the expected size (120 bp). For calculation of the standard values, first the logarithm of the used gDNA concentration was plotted against the threshold cycle value Ct for APP, PS1, and a murine APP gene intron, respectively. The slopes and the intercepts of the standard curves (i.e. linear regressions) were calculated.

In a second step, DNA amounts from controls and ARTE10 mouse gDNA samples were analyzed in parallel. The Ct values were measured and converted to ng gDNA using the corresponding standard curves:  $10^{(Ct \text{ value} - \text{intercept})/\text{slope}}$  [ng gDNA]. Calculated gDNA concentration values of APP, and PS1, each were normalized to murine APP gene intron that

was analyzed in parallel for each tested DNA probe, thus resulting values are defined as relative DNA levels.

qRT-PCR of all tail tissues was performed by Heinz von der Kammer and Antje Willuweit at Evotec AG, Hamburg, Germany.

## 24.2 Mouse brain for histology and autoradiography

Brain tissue was generally preserved, rapidly frozen in fine-crushed dry ice and stored air-tight at -75 °C. For histological analyses, whole or half brains were cut on a Leica CM3050S cryostat (Leica Microsystems, Nussloch, Germany). Frozen sections were mounted on dilute poly-L-lysine hydrobromide coated (mol wt > 300.000, (1:50) 0.01 % w/v in water) microscopy slides.

Based on the histopathological data of the transgenic animal model [267] highest plaque load was expected in anterior cortex, medium plaque load in olfactory bulb and no plaque deposition in the cerebellum. To be able to correlate pathology and imaging findings in cortical and cerebellar regions within every single slice, a cut level close to the horizontal sections in the Paxinos atlas [62] was chosen.

About 120 sections with 10 µm thickness were mounted on about 40 slides. Slices were positioned to show three to four different cut levels on each slide, about 0.5 mm apart. About 5 of these slides were immediately stained with a thionin preparation (Nissl stain) for anatomical orientation within the slide sequence. After drying at ambient conditions the remaining slides were stored at -75 °C until assayed.

## 24.3 Mouse brain tissue for quantitation of A $\beta$ protein levels

Freshly extracted brains of mice were split into half and the cerebellum of each side was taken off by cutting through along the coronal plane between the superior and inferior colliculus. All parts of the brain were stored at -70 °C. All forebrains (right side without olfactory system) of the eight transgenic animals went through ELISA analysis.

## 24.4 Mouse cranium for [ $^3$ H]PiB ex vivo autoradiography

To assess extracerebral uptake of [ $^3$ H]PiB ex vivo the general protocol was slightly modified. Animals were killed at 30 min p.i.. The whole guillotined mouse heads were skinned such that external head glands were preserved at their natural positions. Upper and lower teeth were

taken out. Air in nasal and oral cavities and nasal sinuses was displaced with wallpaper paste by intranasal lavage via a 26 Gauge IV cannula. The heads were deep-frozen at -75 °C in a full wallpaper paste surrounding and cut on a Leica CM3500 cryostat for large tissue blocks (Leica Microsystems, Nussloch, Germany). Horizontal sections with 15 µm thickness were mounted on highly transparent cellulose-acetate tape. They were dried in the cryostat for 2 days and at ambient conditions for another 2 days. The sections on tape were mounted on microscopy slides and stored at -75 °C until autoradiography (Figure 20).



---

## 25. Autoradiography

The animals in the major subgroup of all study groups (Table 6) received [<sup>3</sup>H]PiB (specific activity: 2.78 TBq/mmol, radiochemical purity > 97 %) for ex vivo autoradiographical assessment of brain distribution of the tracer 9.3 ± 1.7 hr after the [<sup>11</sup>C]PiB injection using the same injection protocol as in PET. After induction of isoflurane anesthesia, 6.95 ± 0.81 MBq [<sup>3</sup>H]PiB was injected and flushed with isotonic saline through the catheter system such that the total applied volume was 0.21 ± 0.02 ml. Once the [<sup>3</sup>H]PiB was applied intravenously, anesthesia was immediately switched to peritoneal antagonizable triple anesthesia (MMF) for MR scanning as explained above. Following the MR imaging procedure, the animals were guillotined at 62 ± 2 min p.i., the full brain was removed within 8 ± 2 min post-mortem, rapidly frozen in fine-crushed dry ice and stored at -75 °C until autoradiographical data acquisition.

A total of 64 slides from 24 animals of the study collective were measured (Table 6). A minimum of 2 slides with at least three whole, or alternatively, at least four half horizontal sections were measured for each animal from the transgenic study groups and the old control group. 10 representative animals (6 transgenic and 4 controls) of the 24 were also measured in the digital autographical modality for validation purposes, providing 44 cortical and 43 cerebellar regional measurements. Sections from all animals were measured on tritium plates, providing 204 observations of the neocortical region and 195 observations of the cerebellar region.

### 25.1 Digital autoradiography

Digital autoradiographic images with a field of view of 24 x 32 mm were taken with the M40 series of  $\mu$ -Imager<sup>TM</sup> (Biospace lab, Paris, France) using 10 x 10 cm scintillating foils with 13 ± 1.5  $\mu$ m thickness (Applied Scintillation Technologies, Harlow, England). The resolution with tritium is 20  $\mu$ m, for carbon-11 it is about 40  $\mu$ m, the detection threshold for tritium is 0.4 cpm/mm<sup>2</sup>, for carbon-11 it is 0.7 cpm/mm<sup>2</sup> and the smallest pixel size is 1  $\mu$ m. Instrument acquisition was controlled with  $\mu$ -Acquisition software. Data was exported with BetaVision software (both by Biospace lab). A co-registered optical image was taken with every scan.

Animals from the combined multi-modal subgroups and novel tracer evaluation for [<sup>11</sup>C]IBT were measured in dual-label mode after injection of a cocktail of either [<sup>11</sup>C]PiB or [<sup>11</sup>C]IBT

together with [<sup>3</sup>H]PiB. Individual isotope signals were separated with an automated algorithm (Figure 25 and Figure 26).

## 25.2 Tritium plate autoradiography

A total of 50 slides with deep frozen CNS sections containing [<sup>3</sup>H]PiB were dried in ambient air for 60 min and exposed under two halves of a large storage phosphor screen BAS-IP TR 2040 E (GE Healthcare Lifesciences, Freiburg, Germany). Then, the two plates were scanned with a CR 35 Bio (Raytest, Straubenhardt, Germany) in sensitive 25 µm resolution mode. Scanning and data export was performed with AIDA (Raytest).

Validity and reliability of quantification results as measured by the tritium plate method was tested by measuring all samples from digital autoradiography on the tritium plates as well. At least two slides per transgenic animal containing three to four whole brain or four to five half brain sections were acquired (Table 6)

## 25.3 Quantification of tracer retention on autoradiographs

Lossless export of raw acquisition data to 16-bit grayscale TIFF images was executed with the software packages from the imaging device manufacturers (BetaVision (Biospace), AIDA Image Analyzer (Raytest)) for subsequent processing, analysis and finishing in Adobe Photoshop CS5 Extended (PS5) for Mac (Adobe Systems Inc., San Jose, USA).

Regions for analysis (forebrain, neocortex and cerebellum) were segmented in alpha channels of PS5 with neighboring Thioflavin S-stained sections and the Paxinos atlas as anatomical reference [62]. Integrated densities per region area were measured after background subtraction and used for ROI ratio analyses [216]. Equality and validity of results was confirmed by measuring samples of each group in NIH ImageJ, BetaVision and AIDA and by correlating the results from digital and tritium plate autoradiography.

Color tables for image presentation were imported from NIH ImageJ.

---

## 26. Neurohistological staining

### 26.1 Thionin fast nuclear stain (Nissl)

Fresh tissue mouse brain sections were dried in ambient air for 15 min, immersed in 0.05 % (w/v) thionin acetate in a buffer of 0.1 M acetic acid and 0.1 M potassium acetate for 4 min, mounted in Roti-Histokitt (Carl Roth, Karlsruhe, Germany) and protected with coverslips for rapid anatomical orientation within the set of histological material for each animal.

### 26.2 Thioflavin S staining

Fluorescent staining with Thioflavin S for frozen material was performed similar as reported by Willuweit et al. [267]. Deep frozen mouse brain sections were dried in ambient air for 15 min, immersion-fixed in ice-cold 4 % (w/v) paraformaldehyde (Carl Roth, Karlsruhe, Germany) for 20 min. Sections were equilibrated in water twice for 2 min. Thioflavin S was dissolved at 1 % (w/v) in water, and the solution was filtered. Sections were immersed in 1 % Thioflavin S for 30 min at RT and kept dark, rinsed twice for 2 min in water, and differentiated in two changes of 80 % ethanol (5 min and 1 min), washed in three changes of water (2 min each) and mounted in ProLong Gold antifade mounting medium (Invitrogen, Karlsruhe, Germany) with coverslips. Thioflavin S staining of all sections for A $\beta$  plaque quantification was performed in a single staining procedure to ensure best possible comparability.

### 26.3 A $\beta$ 40 and A $\beta$ 42 immunohistochemistry

Simultaneous double immunofluorescence for frozen material was performed similar to a staining protocol available in the Abcam (Abcam plc, Cambridge, UK) online protocol database [2] with slight modifications. Deep frozen mouse brain sections were dried in ambient air for 15 min, immersion-fixed in ice-cold 4 % (w/v) paraformaldehyde (Carl Roth, Karlsruhe, Germany) for 10 min. Sections were equilibrated in three changes of 1 % PBS (1 min each), permeabilized with 0.25 % Triton X-100 in PBS for 10 min and washed in three changes of PBS (5 min each). They were then blocked with 10 % normal donkey serum in PBS for 45 min, washed quickly in three changes of PBS-Tween20 (0.05 %) and probed with the two primary antibodies (G2-10 (Merck Millipore, Schwalbach, Germany) and AB3 (Araclon Biotech, Zaragoza, Spain)) diluted in 1 % BSA/PBS-Tween20 over night at 8 °C. Afterwards, they were washed in three changes of PBS (5 min each) and incubated with two fluorophore-conjugated

secondary antibodies (A488-D-Rb (Invitrogen, Karlsruhe, Germany) and Cy5-D-Ms (Jackson ImmunoResearch, Suffolk, UK) in 1 % BSA/PBS for 2 hours. After three washes in PBS (5 min each), nuclei were stained by adding 0.5  $\mu$ M DAPI (Sigma, Schnelldorf, Germany) for 1 min. After the final washing steps the tissue was coverslip-mounted with ProLong Gold Antifade mounting medium (Invitrogen/Molecular Probes, Darmstadt, Germany). Double anti- A $\beta$  staining of all sections for A $\beta$  plaque quantification was performed in a single staining procedure to ensure best possible comparability.

Tissue staining of two mouse brain sections and the acquisition of their micrographs for Figure 26 was performed by my PhD colleague, Boris von Reutern, in collaboration with Heinz von der Kammer, at Evotec AG, Hamburg, Germany.

---

## 27. Microscopy

Digital fluorescent micrographs for Acapella™ 2.0 analysis [267] were acquired using a BX51 microscope (Olympus, Hamburg, Germany) with a ColorView II charge-coupled display (CCD) camera (Soft Imaging System, Olympus, Münster, Germany). The micrographs of horizontal mouse brain sections were recorded through a 2x objective followed by a 0.5x TV adaptor.

Entire-view high-resolution MosaiX pictures of horizontal mouse brain sections were created with an AxioImager Z.1 microscope (Carl Zeiss Microimaging, Munich, Germany) on a Zeiss CAN-Bus motor stage (Merzhäuser, Germany) using a 20x/0.5 M27 EC Plan-Neofluar Zeiss lens and Zeiss filter sets no. 49 (DAPI), no. 38 (HE Green Fluorescent Protein), no. 43 (HE DsRed), no. 47 (HE Cyan Fluorescent Protein) and no. 50 (Cy5). Micrographs were acquired with an AxioCam MRm Rev. 3.0 (Carl Zeiss Microimaging, Munich, Germany) camera. Data acquisition was controlled with AxioVision 4.8.1 and conversion of very large tiled MosaiX images to single 16-bit grayscale TIFF files per channel was performed with AxioVision 4.8.2 SE64.



---

## 28. Histological quantification of relative A $\beta$ plaque burden and plaque size distribution

Image analysis was performed in principle as for the characterization of the ARTE10 mouse line [267] with some modifications. Digital images were evaluated with Acapella™ 2.0 data analysis software (PerkinElmer, Hamburg, Germany) using an updated plaque quantification script for specific and sensitive recognition of individual plaques and for quantitative assessment of relative plaque load.

A $\beta$  plaque burden was quantified using two different fluorescent modalities: Thioflavin S-stained sections were analyzed using the single channel method reported previously [267]. Double anti-A $\beta$ 40 and anti-A $\beta$ 42 immunostained sections were analyzed using two channels simultaneously after skew correction.

Regions of interest (neocortex, thalamus and cerebellum) were defined by manual segmentation in accordance with the anatomical delineations given by Paxinos and Franklin [62] using Adobe Photoshop CS5 Extended for Mac (Adobe Systems Inc., San Jose, CA, USA).

For the A $\beta$ 40 channel, observations of smallest plaques were excluded in order to control for mouse-on-mouse non-specificity of the primary antibody. The validity and reliability of this approach was successfully tested against the anti-A $\beta$ 42 and Thioflavin S channels.

All sections contained major portions of the neocortex and cerebellum. The thalamus could be delineated in the majority of these sections. Measurements provided total plaque area per defined regional area (relative total plaque burden) and counts for individual plaque sizes (plaque size distribution).

Right-left comparisons were performed with thirteen animals of the study collective (tg-old (3), tggg-young (3), ctl-young (3) and ctl-old (4)) and the data showed no differences.

Hence, 643 cortical and 411 thalamical regions were measured on horizontal Thioflavin S stained sections (Table 6). Analogously, 158 cortical and 106 thalamical regions were measured on nearby or neighboring horizontal anti-A $\beta$ 40/42 stained sections.

To visualize plaque size distribution in neocortex and thalamus among the study groups with A $\beta$  deposits, measured plaque areas were considered as circles and categorized according to

their radii. To analyze the differences between groups and regions, we histogrammed the individual plaque sizes for each transgenic group and region, estimated Epanechnikov kernel density functions and performed two-sample Kolmogorov-Smirnov tests to test whether the two underlying one-dimensional probability distributions differ.

---

## 29. A $\beta$ protein quantification with ELISA

Differential extraction of soluble and insoluble A $\beta_{x-40}$  and A $\beta_{x-42}$  in human and mouse brain (Table 6) was performed similar as for the characterization of the ARTE10 mouse line [267] with slight modifications. Brain homogenates were prepared as described in chapter 24.3 and deep frozen until assayed. The homogenates were centrifuged at 53000 rpm for 30 min at 4 °C. Supernatant and pellets were stored at -80 °C. Pellets were resuspended in the same volume of 70 % formic acid, kept on ice for 30 min and centrifuged likewise. Resulting supernatants were neutralized with 19 volumes of 1 M Tris pH = 11.3. A $\beta$  peptides were quantified in supernatants of both extractions using commercially available ELISA kits (EZBRAIN40 (G2-10 clone) and EZBRAIN42 (G2-13 clone), Merck Millipore, Schwalbach, Germany). Results are expressed as picogram A $\beta$  per microgram tissue wet weight.

ELISA analysis was performed by Heinz von der Kammer and Antje Willuweit at Evotec AG, Hamburg, Germany.



---

## 30. Combined multi-modal experiment

To gain a large spectrum of information across the various modalities from a single animal, a combined multi-modal *in vivo*, *ex vivo* and *in vitro* experiment with co-administration of either [<sup>11</sup>C]PiB and [<sup>3</sup>H]PiB was performed for four animals of the young study group (2 *tg*<sup>tg</sup>-young and 2 *ctl*-young) (Figure 25). In essence, the methods described above were combined in a streamlined workflow.

After each animal was scanned with CT in the docked PET/CT system, a cocktail of [<sup>11</sup>C]PiB and [<sup>3</sup>H]PiB was injected and a PET image taken over 30 min. After PET, the radioactivity of the whole (still living) animal was measured in a Capintec dose calibrator, the animal killed by decapitation, the whole brain taken out and blood drawn for biodistribution and radioactivity measurement. One half of the brain was dissected for regional brain biodistribution (olfactory system, telencephalon, cerebellum and remaining brain structures (diencephalon, midbrain)) (chapter 23.1) and deep-frozen immediately after gamma counting for later ELISA analysis of soluble and insoluble A $\beta_{x-40}$  and A $\beta_{x-42}$  (chapter 29). The other half was frozen on dry ice and rapidly cut on a cryostat for dual-isotope digital autoradiography (started around 1 hour *p.i.*) with subsequent automated separation of isotope signals (chapter 25.1), and for later histological processing for microscopy (chapter 27) and histological A $\beta$  plaque quantification (chapter 28) with Thiofavin S, anti-A $\beta_{40}$  and anti-A $\beta_{42}$ . Injected doses of [<sup>11</sup>C]PiB in these two subgroups was higher than in the rest of the study collective (Table 6) to retain a sufficient signal for [<sup>11</sup>C]PiB autoradiography while specific activities were remaining on the common clinical routine level.

Variants of this experimental design without plaque analysis and protein quantification were performed for the evaluation and ranking of lead compounds for novel imaging markers (Figure 25 and Figure 26).



---

## 31. Statistical analysis

For statistical analysis and graphical output, all data tables were transformed from Microsoft Excel for Mac 2011 to Stata format with Stat/Transfer 10 (Circle Systems, Seattle, WA, USA) for analysis in Stata/IC 11.2 for Mac (Stata Corp., College Station, TX, USA) if not noted otherwise. Two-sided t-tests with unequal variances were used to test for differences between groups. Significance level was set to 5 % if not specified otherwise. All reported correlations are pair-wise Pearson correlation coefficients ( $r$ ).



---

# Appendix



---

## 32. List of figures

Figure 1: Prediction of global Alzheimer's disease prevalence development. ....	7
Figure 2: Temporal hierarchy of biomarkers in the progression of Alzheimer's disease. ....	10
Figure 3: Plaques of Auguste D. ....	13
Figure 4: In vitro A $\beta$ fibrils and underlying protofilament model. ....	15
Figure 5: First published [ $^{11}\text{C}$ ]PiB PET images in humans. ....	18
Figure 6: Previous PET imaging studies with [ $^{11}\text{C}$ ]PiB in transgenic mice. ....	29
Figure 7: Chemical structure of [ $^{11}\text{C}$ ]IBT. ....	30
Figure 8: IBT - a hybrid of BTA and IMPY backbones. ....	30
Figure 9: Chemical structure of BrIMPY. ....	31
Figure 10: Exemplary [ $^{11}\text{C}$ ]PiB PET and MRI of a transgenic mouse before image fusion. ....	40
Figure 11: Mouse brain PET/MRI image co-registration. ....	41
Figure 12: [ $^{11}\text{C}$ ]PiB / [ $^{18}\text{F}$ ]FDG sequential PET in healthy control. ....	42
Figure 13: Volume-of-interest definition. ....	44
Figure 14: 3D view of VOI definition. ....	45
Figure 15: Small-animal [ $^{11}\text{C}$ ]PiB PET/MRI overview for different stages of A $\beta$ burden. ....	47
Figure 16: Cerebellum with very low A $\beta$ plaque load over all ages. ....	49
Figure 17: [ $^{11}\text{C}$ ]PiB PET binding potential maps for mouse brain. ....	51
Figure 18: PET test-retest results. ....	52
Figure 19: Mouse A $\beta$ plaque pathology in vivo and ex vivo. ....	55
Figure 20: Extracerebral tracer retention. ....	58
Figure 21: Time-activity curve averages per group. ....	64
Figure 22: Thioflavin S and A $\beta$ 40/42 antibodies for histological quantification of A $\beta$ plaques. ....	69
Figure 23: Histological A $\beta$ plaque burden and plaque size distribution in neocortex. ....	71
Figure 24: Cross-validation of PET with other modalities. ....	74
Figure 25: Multi-modal combined experiment with [ $^3\text{H}$ ]PiB / [ $^{11}\text{C}$ ]PiB cocktail. ....	76

Figure 26: Multi-modal combined experiment with [ <sup>11</sup> C]IBT / [ <sup>3</sup> H]PiB cocktail.....	80
Figure 27: Combined ex vivo [ <sup>124</sup> I]BriMPY experiment. ....	82
Figure 28: Translational potential of A $\beta$ PET imaging in transgenic mice. ....	113
Figure 29: Simultaneous access to lateral tail veins with self-built catheters. ....	127
Figure 30: Mouse PET imaging with Focus 120. ....	130
Figure 31: Mouse brain MR imaging with Philips Achieva 1.5 T. ....	133
Figure 32: Co-registration of sagittal ex vivo brain plate to in vivo CT.....	136
Figure 33: Ex vivo biodistribution with [ <sup>11</sup> C]PiB. ....	140

---

### 33. List of tables

Table 1:	Common transgenic mouse models for amyloidosis. ....	22
Table 2:	Small-animal PET scanners and some performance specifications.....	24
Table 3:	A $\beta$ radioligands applied in vivo or ex vivo in animal models of amyloidosis and non-human primates.....	27
Table 4:	Properties of [ $^{11}\text{C}$ ]IBT .....	31
Table 5:	Properties of novel [ $^{124}\text{I}$ ] / [ $^{125}\text{I}$ ]BrIMPY compared to IMPY. ....	32
Table 6:	Mouse study collective and numbers of mice per experiment.....	62
Table 7:	Robustness of PET results.....	65
Table 8:	Regional brain biodistribution of [ $^{11}\text{C}$ ]PiB. ....	67
Table 9:	A $\beta$ 40 and A $\beta$ 42 protein levels (ELISA) for transgenic study groups. ....	72
Table 10:	Multi-modal combined experiment with [ $^3\text{H}$ ]PiB / [ $^{11}\text{C}$ ]PiB cocktail.....	77
Table 11:	Multi-modal combined experiment with [ $^{11}\text{C}$ ]IBT / [ $^3\text{H}$ ]PiB cocktail. ....	82
Table 12:	Combined ex vivo [ $^{124}\text{I}$ ]BrIMPY experiment. ....	82



---

## 34. List of abbreviations

A $\beta$	Amyloid-beta
AD	Alzheimer's disease
ADNI	Alzheimer's Disease Neuroimaging Initiative
ApoE	Apolipoprotein E
APP	Amyloid Precursor Protein
ADRDA	Alzheimer's Disease and Related Disorders Association
Aqua dest.	Distilled / deionized water (Millipore water)
ARTE10	APP/PS1 mouse model (B6;CB-Tg(Thy1-PSEN1*M146V/Thy1-APP*swe)-10Arte)
BBB	blood-brain barrier
B <sub>max</sub>	Maximal number of binding sites
BP	In vitro binding potential
BP <sub>ND</sub>	In vivo binding potential (non-displacable, in vivo)
Bq	Bequerel
BrIMPY	2-(4'-bromophenyl)-6-iodoimidazo[1,2-a]pyridine
BTA	4-(Benzo[d]Thiazol-2-yl)Aniline
<sup>11</sup> C	Carbon-11
[ <sup>11</sup> C]IBT	2-( <i>p</i> -[ <sup>11</sup> C]Methylaminophenyl)-7-methoxyimidazo[2,1- <i>b</i> ]benzothiazole
[ <sup>11</sup> C]PiB	<i>N</i> -[ <sup>11</sup> C-methyl]-6-OH-benzothiazole (= [ <sup>11</sup> C]6-OH-BTA-1)
°C	Degrees Celcius
CAA	Cerebral amyloid angiopathy
C57BL/6	inbred strain of mice, genetic background of ARTE10 model
CBF	Cerebral Blood Flow
CDR	clinical dementia rating scale
CNS	Central Nervous System
CSF	Cerebrospinal fluid
CT	Computer Tomography
ctl	Control (animal)
3D	3-dimensional
DAPI	4',6-diamidino-2-phenylindole
DMSO	Dimethylsulfoxide
DSM-IV	Diagnostic and Statistical Manual of Mental Disorders (4th Ed.)
DVR	Distribution volume ratio

---

EDTA	Ethylenediaminetetraacetic acid
ELISA	Enzyme-linked immunosorbent assay
EtOH	Ethanol
EOS	End of synthesis
$^{18}\text{F}$	Fluorine-18
FAD	Familial form of Alzheimer's disease
FBP	Filtered back projection
$^{18}\text{F}$ FDDNP	2-(1-(2-(N-(2- $^{18}\text{F}$ fluoroethyl)-N-methylamino)naphthalene-6-yl)ethylidene)malononitrile
FDG	$^{18}\text{F}$ -fluoro-deoxy-D-glucose
$^{18}\text{F}$ Florbetaben	(= $^{18}\text{F}$ AV-1 = $^{18}\text{F}$ BAY94-9172)trans-4-(N-methylamino)-4'-{2-[2-(2- $^{18}\text{F}$ fluoroethoxy)-ethoxy]-ethoxy}-stilbene
$^{18}\text{F}$ Florebetapir	(= $^{18}\text{F}$ AV-45 = $^{18}\text{F}$ Amyvid)N-{4-[2-(4-{2-[2-(2- $^{18}\text{F}$ fluoroethoxy)ethoxy]ethoxy}-phenyl)vinyl]phenyl}-N-methylamine
FITC	Fluorescein isothiocyanate
FOV	Field-Of-View
FRE	Fiducial registration error
FTLD	Frontotemporal lobar degeneration
$^{18}\text{F}$ Flutemetamol	(= $^{18}\text{F}$ GE-067) 2-[3- $^{18}\text{F}$ fluoro-4-(methylamino)phenyl]1,3-benzothiazol-6-ol
FWHM	Full width at half maximum
g	Gram
GFP	Green fluorescent protein
$^3\text{H}$	Tritium
HFP	head-first prone (positioning in field-of-view)
HPLC	High performance liquid chromatography
IBT	Imidazo[2,1- <i>b</i> ]benzothiazole
$^{123}\text{I}$	Iodine-123
$^{124}\text{I}$	Iodine-124
$^{125}\text{I}$	Iodine-125
ICD-10	International Statistical Classification of Diseases and Related Health Problems 10th Revision
ID	Injected dose
IF	Immunofluorescence
IMPY	6-iodo-2-(4'-dimethylamino-)phenyl-imidazo[1,2- <i>a</i> ]pyridine
$k'_2$	efflux rate constant
$K_i$	Inhibition constant

---

K <sub>d</sub>	Apparent dissociation constant
l	Liter
P <sub>Oct./PBS</sub>	Partition coefficient between octanol and PBS
LUT	look-up table
M	Molar
MCI	Mild cognitive impairment
min	Minute
MMF	Medetomidine + Midazolam + Fentanyl
MMSE	mini-mental state examination
MRI	Magnetic resonance imaging
MRTM	Multilinear reference tissue model
NDP	Nucleation-dependent polymerization
NIA	National Institute on Aging
NIH	National Institutes of Health
NINCDS	National Institute of Neurological and Communicative Disorders and Stroke
PEI	Polyethyleneimine
PET	Positron emission tomography
μPET	Small-Animal PET
PBE	Phosphate buffered solution with EDTA and ethanol
PBS	Phosphate buffered saline solution
p.i.	Post-injectionem (after administration of substance)
PiB	Pittsburgh compound-B
PS1	Presenilin-1
PS2	Presenilin-2
PSEN1	gene encoding PS1
PSEN2	gene encoding PS2
PVE	Partial volume effect
qRT-PCR	Quantitative real-time polymerase chain reaction
r	Pearson's coefficient
ROI	Region-of-interest
rpm	Rounds per minute
RT	Room temperature
RXR	Retinoid X receptor
SD	Standard deviation
s	Second

SPECT	Single Photon Emission Computed Tomography
SPM	Statistical Parametric Mapping
SRTM	Simplified reference tissue model
SUV	Standardized uptake value
SUVR	Standardized uptake value ratio
T	Tesla
TAC	Time-activity curve
TE	Time-to-echo
Tg	Transgenic
tg/tg	Homozygous
tg	Hemizygous
Thioflavin T	4-(3,6-dimethyl-1,3-benzothiazol-3-ium-2-yl)- <i>N,N</i> -dimethylaniline chloride
TI	Inversion time
TR	Repetition time
VOI	Volume-of-interest
WT	Wild-type

---

## 35. Links and URLs

### **Technische Universität München**

<http://www.phd.med.tum.de>

<http://www.nuk.med.tum.de>

<http://www.i-magine.de>

### **Rodent Atlas Spaces**

<http://www.brain-map.org>

<http://www.mbl.org>

<http://software.incf.org/software/waxholm-space>

<http://www.loni.ucla.edu/Atlases>

### **Alzheimer's Disease**

<http://www.alzforum.org>

<http://www.kompetenznetz-demenzen.de>

<http://www.deutsche-alzheimer.de>

<http://www.alzheimer-haus.de>

<http://www.alzheimer-europe.org>

<http://www.nia.nih.gov/Alzheimers>

<http://www.alz.org>

### **Consortia and Initiatives**

<http://www.eadc.info>

<http://www.neurodegenerationresearch.eu>

<http://www.adni-info.org>

### **Societies and conferences**

<http://www.nuklearmedizin>

<http://www.snm.org>

<http://www.wmis.org>

<http://www.wmicmeeting.org>

<http://www.kenes.com/brain>

<http://www.kenes.com/adpd>

<http://eibsee.web.med.uni-muenchen.de>



---

## 36. List of publications within scope of thesis

### 36.1 International peer-reviewed journals

#### **Small-Animal PET Imaging of Amyloid-Beta Plaques with [<sup>11</sup>C]PiB and its Multi-Modal Validation in an APP/PS1 Mouse Model of Alzheimer's Disease.**

A. Manook, B. H. Yousefi, A. Willuweit, S. Platzer, S. Reder, A. Voss, M. Huisman, M. Settles, F. Neff, J. Velden, M. Schoor, H. von der Kammer, H. J. Wester, M. Schwaiger, G. Henriksen, A. Drzezga

*PLoS ONE* 7 (3): e31310, March 2012 (DOI: 10.1371/journal.pone.0031310)

#### **A Novel 18F-labeled Imidazo[2,1-*b*]benzothiazole (IBT) for High-Contrast PET Imaging of $\beta$ -Amyloid Plaques.**

B. H. Yousefi, A. Drzezga, B. von Reutern, A. Manook, M. Schwaiger, H. J. Wester, G. Henriksen

*ACS Med Chem Lett* 2 (9), pp 673-677, September 2011 (DOI: 10.1021/ML200123w)

**contribution not included in this thesis.**

#### **Synthesis and Evaluation of 11C-labeled Imidazo[2,1-*b*]benzothiazoles (IBTs) as PET Tracers for Imaging Beta-Amyloid Plaques in Alzheimer's disease.**

B. H. Yousefi, A. Manook, A. Drzezga, B. von Reutern, M. Schwaiger, H. J. Wester, G. Henriksen

*J Med Chem* 54 (4), pp 949-956, February 2011 (DOI: 10.1021/jm101129a)

#### **Early-onset and Robust Amyloid Pathology in a New Homozygous Mouse Model of Alzheimer's disease.**

A. Willuweit, J. Velden, R. Godemann, A. Manook, F. Jetzek, H. Tintrup, G. Kauselmann, B. Zevnik, G. Henriksen, A. Drzezga, J. Pohlner, M. Schoor, J. A. Kemp, H. von der Kammer

*PLoS ONE* 4 (11): e7931, November 2009 (DOI: 10.1371/journal.pone.0007931)

#### **Development of an Improved Radioiodinated 2-Phenylimidazo[1,2-*a*]pyridine for Non-invasive Imaging of Amyloid Plaques.**

B. H. Yousefi, A. Manook, B. von Reutern, M. Schwaiger, A. Drzezga, H. J. Wester, G. Henriksen

*Med Chem Com* 3 (7), pp 775-779, July 2012, (DOI: 10.1039/C2md20115a)

## 36.2 International conferences

### **Basics of Methodology for PET imaging of Amyloid Plaques in Mice.**

A. Manook, G. Henriksen, S. Platzer, F. Neff, M. Huisman, B.H. Yousefi, M. Settles, M. Schwaiger, H. J. Wester, A. Drzezga.

*TUMind Symposium 2006 - Molecular Imaging in Dementia*, 9 December 2006, Munich, Germany

**oral presentation**

### **In Vivo Imaging of Amyloid Plaques in a Transgenic Mouse Model of Alzheimer's Disease.**

A. Manook, G. Henriksen, S. Platzer, F. Neff, M. Huisman, B.H. Yousefi, M. Settles, M. Schwaiger, H.J. Wester, A. Drzezga

*Brain and BrainPET'07*, 22 May 2007, Osaka, Japan

**oral presentation (young investigator award)**

### **Feasibility of In Vivo Amyloid Plaque Imaging in a Transgenic Mouse Model of Alzheimer's Disease.**

A. Manook, G. Henriksen, S. Platzer, F. Neff, M. Huisman, B.H. Yousefi, M. Settles, M. Schwaiger, H.J. Wester, A. Drzezga

*Society of Nuclear Medicine 2007*, 54th Annual Meeting, 5 June 2007, Washington D.C., USA

**oral presentation**

### **PET Imaging of Amyloid Plaques with [<sup>11</sup>C]PIB in a Transgenic Mouse Model of Alzheimer's Disease.**

A. Manook, G. Henriksen, S. Platzer, M. Huisman, F. Neff, B.H. Yousefi, M. Settles, M. Schwaiger, H.J. Wester, A. Drzezga

*Joint Molecular Imaging 2007*, 11 September 2007, Providence, USA

**oral presentation**

### **PET Imaging of Beta-Amyloid Plaques in Preclinical Models of Alzheimer's Disease.**

A. Manook, G. Henriksen, B. Yousefi, A. Willuweit, S. Platzer, S. Reder, A. Voss, M. Huisman, M. Settles, F. Neff, J. Velden, M. Schoor, H. von der Kammer, H. J. Wester, M. Schwaiger, A. Drzezga

*Healthy Brain Conference 2011*, 7 June 2011, Oslo, Norway

**invited talk**

### **Development of Metabolically Stabilized <sup>11</sup>C-labeled 2-(4-aminophenyl)benzothiazoles (BTAs) for Imaging of Amyloid Plaques.**

G. Henriksen, A. Westwell, A. Hauser, A. Manook, M. Schwaiger, A. Drzezga and H. Wester

*Society of Nuclear Medicine 2006*, 53rd Annual Meeting, 4 June 2006, San Diego, USA

**co-author**

**[<sup>18</sup>F]FIBT a Newly Developed Tracer allows High-Contrast Imaging of  $\beta$ -Amyloid in different age groups of an APP/PS1 Mouse Model of Alzheimer's disease.**

B.H. Yousefi, A. Drzezga, B. von Reutern, A. Manook, M. Schwaiger, H.J. Wester, G. Henriksen

*EANM'11* - Annual Congress of the European Association of Nuclear Medicine 2011, Birmingham, United Kingdom

**co-author**

**A New <sup>18</sup>F-labeled IBT Tracer allows High-Contrast Imaging of  $\beta$ -Amyloid and Staging in different age group of APP/PS1 Mouse Model of Alzheimer's disease.**

B.H. Yousefi, B. von Reutern, A. Manook, M. Schwaiger, H.J. Wester, A. Drzezga, G. Henriksen

*EMIM 2011* - 6th European Molecular Imaging Meeting, Leiden, Netherlands

**co-author**

**Development of an Improved Radioiodinated Phenyl-imidazo[1,2-a]pyridine for Non-Invasive Imaging of Amyloid Plaques.**

B.H. Yousefi, A. Manook, B. von Reutern, M. Schwaiger, A. Drzezga, H.J. Wester, G. Henriksen

*ISRS 2011* - 19th International Symposium on Radiopharmaceutical Sciences, Amsterdam, Netherlands

**co-author**

### 36.3 National conferences

**In-vivo Darstellung von Amyloid-Plaques mittels [<sup>11</sup>C]PIB microPET in einem neuen doppelt-transgenen APP/PS1 Mausmodell.**

A. Manook, G. Henriksen, S. Platzner, A. Weber, B. H. Yousefi, M. Settles, M. Schwaiger, H. J. Wester, A. Drzezga

*Nuklearmedizin 2008* - 46. Jahrestagung der Deutschen Gesellschaft für Nuklearmedizin, 24 April 2008, Leipzig, Germany

**oral presentation (best abstract)**

### 36.4 Other publications

**Molekulare Bildgebung beim Morbus Alzheimer: Alzheimer Plaques endlich auch im Maushirn mit  $\mu$ PET sichtbar.**

A. Manook

*MedReport* 32 (11), pp 11-12, April 2008

**invited article**



## 37. Bibliography

1. Research Models. Alzheimer Research Forum. Available at: <http://www.alzforum.org/res/com/tra>. Accessed: 27 February 2012
2. Abcam. Double immunofluorescence: simultaneous protocol. Abcam plc. Available at: <http://www.abcam.com/immunosimultaneous>. Accessed: 27 February 2012
3. Aide N, Louis MH, Dutoit S, Labiche A, Lemoisson E, et al. (2007) Improvement of semi-quantitative small-animal PET data with recovery coefficients: a phantom and rat study. *Nucl Med Commun* 28: 813-822.
4. Alzheimer A (1906) Über einen eigenartigen schweren Erkrankungsprozeß der Hirnrinde. 37th meeting of the Southern German psychiatrists. Tuebingen, Germany: Neurologisches Centralblatt. pp. 1129-1136.
5. Alzheimer A (1907) Über eine eigenartige Erkrankung der Hirnrinde. *Allgemeine Zeitschrift für Psychiatrie und Psychisch-gerichtliche Medizin* 64: 146-148.
6. Anstey KJ, Mack HA, Cherbuin N (2009) Alcohol consumption as a risk factor for dementia and cognitive decline: meta-analysis of prospective studies. *Am J Geriatr Psychiatry* 17: 542-555.
7. Antzutkin ON (2004) Amyloidosis of Alzheimer's A $\beta$  peptides: solid-state nuclear magnetic resonance, electron paramagnetic resonance, transmission electron microscopy, scanning transmission electron microscopy and atomic force microscopy studies. *Magn Reson Chem* 42: 231-246.
8. Arimon M, Diez-Perez I, Kogan MJ, Durany N, Giralt E, et al. (2005) Fine structure study of A $\beta$ 1-42 fibrillogenesis with atomic force microscopy. *Faseb J* 19: 1344-1346.
9. Ashe KH, Zahs KR (2010) Probing the biology of Alzheimer's disease in mice. *Neuron* 66: 631-645.
10. Bacskai BJ, Hickey GA, Skoch J, Kajdasz ST, Wang Y, et al. (2003) Four-dimensional multiphoton imaging of brain entry, amyloid binding, and clearance of an amyloid-beta ligand in transgenic mice. *Proc Natl Acad Sci U S A* 100: 12462-12467.
11. Ballard C, Gauthier S, Corbett A, Brayne C, Aarsland D, et al. (2011) Alzheimer's disease. *Lancet* 377: 1019-1031.
12. Bao Q, Newport D, Chen M, Stout DB, Chatzioannou AF (2009) Performance evaluation of the inveon dedicated PET preclinical tomograph based on the NEMA NU-4 standards. *J Nucl Med* 50: 401-408.
13. Barrio JR, Huang SC, Cole G, Satyamurthy N, Petric A, et al. (1999) PET imaging of tangles and plaques in Alzheimer disease with a highly hydrophobic probe. *J Labelled Compd Radiopharm* 42: S194-S195.
14. Basun H, Bogdanovic N, Ingelsson M, Almkvist O, Naslund J, et al. (2008) Clinical and neuropathological features of the arctic APP gene mutation causing early-onset Alzheimer disease. *Arch Neurol* 65: 499-505.
15. Bayer TA, Schafer S, Simons A, Kemmling A, Kamber T, et al. (2003) Dietary Cu stabilizes brain superoxide dismutase 1 activity and reduces amyloid A $\beta$  production in APP23 transgenic mice. *Proc Natl Acad Sci U S A* 100: 14187-14192.
16. Bennhold H (1922) Eine spezifische Amyloidfärbung mit Kongorot [Specific staining of amyloid with Congo red]. *Münch Med Wochenschr* 69: 1537-1538.
17. Bertram L, Lill CM, Tanzi RE (2010) The genetics of Alzheimer disease: back to the future. *Neuron* 68: 270-281.
18. Bertram L, Tanzi RE (2008) Thirty years of Alzheimer's disease genetics: the implications of systematic meta-analyses. *Nat Rev Neurosci* 9: 768-778.
19. Beydoun MA, Beydoun HA, Wang Y (2008) Obesity and central obesity as risk factors for incident dementia and its subtypes: a systematic review and meta-analysis. *Obes Rev* 9: 204-218.

20. Bickel H (2010) Die Epidemiologie der Demenz. In: Gesellschaft DA, editor: Deutsche Alzheimer Gesellschaft.
21. Bloomfield PM, Rajeswaran S, Spinks TJ, Hume SP, Myers R, et al. (1995) The design and physical characteristics of a small animal positron emission tomograph. *Phys Med Biol* 40: 1105-1126.
22. Bloudek LM, Spackman DE, Blankenburg M, Sullivan SD (2011) Review and meta-analysis of biomarkers and diagnostic imaging in Alzheimer's disease. *J Alzheimers Dis* 26: 627-645.
23. Boellaard R (2009) Standards for PET image acquisition and quantitative data analysis. *J Nucl Med* 50 Suppl 1: 11S-20S.
24. Bowman-Rogers M. Love a Good Fight? Check Out Brouhaha Over Amyloid Imaging. Available at: <http://www.alzforum.org/new/detail.asp?id=3048>. Accessed: 27 February 2012
25. Braak H, Braak E (1991) Neuropathological staging of Alzheimer-related changes. *Acta Neuropathol (Berl)* 82: 239-259.
26. Brookmeyer R, Johnson E, Ziegler-Graham K, Arrighi HM (2007) Forecasting the global burden of Alzheimer's disease. *Alzheimers Dement* 3: 186-191.
27. Bussiere T, Friend PD, Sadeghi N, Wicinski B, Lin GI, et al. (2002) Stereologic assessment of the total cortical volume occupied by amyloid deposits and its relationship with cognitive status in aging and Alzheimer's disease. *Neuroscience* 112: 75-91.
28. Cai L, Chin FT, Pike VW, Toyama H, Liow JS, et al. (2004) Synthesis and evaluation of two <sup>18</sup>F-labeled 6-iodo-2-(4'-N,N-dimethylamino)phenylimidazo[1,2-a]pyridine derivatives as prospective radioligands for beta-amyloid in Alzheimer's disease. *J Med Chem* 47: 2208-2218.
29. Cai L, Cuevas J, Temme S, Herman MM, Dagostin C, et al. (2007) Synthesis and structure-affinity relationships of new 4-(6-iodo-H-imidazo[1,2-a]pyridin-2-yl)-N-dimethylbenzeneamine derivatives as ligands for human beta-amyloid plaques. *J Med Chem* 50: 4746-4758.
30. Cai L, Innis RB, Pike VW (2007) Radioligand development for PET imaging of beta-amyloid (A $\beta$ )-current status. *Curr Med Chem* 14: 19-52.
31. Cai L, Liow JS, Zoghbi SS, Cuevas J, Baetas C, et al. (2008) Synthesis and evaluation of N-Methyl and S-Methyl <sup>11</sup>C-Labeled 6-Methylthio-2-(4'-N,N-dimethylamino)phenylimidazo[1,2-a]pyridines as radioligands for imaging beta-amyloid plaques in Alzheimer's disease. *J Med Chem* 51: 148-158.
32. Callahan MJ, Lipinski WJ, Bian F, Durham RA, Pack A, et al. (2001) Augmented senile plaque load in aged female beta-amyloid precursor protein-transgenic mice. *Am J Pathol* 158: 1173-1177.
33. Carpenter AP, Jr., Pontecorvo MJ, Hefti FF, Skovronsky DM (2009) The use of the exploratory IND in the evaluation and development of <sup>18</sup>F-PET radiopharmaceuticals for amyloid imaging in the brain: a review of one company's experience. *Q J Nucl Med Mol Imaging* 53: 387-393.
34. Carson RE, Breier A, de Bartolomeis A, Saunders RC, Su TP, et al. (1997) Quantification of amphetamine-induced changes in [<sup>11</sup>C]raclopride binding with continuous infusion. *J Cereb Blood Flow Metab* 17: 437-447.
35. Carson RE, Channing MA, Blasberg RG, Dunn BB, Cohen RM, et al. (1993) Comparison of bolus and infusion methods for receptor quantitation: application to [<sup>18</sup>F]cyclofexy and positron emission tomography. *J Cereb Blood Flow Metab* 13: 24-42.
36. Chatziioannou AF (2002) Molecular imaging of small animals with dedicated PET tomographs. *Eur J Nucl Med Mol Imaging* 29: 98-114.
37. Chatziioannou AF (2002) PET scanners dedicated to molecular imaging of small animal models. *Mol Imaging Biol* 4: 47-63.
38. Chishti MA, Yang DS, Janus C, Phinney AL, Horne P, et al. (2001) Early-onset amyloid deposition and cognitive deficits in transgenic mice expressing a double mutant form of amyloid precursor protein 695. *J Biol Chem* 276: 21562-21570.
39. Choi SR, Golding G, Zhuang Z, Zhang W, Lim N, et al. (2009) Preclinical properties of <sup>18</sup>F-AV-45: a PET agent for A $\beta$  plaques in the brain. *J Nucl Med* 50: 1887-1894.
40. Chow PL, Stout DB, Komisopoulou E, Chatziioannou AF (2006) A method of image registration for small animal, multi-modality imaging. *Phys Med Biol* 51: 379-390.

41. Christie RH, Bacskai BJ, Zipfel WR, Williams RM, Kajdasz ST, et al. (2001) Growth arrest of individual senile plaques in a model of Alzheimer's disease observed by in vivo multiphoton microscopy. *J Neurosci* 21: 858-864.
42. Chubb C, Inagaki Y, Sheu P, Cummings B, Wasserman A, et al. (2006) BioVision: an application for the automated image analysis of histological sections. *Neurobiol Aging* 27: 1462-1476.
43. Citron M (2004) Strategies for disease modification in Alzheimer's disease. *Nat Rev Neurosci* 5: 677-685.
44. Citron M (2010) Alzheimer's disease: strategies for disease modification. *Nat Rev Drug Discov* 9: 387-398.
45. Citron M, Oltersdorf T, Haass C, McConlogue L, Hung AY, et al. (1992) Mutation of the beta-amyloid precursor protein in familial Alzheimer's disease increases beta-protein production. *Nature* 360: 672-674.
46. Combs CK, Johnson DE, Karlo JC, Cannady SB, Landreth GE (2000) Inflammatory mechanisms in Alzheimer's disease: inhibition of beta-amyloid-stimulated proinflammatory responses and neurotoxicity by PPARgamma agonists. *J Neurosci* 20: 558-567.
47. Corder EH, Saunders AM, Strittmatter WJ, Schmechel DE, Gaskell PC, et al. (1993) Gene dose of apolipoprotein E type 4 allele and the risk of Alzheimer's disease in late onset families. *Science* 261: 921-923.
48. Craft S, Baker LD, Montine TJ, Minoshima S, Watson GS, et al. (2012) Intranasal insulin therapy for Alzheimer disease and amnesic mild cognitive impairment: a pilot clinical trial. *Arch Neurol* 69: 29-38.
49. Craig-Schapiro R, Fagan AM, Holtzman DM (2009) Biomarkers of Alzheimer's disease. *Neurobiol Dis* 35: 128-140.
50. Cramer PE, Cirrito JR, Wesson DW, Lee CY, Karlo JC, et al. (2012) ApoE-Directed Therapeutics Rapidly Clear beta-Amyloid and Reverse Deficits in AD Mouse Models. *Science*.
51. Davies P, Maloney AJ (1976) Selective loss of central cholinergic neurons in Alzheimer's disease. *Lancet* 2: 1403.
52. Dhenain M, El Tannir El Tayara N, Wu TD, Guegan M, Volk A, et al. (2009) Characterization of in vivo MRI detectable thalamic amyloid plaques from APP/PS1 mice. *Neurobiol Aging* 30: 41-53.
53. Dhuria SV, Hanson LR, Frey WH, 2nd (2010) Intranasal delivery to the central nervous system: mechanisms and experimental considerations. *J Pharm Sci* 99: 1654-1673.
54. Drzezga A (2010) Amyloid-plaque imaging in early and differential diagnosis of dementia. *Ann Nucl Med* 24: 55-66.
55. Dubois B, Feldman HH, Jacova C, Dekosky ST, Barberger-Gateau P, et al. (2007) Research criteria for the diagnosis of Alzheimer's disease: revising the NINCDS-ADRDA criteria. *Lancet Neurol* 6: 734-746.
56. Elghetany MT, Saleem A (1988) Methods for staining amyloid in tissues: a review. *Stain Technol* 63: 201-212.
57. EU Joint Programme (JPND) NDR. Transnational call for optimisation of biomarkers and harmonisation of their use. EU Joint Programme - Neurodegenerative Disease Research. Available at: <http://www.neurodegenerationresearch.eu/initiatives/biomarker-transnational-call>. Accessed: 27 February 2012
58. Ferri CP, Prince M, Brayne C, Brodaty H, Fratiglioni L, et al. (2005) Global prevalence of dementia: a Delphi consensus study. *Lancet* 366: 2112-2117.
59. Fischer K, Sossi V, Schmid A, Thunemann M, Maier FC, et al. (2011) Noninvasive nuclear imaging enables the in vivo quantification of striatal dopamine receptor expression and raclopride affinity in mice. *J Nucl Med* 52: 1133-1141.
60. Fischer K, Sossi V, von Ameln-Mayerhofer A, Reischl G, Pichler BJ (2012) In vivo quantification of dopamine transporters in mice with unilateral 6-OHDA lesions using [(11)C]methylphenidate and PET. *Neuroimage* 59: 2413-2422.

61. Fleisher AS, Raman R, Siemers ER, Becerra L, Clark CM, et al. (2008) Phase 2 safety trial targeting amyloid beta production with a gamma-secretase inhibitor in Alzheimer disease. *Arch Neurol* 65: 1031-1038.
62. Franklin KBJ, Paxinos G (2007) *The Mouse Brain in Stereotaxic Coordinates*. Oxford: Academic Press. 360 p.
63. Fratiglioni L, Paillard-Borg S, Winblad B (2004) An active and socially integrated lifestyle in late life might protect against dementia. *Lancet Neurol* 3: 343-353.
64. Freude S, Hettich MM, Schumann C, Stohr O, Koch L, et al. (2009) Neuronal IGF-1 resistance reduces Aβ accumulation and protects against premature death in a model of Alzheimer's disease. *Faseb J* 23: 3315-3324.
65. Games D, Adams D, Alessandrini R, Barbour R, Berthelette P, et al. (1995) Alzheimer-type neuropathology in transgenic mice overexpressing V717F beta-amyloid precursor protein. *Nature* 373: 523-527.
66. Garcia-Alloza M, Robbins EM, Zhang-Nunes SX, Purcell SM, Betensky RA, et al. (2006) Characterization of amyloid deposition in the APP<sup>swe</sup>/PS1<sup>dE9</sup> mouse model of Alzheimer disease. *Neurobiol Dis* 24: 516-524.
67. Gatz M, Reynolds CA, Fratiglioni L, Johansson B, Mortimer JA, et al. (2006) Role of genes and environments for explaining Alzheimer disease. *Arch Gen Psychiatry* 63: 168-174.
68. Glenner GG, Wong CW (1984) Alzheimer's disease and Down's syndrome: sharing of a unique cerebrovascular amyloid fibril protein. *Biochem Biophys Res Commun* 122: 1131-1135.
69. Glenner GG, Wong CW (1984) Alzheimer's disease: initial report of the purification and characterization of a novel cerebrovascular amyloid protein. *Biochem Biophys Res Commun* 120: 885-890.
70. Goate A, Chartier-Harlin MC, Mullan M, Brown J, Crawford F, et al. (1991) Segregation of a missense mutation in the amyloid precursor protein gene with familial Alzheimer's disease. *Nature* 349: 704-706.
71. Goldsbury CS, Wirtz S, Muller SA, Sunderji S, Wicki P, et al. (2000) Studies on the in vitro assembly of a beta 1-40: implications for the search for a beta fibril formation inhibitors. *J Struct Biol* 130: 217-231.
72. Goldsmith HS (2011) A new approach to the treatment of Alzheimer's disease: the need for a controlled study. *J Alzheimers Dis* 25: 209-212.
73. Gordon MN, Holcomb LA, Jantzen PT, DiCarlo G, Wilcock D, et al. (2002) Time course of the development of Alzheimer-like pathology in the doubly transgenic PS1+APP mouse. *Exp Neurol* 173: 183-195.
74. Gordon MN, King DL, Diamond DM, Jantzen PT, Boyett KV, et al. (2001) Correlation between cognitive deficits and Aβ deposits in transgenic APP+PS1 mice. *Neurobiol Aging* 22: 377-385.
75. Graessel E, Stemmer R, Eichenseer B, Pickel S, Donath C, et al. (2011) Non-pharmacological, multicomponent group therapy in patients with degenerative dementia: a 12-month randomized, controlled trial. *BMC Med* 9: 129.
76. Grunder G (2009) "Absolute" or "relative": choosing the right outcome measure in neuroimaging. *Neuroimage* 45: 258-259.
77. Gunn AP, Masters CL, Cherny RA (2010) Pyroglutamate-Aβ: Role in the natural history of Alzheimer's disease. *Int J Biochem Cell Biol* 42: 1915-1918.
78. Gunter C, Dhand R (2002) Human biology by proxy. *Nature* 420: 509-509.
79. Guo WY, Lee JJ, Lin MH, Yang CC, Chen CL, et al. (2007) Merging molecular and anatomical information: a feasibility study on rodents using microPET and MRI. *Nucl Med Commun* 28: 804-812.
80. Haass C (2010) Initiation and propagation of neurodegeneration. *Nat Med* 16: 1201-1204.
81. Haass C, Schlossmacher MG, Hung AY, Vigo-Pelfrey C, Mellon A, et al. (1992) Amyloid beta-peptide is produced by cultured cells during normal metabolism. *Nature* 359: 322-325.

82. Haass C, Selkoe DJ (2007) Soluble protein oligomers in neurodegeneration: lessons from the Alzheimer's amyloid beta-peptide. *Nat Rev Mol Cell Biol* 8: 101-112.
83. Hamer M, Chida Y (2009) Physical activity and risk of neurodegenerative disease: a systematic review of prospective evidence. *Psychol Med* 39: 3-11.
84. Hardy J (2006) The Amyloid Hypothesis: history and alternatives. In: Jucker M, Beyreuther K, Haass C, Nitsch R, Christen Y, editors. *Alzheimer: 100 Years and Beyond*. 1st ed. Berlin Heidelberg: Springer. pp. 151-154.
85. Hardy J, Myers A, Wavrant-De Vrieze F (2004) Problems and solutions in the genetic analysis of late-onset Alzheimer's disease. *Neurodegener Dis* 1: 213-217.
86. Hardy J, Selkoe DJ (2002) The amyloid hypothesis of Alzheimer's disease: progress and problems on the road to therapeutics. *Science* 297: 353-356.
87. Hefendehl JK, Wegenast-Braun BM, Liebig C, Eicke D, Milford D, et al. (2011) Long-term in vivo imaging of beta-amyloid plaque appearance and growth in a mouse model of cerebral beta-amyloidosis. *J Neurosci* 31: 624-629.
88. Herschman HR (2003) Molecular imaging: looking at problems, seeing solutions. *Science* 302: 605-608.
89. Herzig MC, Van Nostrand WE, Jucker M (2006) Mechanism of cerebral beta-amyloid angiopathy: murine and cellular models. *Brain Pathol* 16: 40-54.
90. Herzig MC, Winkler DT, Burgermeister P, Pfeifer M, Kohler E, et al. (2004) Abeta is targeted to the vasculature in a mouse model of hereditary cerebral hemorrhage with amyloidosis. *Nat Neurosci* 7: 954-960.
91. Higuchi M (2009) Visualization of brain amyloid and microglial activation in mouse models of Alzheimer's disease. *Curr Alzheimer Res* 6: 137-143.
92. Hintersteiner M, Enz A, Frey P, Jatton AL, Kinzy W, et al. (2005) In vivo detection of amyloid-beta deposits by near-infrared imaging using an oxazine-derivative probe. *Nat Biotechnol* 23: 577-583.
93. Hirai K, Aliev G, Nunomura A, Fujioka H, Russell RL, et al. (2001) Mitochondrial abnormalities in Alzheimer's disease. *J Neurosci* 21: 3017-3023.
94. Hixson JR (1983) New seeing-eye machines...look inside your body, can save your life. *Vogue*. pp. 238-239, 245-258.
95. Hoffman EJ, Huang SC, Phelps ME (1979) Quantitation in positron emission computed tomography: 1. Effect of object size. *J Comput Assist Tomogr* 3: 299-308.
96. Holcomb L, Gordon MN, McGowan E, Yu X, Benkovic S, et al. (1998) Accelerated Alzheimer-type phenotype in transgenic mice carrying both mutant amyloid precursor protein and presenilin 1 transgenes. *Nat Med* 4: 97-100.
97. Holmes C, Boche D, Wilkinson D, Yadegarfar G, Hopkins V, et al. (2008) Long-term effects of Abeta42 immunisation in Alzheimer's disease: follow-up of a randomised, placebo-controlled phase I trial. *Lancet* 372: 216-223.
98. Hsiao K, Chapman P, Nilsen S, Eckman C, Harigaya Y, et al. (1996) Correlative memory deficits, Abeta elevation, and amyloid plaques in transgenic mice. *Science* 274: 99-102.
99. Huisman MC, Reder S, Weber AW, Ziegler SI, Schwaiger M (2007) Performance evaluation of the Philips MOSAIC small animal PET scanner. *Eur J Nucl Med Mol Imaging* 34: 532-540.
100. Hwang DY, Cho JS, Oh JH, Shim SB, Jee SW, et al. (2005) Early changes in behavior deficits, amyloid beta-42 deposits and MAPK activation in doubly transgenic mice co-expressing NSE-controlled human mutant PS2 and APPsw. *Cell Mol Neurobiol* 25: 881-898.
101. Iacono D, Markesbery WR, Gross M, Pletnikova O, Rudow G, et al. (2009) The Nun study: clinically silent AD, neuronal hypertrophy, and linguistic skills in early life. *Neurology* 73: 665-673.
102. Ichise M, Liow JS, Lu JQ, Takano A, Model K, et al. (2003) Linearized reference tissue parametric imaging methods: application to [<sup>11</sup>C]DASB positron emission tomography studies of the serotonin transporter in human brain. *J Cereb Blood Flow Metab* 23: 1096-1112.

103. Ingvar M, Eriksson L, Rogers GA, Stone-Elander S, Widen L (1991) Rapid feasibility studies of tracers for positron emission tomography: high-resolution PET in small animals with kinetic analysis. *J Cereb Blood Flow Metab* 11: 926-931.
104. Irizarry MC, McNamara M, Fedorchak K, Hsiao K, Hyman BT (1997) APPSw transgenic mice develop age-related A beta deposits and neuropil abnormalities, but no neuronal loss in CA1. *J Neuropathol Exp Neurol* 56: 965-973.
105. Irizarry MC, Soriano F, McNamara M, Page KJ, Schenk D, et al. (1997) Abeta deposition is associated with neuropil changes, but not with overt neuronal loss in the human amyloid precursor protein V717F (PDAPP) transgenic mouse. *J Neurosci* 17: 7053-7059.
106. Ito H, Hietala J, Blomqvist G, Halldin C, Farde L (1998) Comparison of the transient equilibrium and continuous infusion method for quantitative PET analysis of [<sup>11</sup>C]raclopride binding. *J Cereb Blood Flow Metab* 18: 941-950.
107. Jack CR, Jr., Albert MS, Knopman DS, McKhann GM, Sperling RA, et al. (2011) Introduction to the recommendations from the National Institute on Aging-Alzheimer's Association workgroups on diagnostic guidelines for Alzheimer's disease. *Alzheimers Dement* 7: 257-262.
108. Jacobson A, Petric A, Hogenkamp D, Sinur A, Barrio JR (1996) 1,1-dicyano-2-[6-(dimethylamino)naphthalen-2-yl]propene (DDNP): A solvent polarity and viscosity sensitive fluorophore for fluorescence microscopy. *Journal of the American Chemical Society* 118: 5572-5579.
109. Jankowsky JL, Fadale DJ, Anderson J, Xu GM, Gonzales V, et al. (2004) Mutant presenilins specifically elevate the levels of the 42 residue beta-amyloid peptide in vivo: evidence for augmentation of a 42-specific gamma secretase. *Hum Mol Genet* 13: 159-170.
110. Jansson B, Bjork E (2002) Visualization of in vivo olfactory uptake and transfer using fluorescein dextran. *J Drug Target* 10: 379-386.
111. Jawhar S, Wirths O, Bayer TA (2011) Pyroglutamate amyloid-beta (Abeta): a hatchet man in Alzheimer disease. *J Biol Chem* 286: 38825-38832.
112. Johnson AE, Jeppsson F, Sandell J, Wensbo D, Neelissen JA, et al. (2009) AZD2184: a radioligand for sensitive detection of beta-amyloid deposits. *J Neurochem* 108: 1177-1186.
113. Johnson-Wood K, Lee M, Motter R, Hu K, Gordon G, et al. (1997) Amyloid precursor protein processing and A beta42 deposition in a transgenic mouse model of Alzheimer disease. *Proc Natl Acad Sci U S A* 94: 1550-1555.
114. Johnston M, Zakharov A, Papaiconomou C, Salmasi G, Armstrong D (2004) Evidence of connections between cerebrospinal fluid and nasal lymphatic vessels in humans, non-human primates and other mammalian species. *Cerebrospinal Fluid Res* 1: 2.
115. Jones AR, Overly CC, Sunkin SM (2009) The Allen Brain Atlas: 5 years and beyond. *Nat Rev Neurosci* 10: 821-828.
116. Jucker M (2010) The benefits and limitations of animal models for translational research in neurodegenerative diseases. *Nat Med* 16: 1210-1214.
117. Jucker M, Walker LC (2011) Pathogenic protein seeding in Alzheimer disease and other neurodegenerative disorders. *Ann Neurol* 70: 532-540.
118. Jureus A, Swahn BM, Sandell J, Jeppsson F, Johnson AE, et al. (2010) Characterization of AZD4694, a novel fluorinated Abeta plaque neuroimaging PET radioligand. *J Neurochem* 114: 784-794.
119. Kameshima N, Nanjou T, Fukuhara T, Yanagisawa D, Tooyama I (2012) Correlation of Ass deposition in the nasal cavity with the formation of senile plaques in the brain of a transgenic mouse model of Alzheimer's disease. *Neurosci Lett*.
120. Kang J, Lemaire HG, Unterbeck A, Salbaum JM, Masters CL, et al. (1987) The precursor of Alzheimer's disease amyloid A4 protein resembles a cell-surface receptor. *Nature* 325: 733-736.
121. Kemp BJ, Hruska CB, McFarland AR, Lenox MW, Lowe VJ (2009) NEMA NU 2-2007 performance measurements of the Siemens Inveon preclinical small animal PET system. *Phys Med Biol* 54: 2359-2376.
122. Kerchner GA, Boxer AL (2010) Bapineuzumab. *Expert Opin Biol Ther* 10: 1121-1130.

123. Khachaturian ZS (2011) Revised criteria for diagnosis of Alzheimer's disease: National Institute on Aging-Alzheimer's Association diagnostic guidelines for Alzheimer's disease. *Alzheimers Dement* 7: 253-256.
124. Khlistunova I, Biernat J, Wang Y, Pickhardt M, von Bergen M, et al. (2006) Inducible expression of Tau repeat domain in cell models of tauopathy: aggregation is toxic to cells but can be reversed by inhibitor drugs. *J Biol Chem* 281: 1205-1214.
125. Kidd M (1963) Paired helical filaments in electron microscopy of Alzheimer's disease. *Nature* 197: 192-193.
126. Kim JS, Lee JS, Im KC, Kim SJ, Kim SY, et al. (2007) Performance measurement of the microPET focus 120 scanner. *J Nucl Med* 48: 1527-1535.
127. Kirschner DA, Inouye H, Duffy LK, Sinclair A, Lind M, et al. (1987) Synthetic peptide homologous to beta protein from Alzheimer disease forms amyloid-like fibrils in vitro. *Proc Natl Acad Sci U S A* 84: 6953-6957.
128. Klunk WE, Bacskai BJ, Mathis CA, Kajdasz ST, McLellan ME, et al. (2002) Imaging Abeta plaques in living transgenic mice with multiphoton microscopy and methoxy-X04, a systemically administered Congo red derivative. *J Neuropathol Exp Neurol* 61: 797-805.
129. Klunk WE, Debnath ML, Pettegrew JW (1994) Development of small molecule probes for the beta-amyloid protein of Alzheimer's disease. *Neurobiol Aging* 15: 691-698.
130. Klunk WE, Debnath ML, Pettegrew JW (1995) Chrysamine-G binding to Alzheimer and control brain: autopsy study of a new amyloid probe. *Neurobiol Aging* 16: 541-548.
131. Klunk WE, Engler H, Nordberg A, Wang Y, Blomqvist G, et al. (2004) Imaging brain amyloid in Alzheimer's disease with Pittsburgh Compound-B. *Ann Neurol* 55: 306-319.
132. Klunk WE, Lopresti BJ, Ikonovic MD, Lefterov IM, Koldamova RP, et al. (2005) Binding of the positron emission tomography tracer Pittsburgh compound-B reflects the amount of amyloid-beta in Alzheimer's disease brain but not in transgenic mouse brain. *J Neurosci* 25: 10598-10606.
133. Klunk WE, Mathis CA (2008) The future of amyloid-beta imaging: a tale of radionuclides and tracer proliferation. *Curr Opin Neurol* 21: 683-687.
134. Klunk WE, Mathis CA (2008) Whatever happened to Pittsburgh Compound-A? *Alzheimer Dis Assoc Disord* 22: 198-203.
135. Klunk WE, Pettegrew JW, Abraham DJ (1989) Quantitative evaluation of congo red binding to amyloid-like proteins with a beta-pleated sheet conformation. *J Histochem Cytochem* 37: 1273-1281.
136. Klunk WE, Wang Y, Huang GF, Debnath ML, Holt DP, et al. (2001) Uncharged thioflavin-T derivatives bind to amyloid-beta protein with high affinity and readily enter the brain. *Life Sci* 69: 1471-1484.
137. Knoess C, Siegel S, Smith A, Newport D, Richerzhagen N, et al. (2003) Performance evaluation of the microPET R4 PET scanner for rodents. *Eur J Nucl Med Mol Imaging* 30: 737-747.
138. Koo EH, Lansbury PT, Jr., Kelly JW (1999) Amyloid diseases: abnormal protein aggregation in neurodegeneration. *Proc Natl Acad Sci U S A* 96: 9989-9990.
139. Kudo Y, Okamura N, Furumoto S, Tashiro M, Furukawa K, et al. (2007) 2-(2-[2-Dimethylaminothiazol-5-yl]ethenyl)-6- (2-[fluoro]ethoxy)benzoxazole: a novel PET agent for in vivo detection of dense amyloid plaques in Alzheimer's disease patients. *J Nucl Med* 48: 553-561.
140. Kung HF, Kung MP, Zhuang ZP, Hou C, Lee CW, et al. (2003) Iodinated tracers for imaging amyloid plaques in the brain. *Mol Imaging Biol* 5: 418-426.
141. Kung MP, Hou C, Zhuang ZP, Cross AJ, Maier DL, et al. (2004) Characterization of IMPY as a potential imaging agent for beta-amyloid plaques in double transgenic PSAPP mice. *Eur J Nucl Med Mol Imaging* 31: 1136-1145.
142. Kung MP, Hou C, Zhuang ZP, Skovronsky D, Kung HF (2004) Binding of two potential imaging agents targeting amyloid plaques in postmortem brain tissues of patients with Alzheimer's disease. *Brain Res* 1025: 98-105.
143. Kung MP, Hou C, Zhuang ZP, Zhang B, Skovronsky D, et al. (2002) IMPY: an improved thioflavin-T derivative for in vivo labeling of beta-amyloid plaques. *Brain Res* 956: 202-210.

144. Kung MP, Zhuang ZP, Hou C, Jin LW, Kung HF (2003) Characterization of radioiodinated ligand binding to amyloid beta plaques. *J Mol Neurosci* 20: 249-254.
145. Kung MP, Zhuang ZP, Hou C, Kung HF (2004) Development and evaluation of iodinated tracers targeting amyloid plaques for SPECT imaging. *J Mol Neurosci* 24: 49-53.
146. Kuntner C, Kesner AL, Bauer M, Kremslehner R, Wanek T, et al. (2009) Limitations of small animal PET imaging with [<sup>18</sup>F]FDDNP and FDG for quantitative studies in a transgenic mouse model of Alzheimer's disease. *Mol Imaging Biol* 11: 236-240.
147. Kuntner C, Kesner AL, Bauer M, Kremslehner R, Wanek T, et al. (2009) Limitations of Small Animal PET Imaging with [(18)F]FDDNP and FDG for Quantitative Studies in a Transgenic Mouse Model of Alzheimer's Disease. *Mol Imaging Biol*.
148. Kuo YM, Beach TG, Sue LI, Scott S, Layne KJ, et al. (2001) The evolution of A beta peptide burden in the APP23 transgenic mice: implications for A beta deposition in Alzheimer disease. *Mol Med* 7: 609-618.
149. Lachno DR, Romeo MJ, Siemers ER, Vanderstichele H, Coart E, et al. (2011) Validation of ELISA methods for quantification of total tau and phosphorylated-tau181 in human cerebrospinal fluid with measurement in specimens from two Alzheimer's disease studies. *J Alzheimers Dis* 26: 531-541.
150. Lammertsma AA, Bench CJ, Hume SP, Osman S, Gunn K, et al. (1996) Comparison of methods for analysis of clinical [<sup>11</sup>C]raclopride studies. *J Cereb Blood Flow Metab* 16: 42-52.
151. Lassen NA (1992) Neuroreceptor quantitation in vivo by the steady-state principle using constant infusion or bolus injection of radioactive tracers. *J Cereb Blood Flow Metab* 12: 709-716.
152. Lee Y, Back JH, Kim J, Kim SH, Na DL, et al. (2010) Systematic review of health behavioral risks and cognitive health in older adults. *Int Psychogeriatr* 22: 174-187.
153. Levy-Lahad E, Wasco W, Poorkaj P, Romano DM, Oshima J, et al. (1995) Candidate gene for the chromosome 1 familial Alzheimer's disease locus. *Science* 269: 973-977.
154. Lockhart A, Lamb JR, Osredkar T, Sue LI, Joyce JN, et al. (2007) PIB is a non-specific imaging marker of amyloid-beta (A $\beta$ ) peptide-related cerebral amyloidosis. *Brain*.
155. Lockhart A, Ye L, Judd DB, Merritt AT, Lowe PN, et al. (2005) Evidence for the presence of three distinct binding sites for the thioflavin T class of Alzheimer's disease PET imaging agents on beta-amyloid peptide fibrils. *J Biol Chem* 280: 7677-7684.
156. Logan J, Fowler JS, Volkow ND, Wang GJ, Ding YS, et al. (1996) Distribution volume ratios without blood sampling from graphical analysis of PET data. *J Cereb Blood Flow Metab* 16: 834-840.
157. Lomakin A, Chung DS, Benedek GB, Kirschner DA, Teplow DB (1996) On the nucleation and growth of amyloid beta-protein fibrils: detection of nuclei and quantitation of rate constants. *Proc Natl Acad Sci U S A* 93: 1125-1129.
158. Lopresti BJ, Klunk WE, Mathis CA, Hoge JA, Ziolkowski SK, et al. (2005) Simplified quantification of Pittsburgh Compound B amyloid imaging PET studies: a comparative analysis. *J Nucl Med* 46: 1959-1972.
159. Lowenberg K, Waggoner RW (1934) Familial Organic Psychosis (Alzheimer's Type). *Arch Neurol Psychiatry* 31: 737-754.
160. Luengo-Fernandez R, Leal J, Gray AM (2011) Cost of dementia in the pre-enlargement countries of the European Union. *J Alzheimers Dis* 27: 187-196.
161. Maeda J, Ji B, Irie T, Tomiyama T, Maruyama M, et al. (2007) Longitudinal, quantitative assessment of amyloid, neuroinflammation, and anti-amyloid treatment in a living mouse model of Alzheimer's disease enabled by positron emission tomography. *J Neurosci* 27: 10957-10968.
162. Mahler ME, Cummings JL, Benson DF (1987) Treatable dementias. *West J Med* 146: 705-712.
163. Maiorini AF, Gaunt MJ, Jacobsen TM, McKay AE, Waldman LD, et al. (2002) Potential novel targets for Alzheimer pharmacotherapy: I. Secretases. *J Clin Pharm Ther* 27: 169-183.
164. Manook A, Yousefi BH, Willuweit A, Platzer S, Reder S, et al. (2012) Small-Animal PET Imaging of Amyloid-Beta Plaques with [<sup>11</sup>C]PiB and Its Multi-Modal Validation in an APP/PS1 Mouse Model of Alzheimer's Disease. *PLoS ONE* 7: e31310.

165. Mark RJ, Pang Z, Geddes JW, Uchida K, Mattson MP (1997) Amyloid beta-peptide impairs glucose transport in hippocampal and cortical neurons: involvement of membrane lipid peroxidation. *J Neurosci* 17: 1046-1054.
166. Masliah E, Crews L, Hansen L (2006) Synaptic remodeling during aging and in Alzheimer's disease. *J Alzheimers Dis* 9: 91-99.
167. Masuda H, Okano HJ, Maruyama T, Yoshimura Y, Okano H, et al. (2008) In vivo imaging in humanized mice. *Curr Top Microbiol Immunol* 324: 179-196.
168. Mathis CA, Bacskai BJ, Kajdasz ST, McLellan ME, Frosch MP, et al. (2002) A lipophilic thioflavin-T derivative for positron emission tomography (PET) imaging of amyloid in brain. *Bioorg Med Chem Lett* 12: 295-298.
169. Mathis CA, Wang Y, Holt DP, Huang GF, Debnath ML, et al. (2003) Synthesis and evaluation of <sup>11</sup>C-labeled 6-substituted 2-arylbenzothiazoles as amyloid imaging agents. *J Med Chem* 46: 2740-2754.
170. Maurer K (2006) Historical background of Alzheimer's research done 100 years ago. *J Neural Transm* 113: 1597-1601.
171. Maurer U (2002) *Alois Alzheimer - His Life and Work with Text and Photographs*; Maurer K, editor. Marburg: Pre Press Print Production Service & Verlag. 190 p.
172. McGowan E, Sanders S, Iwatsubo T, Takeuchi A, Saido T, et al. (1999) Amyloid phenotype characterization of transgenic mice overexpressing both mutant amyloid precursor protein and mutant presenilin 1 transgenes. *Neurobiol Dis* 6: 231-244.
173. McKhann G, Drachman D, Folstein M, Katzman R, Price D, et al. (1984) Clinical diagnosis of Alzheimer's disease: report of the NINCDS-ADRDA Work Group under the auspices of Department of Health and Human Services Task Force on Alzheimer's Disease. *Neurology* 34: 939-944.
174. McKhann GM, Knopman DS, Chertkow H, Hyman BT, Jack CR, Jr., et al. (2011) The diagnosis of dementia due to Alzheimer's disease: Recommendations from the National Institute on Aging-Alzheimer's Association workgroups on diagnostic guidelines for Alzheimer's disease. *Alzheimers Dement* 7: 263-269.
175. Meyer PT, Hellwig S, Amtage F, Rottenburger C, Sahm U, et al. (2011) Dual-Biomarker Imaging of Regional Cerebral Amyloid Load and Neuronal Activity in Dementia with PET and <sup>11</sup>C-Labeled Pittsburgh Compound B. *J Nucl Med* 52: 393-400.
176. Mirra SS, Heyman A, McKeel D, Sumi SM, Crain BJ, et al. (1991) The Consortium to Establish a Registry for Alzheimer's Disease (CERAD). Part II. Standardization of the neuropathologic assessment of Alzheimer's disease. *Neurology* 41: 479-486.
177. Mizuta T, Kitamura K, Iwata H, Yamagishi Y, Ohtani A, et al. (2008) Performance evaluation of a high-sensitivity large-aperture small-animal PET scanner: ClairvivoPET. *Ann Nucl Med* 22: 447-455.
178. Moghbel MC, Saboury B, Basu S, Metzler SD, Torigian DA, et al. (2012) Amyloid-beta imaging with PET in Alzheimer's disease: is it feasible with current radiotracers and technologies? *Eur J Nucl Med Mol Imaging* 39: 202-208.
179. Murrell J, Farlow M, Ghetti B, Benson MD (1991) A mutation in the amyloid precursor protein associated with hereditary Alzheimer's disease. *Science* 254: 97-99.
180. Mustafiz T, Portelius E, Gustavsson MK, Holtta M, Zetterberg H, et al. (2011) Characterization of the Brain beta-Amyloid Isoform Pattern at Different Ages of Tg2576 Mice. *Neurodegener Dis*.
181. Nesterov EE, Skoch J, Hyman BT, Klunk WE, Bacskai BJ, et al. (2005) In vivo optical imaging of amyloid aggregates in brain: design of fluorescent markers. *Angew Chem Int Ed Engl* 44: 5452-5456.
182. Newberg AB, Wintering NA, Plossl K, Hochold J, Stabin MG, et al. (2006) Safety, biodistribution, and dosimetry of <sup>123</sup>I-IMPY: a novel amyloid plaque-imaging agent for the diagnosis of Alzheimer's disease. *J Nucl Med* 47: 748-754.
183. Nicoll JA, Wilkinson D, Holmes C, Steart P, Markham H, et al. (2003) Neuropathology of human Alzheimer disease after immunization with amyloid-beta peptide: a case report. *Nat Med* 9: 448-452.

184. Niwa K, Kazama K, Younkin SG, Carlson GA, Iadecola C (2002) Alterations in cerebral blood flow and glucose utilization in mice overexpressing the amyloid precursor protein. *Neurobiol Dis* 9: 61-68.
185. Noda A, Murakami Y, Nishiyama S, Fukumoto D, Miyoshi S, et al. (2008) Amyloid imaging in aged and young macaques with [<sup>11</sup>C]PIB and [<sup>18</sup>F]FDDNP. *Synapse* 62: 472-475.
186. Okamura N, Suemoto T, Shimadzu H, Suzuki M, Shiomitsu T, et al. (2004) Styrylbenzoxazole derivatives for in vivo imaging of amyloid plaques in the brain. *J Neurosci* 24: 2535-2541.
187. Okamura N, Suemoto T, Shiomitsu T, Suzuki M, Shimadzu H, et al. (2004) A novel imaging probe for in vivo detection of neuritic and diffuse amyloid plaques in the brain. *J Mol Neurosci* 24: 247-255.
188. Ono M, Watanabe R, Kawashima H, Cheng Y, Kimura H, et al. (2009) Fluoro-pegylated chalcones as positron emission tomography probes for in vivo imaging of beta-amyloid plaques in Alzheimer's disease. *J Med Chem* 52: 6394-6401.
189. Ono M, Watanabe R, Kawashima H, Kawai T, Watanabe H, et al. (2009) (<sup>18</sup>F)-labeled flavones for in vivo imaging of beta-amyloid plaques in Alzheimer's brains. *Bioorg Med Chem*.
190. Ono M, Wilson A, Nobrega J, Westaway D, Verhoeff P, et al. (2003) <sup>11</sup>C-labeled stilbene derivatives as Abeta-aggregate-specific PET imaging agents for Alzheimer's disease. *Nucl Med Biol* 30: 565-571.
191. Pfluger T, Vollmar C, Wismuller A, Dresel S, Berger F, et al. (2000) Quantitative comparison of automatic and interactive methods for MRI-SPECT image registration of the brain based on 3-dimensional calculation of error. *J Nucl Med* 41: 1823-1829.
192. Philipson O, Lord A, Gumucio A, O'Callaghan P, Lannfelt L, et al. (2010) Animal models of amyloid-beta-related pathologies in Alzheimer's disease. *Febs J* 277: 1389-1409.
193. Poisnel G, Dhilly M, Moustie O, Delamare J, Abbas A, et al. (2012) PET imaging with [<sup>18</sup>F]AV-45 in an APP/PS1-21 murine model of amyloid plaque deposition. *Neurobiol Aging*.
194. Price JC, Klunk WE, Lopresti BJ, Lu X, Hoge JA, et al. (2005) Kinetic modeling of amyloid binding in humans using PET imaging and Pittsburgh Compound-B. *J Cereb Blood Flow Metab* 25: 1528-1547.
195. Prusiner SB (1984) Some speculations about prions, amyloid, and Alzheimer's disease. *N Engl J Med* 310: 661-663.
196. Querfurth HW, LaFerla FM (2010) Alzheimer's disease. *N Engl J Med* 362: 329-344.
197. Radde R, Bolmont T, Kaeser SA, Coomaraswamy J, Lindau D, et al. (2006) Abeta42-driven cerebral amyloidosis in transgenic mice reveals early and robust pathology. *EMBO Rep* 7: 940-946.
198. Radde R, Duma C, Goedert M, Jucker M (2008) The value of incomplete mouse models of Alzheimer's disease. *Eur J Nucl Med Mol Imaging* 35 Suppl 1: S70-74.
199. Raymond S, Skoch J, Hills I, Nesterov E, Swager T, et al. (2008) Smart optical probes for near-infrared fluorescence imaging of Alzheimer's disease pathology. *European Journal of Nuclear Medicine and Molecular Imaging* 35: 93-98.
200. Richards JG, Higgins GA, Ouagazzal AM, Ozmen L, Kew JN, et al. (2003) PS2APP transgenic mice, coexpressing hPS2mut and hAPP<sup>swe</sup>, show age-related cognitive deficits associated with discrete brain amyloid deposition and inflammation. *J Neurosci* 23: 8989-9003.
201. Rinne JO, Brooks DJ, Rossor MN, Fox NC, Bullock R, et al. (2010) <sup>11</sup>C-PiB PET assessment of change in fibrillar amyloid-beta load in patients with Alzheimer's disease treated with bapineuzumab: a phase 2, double-blind, placebo-controlled, ascending-dose study. *Lancet Neurol* 9: 363-372.
202. Rogaeve EI, Sherrington R, Rogaeve EA, Levesque G, Ikeda M, et al. (1995) Familial Alzheimer's disease in kindreds with missense mutations in a gene on chromosome 1 related to the Alzheimer's disease type 3 gene. *Nature* 376: 775-778.
203. Rowe CC, Ackerman U, Browne W, Mulligan R, Pike KL, et al. (2008) Imaging of amyloid beta in Alzheimer's disease with <sup>18</sup>F-BAY94-9172, a novel PET tracer: proof of mechanism. *Lancet Neurol* 7: 129-135.

204. Rowe CC, Villemagne VL (2011) Brain Amyloid Imaging. *Journal of nuclear medicine : official publication, Society of Nuclear Medicine*.
205. Salloway S, Sperling R, Gilman S, Fox NC, Blennow K, et al. (2009) A phase 2 multiple ascending dose trial of bapineuzumab in mild to moderate Alzheimer disease. *Neurology* 73: 2061-2070.
206. Samaroo HD, Opsahl AC, Schreiber J, O'Neill SM, Marconi M, et al. (2011) High throughput object-based image analysis of beta-amyloid plaques in human and transgenic mouse brain. *J Neurosci Methods*.
207. Saraiva AA, Borges MM, Madeira MD, Tavares MA, Paula-Barbosa MM (1985) Mitochondrial abnormalities in cortical dendrites from patients with Alzheimer's disease. *J Submicrosc Cytol* 17: 459-464.
208. Schafers KP, Reader AJ, Kriens M, Knoess C, Schober O, et al. (2005) Performance evaluation of the 32-module quadHIDAC small-animal PET scanner. *J Nucl Med* 46: 996-1004.
209. Schellenberg GD, Bird TD, Wijsman EM, Orr HT, Anderson L, et al. (1992) Genetic linkage evidence for a familial Alzheimer's disease locus on chromosome 14. *Science* 258: 668-671.
210. Schenk D, Barbour R, Dunn W, Gordon G, Grajeda H, et al. (1999) Immunization with amyloid-beta attenuates Alzheimer-disease-like pathology in the PDAPP mouse. *Nature* 400: 173-177.
211. Scheuner D, Eckman C, Jensen M, Song X, Citron M, et al. (1996) Secreted amyloid beta-protein similar to that in the senile plaques of Alzheimer's disease is increased in vivo by the presenilin 1 and 2 and APP mutations linked to familial Alzheimer's disease. *Nat Med* 2: 864-870.
212. Schiffer WK, Mirrione MM, Biegon A, Alexoff DL, Patel V, et al. (2006) Serial microPET measures of the metabolic reaction to a microdialysis probe implant. *J Neurosci Methods* 155: 272-284.
213. Schiffer WK, Mirrione MM, Dewey SL (2007) Optimizing experimental protocols for quantitative behavioral imaging with 18F-FDG in rodents. *J Nucl Med* 48: 277-287.
214. Schöll M, Almkvist O, Graff C, Nordberg A (2011) Amyloid imaging in members of a family harbouring the Arctic APP mutation. *Alzheimer's & dementia : the journal of the Alzheimer's Association* 7: S303.
215. Schoonenboom NS, Mulder C, Vanderstichele H, Van Elk EJ, Kok A, et al. (2005) Effects of processing and storage conditions on amyloid beta (1-42) and tau concentrations in cerebrospinal fluid: implications for use in clinical practice. *Clin Chem* 51: 189-195.
216. Sedgewick G (2008) *Scientific Imaging with Photoshop: Methods, Measurement, and Output*. Berkeley, CA, USA: New Riders. 312 p.
217. Seidel J, Vaquero JJ, Green MV (2003) Resolution uniformity and sensitivity of the NIH ATLAS small animal PET scanner: Comparison to simulated LSO scanners without depth-of-interaction capability. *IEEE Trans Nucl Sci* 50: 1347-1350.
218. Selkoe DJ (2002) Alzheimer's disease is a synaptic failure. *Science* 298: 789-791.
219. Selkoe DJ, Bell DS, Podlisny MB, Price DL, Cork LC (1987) Conservation of brain amyloid proteins in aged mammals and humans with Alzheimer's disease. *Science* 235: 873-877.
220. Seneca N, Cai L, Liow JS, Zoghbi S, Gladding R, et al. (2009) Low Retention of [S-methyl-11C]MeS-IMPY to Beta-Amyloid Plaques in Patients with Alzheimer's Disease. *Curr Radiopharm* 2: 129-136.
221. Seneca N, Cai L, Liow JS, Zoghbi SS, Gladding RL, et al. (2007) Brain and whole-body imaging in nonhuman primates with [11C]MeS-IMPY, a candidate radioligand for beta-amyloid plaques. *Nucl Med Biol* 34: 681-689.
222. Serdons K, Van Laere K, Janssen P, Kung HF, Bormans G, et al. (2009) Synthesis and evaluation of three 18F-labeled aminophenylbenzothiazoles as amyloid imaging agents. *J Med Chem* 52: 7090-7102.
223. Serdons K, Verduyck T, Vanderghinste D, Cleynhens J, Borghgraef P, et al. (2009) Synthesis of 18F-labelled 2-(4'-fluorophenyl)-1,3-benzothiazole and evaluation as amyloid imaging agent in comparison with [11C]PIB. *Bioorg Med Chem Lett* 19: 602-605.
224. Sherrington R, Rogaev EI, Liang Y, Rogaeva EA, Levesque G, et al. (1995) Cloning of a gene bearing missense mutations in early-onset familial Alzheimer's disease. *Nature* 375: 754-760.

225. Shoghi KI (2009) Quantitative small animal PET. *Q J Nucl Med Mol Imaging* 53: 365-373.
226. Shoghi-Jadid K, Small GW, Agdeppa ED, Kepe V, Ercoli LM, et al. (2002) Localization of neurofibrillary tangles and beta-amyloid plaques in the brains of living patients with Alzheimer disease. *Am J Geriatr Psychiatry* 10: 24-35.
227. Sigurdsson EM, Wisniewski T, Frangione B (2002) Infectivity of amyloid diseases. *Trends Mol Med* 8: 411-413.
228. Sokoloff L, Reivich M, Kennedy C, Des Rosiers MH, Patlak CS, et al. (1977) The [<sup>14</sup>C]deoxyglucose method for the measurement of local cerebral glucose utilization: theory, procedure, and normal values in the conscious and anesthetized albino rat. *J Neurochem* 28: 897-916.
229. Sperling RA, Aisen PS, Beckett LA, Bennett DA, Craft S, et al. (2011) Toward defining the preclinical stages of Alzheimer's disease: Recommendations from the National Institute on Aging-Alzheimer's Association workgroups on diagnostic guidelines for Alzheimer's disease. *Alzheimers Dement* 7: 280-292.
230. Sperling RA, Johnson KA (2012) Dementia: new criteria but no new treatments. *Lancet Neurol* 11: 4-5.
231. Storandt M, Head D, Fagan AM, Holtzman DM, Morris JC (2012) Toward a multifactorial model of Alzheimer disease. *Neurobiol Aging*.
232. Sturchler-Pierrat C, Abramowski D, Duke M, Wiederhold KH, Mistl C, et al. (1997) Two amyloid precursor protein transgenic mouse models with Alzheimer disease-like pathology. *Proc Natl Acad Sci U S A* 94: 13287-13292.
233. Sturchler-Pierrat C, Staufenbiel M (2000) Pathogenic mechanisms of Alzheimer's disease analyzed in the APP23 transgenic mouse model. *Ann N Y Acad Sci* 920: 134-139.
234. Suemoto T, Okamura N, Shiomitsu T, Suzuki M, Shimadzu H, et al. (2004) In vivo labeling of amyloid with BF-108. *Neurosci Res* 48: 65-74.
235. Suthana N, Haneef Z, Stern J, Mukamel R, Behnke E, et al. (2012) Memory enhancement and deep-brain stimulation of the entorhinal area. *N Engl J Med* 366: 502-510.
236. Svedberg MM, Rahman O, Hall H (2012) Preclinical studies of potential amyloid binding PET/SPECT ligands in Alzheimer's disease. *Nucl Med Biol*.
237. Tai C, Chatziioannou A, Siegel S, Young J, Newport D, et al. (2001) Performance evaluation of the microPET P4: a PET system dedicated to animal imaging. *Phys Med Biol* 46: 1845-1862.
238. Tai YC, Ruangma A, Rowland D, Siegel S, Newport DF, et al. (2005) Performance evaluation of the microPET focus: a third-generation microPET scanner dedicated to animal imaging. *J Nucl Med* 46: 455-463.
239. Tanzi RE, Bertram L (2005) Twenty years of the Alzheimer's disease amyloid hypothesis: a genetic perspective. *Cell* 120: 545-555.
240. Tanzi RE, Gusella JF, Watkins PC, Bruns GA, St George-Hyslop P, et al. (1987) Amyloid beta protein gene: cDNA, mRNA distribution, and genetic linkage near the Alzheimer locus. *Science* 235: 880-884.
241. Teipel SJ, Buchert R, Thome J, Hampel H, Pahnke J (2011) Development of Alzheimer-disease neuroimaging-biomarkers using mouse models with amyloid-precursor protein-transgene expression. *Prog Neurobiol*.
242. Teng E, Kepe V, Frautschy SA, Liu J, Satyamurthy N, et al. (2011) [<sup>18</sup>F]-FDDNP microPET imaging correlates with brain Abeta burden in a transgenic rat model of Alzheimer disease: Effects of aging, in vivo blockade, and anti-Abeta antibody treatment. *Neurobiol Dis*.
243. Ter-Pogossian MM, Phelps ME, Hoffman EJ, Mullani NA (1975) A positron-emission transaxial tomograph for nuclear imaging (PETT). *Radiology* 114: 89-98.
244. Thie JA (2004) Understanding the standardized uptake value, its methods, and implications for usage. *J Nucl Med* 45: 1431-1434.
245. Toyama H, Ye D, Ichise M, Liow JS, Cai L, et al. (2005) PET imaging of brain with the beta-amyloid probe, [<sup>11</sup>C]6-OH-BTA-1, in a transgenic mouse model of Alzheimer's disease. *Eur J Nucl Med Mol Imaging* 32: 593-600.

246. Tycko R (2006) Molecular structure of amyloid fibrils: insights from solid-state NMR. *Q Rev Biophys* 39: 1-55.
247. Tycko R (2006) Solid-state NMR as a probe of amyloid structure. *Protein Pept Lett* 13: 229-234.
248. US Department of Health & Human Services H. Fact Sheet: We Can't Wait: Taking Action on Alzheimer's Disease. US Department of Health & Human Services, (HSS). Available at: [http://www.hhs.gov/news/press/2012pres/02/factsheet\\_alzheimers.html](http://www.hhs.gov/news/press/2012pres/02/factsheet_alzheimers.html). Accessed: 8 February 2012
249. Valenzuela MJ, Sachdev P (2006) Brain reserve and dementia: a systematic review. *Psychol Med* 36: 441-454.
250. van Groen T, Kiliaan AJ, Kadish I (2006) Deposition of mouse amyloid beta in human APP/PS1 double and single AD model transgenic mice. *Neurobiol Dis*.
251. Vanderstichele H, Van Kerschaver E, Hesse C, Davidsson P, Buyse MA, et al. (2000) Standardization of measurement of beta-amyloid(1-42) in cerebrospinal fluid and plasma. *Amyloid* 7: 245-258.
252. Vassar PS, Culling FA (1959) Fluorescent stains with special reference to amyloid and connective tissue. *Arch Pathol* 68: 487.
253. Vaughan DW, Peters A (1981) The structure of neuritic plaque in the cerebral cortex of aged rats. *J Neuropathol Exp Neurol* 40: 472-487.
254. Villemagne VL, Klunk WE, Mathis CA, Rowe CC, Brooks DJ, et al. (2012) Abeta Imaging: feasible, pertinent, and vital to progress in Alzheimer's disease. *Eur J Nucl Med Mol Imaging* 39: 209-219.
255. Vina J, Lloret A (2010) Why women have more Alzheimer's disease than men: gender and mitochondrial toxicity of amyloid-beta peptide. *J Alzheimers Dis* 20 Suppl 2: S527-533.
256. Virdee K, Cumming P, Caprioli D, Jupp B, Rominger A, et al. (2012) Applications of positron emission tomography in animal models of neurological and neuropsychiatric disorders. *Neurosci Biobehav Rev*.
257. Visser EP, Disselhorst JA, Brom M, Laverman P, Gotthardt M, et al. (2009) Spatial resolution and sensitivity of the Inveon small-animal PET scanner. *J Nucl Med* 50: 139-147.
258. von Kienlin M, Kunnecke B, Metzger F, Steiner G, Richards JG, et al. (2005) Altered metabolic profile in the frontal cortex of PS2APP transgenic mice, monitored throughout their life span. *Neurobiol Dis* 18: 32-39.
259. Vowles GH, Francis RJ (2002) Amyloid. In: Bancroft JD, Gamble M, editors. *Theory and Practice of Histological Techniques*. 5th ed. Edinburgh: Churchill Livingstone. pp. 303-324.
260. Wagner HN, Jr. (1998) A brief history of positron emission tomography (PET). *Semin Nucl Med* 28: 213-220.
261. Wang J, Tanila H, Puolivali J, Kadish I, van Groen T (2003) Gender differences in the amount and deposition of amyloidbeta in APP<sup>sw</sup> and PS1 double transgenic mice. *Neurobiol Dis* 14: 318-327.
262. Wang Y, Seidel J, Tsui BM, Vaquero JJ, Pomper MG (2006) Performance evaluation of the GE healthcare eXplore VISTA dual-ring small-animal PET scanner. *J Nucl Med* 47: 1891-1900.
263. Wengenack TM, Reyes DA, Curran GL, Borowski BJ, Lin J, et al. (2011) Regional differences in MRI detection of amyloid plaques in AD transgenic mouse brain. *Neuroimage* 54: 113-122.
264. Wengenack TM, Whelan S, Curran GL, Duff KE, Poduslo JF (2000) Quantitative histological analysis of amyloid deposition in Alzheimer's double transgenic mouse brain. *Neuroscience* 101: 939-944.
265. Whitehouse PJ, George DR, D'Alton S (2011) Describing the dying days of "Alzheimer's disease". *J Alzheimers Dis* 24: 11-13.
266. Wilcock DM, Colton CA (2009) Immunotherapy, vascular pathology, and microhemorrhages in transgenic mice. *CNS Neurol Disord Drug Targets* 8: 50-64.
267. Willuweit A, Velden J, Godemann R, Manook A, Jetzek F, et al. (2009) Early-onset and robust amyloid pathology in a new homozygous mouse model of Alzheimer's disease. *PLoS ONE* 4: e7931.

268. Wimo A, Jonsson L, Gustavsson A, McDaid D, Ersek K, et al. (2011) The economic impact of dementia in Europe in 2008-cost estimates from the Eurocode project. *Int J Geriatr Psychiatry* 26: 825-832.
269. Wirhth O, Multhaup G, Czech C, Blanchard V, Moussaoui S, et al. (2001) Intraneuronal Abeta accumulation precedes plaque formation in beta-amyloid precursor protein and presenilin-1 double-transgenic mice. *Neurosci Lett* 306: 116-120.
270. Wisniewski T, Sadowski M (2008) Preventing beta-amyloid fibrillization and deposition: beta-sheet breakers and pathological chaperone inhibitors. *BMC Neurosci* 9 Suppl 2: S5.
271. World Health Organization W. International Statistical Classification of Diseases and Related Health Problems 10th Revision. World Health Organization (WHO). Available at: <http://apps.who.int/classifications/icd10/browse/2010/en>.
272. Wyss-Coray T, Mucke L (2002) Inflammation in neurodegenerative disease--a double-edged sword. *Neuron* 35: 419-432.
273. Yan P, Bero AW, Cirrito JR, Xiao Q, Hu X, et al. (2009) Characterizing the appearance and growth of amyloid plaques in APP/PS1 mice. *J Neurosci* 29: 10706-10714.
274. Ye L, Morgenstern JL, Lamb JR, Lockhart A (2006) Characterisation of the binding of amyloid imaging tracers to rodent Abeta fibrils and rodent-human Abeta co-polymers. *Biochem Biophys Res Commun* 347: 669-677.
275. Younkin SG (1998) The role of A beta 42 in Alzheimer's disease. *J Physiol Paris* 92: 289-292.
276. Yousefi B, Manook A, Reutern BV, Schwaiger M, Drzezga A, et al. (2012) Development of an improved radioiodinated 2-phenylimidazo[1,2-a]pyridine for non-invasive imaging of amyloid plaques. *MedChemComm* 3: 775-779.
277. Yousefi BH, Drzezga A, von Reutern B, Manook A, Schwaiger M, et al. (2011) A novel 18F-labeled imidazo[2,1-b]benzothiazole (IBT) for high-contrast PET imaging of  $\beta$ -amyloid plaques. *ACS Medicinal Chemistry Letters* 2: 673-677.
278. Yousefi BH, Manook A, Drzezga A, von Reutern B, Schwaiger M, et al. (2011) Synthesis and evaluation of 11C-labeled imidazo[2,1-b]benzothiazoles (IBTs) as PET tracers for imaging beta-amyloid plaques in Alzheimer's disease. *J Med Chem* 54: 949-956.
279. Zhang W, Oya S, Kung MP, Hou C, Maier DL, et al. (2005) F-18 stilbenes as PET imaging agents for detecting beta-amyloid plaques in the brain. *J Med Chem* 48: 5980-5988.
280. Zheng MQ, Yin DZ, Zhang L, Lei B, Cheng DF, et al. (2008) Biological characters of [18F]O-FEt-PIB in a rat model of Alzheimer's disease using micro-PET imaging. *Acta Pharmacol Sin* 29: 548-554.
281. Zhuang ZP, Kung MP, Wilson A, Lee CW, Plossl K, et al. (2003) Structure-activity relationship of imidazo[1,2-a]pyridines as ligands for detecting beta-amyloid plaques in the brain. *J Med Chem* 46: 237-243.





